Searches for new non-resonant phenomena in high-mass dilepton final states with the ATLAS detector at the Large Hadron Collider

Deshan Kavishka Abhayasinghe

Department of Physics
Royal Holloway, University of London

A thesis submitted to the University of London
for the degree of Doctor of Philosophy

Declaration

I declare that the work presented in this thesis is my own. Where the work of others has been consulted, this has been indicated in the text.

Chapters 2, 3, 5, and 6 provide descriptions of the theoretical and experimental topics that are relevant for this thesis. The chapters were written based on previous literature, which include: papers, technical reports and academic text. I was one of two analysis contacts for the result presented in this thesis, which included planning the analysis and leading team members towards publication of the result [1]. Chapters 7 and 8 include work carried out in collaboration with the team, where work by members of the group have been explicitly referenced. My original work in close collaboration with the other analysis contact is presented in Chapters 4 and 10 to 12. In addition, the other contact and I created and developed the framework used for the background estimation and statistical analysis of the results. All plots and tables in this thesis were produced by me, unless otherwise stated.

Furthermore, I performed the statistical analysis in the search for contact interactions in the electron channel at $\sqrt{s} = 13\,\text{TeV}$ with an integrated luminosity of $36.1\,\text{fb}^{-1}$ [2]. Additionally, I worked in collaboration on a complementary background estimation procedure for the dilepton resonance search performed at $\sqrt{s} = 13\,\text{TeV}$ with an integrated luminosity of $139\,\text{fb}^{-1}$ [3]. These analyses are not discussed explicitly the thesis.

Deshan Kavishka Abhayasinghe
July 2020

Abstract

A search for new physics with non-resonant signals in dielectron and dimuon final states in mass ranges above 2 TeV is presented. The data, corresponding to an integrated luminosity of 139 fb^{-1}, were recorded by the ATLAS experiment in proton–proton collisions at a centre-of-mass energy of 13 TeV during Run-2 of the Large Hadron Collider. A data-driven background extrapolation procedure is utilised to model the contribution from background processes. The benchmark signal model considered is the four-fermion contact-interaction, which results in an enhancement of the dilepton event rate at the TeV mass scale. No significant deviation from the expected background is observed in data. Observed and expected 95% CL limits on the contact interaction energy scale reach 35.8 TeV and 37.6 TeV, respectively. In addition, 95% CL limits on the number of events and visible cross section times branching fraction for new physics processes are provided.

Acknowledgements

First, and foremost, I would like to thank Véronique Boisvert, I am eternally grateful for her encouragement, support and patience throughout my PhD. My thanks is extended to Tracey Berry for giving me this amazing opportunity. I would like to thank Glen Cowan for passing down his wisdom on all things statistics. I would also like to thank the ATLAS group at Royal Holloway for many interesting and useful discussions that have helped me with my research.

I would like to thank Aaron White for working with me as analysis contact over the course of the analysis and putting up with me. I can confidently say this analysis would not be possible without his help. I am thankful for the extensive discussions, never-ending meetings, and arduous debugging sessions we had.

There were numerous people that have made my time at CERN enjoyable. David and Joe for their friendship. Adam for the many hours we have spent discussing statistical concepts and his continued friendship and support during my PhD. Noam Tal Hod for acting as a surrogate supervisor at CERN and putting up with my endless questions. The dilepton analysis team for the collaboration and the feedback during our many meetings. My flatmates Lewis Wilkins and Eddie Thorpe who kept me sane throughout my time at CERN. Special thanks must go to Lewis, we started our PhD together at Royal Holloway and he has been an invaluable friend throughout my PhD. I do not think I have spent more time with any one person than I have with Lewis during my time at CERN and there has never been a dull moment.

To Vasilis and Umit, who have been a constant throughout my entire education, thank you for all the crazy adventures and for always being there. Neil and Chanat, my oldest friends, I am grateful for the many dinners, nights out and welcome distractions you have provided me, which have kept me sane.

No words can express my gratitude towards my family. Amma, Thatha and Manji, I would not be the person I am today without you. I owe you everything.

To Natalia, who has been with me from the start of this journey. You have stayed with me through all of my ups and down, travelling and the countless late nights that I had to spend working. Thank you for all of your love, support and encouragement. $\Sigma\epsilon'$ $\alpha\gamma\alpha\pi\acute{\omega}$.

Contents

Figures

Tables

In memory of Sudheera Nanayakkara (Ammi)

Chapter 1

Introduction

The Standard Model of particle physics has had tremendous success in providing a description of the known universe. There has been excellent agreement between Standard Model predictions and experimental observations from particle physics experiments. The most recent validation of the Standard Model was via the observation of the Higgs boson by the ATLAS and CMS experiments at the LHC in 2012 [7, 8].

Despite the successes of the Standard Model, the theory fails to describe a range of observations, mostly from non-collider physics experiments. First and foremost of these phenomena is gravity, which is not included in the Standard Model. Additionally, from a cosmological view, the Standard Model constituents compose only 4.9% of the observed universe [9, 10]. The remaining contributions come from *dark matter* and *dark energy*. Another experimental hint from cosmology is the matter/ anti-matter asymmetry in the universe. These signatures hint at the existence of physics beyond the Standard Model.

The Standard Model currently includes all of the known particles, however physics beyond the standard model indicates that there may be more particles yet to be discovered. Such new particles may not have yet been discovered as the energy required to produce them might be larger than what is achieved by current accelerators, and hence can not be searched for in conventional resonance searches. However, it is possible to detect the effects processes in low-energy regimes in the form of non-resonant signatures. Previously, such searches had relied

on the production of Monte Carlo to model the background and signal processes, where samples with very large numbers of events were needed to be produced, resulting in huge demands on the available computing resources. Additionally, there was a large impact on the analysis from uncertainties on the parton density function (PDF). These uncertainties were not calculated in a clearly defined method, and in some cases an overestimate of the uncertainty was provided. To reduce the strain on resources from the Monte Carlo and to reduce the effects of the PDF uncertainties the analysis discussed in this thesis presents a novel data-driven approach to search for non-resonant phenomena in dilepton final states. The analysis presented in this thesis has been published by the ATLAS experiment [1].

The thesis is organised in the following way. Chapter 2 provides an overview of the Standard Model of particle physics. Chapter 3 motivates the search for beyond the Standard Model physics, and provides a brief overview of effective field theories. The chapter concludes with a description of the benchmark contact interaction model searched for in this thesis. Chapter 5 provides an overview of the LHC accelerator and infrastructure, where a detailed outline of the ATLAS detector and its components are provided. The production and use of Monte Carlo simulations and the reconstruction and identification of physics objects are outlined in Chapter 6. The event selection applied to the data is provided in Chapter 7. Chapter 8 outlines the data, background and signal samples, and their associated uncertainties are described in Chapter 9. The data-driven background estimation method is described in Chapter 10 and the uncertainties associated with the estimate is described in Chapter 11. A detailed description of the statistical analysis is given in Chapter 4. Finally, the results are presented in Chapter 12.

Part I

Theory

Chapter 2

The Standard Model of particle physics

The Standard Model (SM) of particle physics is a quantum field theory (QFT) with multiple interacting fields and symmetries. It was developed during the second half of the 20^{th} century. There has been excellent agreement between the predictions of the SM and experimental data from particle physics experiments. An overview of the standard model is presented in Section 2.1. The SM Lagrangian is described in Section 2.2, outlining each of its components.

2.1 Introduction

Fundamental mathematical concepts

The mathematical structure of the SM is given by a gauge quantum field theory [11]. In both classical and quantum field theory, the dynamics of a system are described by the Lagrangian density, which henceforth will be referred to simply as the Lagrangian. Consider the Lagrangian for a massive complex field, ψ, with mass, m,

$$\mathcal{L} = \partial^{\mu}\bar{\psi}\partial_{\mu}\psi - m\bar{\psi}\psi, \tag{2.1}$$

where the first term is referred to as the kinetic term and the second term is the mass term of the field. The Lagrangian can be used to calculate the scattering amplitudes of reactions using

well-defined methods [12] and the interactions can be expressed in terms of diagrams known as Feynman diagrams [13]. The use of Feynman diagrams simplifies the process of calculation of the scattering amplitudes.

In natural units, all quantities are measured in units of powers of energy. For example, $[m] = E^1$, where $[m]$ corresponds to the dimensionality of m. The fundamental quantity in mechanics is the action, S, the time integral of a Lagrangian [11]

$$S = \int \mathcal{L}\, d^4x. \tag{2.2}$$

The principle of least action states that when a system evolves from one configuration to another with a given time, it does so along the *path* for which S is a minimum. The action is dimensionless, therefore the Lagrangian has dimensionality $[\mathcal{L}] = E^4$.

Symmetries are central to our current understanding of particle physics. In particle physics, a symmetry of the universe is expressed by requiring that all physical predictions are unchanged or invariant under the same set of transformations. The importance of the concept of symmetries originates from Noether's theorem [14], stipulating that for every continuous symmetry there is a corresponding conservation law. In the context of field theory, one of the cornerstones in the construction of the SM is the notion of gauge symmetry. The Lagrangian defined in Equation 2.1 is invariant with respect to rotation with angle α in the complex plane

$$\psi(x) \to \psi(x)e^{i\alpha}\ ,\ \bar{\psi}(x) \to \bar{\psi}e^{-i\alpha}. \tag{2.3}$$

Therefore, it can be said that the Lagrangian is invariant under global one-dimensional unitary transformations, U(1), where global denotes that α is the same for any value of x [15]. However, if α depends on x the U(1) symmetry is broken. Hence, the Lagrangian is not invariant under a local U(1) transformation. The required gauge invariance can be restored by replacing the derivative in Equation 2.1 with a *covariant* derivative, D_μ, defined as

$$D_\mu = \partial_\mu + iqA_\mu(x), \tag{2.4}$$

where $A_\mu(x)$ is a new field that transforms as $A_\mu \rightarrow A_\mu - \frac{1}{q}\partial_\mu\alpha(x)$ and q is the coupling strength between the field ψ and A_μ. Therefore, the Lagrangian is now invariant under local U(1) transformation. The introduced field, A_μ, is known as a *gauge field*, and the Lagrangian under these modifications is known as a *gauge theory*. The number of gauge fields required to restore a given local symmetry is related to the number of generators in the symmetry group, for example, U(1) is a symmetry group with one generator, which results in the addition of a single gauge field.

Overview of Standard Model

The SM is a gauge theory that describes elementary particles and their fundamental interactions (excluding gravity). Interactions of the SM are considered in terms of fields, ψ, of half-integer spin fermions and integer spin gauge bosons, ϕ. The fermions consist of 12 particles (with their corresponding anti-particles) in total classified into quarks and leptons. The gauge bosons mediate the fundamental forces between the fermions. The SM describes three fundamental forces: the electromagnetic, the weak, and the strong interaction. The different properties (mass, charge and spin) of the SM particles are summarised in Figure 2.1.

The full gauge symmetry group of the SM is given by $\mathrm{SU(3)_C} \otimes \mathrm{SU(2)_L} \otimes \mathrm{U(1)_Y}$, where SU(n) is a special unitary group with n dimension [15]. The indices C, L, Y represent the *colour* (strong interaction), *weak isospin* and *weak hypercharge* (both electroweak interactions), respectively. The electroweak theory unifies the electromagnetic and weak interactions and is based on the conservation of electric charge, Q, which is convolved with the weak isospin and hypercharge (described in Section 2.2). The description of the strong interaction is based on the theory of Quantum Chromodynamics (QCD) [16]. The conserved quantity in QCD is the colour charge (C), and it is represented by three possible colours: for example these could be red, green, and blue.

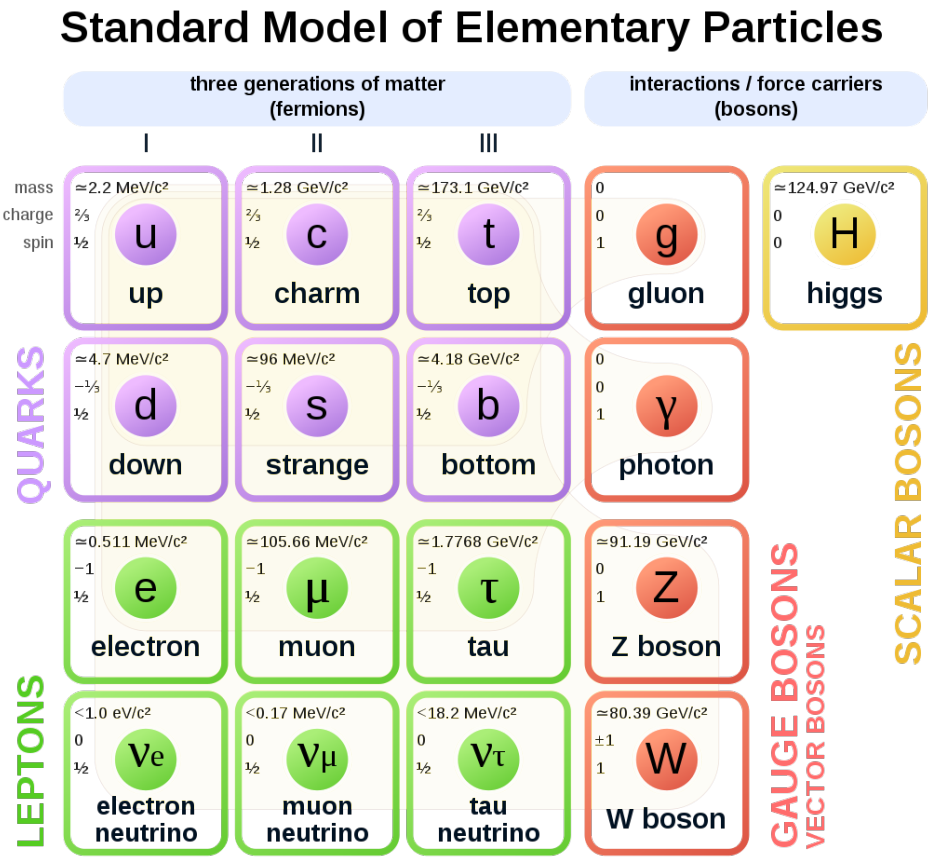

Figure 2.1 Overview of the fundamental fermions and bosons in the Standard Model. The mass, charge and spin of each particle is given [4].

2.2 The standard model Lagrangian

The SM can be expressed by the following Lagrangian

$$\mathcal{L}_{\text{SM}} = \mathcal{L}_{\text{Fermions}} + \mathcal{L}_{\text{Gauge}} + \mathcal{L}_{\text{Higgs}} + \mathcal{L}_{\text{Yukawa}}. \tag{2.5}$$

The following sections will review each of the components of the SM Lagrangian. These sections are based on [13, 17].

2.2.1 Fermion fields

The first component of the Lagrangian in Equation 2.5 describes the propagation and interactions of fermions. There are three generations of particles observed in the fermion sector, where each generation has the same fundamental properties except for the different masses. The fermions can be categorised into three distinct types: Weyl, Dirac and Majorana. Weyl fermions are massless, Dirac fermions are massive, and Majorana fermions are particles that are the same as their antiparticle. In the SM, fermions are considered to be Dirac fermions, with the exception of neutrinos, as their nature is not yet determined to be Dirac or Majorana.

The quark fields are represented as colour triplets transforming with the corresponding representation of SU(3). Whereas, the lepton fields are colourless, which results in them not being charged under the strong interaction. Therefore, fermions are categorised into families of particles that interact via the strong interaction and ones that do not, and these are termed quarks and leptons, respectively. Each lepton generation contains an electrically-charged particle and one which has neutral charge. The quark generations are split into up-type and down-type quarks that have an electric charge of $+\frac{2}{3}$ and $-\frac{1}{3}$, respectively.

An individual fermion field can be described by the following Dirac Lagrangian

$$\mathcal{L}_{\text{Fermion}} = \bar{\psi}\left(i\gamma^{\mu}\partial_{\mu} - m\right)\psi, \tag{2.6}$$

where γ^μ are the Dirac matrices [18]. Imposing gauge invariance under $\mathrm{SU(2)_L}$ and $\mathrm{U(1)_Y}$ rotations, the Dirac Lagrangian can be written in terms of the covariant derivative, D_μ, where the partial derivatives are replaced by the covariant derivative. The full description of the covariant derivative describing the interaction of the fermion field with the gauge field is given in Section 2.2.2.

The distinction between *left-handed* and *right-handed* fermions are made in the SM. The left-handed fermions are grouped into weak isospin doublets with $T = \frac{1}{2}$, and the right-handed fermions are grouped into weak isospin singlets with $T = 0$, where T is the weak isospin.

In the Lagrangian for the electroweak unification, the weak hypercharge, Y, is defined in terms of the electric charge Q and the third component of the weak isospin T^3 by the equation

$$Y = 2Q - 2T^3. \tag{2.7}$$

This results in $Y = -1, -\frac{1}{3}$ for the weak isospin doublets and $Y = -2, \frac{4}{3}, -\frac{2}{3}$ for the weak isospin singlets. Table 2.1 shows the quantum numbers of the generations of both left- and right-handed fermions under the electroweak symmetry group. A consequence of the left-handed doublets and the right-handed singlets is that the Dirac mass terms for the fermion fields are not gauge invariant under the $\mathrm{SU(2)_L} \otimes \mathrm{U(1)_Y}$ transformations. Therefore an alternative mechanism is needed to impose gauge invariance. The alternative mechanism will be introduced in Section 2.2.3. The right-handed neutrinos are often omitted from the construction of the SM, as they have not yet been observed experimentally, but appear in many models for generating the experimentally-observed neutrino mass [19].

2.2.2 Gauge fields

The second component of the SM Lagrangian, $\mathcal{L}_{\mathrm{Gauge}}$, describes the propagation of gauge bosons. The gauge field Lagrangian is given by

$$\mathcal{L}_{\mathrm{Gauge}} = -\frac{1}{4} G^a_{\mu\nu} G_a^{\mu\nu} - \frac{1}{4} W^a_{\mu\nu} W_a^{\mu\nu} - \frac{1}{4} B_{\mu\nu} B^{\mu\nu}, \tag{2.8}$$

	Generation			Quantum Numbers			
	1	2	3	T	T^3	Q	Y
quarks	u_L	c_L	t_L	$\frac{1}{2}$	$+\frac{1}{2}$	$+\frac{2}{3}$	$+\frac{1}{3}$
	d_L	s_L	b_L	$\frac{1}{2}$	$-\frac{1}{2}$	$-\frac{1}{3}$	$-\frac{1}{3}$
	u_R	c_R	t_R	0	0	$+\frac{2}{3}$	$+\frac{4}{3}$
	d_R	s_R	b_R	0	0	$-\frac{1}{3}$	$-\frac{2}{3}$
leptons	$\nu_{e,L}$	$\nu_{\mu,L}$	$\nu_{\tau,L}$	$\frac{1}{2}$	$+\frac{1}{2}$	+1	0
	$\nu_{e,R}$	$\nu_{\mu,R}$	$\nu_{\tau,R}$	0	0	0	0
	e_R	μ_R	τ_R	$\frac{1}{2}$	$+\frac{1}{2}$	-1	-1
	e_L	μ_L	τ_L	0	0	-2	-1

Table 2.1 List of Standard Model fermions and their properties. The quantum numbers for the left (L) and right (R) fermions are given; weak isospin (T) with its third component T^3, hypercharge (Y) and charge (Q).

where the fields correspond to transformations of their respective symmetry groups, B_μ are the gauge fields corresponding to the $\mathrm{U(1)_Y}$ transformation, W_μ^a with $a = 1, 2, 3$ corresponds to the $\mathrm{SU(2)_L}$ transformation and G_μ^a with $a = 1, .., 8$ corresponds to the transformations under $\mathrm{SU(3)_C}$.

The differences between these fields are a result of the different nature of the corresponding symmetry groups. Self-interactions between the W_μ and G_μ gauge fields are possible due to the non-abelian nature of the $\mathrm{SU(2)_L}$ and $\mathrm{SU(3)_C}$ groups. Whereas, due to the abelian nature of the $\mathrm{U(1)_Y}$ group, self-interactions between the fields are not possible.

As mentioned in Section 2.2.1, a covariant derivative, D_μ, is defined to describe the coupling between the fermion fields and gauge fields. The full covariant derivative for a fermion interacting with all three fields (e.g. quarks) is defined as

$$D_\mu \psi = \left(\partial_\mu - i g_s \frac{\lambda_a}{2} G_\mu^a - i g T_a W_\mu^a - i g' Y B_\mu \right) \psi, \tag{2.9}$$

where g', g and g_s are the coupling constants of the $\mathrm{U(1)_Y}$, $\mathrm{SU(2)_L}$ and $\mathrm{SU(3)_C}$ interactions, respectively. The terms λ_a, T_a and Y are the generators of the respective fields. The $\mathrm{SU(3)_C}$

gauge field is omitted for fermions that do not interact via the strong force. Therefore, the partial derivatives in the Dirac lagrangian is replaced, and the interactions for the electroweak and QCD components can be determined.

The electroweak interaction

Historically the electromagnetic and weak interactions were developed separately. The electromagnetic force is mediated by massless photons that propagate over an infinite range. The photons can interact with any particles which carry an electrical charge. The theory that describes the electromagnetic interaction is Quantum Electrodynamics (QED). The weak nuclear interaction acts on short length and time scales due to the large mass of its force carriers ($W^{\pm}$ and Z). Whereas, the weak bosons interact with left-handed fermions carrying a weak isospin quantum number. The weak force has two types of interactions: a charged current and a neutral current interaction.

The unification of the two theories, the electroweak theory was developed by Glashow, Salam and Weinberg et al. [20–22]. As a result, the electroweak theory is sometimes also referred to as the *GSW* theory. The electroweak interactions are described by the $\mathrm{SU(2)_L} \otimes \mathrm{U(1)_Y}$ symmetry group. The requirement for gauge invariance under these two symmetry groups leads to the following Lagrangian

$$\mathcal{L}_{\mathrm{EW}} = \bar{\psi} \not{D} \psi - \frac{1}{4} W^{a}_{\mu\nu} W_{a}^{\mu\nu} - \frac{1}{4} B_{\mu\nu} B^{\mu\nu}, \tag{2.10}$$

where $\not{D} = \gamma^{\mu} D_{\mu}$, and is the covariant derivative with the $\mathrm{SU(3)_C}$ gauge fields omitted. The physical mass eigenstates of the charged $W^{\pm}_{\mu}$ fields can be obtained via a linear combination of W^{1}_{μ} and W^{2}_{μ}. The mass eigenstates of the Z boson field, Z_{μ}, and the photon field, A_{μ} is obtained via rotations of the fields W^{3}_{μ} and B_{μ} around the weak mixing angle, θ_W, to give

$$W^{\pm}_{\mu} = \frac{1}{2} \left(W^{1}_{\mu} + W^{2}_{\mu} \right), \tag{2.11}$$

and

$$\begin{pmatrix} A_\mu \\ \\ Z_\mu \end{pmatrix} = \begin{pmatrix} \cos\theta_W & \sin\theta_W \\ \\ -\sin\theta_W & \cos\theta_W \end{pmatrix} \begin{pmatrix} B_\mu \\ \\ W_\mu^3 \end{pmatrix}. \tag{2.12}$$

Experimental results have confirmed the existence of the $W^\pm$ and Z bosons, with masses of $m_W = 80.379 \pm 0.012$ and $m_Z = 91.188 \pm 0.002$ GeV, respectively [5]. However, the inclusion of the boson and fermion mass terms in the SM Lagrangian violates the $\mathrm{SU(2)_L} \otimes \mathrm{U(1)_Y}$ symmetry, resulting in a non-normalisable theory. Therefore, this requires the introduction of the theory of spontaneous symmetry breaking, commonly known as the Higgs mechanism (Section 2.2.3).

Quantum Chromodynamics

The $\mathrm{SU(3)_C}$ symmetry group corresponds to the strong nuclear force, and its interactions are described by Quantum Chromodynamics (QCD). Much of the structure and notation of the resulting gauge interactions have already been discussed. However, there are significant differences that are a result of the $\mathrm{SU(3)_C}$ group. The couplings between the quarks and gluons are defined from the $\mathrm{SU(3)_C}$ symmetry group, where colour charge is the conserved quantity. As a result of the eight generators of $\mathrm{SU(3)_C}$ there are eight associated gauge bosons (gluons). The gluons are colour charged, massless and have no electric charge. The Lagrangian for the quark interactions can be written as

$$\mathcal{L}_{\text{Quark}} = \frac{g_s}{2} \bar{\psi}_q \left(\gamma_\mu \lambda_a G_\mu^a \right) \psi_q, \tag{2.13}$$

where g_s is the coupling constant of the strong interaction and G_μ^a corresponds to the gluon field strength tensor. The coupling constant, g_s, is expressed as $\alpha_s = \frac{g_s^2}{4\pi}$ for convenience, and is a fundamental parameter of QCD, along with the quark masses. Using the QCD parameters, a scattering amplitude in a reaction between the initial and final state particles can be evaluated in powers of α_s. However, in QFT there will be ultraviolet (UV) divergences that are a result of Feynman diagrams containing loops. The divergences need to be fixed using a renormalisation procedure, which involves including a scale, μ_R, above which the UV divergences are removed.

The dependence of the strength of the coupling on the scale (Q^2) is derived using the renormalisation group equation (RGE) [5], which is expressed as

$$Q^2 \frac{\partial \alpha_s}{\partial Q^2} = \beta(\alpha_s) = -\beta_0 \alpha_s^2 (1 + \beta_1 \alpha_s + \beta_2 \alpha_s^2 + ..), \tag{2.14}$$

where $\beta_0 = (33 - 2n_f)/(12\pi)$ is known as the 1-loop β function coefficient and n_f denotes the number of quark flavours. Figure 2.2 depicts the dependence of α_s on energy scale. This defines the characteristic properties of the QCD interactions: *asymptotic freedom* and *quark confinement*. As Q^2 increases the coupling of the strong interaction tends to zero. This process is known as asymptotic freedom, and it is observed experimentally, as shown in Figure 2.2. However, as Q^2 gets smaller, the coupling between the quarks becomes stronger and prevents them from existing as isolated particles. This phenomenon is known as quark confinement. The increase in potential energy as Q^2 increases is significant enough to create quark and anti-quark pairs in a process known as *hadronisation*.

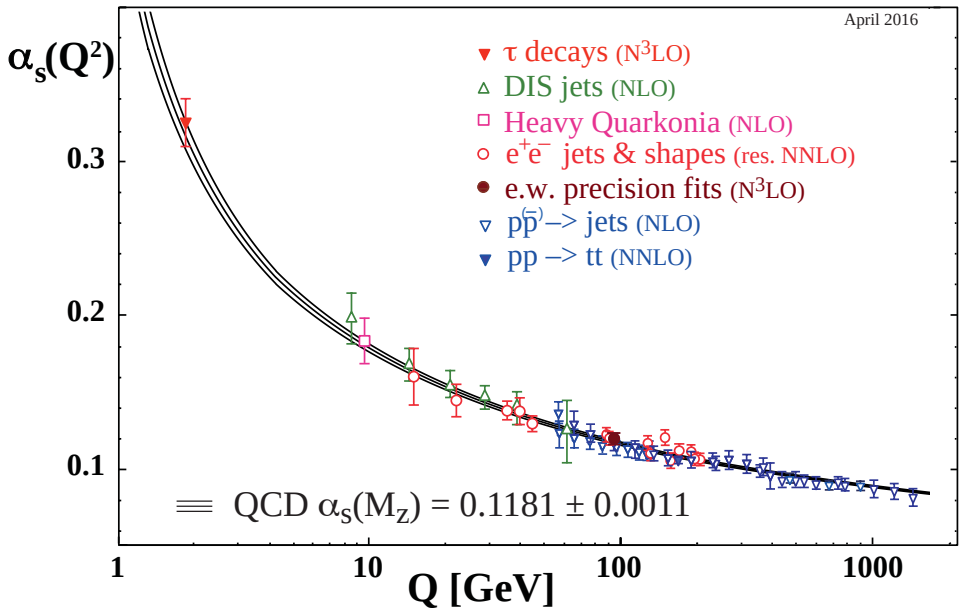

Figure 2.2 Summary of experimental measurements of α_s as a function of energy scale Q [5].

2.2.3 Electroweak symmetry breaking

As described in the previous sections, the inclusion of explicit mass terms for the fermions and bosons violates the electroweak gauge symmetry. Therefore, the Brout-Englert-Higgs mechanism [23, 24], commonly referred to as the Higgs mechanism, is used to introduce gauge-invariant mass terms for the particles. A new field is introduced which has gauge-invariant transformations under $\mathrm{SU(2)_L} \otimes \mathrm{U(1)_Y}$. It can be a complex scalar field in the SM Lagrangian that is an isospin doublet with hypercharge $Y = \frac{1}{2}$, defined as

$$\Phi = \begin{pmatrix} \phi^+ \\ \phi^0 \end{pmatrix} = \frac{1}{\sqrt{2}} \begin{pmatrix} \phi_1 + i\phi_2 \\ \phi_3 + i\phi_4 \end{pmatrix}. \tag{2.15}$$

The gauge invariant Higgs Lagrangian is then defined as

$$\begin{aligned} \mathcal{L}_{\text{Higgs}} &= (D^\mu \Phi)^\dagger (D^\mu \Phi) - V(\Phi), \\ V(\Psi) &= -\mu^2 \Phi^\dagger \Phi + \lambda (\Phi^\dagger \Phi)^2, \end{aligned} \tag{2.16}$$

using the covariant derivative defined in Section 2.2.2, where the potential is given in terms of the free parameters μ and λ. For $\mu^2 > 0$ the potential has a minimum at $\phi = 0$, where the minimum corresponds to the vacuum. This corresponds to a Lagrangian with scalar particles of mass μ. However, when $\mu^2 < 0$, the potential has a degenerate minimum at $v = \mu/\sqrt{\lambda}$, where v is the *vacuum expectation value*, and results in spontaneous symmetry breaking. In the potential, the self-coupling parameter λ is chosen to be positive to ensure that the potential is bounded from below. The fields are chosen such that $\phi_1 = \phi_2 = \phi_4 = 0$ and $\phi_3 = v + h(x)$. The scalar field, $h(x)$, is identified as the Higgs field. The minimum of the potential after the spontaneous symmetry breaking occurs for the neutral component of the scalar field doublet to preserve U(1) symmetry. The non-zero vacuum expectation value results in the breaking of the $\mathrm{SU(2)_L} \otimes \mathrm{U(1)_Y}$ symmetry to $\mathrm{U(1)_{EM}}$ symmetry. After symmetry breaking, Φ takes the form

$$\Phi = \begin{pmatrix} 0 \\ v + h(x) \end{pmatrix}. \tag{2.17}$$

Using the Lagrangian in Equation 2.16, and expanding the kinetic terms, results in a series of terms describing the interactions of the gauge bosons with the vacuum and the Higgs field. This leads to the vector boson masses,

$$\begin{aligned} m_W &= \frac{gv}{2}, \\ m_Z &= \frac{1}{2}(g^2 + g'^2)^{\frac{1}{2}} v, \end{aligned} \tag{2.18}$$

and the photon remains massless. The masses acquired by the $W^{\pm}$ and Z gauge bosons are expected by Goldstone's theorem [25], which states that the vanishing degrees of freedom under $\mathrm{SU(2)_L}$ correspond to Goldstone bosons that are "eaten" to give mass to the associated gauge fields.

Using the scalar doublet defined in Equation 2.17, fermion masses can also be incorporated. Using the first generation of quarks as an example and defining the $\mathrm{SU(2)_L}$ doublet for left-handed quarks, a Yukawa Lagrangian can be written as,

$$\mathcal{L}_{\text{Yukawa}} = -\lambda_d Q_L \Phi d_R - \lambda_u Q_L \tilde{\Phi} u_R + h.c, \tag{2.19}$$

where λ_d and λ_u are the Yukawa couplings of the down- and up-type quarks, respectively. h.c refers to the addition of the Hermitian conjugate of the Higgs doublet. The fermion masses are found to be proportional to the vacuum expectation value of the Higgs field, given by the following relation

$$m_d = \frac{\lambda_d v}{\sqrt{2}}, \quad m_u = \frac{\lambda_u v}{\sqrt{2}}. \tag{2.20}$$

However, the mass terms for the neutrinos are often omitted from the SM. The inclusion of neutrino mass terms would require an extraordinarily large mass difference between the charged and neutral leptons within each lepton generation.

Finally, after electroweak symmetry breaking, and the Higgs field acquiring the vacuum expectation value, the Higgs mass is given as

$$m_h = \sqrt{2\lambda}v. \tag{2.21}$$

In 2012, the SM Higgs boson was discovered with $m_h \sim 125.09\,\text{GeV}$ [7, 8] by the ATLAS and CMS collaborations at CERN.

2.3 Phenomenology of Proton-Proton collisions

The hadron-hadron scattering processes which occur at the LHC and other collider experiments can be classified as either *hard* or *soft*. When protons collide, their constituents may interact directly and exchange a substantial fraction of their protons momentum, known as hard-scattering. Processes such as W and Z production occur at high energy scales, therefore perturbative QCD can provide their cross sections with good precision.

In this section, the partonic structure of the proton is outlined, and the production of events that are of interest to the physics analysis in this thesis is also discussed.

2.3.1 The structure of the proton

The quantum number of hadrons are given given according to the quark model, by either the three or two valence quarks for baryons or mesons, respectively. For protons these are two u-quarks and one d-quark. The valence quarks are bound by the exchange of gluons, where several processes can occur. For example, a gluon can split into a $q\bar{q}$-pair. These dynamically changing quarks are called sea quarks, since they form a sea of $q\bar{q}$-pairs. Additionally, the valence quarks or gluons themselves can radiate a gluon. All objects inside the proton, gluons, valence- and sea-quarks are referred to as partons.

During inelastic proton-proton collisions, only the partons inside the protons interact. Therefore, the total center-of-mass energy of the colliding proton is not available during the

collision. Each parton will carry a fraction of their respective proton's total energy. Within the context of proton-proton collisions, the probability of a given parton within a proton to interact with another parton of a different proton is given by the parton distribution function (PDF). The PDFs are obtained through deep inelastic scattering experiments, and depend on the momentum transfer of the collision, Q^2, and the fraction of the protons momentum carried by each parton involved in the collision, x. Figure 2.3 shows the resulting PDF shapes as a function of x for each parton at $Q^2 = 10$ GeV^2 and $Q^2 = 10^4$ GeV^2.

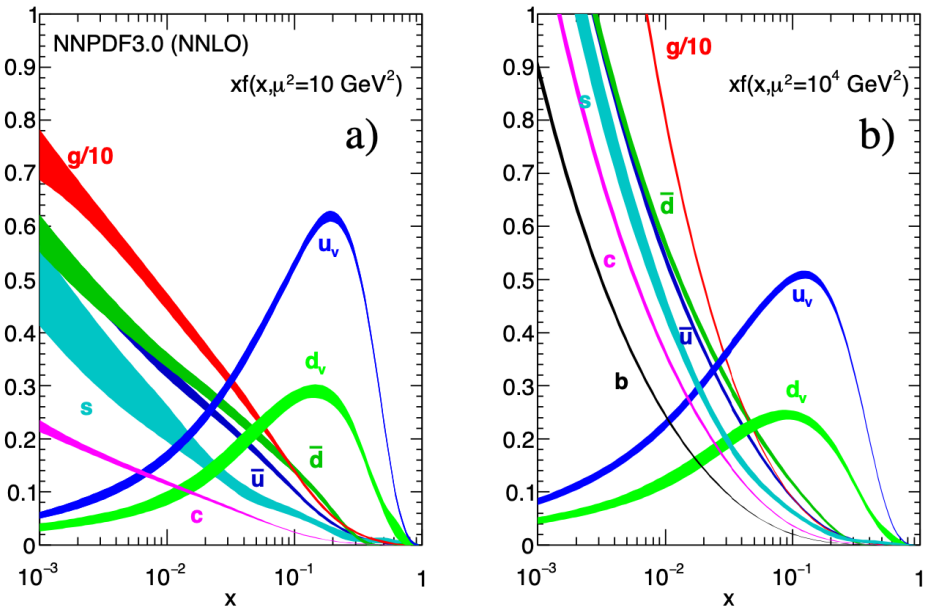

Figure 2.3 Parton distribution functions of proton constituents as a function of the momentum fraction x of the partons relative to the proton momentum, for momentum transfers $Q^2 = 10$ GeV^2 and $Q^2 = 10^4$ GeV^2 [6].

2.3.2 Dilepton production

The analysis described in this thesis measures the dilepton (e^+e^- and $\mu^+\mu^-$) invariant-mass spectrum to search for a signal. The dominant hard-scattering processes that produce events with dilepton pairs, that are considered in the analysis, are described in this section.

The Drell-Yan process [26] is the most significant lepton pair production mechanism in hadronic collisions. The process involves the production of a lepton pair $\ell^+\ell^-$ at a hadron

collider by quark-antiquark annihilation. In the basic Drell-Yan process, the $q\bar{q}$-pair annihilates to a virtual photon $q\bar{q} \to \gamma^* \to \ell^+\ell^-$. The cross-section for this process at leading order is easily obtained from the fundamental QED $e^+e^- \to \mu^+\mu^-$ cross-section, where the appropriate colour and charge factors are added [27],

$$\hat{\sigma}(q\bar{q} \to \gamma^* \to \ell^+\ell^-) = \frac{4\pi\alpha^2}{3\hat{s}} \frac{1}{N_C} Q_q^2, \tag{2.22}$$

where $\hat{s}$ is the center of mass energy of the incoming partons, Q_q is the charge of the quarks and $1/N_C = 1/3$ is a colour factor, where only three colour combinations are possible since the intermediate state has to be colourless. If the collision energy is below the Z mass, the intermediate state is an off-shell photon. The partonic center of mass energy is equal to the mass of the virtual photon and the invariant mass of the dilepton pair, and is given by

$$\sqrt{\hat{s}} = m_{\gamma^*} = m_{\ell\ell} = \sqrt{(p_{\ell^+} + p_{\ell^-})^2}, \tag{2.23}$$

where $p_{\ell^\pm}$ are the momentum four vectors of the leptons. Comparing equation (2.22) and (2.23), one can see that $\hat{\sigma} \propto 1/m_{\ell\ell}^2$. If the collision energy is equal to the Z mass, the process can take place via the exchange of a Z boson, leading to a Breit-Wigner resonance in the spectrum of the invariant-mass near the mass of the Z boson. The exchange via a virtual photon and a Z boson interfere. The Feynman diagram for the Drell-Yan process is given by

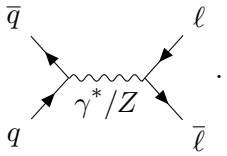

. (2.24)

Diboson production is the second largest source of dilepton events. The leading-order production of these events is through the $q\bar{q}$ initial state. The Feynman diagrams for diboson

production is given by

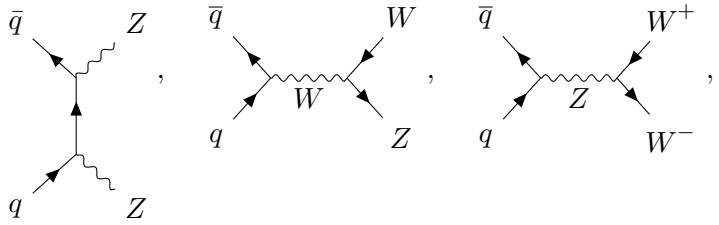

(2.25)

where the vector bosons will decay into dilepton pairs in the case of the Z production and a lepton and neutrino pair in the $W^{\pm}$ production.

The third largest contribution arises from the production of pairs of top quarks ($t\bar{t}$). The Feynman diagrams for the leading order production of $t\bar{t}$-paris is given by

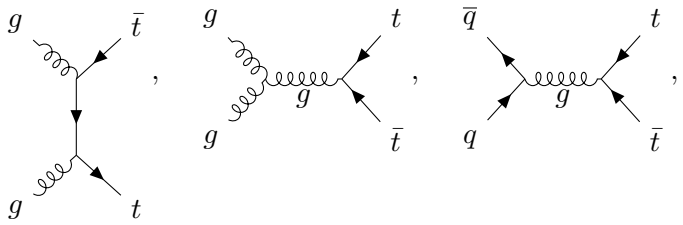

(2.26)

where the top quark will rapidly decay to a W and a lighter quark final state and result in the production of dilepton pairs.

Chapter 3

Beyond the Standard Model

The Standard Model of particle physics has had tremendous success in describing the majority of the observed phenomena so far. However, there remain several critical unanswered questions from experimental signatures that do not fit within the framework of the SM. These signatures hint towards physics beyond the Standard Model (BSM). The motivation to look for BSM physics is outlined in Section 3.1. This thesis focuses on a search for contact interaction (CI) models in dilepton final states. The four-fermion contact interaction model belongs to a subset of a broad range of effective field theory models. Section 3.2 provides a brief overview of effective field theories, where an example of a well-known effective field theory is given. The specific CI interaction model used in the analysis of this thesis is outlined in Section 3.3.

3.1 Motivation

The SM mechanism to generate neutrino masses relies on unobserved right-handed neutrinos, and requires significant parameter tuning to describe the size of the observed neutrino masses [28]. The search for answers to these questions is one such motivation for BSM theories. Many BSM theories attempt to explain these two phenomena.

An additional observed shortcoming of the SM, and one of the strongest motivations for BSM models, is a result of an internal inconsistency of the SM itself. The observed Higgs

mass is $\sim 100\,\text{GeV}$ and is a result of the electroweak symmetry breaking scale. There is a vast difference between this and the Plank scale ($\sim 10^{19}$ GeV), with no other scale present in between. The Plank scale is where quantum gravitational effects become dominant. Therefore, the Higgs mass is sensitive to large vacuum fluctuations and can result in corrections from one-loop diagrams of virtual particles, where an infinite number of corrections could exist. In order to counter these corrections, the measured Higgs mass needs to be finely tuned between the bare mass and the radiative corrections [29]. This fine-tuning motivates the existence of TeV scale physics, which would cancel some of the divergent corrections. *Supersymmetry* (SUSY) is one possible theory that attempts to explain the observed hierarchy problem [30]. However, SUSY has not yet been observed, thus introducing a new SUSY breaking scale, which results in some fine-tuning. An alternative approach to mitigate the hierarchy problem is by the introduction of some large extra dimensions, where gravity is allowed to propagate in these new dimensions [31].

3.2 Brief overview of effective field theory

An effective field theory (EFT) is a low-energy approximation of a full QFT. With the use of an EFT indirect effects of particles with masses well beyond what is currently possible to be experimentally probed can be quantified. The EFT approach is based on the property of decoupling [32], which refers to the screening of high-energy phenomena for interactions at lower energy scales. Using the expansion of the propagator of a massive particle with mass m,

$$\frac{1}{q^2 - m^2} = -\frac{1}{m^2}(1 + \frac{q^2}{m^2} + ..), \tag{3.1}$$

where q^2 is the momentum transfer of the particle. It is clear that when $m^2 \gg q^2$, the propagation of the particle is suppressed. This is also apparent from the uncertainty principle, where the range of the force reduces as the mass of the mediator particle increases. Therefore, the mass of a mediator can be taken large enough that the propagator connecting interaction vertices is reduced to a point, resulting in a *contact interaction*. This results in the reduction of many possible high-energy theories into smaller sets of EFT operators. The EFT operators

allow the construction of an effective Lagrangian describing the interactions at lower energies only in terms of SM fields.

Historically a *top-down* approach was favoured, where a consistent theory valid at very high scales is defined, and observations are constructed within that framework. However, due to lack of observations of new BSM heavy states at the LHC validating such models, the focus has shifted to a *bottom-up* model building. The bottom-up approach considers the SM as the low-energy gauge theory within a theory at higher energy scales Λ_{BSM}. Higher-order operators can be added to the SM, and a general effective Lagrangian can be written as

$$\begin{aligned} \mathcal{L}_{\text{EFT}} &= \mathcal{L}_{\text{SM}} + \mathcal{L}_{\text{D}}, \\ \mathcal{L}_{\text{D}} &= \sum_i \frac{c_i}{\Lambda_{\text{BSM}}^{D-4}} \mathcal{O}_i^{(D)}. \end{aligned} \tag{3.2}$$

$\mathcal{L}_{\text{SM}}$ is the dimension-four SM Lagrangian, Λ_{BSM} is the mass scale for BSM, $\mathcal{O}_i$ are dimension D effective operators, and c_i are dimensionless couplings that specify the strength of the BSM interactions, known as *Wilson coefficients*.

The SM operators are dimension-four (Chapter 2), which allows them to be renormalisable. However, the effective operators are not renormalisable as they are of dimension $D \geq 5$. Therefore, the effective theory is only valid valid up to energies much lower than the scale Λ_{BSM}. The full effective Lagrangian is an infinite series. However, the inverse of the scale Λ_{BSM} plays an important role, where dimensional analysis and the ratio between the energy scale of the experiment and energy scale is used to keep only terms that are dimension-four. This procedure is known as power counting [33].

There is only one dimension-five operator that is gauge invariant and is known as the Weinberg operator [34], which can be used to give Majorana neutrino masses through electroweak symmetry breaking [35].

The work presented in this thesis is restricted to dimension-six. The list of EFT operators was first classified in 1986 [36], and contains 80 dimension-six operators for each flavour. There are several ways of reducing the operators, as transformations between operators are possible.

The *Warsaw basis* [37] was the first complete and non-redundant set of dimension-6 operators that were proposed. This thesis focuses on dilepton final states, therefore only quark-lepton interactions will be considered. Some examples of general lepton-quark four-fermion contact interaction can be parameterised by the following dimension-six operators [38],

$$\begin{aligned} \mathcal{O}_{\ell q}^{(1)} &= (\bar{\ell}\gamma^{\mu}\ell)(\bar{q}\gamma_{\mu}q), \qquad \mathcal{O}_{\ell q}^{(3)} = (\bar{\ell}\sigma_{I}\gamma^{\mu}\ell)(\bar{q}\sigma_{I}\gamma_{\mu}q), \\ \mathcal{O}_{eu} &= (\bar{e}\gamma^{\mu}e)(\bar{u}\gamma_{\mu}u), \qquad \mathcal{O}_{ed} = (\bar{e}\gamma^{\mu}e)(\bar{d}\gamma_{\mu}d), \\ \mathcal{O}_{\ell u} &= (\bar{\ell}\gamma^{\mu}\ell)(\bar{u}\gamma_{\mu}u), \qquad \mathcal{O}_{\ell d} = (\bar{\ell}\gamma^{\mu}\ell)(\bar{d}\gamma_{\mu}d), \end{aligned} \tag{3.3}$$

where ℓ and q are the SM lepton and quark doublets, respectively.

Fermi theory

The classic example of an EFT approach is the Fermi theory of low-energy weak interactions. The full UV theory is the SM, and it is matched to the EFT by considering a theory valid at small momenta compared to $m_{Z,W}$ [32]. Muon decay, $\mu \to e\nu_{\mu}\bar{\nu}_{e}$, is considered as an example, where the SM energy scale ($\Lambda_{\text{BSM}} \sim 80.8\,\text{GeV}$) is much higher than that of the interaction ($m_{\mu} \sim 100\,\text{GeV}$).

In the SM, the decay amplitude is given by

$$\mathcal{M} = -\left(\frac{g}{\sqrt{2}}\right)^{2} [\bar{\nu}_{\mu}\frac{1}{2}\gamma^{\mu}(1-\gamma^{5})\mu] \left[\frac{g_{\mu\nu} - q_{\mu}q_{\nu}/m_{W}^{2}}{q^{2} - m_{W}^{2}}\right] [\bar{e}\frac{1}{2}\gamma^{\mu}(1-\gamma^{5})\nu_{e}]. \tag{3.4}$$

Considering the low-energy limit where $m_{W}^{2} \gg q^{2}$, the propagator can be expanded as shown in Equation 3.1. Retaining only the first term of the expansion the amplitude can now be written as

$$\mathcal{M} = \frac{g^{2}}{8m_{W}^{2}} g_{\nu\mu}[\bar{\nu}_{\mu}\gamma^{\mu}(1-\gamma^{5})\mu][\bar{e}\gamma^{\mu}(1-\gamma^{5})\nu_{e}]. \tag{3.5}$$

The Feynman diagram for the process is given by

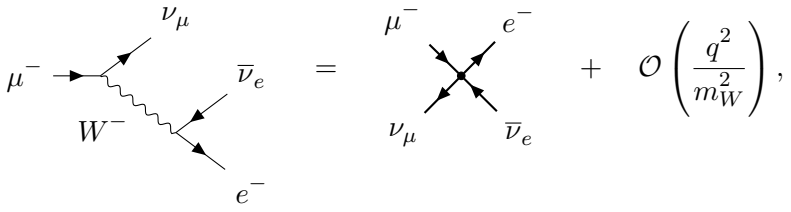

(3.6)

where the first term corresponds to the SM diagram for the decay of the muon, the right-hand side of the equation shows the effective vertex and the higher-order correction terms.

In the Fermi effective theory, weak interactions are described by four-fermion contact interaction, with coupling c/Λ^2, where c is the Wilson coefficient and Λ is the scale of the EFT. This results in the amplitude

$$\mathcal{M} = \frac{c}{4\Lambda^2} g_{\nu\mu}[\bar{\nu}_\mu \gamma^\mu (1-\gamma^5)\mu][\bar{e}\gamma^\mu(1-\gamma^5)\nu_e]. \tag{3.7}$$

Hence, by comparing Equations 3.5 and 3.7, the amplitude from the SM and Fermi theory can be matched by setting $\Lambda = m_W^2$ and $c = g^2/2$. The Fermi constant, G_F, is related to the EFT coupling by

$$\frac{G_F}{\sqrt{2}} = \frac{c}{4\lambda^2} = \frac{g_W^2}{8m_W^2}. \tag{3.8}$$

3.3 Four-fermion contact interaction

The search presented in this thesis focuses on one dimension-six operator: $\mathcal{O}_{\ell q}^{(1)} = (\bar{\ell}\gamma^\mu \ell)(\bar{q}\gamma_\mu q)$, which can be used to postulate the existence of the constituents of quarks and leptons, known as *preons* [39, 40], as a possible solution to the hierarchy problem in the SM. If quarks and leptons are composite, with at least one common constituent, the interaction of these constituents could manifest itself through an effective four-fermion CI at energies well below the compositeness

scale. The Lagrangian for such processes is defined as

$$\begin{aligned}\mathcal{L} = \frac{g^2}{2\Lambda^2}\{&\eta_{LL}\left(\bar{q}_L\gamma_\mu q_L\right)\left(\bar{\ell}_L\gamma^\mu\ell_L\right) + \eta_{RR}\left(\bar{q}_R\gamma_\mu q_R\right)\left(\bar{\ell}_R\gamma^\mu\ell_R\right) + \\ &\eta_{LR}\left(\bar{q}_L\gamma_\mu q_L\right)\left(\bar{\ell}_R\gamma^\mu\ell_R\right) + \eta_{RL}\left(\bar{q}_R\gamma_\mu q_R\right)\left(\bar{\ell}_L\gamma^\mu\ell_L\right)\},\end{aligned} \tag{3.9}$$

where g is a coupling constant and chosen such that $g^2/4\pi = 1$ for convention [39], γ are the Dirac matrices and the spinors $q_{L,R}$ are the left-handed and right-handed quark fields, respectively, and ℓ are the fermion fields. The parameters η_{ij}, where i and j are L or R, define the chiral structure (left or right) of the new interaction. Specific models are chosen by assigning η_{ij} to be -1, 0 or $+1$. A chiral model can be chosen in the follow way

$$\begin{aligned}\mathcal{L}_{LL} &= \mathcal{L}(\eta_{LL} = \pm1, \eta_{LR} = 0, \eta_{RL} = 0, \eta_{RR} = 0),\\ \mathcal{L}_{LR} &= \mathcal{L}(\eta_{LL} = 0, \eta_{LR} = \pm1, \eta_{RL} = 0, \eta_{RR} = 0),\\ \mathcal{L}_{RL} &= \mathcal{L}(\eta_{LL} = 0, \eta_{LR} = 0, \eta_{RL} = \pm1, \eta_{RR} = 0),\\ \mathcal{L}_{RR} &= \mathcal{L}(\eta_{LL} = 0, \eta_{LR} = 0, \eta_{RL} = 0, \eta_{RR} = \pm1).\end{aligned} \tag{3.10}$$

The scattering amplitudes for the fermions can interfere either constructively or destructively with the SM Drell-Yan process (DY). Whether the interference is constructive or destructive is dependent on the sign of η_{ij}. For example, the model destructively interferes with the DY for $\eta_{ij} = +1$ and constructively interferes for $\eta_{ij} = -1$. Therefore, the combination of the interference and chiral models result in eight separate CI interaction models that can be tested.

The leading-order production mechanism for DY with an additional CI interaction process for dilepton final states is given by

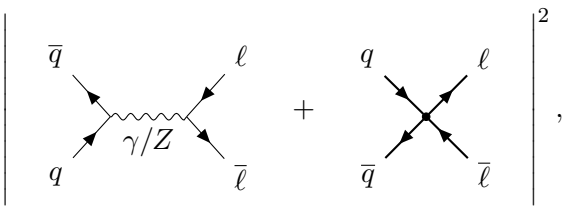

, (3.11)

where the fist term corresponds to the DY process and the second term to the CI process.

The differential cross-section with respect to the invariant mass, $m_{\ell\ell}$, for the process $q\bar{q} \to \ell\ell$ in the presence of such contact interactions is given by

$$\frac{d\sigma}{dm_{\ell\ell}} = \frac{d\sigma_{\mathrm{DY}}}{dm_{\ell\ell}} - \eta_{ij}\frac{F_{\mathrm{I}}}{\Lambda^2} + \frac{F_{\mathrm{C}}}{\Lambda^4}, \tag{3.12}$$

where the first term accounts for the $q\bar{q} \to Z/\gamma* \to \ell\ell$ (DY) process, the second term corresponds to the interference between the DY and CI processes, and the third term gives the pure CI process. F_I and F_C are functions of differential cross-section with respect to $m_{\ell\ell}$ for the interference term and the pure CI term, respectively, and do not depend on Λ [39]. The relative impact of the interference and pure CI term are dependent on both $m_{\ell\ell}$ and Λ.

3.4 Previous contact interaction searches

There has been a wide range of searches for CIs in many different experiments. Previous searches for quark-lepton compositeness have been performed at LEP [41, 42], HERA [43, 44], and the Tevatron [45, 46].

The strongest exclusion limits at LEP were from the ALEPH experiment. The differential cross-section for $e^+e^- \to f\bar{f}$ as a function of polar angle θ was utilised to discriminate between Standard Model prediction and contact interaction signals. The limits on the scale of contact interactions Λ are in the range 2 - 17 TeV [41]. The ZEUS detector at HERA utilised two datasets, $e^+p \to e^+X$ and $e^-p \to e^-X$ in search of CI signals. The analysis compared the measured Q^2 distribution with predictions from MC simulation. Limits on contact interaction models ranges from 1.7 - 6.2 TeV [44]. The DØ collaboration at Tevatron set limits on the energy scale of quark-electron compositeness using data collected in proton-proton collisions. The differential cross-section $d\sigma/dm$ in the dielectron channel was used to distinguish between CI and SM prediction. Limits on contact interaction model range from 3.3 - 5.1 TeV [46].

The most recent result from the CMS experiment in the search for contact interactions was performed at $\sqrt{s} = 13\,\mathrm{TeV}$ with an integrated luminosity of $36\,\mathrm{fb}^{-1}$ [47]. The CMS Collaboration has set 95% C.L. exclusion limits on the $\ell\ell qq$ contact interaction scale that

range from $\Lambda_{LL} > 20\,\text{TeV}$ for the destructive interference to $\Lambda_{RR} > 32\,\text{TeV}$ for the constructive interference, for the left-left and the right-right models, respectively.

The strongest exclusion limits for $\ell\ell qq$ was set by the ATLAS experiment, where the search was performed at $\sqrt{s} = 13\,\text{TeV}$ with an integrated luminosity of $36.1\,\text{fb}^{-1}$ [2]. Lower limits on the CI interaction energy scale Λ was set for the combined electron and muon channel at a 95% confidence level on the left-left model at $\Lambda = 40\,\text{TeV}$ for the constructive interference. A detailed comparison of the previous ATLAS results with the results from this thesis are given in Chapter 12.

In contrast to the LEP and ZEUS experiments the ATLAS and CMS results utilise the dilepton invariant-mass spectrum to distinguish between the Standard Model prediction and CI signals. Both experiments rely on Monte-Carlo generation to model the SM expectation. The analysis presented in this thesis uses a data-driven approach to search for non-resonant phenomena such as contact interactions in dilepton final states. The Standard Model expectation is modelled using a functional fit to a low-mass control region and extrapolation to a high-mass signal region.

Chapter 4

Overview of statistical concepts

The following chapter provides an overview of the concepts and procedure used in the statistical analysis performed on the analysis presented in this thesis. An overview of the interpretation of probability is given in Section 4.1, where the interpretation used in the analysis is also provided. The construction of the likelihood used in the analysis and the method used to estimate its associated parameters are provided in Section 4.2. Section 4.3 describes the treatment of the systematic uncertainties considered in the analysis. Section 4.4 describes the procedure of testing the compatibility of the data with respect to a hypothesis in the context of potential discovery, or setting a limit. Finally, Section 4.5 discusses the two possible methods available for the interpretation of results in the context of CI models, where the final method used will be outlined.

4.1 Interpretation of probability

The interpretation of measured observables after performing a measurement forms one of the main challenges in experimental particle physics. Statistical methods are used to quantify the relationship between some measured observables and parameters in a model. In the analysis presented in this thesis, the goal is testing different non-resonant signal models by measuring the number of events with different values of dilepton mass. The estimated signal yield and the estimated background yield can be used to determine the agreement of non-resonant,

i.e. Contact Interactions scenarios (Chapter 3), with data, and infer values of parameters in non-resonant models.

A central concept in statistics in particle physics is that of uncertainty, which can originate from several different sources. For example, uncertainties can be the result of the lack of knowledge of the experiment, or the consequence of a more fundamental random nature in the system due to quantum mechanics. A variable is said to be random when it is not known or cannot be predicted with complete certainty [48]. The concept of probability can be used to quantify the degree of randomness. Kolmogorov formulated a mathematical definition of probability as a set of axioms [49].

The interpretation of probability can take two forms. The frequentist interpretation, and another known as subjective or Bayesian probability is also used. The frequentist notion of probability of an event is defined as the limit of its relative frequency in a large number of trials. A large number of trials forms an ensemble, where in particle physics an ensemble can be formed by repeating the experiment multiple times. In frequentist probabilities, the true values of the parameters are states of nature and not the outcome of the experiment. The Bayesian definition of probability is based on a degree of belief. Therefore, Bayesian probabilities can be assigned to hypothesis on states of nature. The practical consequence of Bayesian probabilities is that for various parameters a prior probability must be supplied, which describes one's belief about its true value.

The frequentist interpretation of probability is used for analysis in this thesis. The frequentist vs. Bayesian choice is an ongoing debate in the community and the high-energy physics community mainly uses frequentist methods as they do not require specific prior degrees of belief. The use of the frequentist interpretation does not indicate an inherent merit over the Bayesian interpretation, but rather highlights the technically simple implementation of the frequentist interpretation.

4.2 Parameter estimation

One of the most common tasks in high energy physics is an estimation of some model parameter [48], commonly known as the parameter of interest (POI), e.g. a number of signal events or signal strength in search for new physics. Additional parameters that also affect the model that are not the POI are known as nuisance parameters, this is described in detail in Section 4.3. The POI can be estimated by measuring a set of *observables*, x, whose probability depends on the POI. Depending on the analysis, different quantities can be utilised as *observables*, e.g. the analysis described in this thesis uses the dielectron and dimuon invariant mass. Replication of the experiment multiple times results in different values of x, which results in a *probability density function* of x, written as $f(x;\alpha)$, where α is used to represent any parameters associated with the physical theory or an unknown property associated with the detector response.

When considering a dataset with many events, $\mathcal{D} = (x_1, .., x_n)$, the probability density is given by the product of the densities for each event. In counting experiments, such as the one described in this analysis, the total number of selected events is also a random variable, where the total number of observed events, n, fluctuates around the expected number of events, ν, according to a Poisson distribution. When considering binned data, common to most analyses, histograms are defined that yield a certain number of entries $n = (n_1, .., n_N)$ in N bins. The expected number of events in the entries for a bin is given by

$$\nu(\alpha) = n_{\text{tot}} \int_{x_{i,\text{min}}}^{x_{i,\text{max}}} f(x;\alpha)\ dx, \tag{4.1}$$

where $x_{i,\text{min}}$ and $x_{i,\text{max}}$ are the bin limits, and n_{tot} is the total number of events in the dataset. The expected number of events are estimated for each of the signal regions (SRs) defined in the analysis, where the bin limits corresponds to the start and end of the signal region as defined in Chapter 10. A likelihood function for the total probability distribution can be defined

$$\mathcal{L}(n;\alpha) = \frac{\nu^n e^{-\nu}}{n!}. \tag{4.2}$$

For the single-bin counting experiment used in the analysis $N = 1$ due to only one bin used for the statistical analysis. The expected number of events in the bin can be defined as $\nu = \nu_S + \nu_B$, where ν_B is the SM expected background events, and ν_S is the signal events in the bin. The POI used in this analysis is ν_S. Using the likelihood function, one can estimate the POI given the collected data.

An *estimator*, $\hat{\alpha}(\mathcal{D})$ is some function of the data and its value is used to estimate the true value of some parameter α. There are various properties that an estimator must satisfy to be considered a *good* estimator, e.g. bias, variance, consistency [50]. Consistency is the requirement that the estimator should converge to the true value in the limit of infinite statistics. A bias of an estimator is defined as the difference between the expectation value of the estimator, $E[\hat{\alpha}]$, and the true value of α. Variance is defined as $var[\hat{\alpha}] = E\left[(\alpha - E[\hat{\alpha}])^2\right]$. There is a clear trade-off between bias and variance, in the class of unbiased estimators, there is a well-defined minimum variance bound [51]. When interpreting the results in the context of CI interaction models, S can be expressed as a function of CI energy scale Λ, as describe in Chapter 3, where Λ can also be considered the POI. This allows for the results to be either interpreted directly in terms of lambda or the reinterpretation of the results from the number of signal events, ν_S.

The most commonly used estimator is the maximum likelihood estimator (MLE), defined as the value of α, which maximises the likelihood function. In practice, due to computational efficiency, this is done by minimising $-\log \mathcal{L}$. For multi-parameter likelihood functions, the various components of α_p are referred to as *floating* parameters. The MLE method can be generalised and is used to determine the *best-fit* values for the parameters used in the background estimation. The minimisation is handled by the Minuit [52] tool in the RooFit framework.

Combination of channels

Probability models can be constructed to describe several channels defined by some associated selection criteria simultaneously. The likelihood in Equation 4.2 can be redefined for the

combination of electron and muon channels

$$\mathcal{L}(n_c;\alpha) = \prod_{\text{c } \in \text{ channels}} \frac{\nu_c^{n_c} e^{-\nu_c}}{n_c!}, \tag{4.3}$$

where c represents the channels being considered and α are the parameters associated with the model. For simplicity of notation, the discussion below focuses only on a single channel. However, the procedure described below is applied to the combined model as well.

4.3 Treatment of systematic uncertainties

In the example likelihood given in Equation 4.2, there are additional parameters that also affect the distributions of the observables that are not the POI. These parameters are known as *nuisance parameters* (θ), since they must be accounted for regardless of the interest to the analysis. These are related to systematic uncertainties affecting the signal and background normalisation and shape. Using the methods described in Chapter 11, $\pm 1\sigma$ up and down variations of θ are constructed. Once the uncertainties have been estimated, a constraint term $f(\tilde{\theta};\theta,\sigma_\theta)$ is multiplied by the likelihood. A Gaussian penalty term is used for the constraint term in the analysis. The Gaussian constraint is parameterised such that $\tilde{\theta} = 0$ is the nominal value of the parameter, and $\tilde{\theta} \pm 1$ are the $\pm 1\sigma$ variations. The $\tilde{\theta}$ values are treated on the same footing as the measurement, and they are independent from other parts of the data. Therefore, the joint probability of n and $\tilde{\theta}$ is given by the product of their probabilities. The likelihood can be redefined as

$$\mathcal{L}(n;\nu_S,\theta) = \frac{\nu^n e^{-\nu}}{n!} \times \prod_{j=1}^{N} \frac{1}{\sqrt{2\pi}\sigma_j} e^{\frac{-(\tilde{\theta}_j - \theta_j)}{2\sigma_j^2}}, \tag{4.4}$$

where θ_j is the nuisance parameter corresponding to systematic j, σ_j are the 1σ variations and the expected number of events is a function of the POI and the nuisance parameters, $\nu = \nu_S + \nu_B(\theta)$.

When the data are fit using the full likelihood in Equation 4.4, both the POI and nuisance parameters are estimated to minimise the likelihood. However, in some scenarios, standard

deviation of the nuisance parameter after the fit can be substantially smaller than what entered into the constraint term, indicating an inherent mismodelling of the likelihood. The *post-fit* pulls are used to quantify the degree to which the estimate of the nuisance parameter, $\hat{\theta}$, deviates from the nominal value, $\tilde{\theta}$, given the uncertainty after fitting, $\hat{\sigma}_{\hat{\theta}}$. The pull of a nuisance parameter is defined as

$$\text{pull} = \frac{\hat{\theta} - \tilde{\theta}}{\hat{\sigma}_{\hat{\theta}}}. \tag{4.5}$$

Deviation from the central value of the nuisance parameter will indicate features of the data not described by the model. The pulls of the nuisance parameters from the fit to data are shown in Chapter 12.

The impact of the nuisance parameter on the parameter of interest is defined as

$$\text{Impact} = \Delta\hat{\nu}_S = \hat{\hat{\nu}}_S(\theta \pm \sigma_\theta) - \hat{\nu}_S, \tag{4.6}$$

where, $\hat{\hat{\nu}}_S(\theta \pm \sigma_\theta)$, is the fitted value of ν_S with the nuisance parameter fixed at its nominal value ($\tilde{\theta}$) plus or minus its standard deviation, resulting in the *prefit* impact. The postfit impact is given by the nuisance parameter fixed at its estimated value ($\hat{\theta}$) plus or minus its standard deviation.

4.4 Hypothesis tests

Hypothesis tests are an additional statistical tool used in the analysis to test the compatibility of the data collected with respect to two hypotheses, rejecting one over the other based on experimental observations. Two hypotheses are defined: an *alternative hypothesis* (H_1) and a *null hypothesis* (H_0), where H_0 is synonymous with the hypothesis that will be tested. When considering an observed excess of events for a potential discovery, H_0 is defined as the expectation solely based on the SM background expectation, also referred to as the background-only hypothesis. whilst H_1 is defined as the expectation from SM background and a BSM process, e.g. CIs, is referred to as the signal+background hypothesis. The claim of discovery

is that the data are incompatible with the background-only hypothesis. When no significant excess is observed, the incompatibility of the data with signal+background hypothesis is tested, and a potential signal can be excluded.

In order to distinguish between the two hypothesis a *test statistic*, $\mathcal{T}(\mathcal{D})$ is constructed such that the value of $\mathcal{T}$ will be different dependant on the hypothesis. An *acceptance region* is defined, such that if $\mathcal{T}(\mathcal{D}) < k_\alpha$, then H_0 is accepted. The test statistic is defined such that it minimises the probability at which H_0 is rejected when it is true, known as a Type-I error. In contrast, a Type-II errors describes accepting H_0 when H_1 is true, denoted by β. A test statistic is chosen such that it maximises the power of a test, $1-\beta$, by fixing size of the test (α). There are a multitude of test statistics that can be used. The most powerful test with respect to a single alternative hypothesis is given by the likelihood ratio $\mathcal{T}(\mathcal{D}) = \mathcal{L}(n;\nu_{S+B})/\mathcal{L}(n;\nu_B)$ according to the Neyman-Pearson lemma [48]. A generalisation of the likelihood ratio known as the *profile likelihood ratio* is defined as

$$\lambda(\nu_S) = \frac{\mathcal{L}(\nu_S;\hat{\hat{\theta}}(\nu_S))}{\mathcal{L}(\hat{\nu}_S,\hat{\theta})}, \tag{4.7}$$

where the *conditional maximum likelihood estimate*, $\hat{\hat{\theta}}(\nu_S)$, is the value of θ that maximises the likelihood function with ν_S fixed. The profile likelihood test statistic is used in many of the LHC experiments, including ATLAS. The test statistic is used to define the final test statistic relevant to analyses

$$q_{\nu_S} = -2\ln\lambda(\nu_S), \tag{4.8}$$

where it is used to quantify the compatibility of the observed data for a given hypothesis. The probability to have obtained data with a certain property assuming a hypothesis [51] is given by the p-value,

$$p_{\nu_S} = \int_{q_{\nu_s,obs}}^{\infty} f(q_{\nu_S};\nu_S,\theta)\ dq_{\nu_S}, \tag{4.9}$$

where $f(q_{\nu_S};\nu_S,\theta)$ is the probability density function of the test statistic under the hypothesis ν_S, and $q_{\nu_S,obs}$ is the test statistic of the observed data. As p_{ν_S} gets smaller, the confidence that the assumed hypothesis is true decreases.

For discovery, the null hypothesis ($\nu_S = 0$) must be rejected. This compatibility is based on the following p-value

$$p_0 = \int_{q_{\nu_S,obs}}^{\infty} f(q_0; 0, \hat{\hat{\theta}}(\nu_S = 0))\ dq_{\nu_S}. \tag{4.10}$$

It is customary to convert the p-value into the sigma of a standard Gaussian, defined as

$$Z = \Phi^{-1}(1 - p_0), \tag{4.11}$$

where Φ^{-1} is the inverse of a cumulative distribution for a standard Gaussian. The significances for evidence or a discovery correspond to 3σ and 5σ, respectively. These correspond to values of $p_0 = 1.3 \times 10^{-3}$ and $p_0 = 2.9 \times 10^{-7}$ for 3σ and 5σ, respectively.

When no significant excess is observed in data, a limit on the number of signal events or CI Λ scale is set. For limit setting the test statistic, $\tilde{q}_{\nu_S}$, is used to test the hypothesis of the signal being produced at ν_S from the alternative hypothesis at $\nu_S' < \nu_S$ [53],

$$\tilde{q}_{\nu_S} = \begin{cases} -2\ln\frac{\mathcal{L}(\nu_S,\hat{\hat{\theta}}(\nu_S))}{\mathcal{L}(0,\hat{\hat{\theta}}(0))} & \text{for } \hat{\nu_S} < 0, \\ -2\ln\frac{\mathcal{L}(\nu_S,\hat{\hat{\theta}}(\nu_S))}{\mathcal{L}(\hat{\nu}_s,\hat{\theta})} & \text{for } 0 \leq \hat{\nu}_s \leq \nu_S, \\ 0 & \text{for } \hat{\nu}_s > \nu. \end{cases} \tag{4.12}$$

A p-value can be defined for the hypothesis using the above test statistic and Equation 4.9,

$$p_{\nu_S} = \int_{\tilde{q}_{\nu_S,obs}}^{\infty} f(\tilde{q}_{\nu_S}; \nu_S, \hat{\hat{\theta}}(\nu_S))\ d\tilde{q}_{\nu_S}. \tag{4.13}$$

It was previously defined if the test statistic is outside the acceptance region α, the hypothesis is rejected. Using this definition, $p_{\nu_S} \geq \alpha$ is referred to as the *confidence level* (CL) that includes the true value of the POI with probability larger than $1 - \alpha$. This definition of CL would then

lead to the statement that the confidence interval covers the true value of the parameter with a CL larger than $1 - \alpha$. The CL value of the upper limit is commonly chosen as 95% for ATLAS and CMS results. Signal hypothesis will be tested until the point at which the signal hypothesis is found that is no longer excluded at the 95% confidence interval.

$\mathrm{CL_s}$ construction

Once a statement on the exclusion of a model has been made, the model is no longer considered essential to be searched. Therefore, the metric by which analyses can claim a model has been excluded has been studied in great detail. The p-value discussed above can be subjected to statistical fluctuations and can lead to non-physical exclusions when a downward fluctuation in the observed number of events occurs. This would result in premature exclusions of new physics models.

Two methods are constructed to tackle this problem by the high-energy particle physics community: the power-constrained limit (PCL) [54] and the $\mathrm{CL_s}$ formalism [55, 56]. The PCL method is not used widely used in the community but represents a cutoff at a positive value of the POI everywhere. The more widely accepted, $\mathrm{CL_s}$ formalism is constructed to reduce the likelihood of excluding signal hypotheses that a search is not otherwise sensitive. The $\mathrm{CL_s}$ formalism is defined as the ratio of two p-values:

$$\mathrm{CL_s} = \frac{p_{\nu_S}}{1 - p_{\nu_B}} \tag{4.14}$$

where p_{ν_B} is the p-value derived from the same test statistic under the background-only hypothesis. The negative fluctuations will be moderated by the denominator, which is the same test statistic as the numerator, but with $\nu_S = 0$. The $\mathrm{CL_s}$ formalism is mainly used to perform hypothesis tests aimed at excluding signal models.

Expected limit

The expected limit is an important quantity which indicates the sensitivity of an analysis. The expected limit and corresponding upper and lower bounds are calculated by sampling a distribution of the limits produced from many background-only MC toy experiments and taking the median value of the expected limit distribution, and its 95% and 68% quantiles. The median value is taken instead of the mean, as it is invariant to the choice of significance or p-value. The distribution of the limit is given by $f(\nu_{S,\mathrm{up}}; 0, \hat{\hat{\theta}}(\nu_S = 0, obs))$, where the nuisance parameters have a profiled value based on the observed data. The 1σ and 2σ bounds indicate the rage of fluctuations that one expects for the limit under the assumption of the background-only model.

Figure 4.1 depicts the distribution of limits from toy MC experiments in the constructive and destructive SRs in the electron and muon channel. The results are based on 2000 toy experiments. The 68% and 95% quantiles of the distribution corresponding to the one and two sigma error bands, respectively, are indicated on the distributions by the yellow and green bands. The Non-Gaussian behaviour observed in the distributions leads to an asymmetry in the 1σ and 2σ bands. This is due to the distribution of the test statistic becoming discrete when there are low number of events in the signal regions; this is especially prominent in the muon destructive signal regions and can be seen in the final results in Chapter 12.

Asymptotic approximation

In addition to the MC approach described above, the confidence interval can be calculated using asymptotic formulae [53]. This approximation is based on theorems by Wilks and Wald [57], which show that for sufficiently large data sample, the distribution of the likelihood-ratio based test statistic follows a Gaussian distribution. Therefore, $-2\ln\mathcal{L}(\nu_S)$ will follow a χ^2 distribution. The probability p_0 can be directly calculated from q_0 as [53]

$$p_0 = 1 - \Phi\left(\sqrt{q_0}\right), \tag{4.15}$$

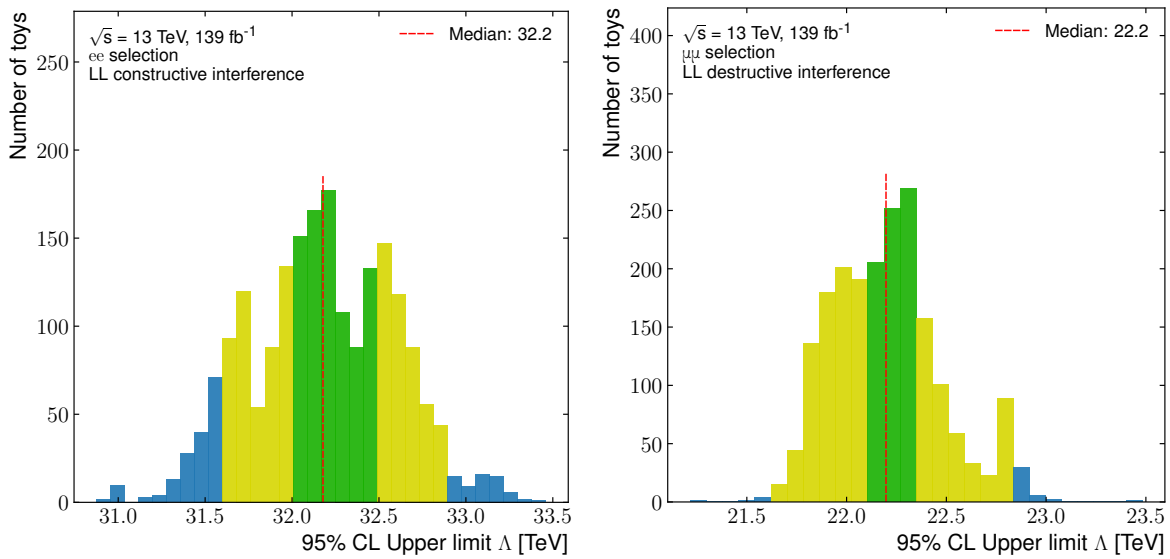

Figure 4.1 Expected limit distribution for 2000 toy MC experiments in the electron constructive (left) and muon destructive (right) signal region for the LL CI model. The dashed line indicates the median of the distribution. The green and yellow bands correspond to the 68% and 95% quantiles, respectively, of the distribution.

and the significance takes the form $Z = \sqrt{q_0}$. The asymptotic approach considerably reduces the computing time and resources required.

Due to the assumed distribution of the test statistic, for Poisson-like distributions with low statistics limits obtained using the asymptotic approximation may overestimate the limit. The single-bin signal regions defined at high invariant mass for the analysis have a small number of events. Therefore, the asymptotic approximation is deemed insufficient for the analysis. A comparison of the expected limits from the MC method and the asymptotic approximation is shown in Figure 4.2. The results from the asymptotic approach predict an expected limit that is optimistic compared to the toy approach.

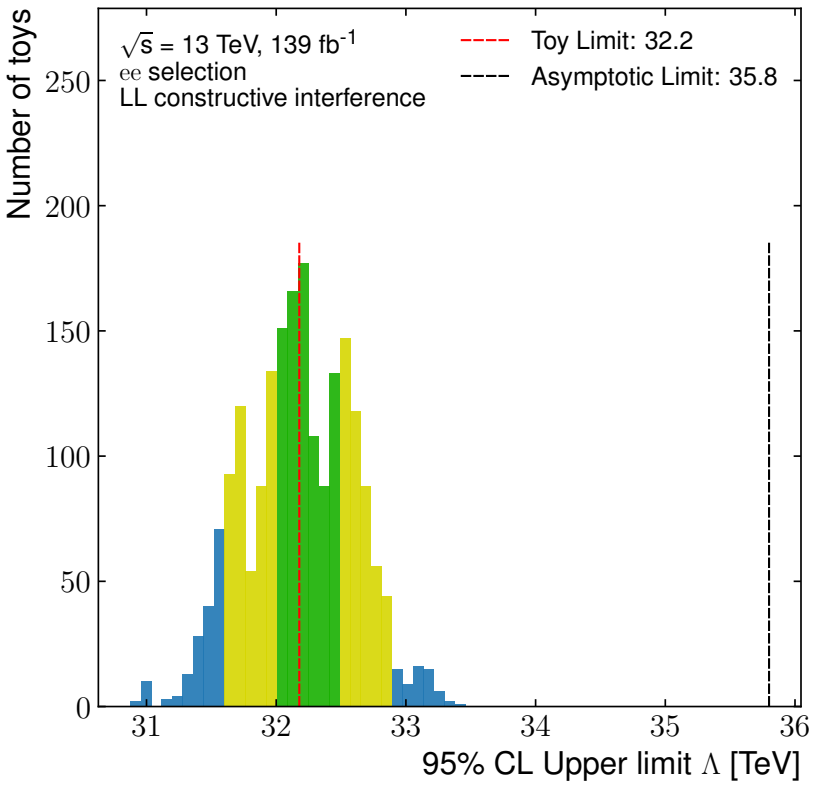

Figure 4.2 Comparison of expected limit from the toy MC method and the asymptotic approximation in constructive electron signal region for the LL chiral CI model. The expected limit from the toy MC method and the asymptotic approximation is shown by the red and black dashed lines, respectively.

4.5 Choice of parameter of interest

The formalism above focus on the number of signal events ν_S as the parameter of interest. This choice of POI allows to search for non-resonant signals and set limits in terms of the number of signal events in the signal region. There are two possible methods to interpret the results in terms of CI models: a reinterpretation of the model-independent limits in terms of CI models using the CI signal MC, and the other where the ν_S is parameterised in terms of the CI energy scale Λ and limits are set on CI models directly.

There are several steps involved with the reinterpretation of the model-independent limits on ν_S in the context of CI models. The CI interaction signal MC is used to map the expected number of signal events for a given model to the number of signal events. The constructive signal region results are expected to be used for constructive interference CI models, whereas the destructive interference signal region results are used for destructive models. Once an interference model has been chosen, the limits on the number of signal events are mapped to the different chiral models of the CI reweighted templates described in Section 8.2.2. A linear interpolation is performed between reweighted Λ points to allow for signal events to be extracted between reweighted Λ points. Figures 4.3 to 4.6 depict the reinterpretation of the ν_S expected limits in the context of the CI Λ limits. It is important to note that the uncertainty on the signal yield has not been taken into consideration. The procedure in including the uncertainties would involve taking the experimental uncertainty on the CI signal model and varying the expected yield by the uncertainty and calculating the corresponding limit.

Interpretation of the results directly on the CI energy scale Λ involves parametrising the expected signal yield, ν_S in terms of Λ. The parameterisation can be achieved by a small modification to the custom PDF class created described in Section 8.2.2, where the integral of the expected number of signal events in the SR is provided as a function of Λ. This allows the POI to be defined as Λ. The expected number of events predicted in the signal yield can then be written as $\nu = \nu_B + \nu_S(\Lambda)$. An advantage of using Λ as the POI is that it uses a common parameter between the electron and muon channels. This allows the likelihood to be defined for the combination of the electron and muon channels in terms of Λ. The limits set on the

number of events for the combined channel has no trivial mapping to Λ, due to the different detector efficiencies in the electron and muon channels.

The expected limits in the electron and muon channels are compared for the two choices of POI in Table 4.1. The limits shown indicate that there is a little difference between interpreting the limits directly on Λ and reinterpreting them from the limits on the number of signal events. However, due to the added benefit of being able to easily provide limits on the combined electron and muon channels, the final results on the CI models are interpreted directly in terms of Λ. Nevertheless, the model-independent limits on ν_S are still presented to facilitate reinterpretation into other non-resonant BSM models.

			Expected limit [TeV]			
Int.	Channel	POI	LL	LR	RL	RR
Constructive	e^+e^-	Λ	31.1	28.9	28.7	30.9
		ν_S	31.1	28.8	28.7	30.9
	$\mu^+\mu^-$	Λ	29.8	27.6	27.5	29.6
		ν_S	29.8	27.6	27.5	29.6
Destructive	e^+e^-	Λ	23.0	24.4	24.4	23.2
		ν_S	23.0	24.4	24.4	23.2
	$\mu^+\mu^-$	Λ	22.6	24.0	24.2	22.8
		ν_S	22.6	24.1	24.1	22.8

Table 4.1 Comparison of expected limits from reinterpreting the results in terms of Λ from limits on the number of signal events (ν_S) and limits set directly on Λ as the parameter of interest. The limits are shown for the various CI chiral and interference models in the electron and muon channels.

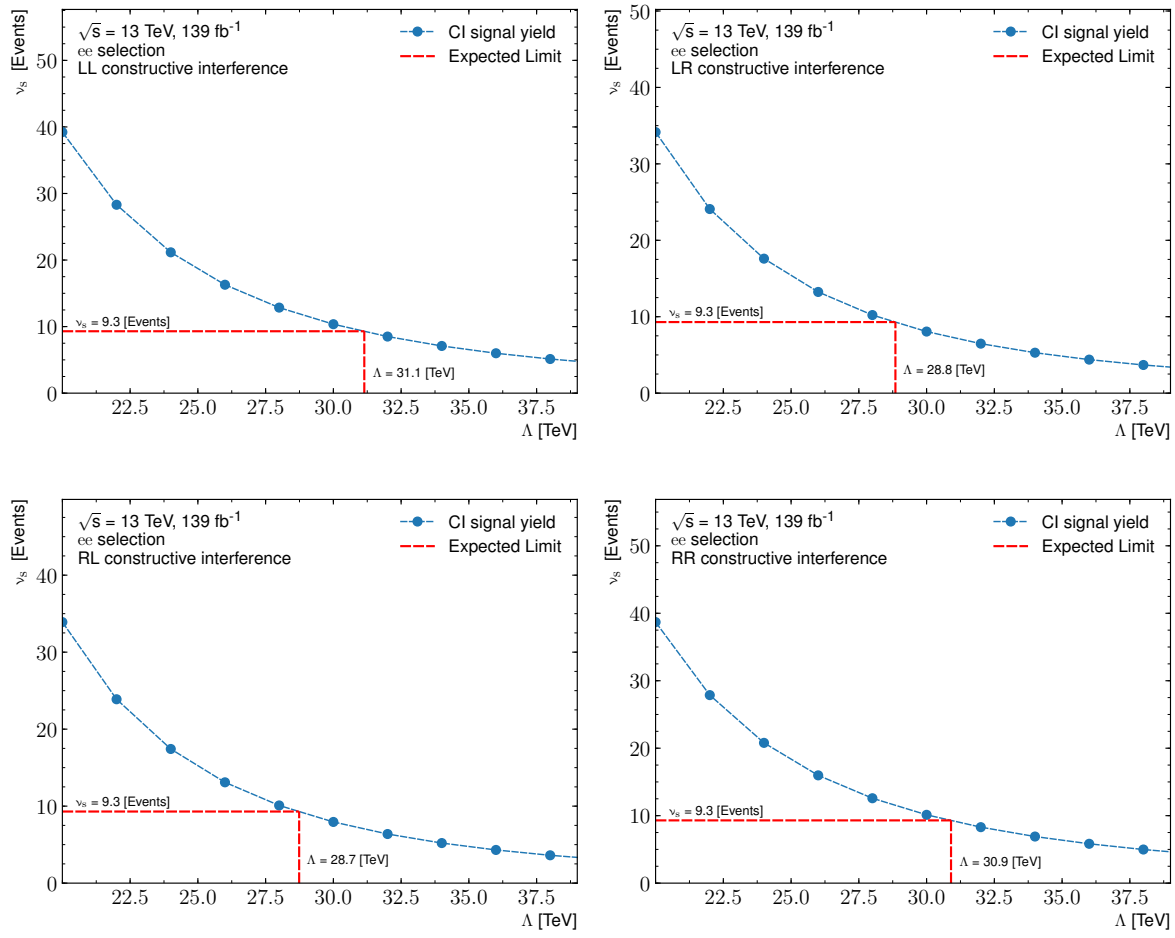

Figure 4.3 Distribution of the expected yield in the signal region corresponding to Λ values. The expected limit on the number of signal events is depicted and the mapping to its Λ value. The constructive interference signal regions are shown for the electron channel.

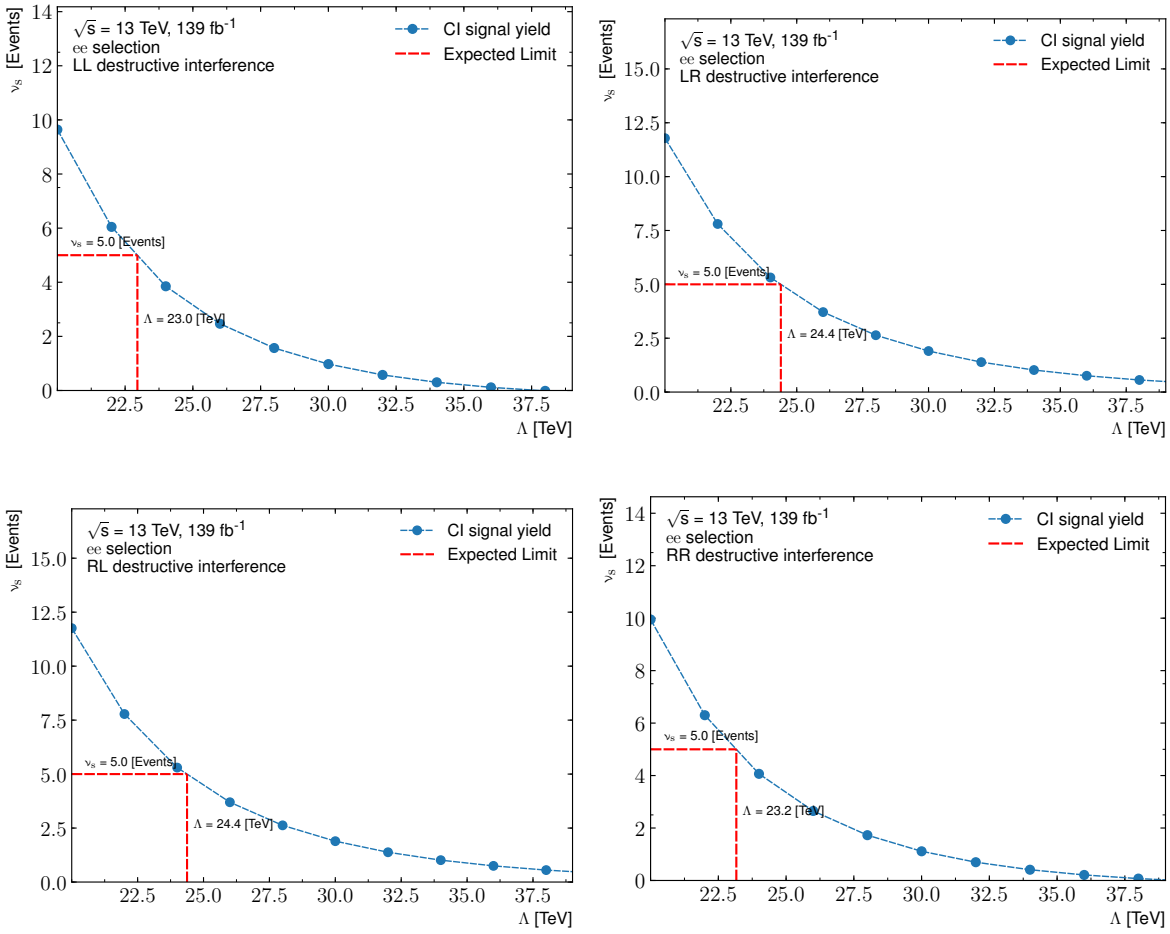

Figure 4.4 Distribution of the expected yield in the signal region corresponding to Λ values. The expected limit on the number of signal events is depicted and the mapping to its Λ value. The destructive interference signal regions are shown for the electron channel.

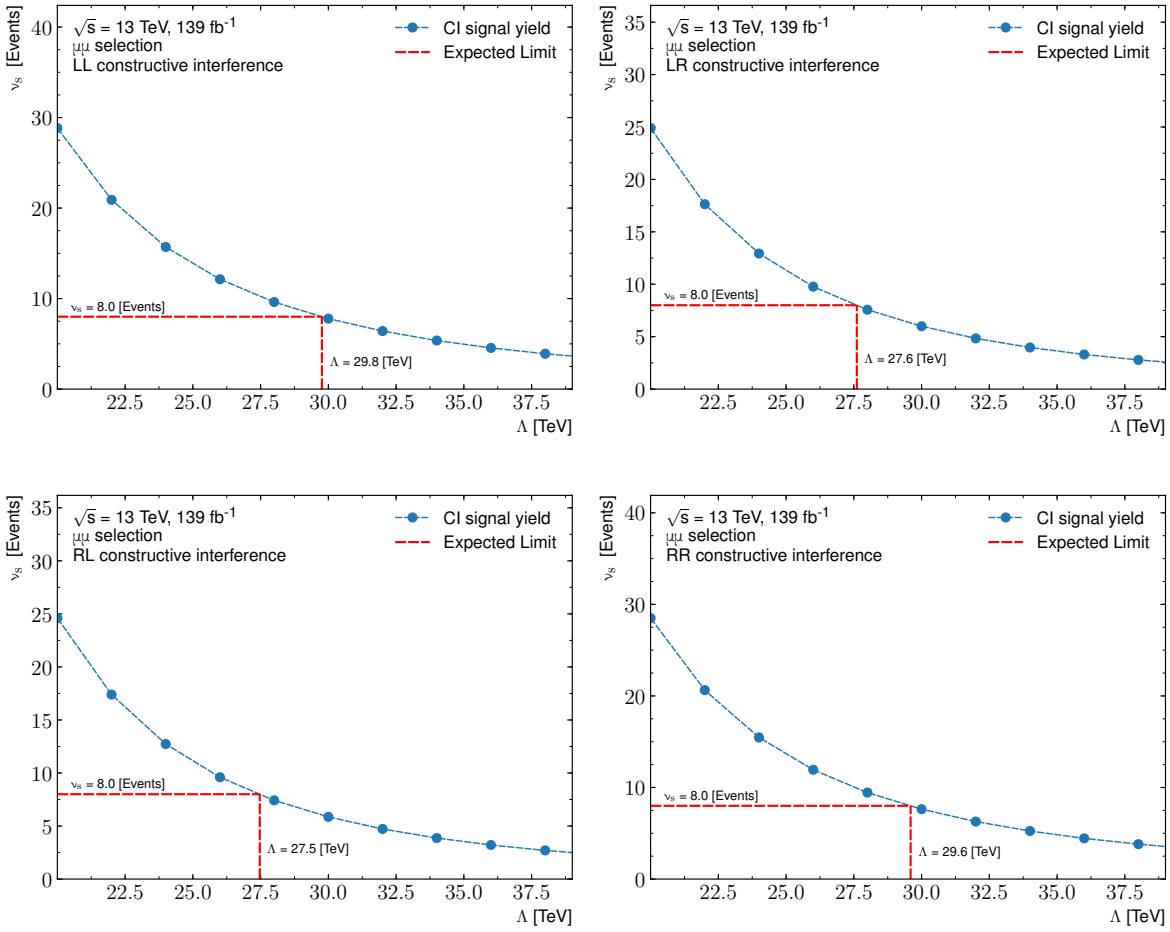

Figure 4.5 Distribution of the expected yield in the signal region corresponding to Λ values. The expected limit on the number of signal events is depicted and the mapping to its Λ value. The constructive interference signal regions are shown for the muon channel.

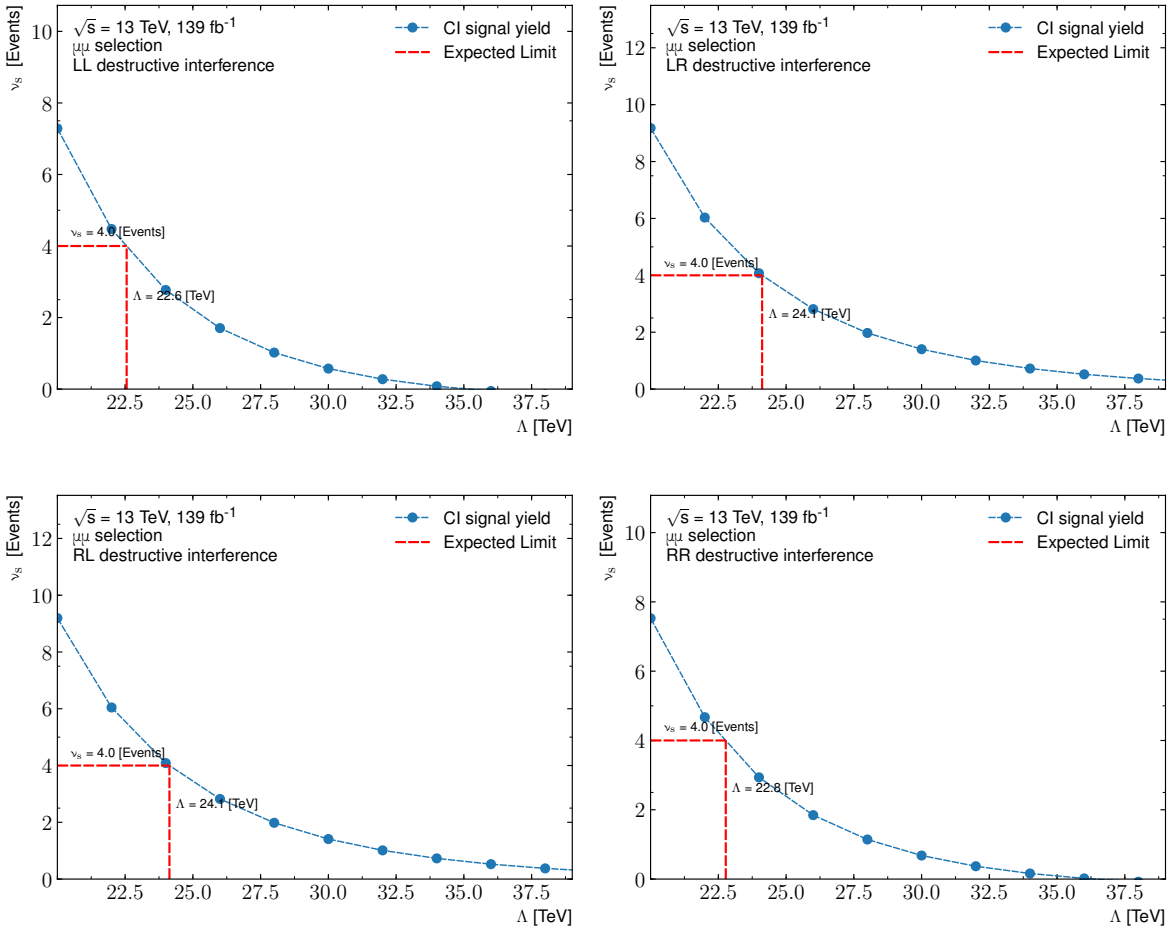

Figure 4.6 Distribution of the expected yield in the signal region corresponding to Λ values. The expected limit on the number of signal events is depicted and the mapping to its Λ value. The destructive interference signal regions are shown for the muon channel.

Part II

Experiment

Chapter 5

Experimental Setup

This section will describe in detail the experimental apparatus used to produce results needed for the analysis carried out in Part III. The complex machinery of the accelerating system is outlined in Section 5.1. Section 5.2 describes the detector system and provides an overview of the filtering and processing of the data acquired by the detector.

5.1 The Large Hadron Collider

The Large Hadron Collider (LHC) [58] operated by the European Organisation for Nuclear Research (CERN) is currently the largest and most powerful particle accelerator in the world. The LHC ring is about 100 m underground at the French-Swiss border close to Geneva, and has a circumference of 27 km. Predominantly performing proton-proton (pp) collisions with a design centre-of-mass collision energy of $\sqrt{s} = 14\,\text{TeV}$ and an instantaneous luminosity of $10^{34}\,\text{cm}^{-2}\text{s}^{-1}$. Whilst the LHC also allows to accelerate heavy ions (e.g. Pb and Xe), the heavy-ion program is not discussed further, as only pp collision data is used for the presented studies in this thesis.

The LHC is supported by a chain of pre-accelerators which are used to ramp protons to the required input energy of 450 GeV [59, 60]. A schematic of the LHC accelerator chain is shown in Figure 5.1. The process begins by stripping off orbiting electrons from hydrogen to obtain

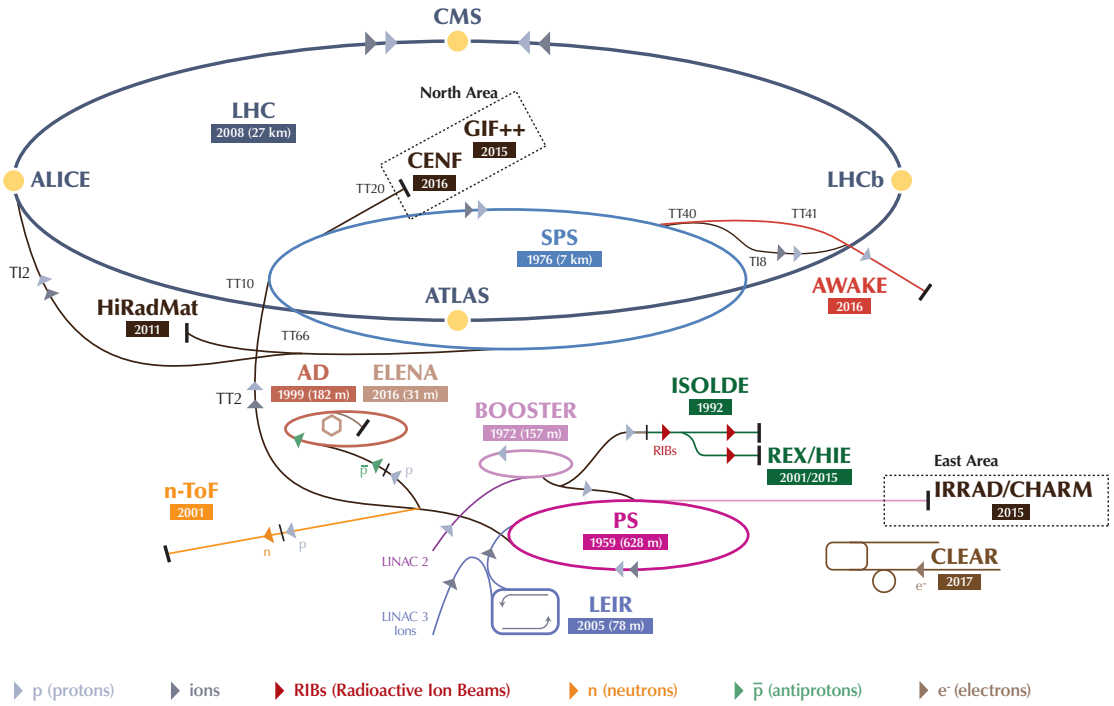

Figure 5.1 The CERN accelerator complex in 2018, including the LHC and the pre-accelerators [61].

protons. This is done by the *Linac 2*, a linear accelerator which also accelerates the protons to an energy of 50 MeV. These proton beams are then fed into the *Proton Synchrotron Booster* (PSB), first of a series of circular accelerators that accelerate the protons to an energy of 1.4 GeV. The beams then enter the 628 m long *Proton Synchrotron* (PS) where the proton beams are accelerated to a beam energy of 25 GeV and injected into the *Super Proton Synchrotron* (SPS). At the penultimate stage of the acceleration in the 6.9 km ring of the SPS, the proton beam reaches the required beam energy of 450 GeV arranged in 240 bunches. After the SPS, the protons injected into counter-circulating LHC rings to be accelerated to their maximum energy, where collisions under stable conditions are achieved.

There are a total of 1232 dipole magnets installed in the LHC that are used to steer the proton beams around each ring. For proton energies of 7 TeV, a magnetic field of 8.3 T is required in these dipoles. To keep the beams focused and achieve small beam size at the interaction point quadrupole and higher-order magnets are used.

In total there are a maximum of 3564 possible bunch positions with a spacing of 25 ns available at the LHC. However, due to rise-time constraints of the injector and beam-dump kicker magnets, this is reduced to 2808 with approximately 10^{11} protons per bunch. The filling choice of the LHC ring is the so-called bunch scheme. The bunches are typically clustered in what are called bunch trains.

The two circulating protons beams intersect at four interaction points where the main experiments are installed around the LHC. CMS [62] and ATLAS [63], two general-purpose detectors allow precision measurements of SM processes, including the properties of the Higgs boson, and allow for the search for physics beyond the SM. LHCb [64] and ALICE [65] are two lower rate specialised detectors studying the properties of flavour physics and heavy-ion physics, respectively. To study the properties of particles with very low scattering angles from the beam (i.e. forward physics), TOTEM [66] and LHCf [67], two additional smaller experiments were also installed at the LHC.

5.2 The ATLAS detector

The ATLAS experiment is the world's largest general-purpose detector. Situated at one of the interaction points around the LHC, it is 4 m in length and 25 m in height and weighs approximately 7000 t. ATLAS consists of several sub-detector systems arranged in sequential layers. Several electromagnet systems provide a strong magnetic field coverage across the detector body. The *Inner Detector (ID)* located nearest to the interaction point, provides position and momentum information for charged particles emerging from the collisions. Two calorimeter systems, the *Electromagnetic Calorimeter* and the *Hadronic Calorimeter* are used to measure the energy of charged and neutral particles. The *Muon Spectrometer* forming the

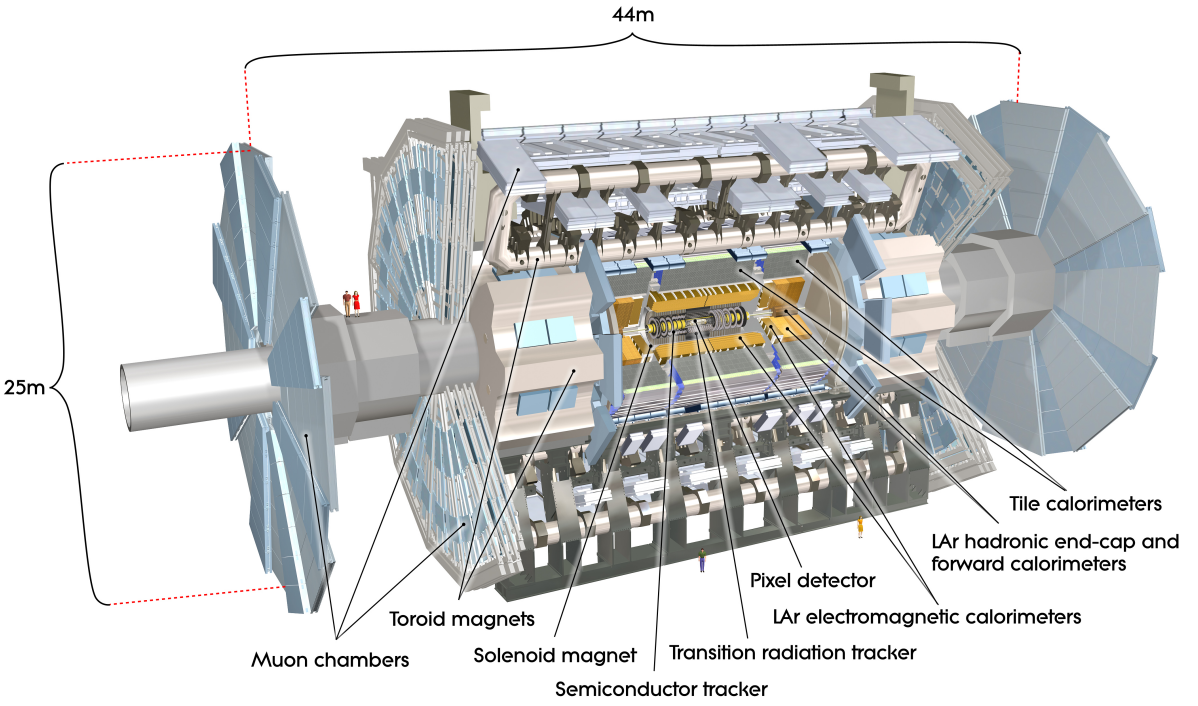

;

Figure 5.2 Schematic overview of the ATLAS detector highlighting the major subdetector components within it [68].

outermost layer of the detector, provides momentum measurements for muons. An overview of the ATLAS detector and its subsystems is outlined in Figure 5.2.

ATLAS coordinate system and kinematic quantities

ATLAS uses a right-handed coordinate system with its origin in the centre of the detector at the interaction point. The x-axis is aligned such that it points towards the centre of the LHC ring, the positive y-axis points upwards, and the z-axis is defined going along the beam-pipe. An angular system is used where r is the radial distance from the point of interest, ϕ is the azimuthal angle in the x-y transverse plane and the polar angle θ. *Pseudorapidity*, $\eta = -\log\tan\frac{\theta}{2}$, is used as a dimensionless measure of θ. The change in η is invariant under Lorentz boosts along the beam axis. The distances between objects are defined in the azimuthal-pseudorapidity space as $\Delta R^2 = \Delta\eta^2 + \Delta\phi^2$.

The momentum of an object is expressed in Cartesian coordinates as $\mathbf{p} = (p_x, p_y, p_z)$, where p_x, p_y and p_z are the momentum in the x,y and z directions, respectively. The *invariant-mass*, $m_{\ell\ell}$, is one of the most central quantities calculated from observations that is used throughout this thesis. The invariant-mass is defined as the squared energy minus the squared momentum of a system. The missing transverse momentum of an object, p_{T}, is defined as the projection of momentum in the x-y plane. transverse momentum is given by

$$p_{\mathrm{T}} = \sqrt{p_x^2 + p_y^2} \,. \tag{5.1}$$

5.2.1 Inner Detector

The Inner Detector (ID) [69], embedded in a 2 T solenoid magnetic field, allows for the tracking of charged particles near to the interaction point. It is designed to achieve high-precision measurements of momentum and measurements of primary and secondary vertices of collisions in the range $|\eta| \leq 2.5$. It is composed of three independent detector technologies: the *pixel detector*, *semi-conductor tracker (SCT)*, *transition radiation tracker (TRT)* and the *insertable B-layer* as shown in Figure 5.3.

Pixel detector

The innermost part of the ID closest to the interaction point is the pixel detector. It provides high-resolution information on the location of charged particles. It is formed of four concentric cylindrical layers, the *Insertable B-Layer (IBL)* [70], added in 2014, and three additional layers in the barrel region. The layers of the pixel detector are based on silicon semiconductor technologies. This allows the detection of charged particles when traversing through the doped silicon, where an electron-hole pair is formed resulting in a current. The semiconductor sensors are arranged in a grid and provide fine granularity position information. The IBL pixels are situated at a distance of $R = 33.25\,\mathrm{mm}$ from the centre of the beam pipe and have a size of $50\,\mu\mathrm{m} \times 250\,\mathrm{nm}$ in $R \times \phi, z$, with an intrinsic resolution of $8\,\mu\mathrm{m} \times 40\,\mu\mathrm{m}$. The outer layer pixels measure $50\,\mu\mathrm{m} \times 400\,\mathrm{nm}$ with an intrinsic resolution of $10\,\mu\mathrm{m} \times 115\,\mu\mathrm{m}$ [69]. With the addition

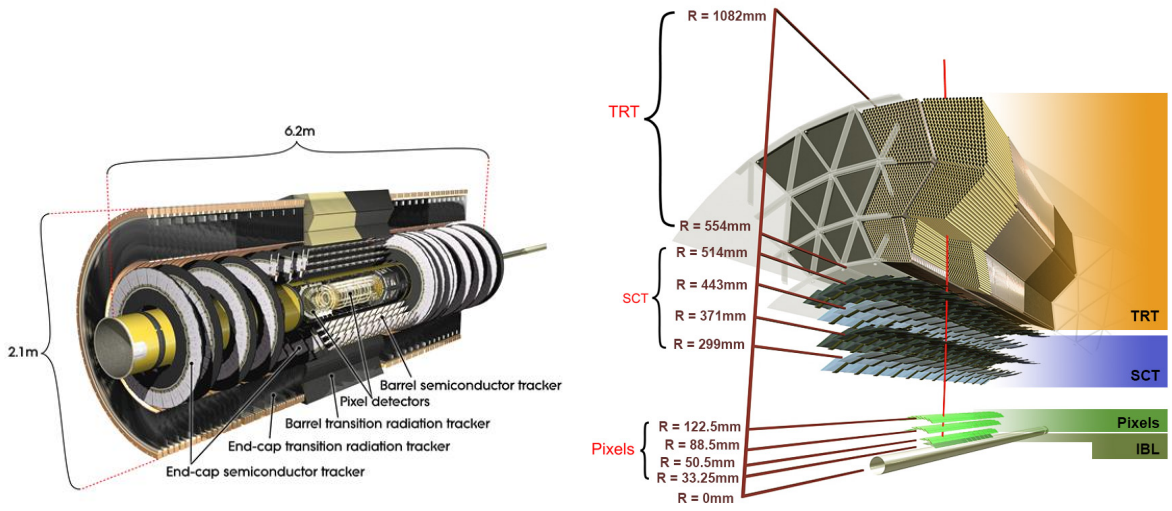

Figure 5.3 Illustration of the ATLAS inner detector, containing the pixel detector, semiconductor tracker (SCT), transition radiation tracker (TRT)and the *insertable B-layer*. The components of the inner detector are shown along the beam-pipe (left) and a slice of the inner detector (right).

of the IBL, the position resolution of primary and secondary vertices was improved to 10 nm in Rϕ and 115 µm in z [71].

Semiconductor tracker

Based on silicon sensors, the SCT is located 299 mm from the interaction point. The SCT detects charged particles through the same mechanism as the pixel detector. However, instead of pixels, it uses long strip sensors arranged in four cylindrical layers in the barrel region and nine disks in the end-caps. The SCT strip modules are arranged in pairs with a 40 mrad relative angle to provide a two-dimensional position measurement. This provides two independent hits that allows for the measurement of (r, ϕ) and improving the ϕ measurements of particles. In the barrel region for each track four space points with an intrinsic resolution of 17 µm, in Rϕ and 580 µm in z can be obtained.

Transition radiation tracker

Located 563 mm from the interaction point the TRT is the outermost component of the ID. The TRT is formed of approximately 370000 gas-filled straw tube detectors. Each straw tube is a hollow cylinder with a diameter of 4 mm containing a central tungsten wire filled with a gas mixture predominantly made out of Xenon. The tungsten wire along with the tube forms a capacitor, where the wire is the anode, and the surrounding tube acts as the cathode. When charged particles pass through the tube, the gas is ionised, producing an avalanche of electrons. The avalanche of electrons is detected as an electric current in the wire. The TRT has 73 straw planes in the barrel region, spaced horizontally at a distance $563\,\text{mm} < R < 1066\,\text{mm}$ and $|z| < 712\,\text{mm}$ from the interaction point, and 160 straw planes in the end-caps orientated in the radial direction. This results in on average 30 to 40 hits detected per particle by the TRT. The TRT straws have an intrinsic resolution of 130 µm in the $R\phi$ plane.

The TRT additionally consists of polypropylene fibres and polypropylene foils interleaved between the straw tubes in the barrel and end-cap modules respectively. Charged particles passing through the polypropylene undergo transition radiation. Transition radiation is produced when ultra-relativistic particles travel through the boundary of two materials with different dielectric constants. This radiation corresponds to photons and is proportional to the relativistic factor, γ, of the incident particle. Therefore, it will be higher for electrons compared to pions. This difference is crucial for differentiating between electrons and pions.

5.2.2 Calorimeters

The ATLAS calorimetry system consists of the electromagnetic and the hadronic calorimeters and is located closest to the beam pipe after the ID outside of the solenoid magnet. They are designed to measure the position and energy of particles emerging from the interaction point. They use materials which have a high probability of particles interacting with them. The electromagnetic and hadronic calorimeters are specialised in measuring the energies of γ and e, and hadrons, respectively. Neutral particles like γ and neutral hadrons, which do not induce a signal in the ID, can be identified in the calorimeters. This allows for nearly all

Standard Model particles to be identified except for weakly interaction neutrinos and μ, which have minimal interactions within the distance of the calorimeters and the interaction point.

High energy particles produce particle showers of lower-energy particles that travel through the calorimeter material. Therefore, it is essential to ensure that particle showers are contained within the calorimeters when designing them. The depth of a calorimeter material can be characterised by a particles radiation length (χ_0), and its nuclear interaction length (λ). Nuclear interaction length is defined as the mean distance a particle travels in a medium before undergoing a nuclear interaction. Due to electromagnetic interactions with the surrounding material, over one radiation length, a particle loses all but on average e^{-1} its original energy.

ATLAS using sampling calorimeters for both the electromagnetic and hadronic calorimeters. The Calorimeter materials have been selected to either be ionised or scintillate when particle a particle shower enters, which results in a measurable electrical signals. A particles energy can be calculated by summing the total radiation produced by a shower in the active layers.

Electromagnetic calorimeter

The electromagnetic calorimeter is designed to fully measure the energies of electrons (and positrons), and photons. Measurements of the energies of particles are made by inducing electromagnetic showers when the particle interacts with a dense material. For electrons, the shower is primarily initiated by bremsstrahlung, while for photons it is initiated by pair production. Shower particles are then detected by the detecting layers of the calorimeter interleaved with layers of dense material.

The electromagnetic calorimeter uses liquid argon (LAr) as its scintillator material and lead plates as its shower inducing material. Liquid argon component of the calorimeter was chosen due to its stability of response over a long period while being exposed to radiation [73]. It is divided into the barrel and end-cap regions highlighted in Figure 5.4.

In the barrel region, the electromagnetic calorimeter is split into three regions of different granularity. The innermost layer of the calorimeter has a fine granularity in η. The thickest

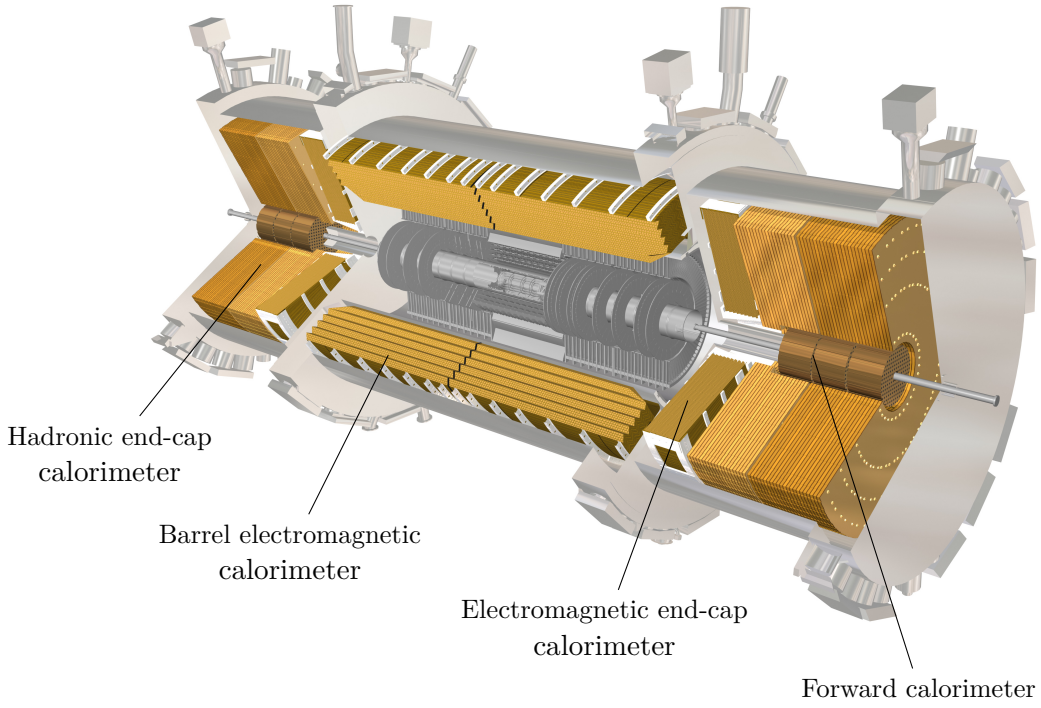

Figure 5.4 Illustration highlighting the liquid argon components of the ATLAS calorimeters [72].

layer of the electromagnetic calorimeter is the second layer, arranged in a square grid, which aids in locating the primary vertices of particles. Combining the measurements of the first two layers allows for locating the origin of neutral particles that do not leave tracks in the ID. The final layer, with the largest granularity, is used to estimate the energy lost beyond the electromagnetic calorimeter and to distinguish between electromagnetic and hadronic showers. A sketch of the barrel module is shown in Figure 5.5, where the cell granularity of each section is visible.

In the forward region, each end-cap electromagnetic calorimeter consists of two coaxial wheels separated by 3 mm. The inner wheels are constructed similarly to the barrel calorimeters shown in Figure 5.5. The other wheels do not have a third layer, and the majority of the thickness is composed of the first two layers.

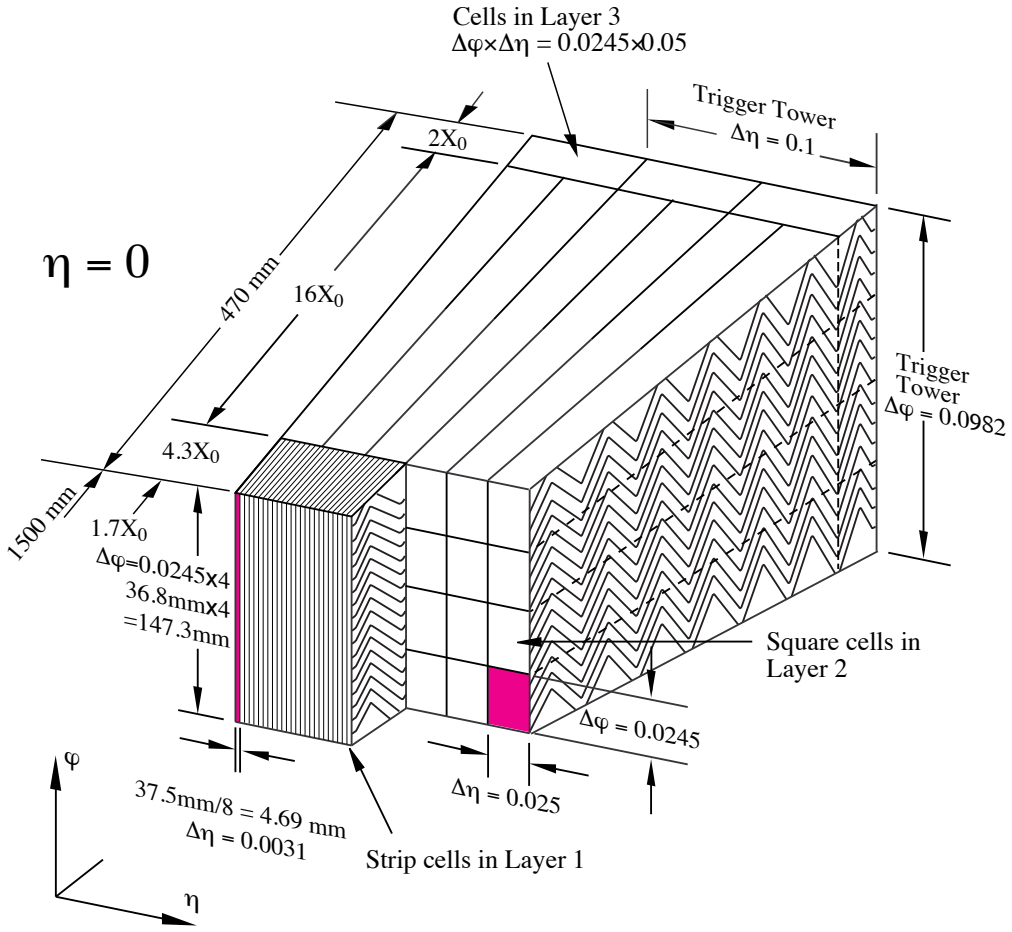

Figure 5.5 Drawing showing a section of the barrel electromagnetic calorimeter. The liquid argon cells are arranged into three distinct layers, with granularity decreasing for larger radius [63].

Hadronic calorimeter

The hadronic calorimeter, like the electromagnetic one, is a sampling calorimeter. Unlike the electromagnetic calorimeter, it uses steel as the shower-inducing material and scintillating plastic tiles [74]. The hadronic showers originate from interactions of incoming hadrons with the shower inducing material. The tile calorimeter sits in the barrel region at $|\eta| < 1.7$ where it is divided into the tile barrel $|\eta| < 1.0$ followed by the extended barrels covering $0.8 < |\eta| < 1.7$. The barrel and extended barrels are divided azimuthally into 64 modules. On the edges of the tiles, wavelength shifting fibres are used to extract signals by guiding them into photomultiplier tubes.

The hadronic end-cap calorimeter covers $1.5 < |\eta| < 3.2$ using LAr technology. It consists of two wheels per end-cap and uses copper as the shower-inducing material. In each end-cap two independent wheels are placed with 50 mm copper plates. A greater containment is achieved compared to the tile calorimeter by placing 12 nuclear interaction lengths of material before the muon spectrometers.

Forward calorimeters

The forward calorimeter provides additional coverage in the range $3.1 < |\eta| < 4.9$ and is designed to measure the energies of both electromagnetic and hadronic showers [73]. It consists of three modules, each using LAr as the detecting material. Copper rods are placed parallel to the beam axis in the innermost layer, is optimised for electromagnetic showers. Tungsten rods are used for the second and third layers as the shower-inducing material to measure the energy of hadronic particles.

Performance

Many analyses in ATLAS require an excellent energy resolution. Based on test beam-data, the calorimeter energy resolution is summarized in Table 5.1.

	Detector component	Resolution
EM	Barrel and end-cap	$\sigma_E/E = 10\%/\sqrt{E} \oplus 0.7\%$
Hadronic	Barrel and end-cap	$\sigma_E/E = 50\%/\sqrt{E} \oplus 3\%$
	Forward	$\sigma_E/E = 100\%/\sqrt{E} \oplus 10\%$

Table 5.1 ATLAS calorimetry energy resolution, as obtained from beam-test data [75, 76].

5.2.3 Muon spectrometer

The outermost portion of the ATLAS detector consists of the muon spectrometer [77] as shown in Figure 5.6. Muons can traverse through most of the ATLAS detector with minimal interactions as the effects of bremsstrahlung is reduced, due to the muons larger mass. Tracking chambers are used to measure the paths of muons. A series of toroidal magnets generate a strong magnetic field in the barrel and end-cap regions, from which the muon momentum can be measured via *sagitta, s* [78] of the curved trajectory, by

$$\frac{p_{\mathrm{T}}}{q} = \frac{L^2 B}{8s}, \tag{5.2}$$

where L is the length of the path in a constant magnetic field B, and q is the electric charge of the particle.

In the barrel toroid there are eight coils which provide bending the the region $|\eta| < 1.4$ and in the region $1.6 < |\eta| < 2.7$ the tracks are bent by two smaller end-cap magnets which are inserted into both ends of the barrel toroid. The transition region, $1.4 < |\eta| < 1.6$ consists of a combination of barrel and end-cap fields which provide magnetic deflection.

The muon spectrometer is composed of modules which use different detection technologies. These modules are organised into barrel and end-cap modules. Precise measurements of the η position of the muons are performed in the barrel region by the *monitored drift tubes* (MDTs) which allow for precise measurements of the muon momentum. The MDTs function similarly to the straw tube TRT in the ATLAS inner detector. They are formed of 30 nm tubes with a central tungsten wire, which is filled with a gas mixture of $\mathrm{Ar/CO_2}$ held at 3 bar. The MDT

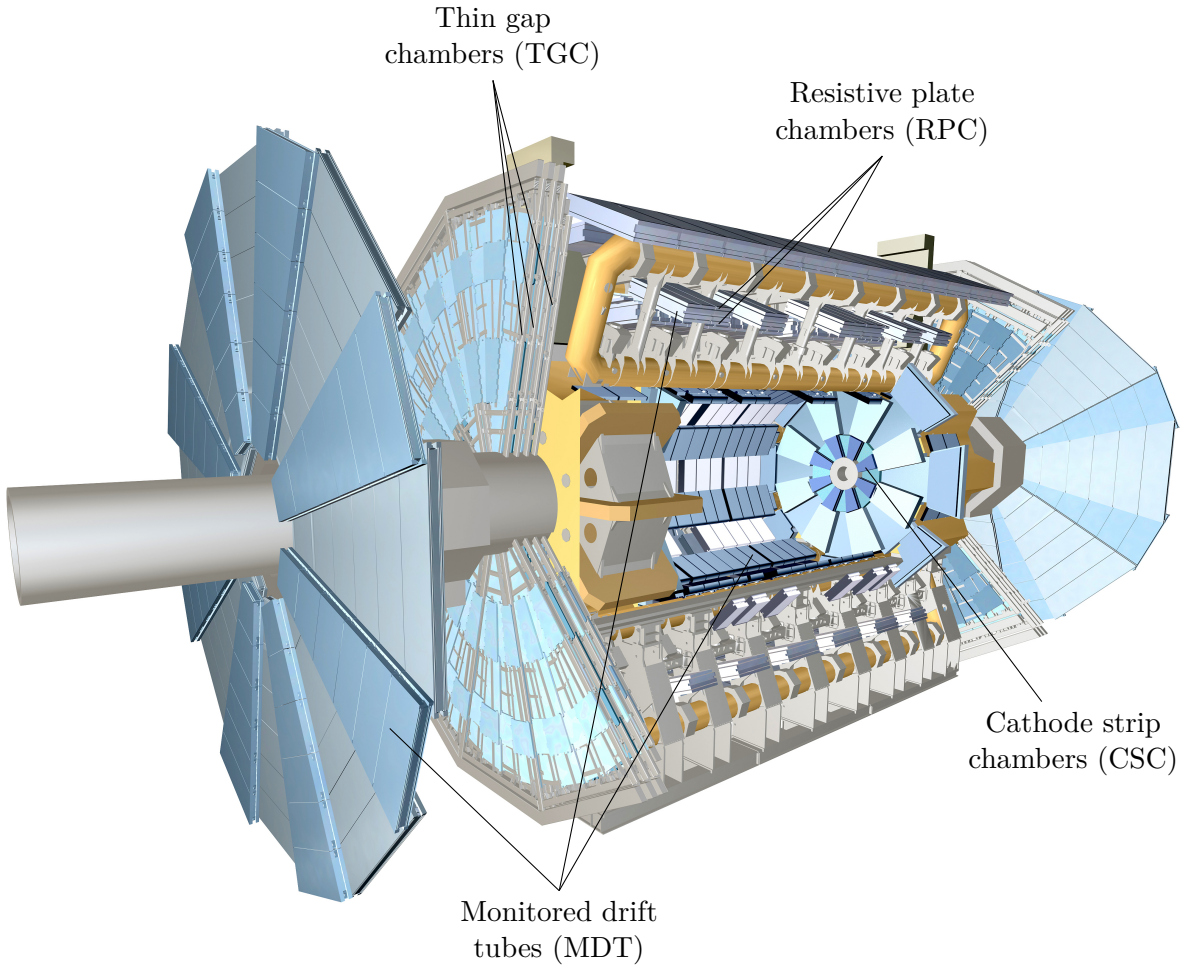

Figure 5.6 Illustration of the ATLAS muon spectrometer components. The toroid magnet coils are also shown in yellow [79].

modules are located in and on the eight coils of the superconducting barrel toroid magnet. The first layer allows for a coverage $|\eta| < 2.0$ and the second and third layers have a coverage of $|\eta| < 2.7$. The MDT spatial resolution is 80 µm and 35 µm per chamber due to having multiple layers of tubes per chamber which provide multiple hits.

The innermost layer consists of the *cathode-strip chambers* (CSCs), located in the region $2.0 < |\eta| < 2.7$. The CSC chambers are multi-wire proportional chambers with cathode planes segmented into strips in orthogonal directions in order to provide radial and transverse measurements. The space between the two planes is filled with a gas mixture mainly formed of Ar. Muons will ionise the gas, and positive ions are collected and read out by copper strips. The ϕ coordinate is measured by the time taken for the induced charges to drift to the cathode. CSC modules are formed of four stacked CSC planes, and these achieve a combined resolution of 40 µm in the η direction and 4 mm in the ϕ direction.

Together the CSCs and the MDTs form the precision tracking chambers and provide state of the art precision measurements of the muon p_T. A muon p_T resolution of $\sigma_{p_T}/p_T = 10\%$ at $p_T = 1\,\text{TeV}$ is achieved.

Special chambers are used to trigger on muons. The fast muon chambers provide signals within 25 ns after the passage of a particle, which allows to tag the beam crossing. This measures both the coordinates of the track, in the bending plane (η) and the non-bending plane (ϕ). In the barrel region, where $|\eta| < 1.05$, *resistive plate chambers* (RPC) are used which provide a resolution of 10 mm in both the z and ϕ directions. The RPCs are formed of two parallel plates made from a highly resistive plastic laminate with a gas mixture in between the plates. A strong electric field is placed between the resistive plates. The gas between the plates is ionised by passing muons, inducing an avalanche of electrons which creates a measurable signal in the form of current spikes in matrices of aluminium strips on the back of the resistive strips. In the end-cap region, where $1.05 < |\eta| < 2.4$, *thin gap chambers* (TGCs) are installed. Similar to the CSCs, the TCGs are multi-wire proportional chambers. For the TGC modules, the distance between the wire and strips is smaller than the distance between the wires, resulting in a smaller uniform region of the electric field. This allows for the electrons formed in the

gas ionisation to drift to the wires faster. The TGCs provide muon track information with a precision of 2 - 7 mm in the η direction and 3 - 7 mm in the ϕ direction.

5.2.4 Trigger and Data Acquisition System

The ATLAS trigger system is used to manage the high rate of LHC collisions, reducing the event rate from 40 MHz to $\mathcal{O}(100\,\text{kHz})$ at which events can be written to mass storage. This is done by partially reconstructing events during data taking and identifying events of interest to record. The trigger system must balance a good rejection of background events while maintaining a high rate of interesting events being saved. A chain of decision-making algorithms in hardware and software is utilised. For Run-2, the ATLAS trigger system uses a two-level system; the Level 1 (L1) hardware trigger and the High-Level Trigger (HLT) software trigger. The data acquisition (DAQ) system controls the data flow when trigger decisions have been received. An overview of the components of the ATLAS trigger and DAQ systems outlined in Figure 5.7.

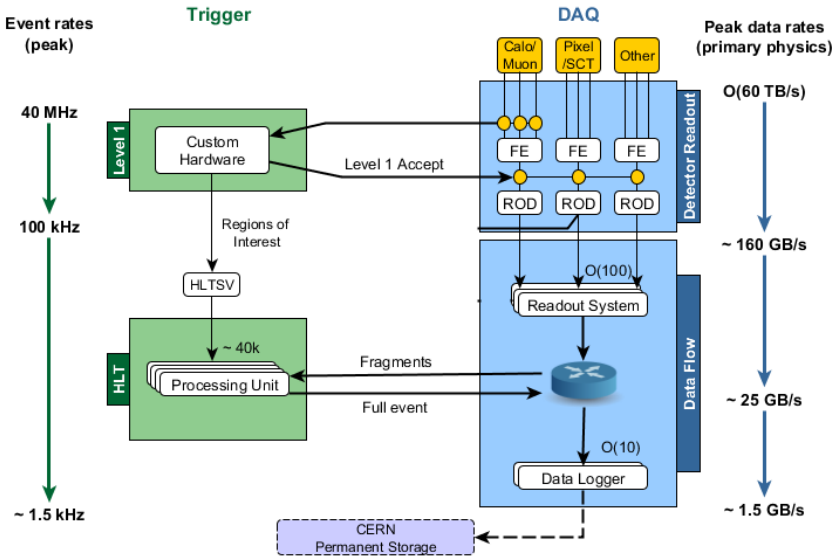

Figure 5.7 Schematic overview of the ATLAS trigger and data acquisition system, adapted from [80].

Level 1 trigger

The hardware-based L1 trigger is designed to reduce the event rate from 40 MHz to 100 kHz. Information from the muon trigger chambers and the calorimeters are used in the L1 trigger. The L1 trigger is divided into three parts: the L1 calorimeter trigger (L1Calo), the L1 muon trigger (L1Muon) and the central trigger processor (CTP).

The *calorimeter trigger* relies on FPGAs. On-detection electronics provide the sum of the analogue signals of hadronic and electromagnetic calorimeter cells in special trigger towers, with typical granularity of approximately $\Delta\eta \times \Delta\phi = 0.1 \times 0.1$. The analogue signals are digitised by a preprocessor (PPr). Once the signals have been digitised, they are converted to E_T using look-up tables, and a series of selections filter the event signatures for e, γ, hadronically-decaying τ, and jets. The object counts that survive each threshold is passed to the CTP.

The RPC and TGC of the muon spectrometer use a simple tracking algorithm to identify muon candidates who fall into six p_T windows from 5 GeV to 35 GeV. The bunch crossing in which the signal originates can be determined from the time of flight due to the time resolution of the trigger chambers. The information from the RPC and TGC are combined in the muon-to CTP-interface (MuCTPI) and forwarded to the CTP.

The *topological trigger* system (L1Topo) [81] operates between L1Calo, L1Muon systems and the CTP. It receives input from the L1Calo and L1Muon systems in the form of trigger objects, combining the information and applying algorithmic cuts it can discriminate event topologies and shapes. The surviving trigger objects are passed to the CTP.

The CTP makes decisions on accepting or rejecting an event by combining the information from the trigger subsystems. It can be programmed with up to 96 trigger menu items that define different event selection rules. Additional requirements on prescale or deadtime can be used to reject events by the CPT further. Prescale requirements refer to trigger menu items that have been prescaled as to dampen the acceptance rate of events which pass the cuts. The time difference between L1 accept signals in which front-end drivers or HLT components of the trigger and DAQ system are saturated is referred to as deadtime. Regions of interest (RoIs) are

identified by the L1 trigger which could contain high p_T leptons, photons or jets and passed to the HLT, to reduce processing time.

High level trigger

The ATLAS HLT [80, 82] performs software-based reconstruction of events which pass the L1 trigger, running on processor farms consisting of 80000 CPU cores. The *inner detector trigger* is responsible for the track reconstruction of measurements made by the inner detector. The reconstructed tracks are matched to measurements by the sub-detectors providing reconstruction of physics objects. This allows the HLT to differentiate between photons and electrons, and to tag jets which contain b quarks.

Due to the flexibility of software implementations and large-scale parallel processing, HLT algorithms can be more complicated than those in L1. HLT algorithms are combined into chains that are applied to the event data sequentially. These algorithms may use the RoIs provided by the L1 trigger, where the processing rate can be increased and reduce the latency. When an event survives an algorithm chain from the HLT, it is accepted and read out into permanent storage. An event rate of 1 kHz is achieved by the HLT.

Trigger configurations

The ATLAS trigger is based on many individual *trigger chains*, referred to as triggers. The trigger system is configured to record collisions of interest, while limiting the processing load, allowing for a reasonable throughput. Each trigger defines selections on one or more reconstructed objects by the L1 trigger, followed by selection in the HLT trigger. Therefore, the HLT and L1 systems must use compatible modes of operations.

5.3 Luminosity

For a detector the total luminosity of collisions recorded, L, is given by,

$$\sigma L = N = \sigma \int \mathcal{L} dt, \tag{5.3}$$

where N is the recoded number of events, σ is the total inelastic cross section, and $\mathcal{L}$ is the instantaneous luminosity. $\mathcal{L}$ is given by [83]

$$L = \frac{n_b f N_1 N_2}{2\pi \Sigma_x \Sigma_y} F, \tag{5.4}$$

where f is the revolution frequency, n_b is the number of colliding bunches with $N_{1(2)}$ protons, $\Sigma_{x(y)}$ the mean beam width in the x(y) direction. The luminosity detectors are calibrated to the inelastic cross section using van-der-Meer (VdM) scans [84, 85].

The total luminosity delivered per data-taking period at $\sqrt{s} = 13\,\text{TeV}$ is shown in Figure 5.8a. The cumulative luminosity delivered by the LHC and recorded by ATLAS is presented in Figure 5.8b. Due to inefficiencies in data acquisition, the recorded luminosity is lower than what is delivered by the LHC.

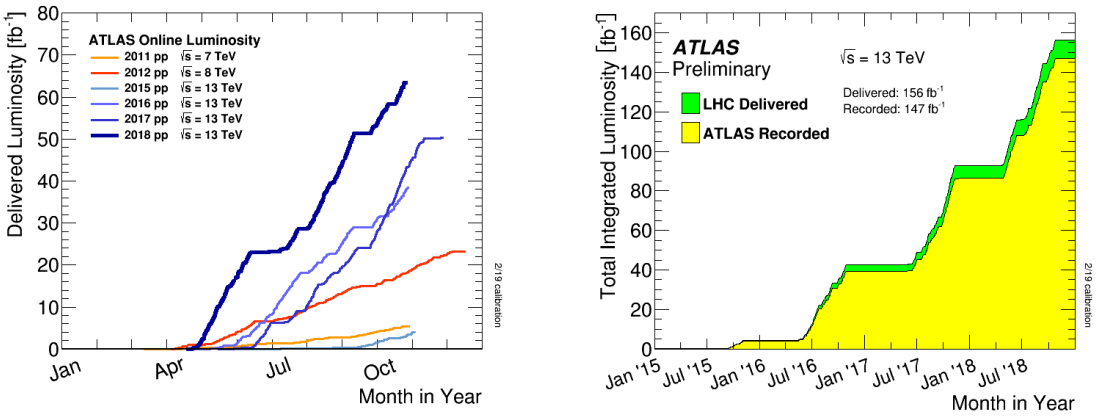

(a) **(b)**

Figure 5.8 (a) Cumulative luminosity versus time delivered to ATLAS (green) and recorded by ATLAS (yellow) during stable beams for pp collisions at 13 TeV centre-of-mass energy in LHC Run-2. (b) Cumulative luminosity versus day delivered to ATLAS during stable beams and for high energy p-p collisions [86].

Chapter 6

Simulation and Reconstruction

In order to perform physics analyses, signals collected by the ATLAS detector are reconstructed into meaningful physics objects. This chapter presents the concept of *Monte-Carlo* simulation. It is introduced as a method to estimate predicted rates of specific SM and BSM processes. Also, a description of the reconstruction and identification of physics objects is provided in this chapter.

6.1 Event simulation

The theoretical understanding of high-energy physics processes are tested by making comparisons of experimental data with theoretical predictions. These comparisons usually utilise simulated collision events that can be analysed. Production of simulated data requires the theoretical modelling of many aspects of pp collisions and their resulting products. The simulation process is separated into collision event generation and detector simulation.

The simulation of collision events is split into two main parts: firstly, the simulation of the matrix element process, and then the resulting parton shower and hadronisation process. A predicted cross-section is calculated by integrating the matrix element over the phase space of the final state. Detailed knowledge of the distribution of partons in each proton is required in the form of *parton distribution functions* (PDFs), to correctly predict the cross-section and

kinematics of a process. The PDFs give the probability for a parton of a given type to be found with some fraction of the proton's initial momentum. The matrix element calculations are performed at fixed-order in perturbation theory. Therefore, the production of quarks and gluons beyond the order of the calculation is required to be handled separately.

High-energy outgoing quarks and gluons emit QCD radiation as the scale of the process evolves. The emission of QCD radiation is in the form of *parton showers*, which are higher-order emissions of additional gluons, or the forming of quarks via the splitting of gluons. The production of such processes are modelled by the *DGLAP equations* [87–89]. The DGLAP equations scale the probabilities for a given type of parton to split into additional partons as a function of energy until the partonic energy scale has reached about 1 GeV. Below this energy threshold, the lone quarks and gluons form colourless objects (mesons and baryons) in a process called *hadronisation*. This process is simulated with non-perturbative models [90, 91]. Finally, decays of short-lived particles ($c\tau < 10\,\text{mm}$), who do not have a long enough lifetime to interact with the ATLAS detector are simulated at this stage.

Several different simulation groups specialise in matrix element simulations and parton shower simulations. A dedicated combination package handles a careful matching of the simulation of the matrix element, and parton shower simulations, which is then used to produce individual datasets of simulated events. Additionally, the pileup interactions between other protons in the beam are also overlaid on the produced hard scatter simulated events to produce a full description of the colliding beams.

The simulation of the interactions of the particles produced in collisions is handled by the GEANT4 simulation software [92–94], which provides a detailed computer model of the ATLAS detector materials, geometry and also includes the wiring in the detector. The output of the detector simulation is treated the same as measurements of real data events made by the detector to preserve the compatibility between the simulated and real reconstructed data.

Full simulation of interactions with the detector can be computationally intensive and results in a significant use of resources for the experiment. The analysis presented in this thesis requires multiple samples of large numbers of events to be produced to be sensitive to new

physics phenomena. The analysis described in this thesis introduces an alternative method that does not rely on the production of large simulated datasets which require full detector simulation, drastically reducing the strain on available resources. Simulation of objects at generator level before detector simulation is referred to as *truth*-level, whereas objects produced after the detector simulation is referred to as *reconstructed (reco)*-level.

6.2 Reconstruction of physics objects

The reconstruction, identification and isolation of the types of physics objects used in the thesis are described in this section.

6.2.1 Tracks and vertex reconstruction

The identification of tracks are essential in the reconstruction of physics objects and in identifying interaction vertices. Track reconstruction aims to describe the trajectory of a particle through the inner detector. Additionally, the muon tracks are also reconstructed in the muon spectrometer described in Section 5.2.3. A series of sequential algorithms are used to reconstruct tracks from the inner detector readout [95].

Measurements from the pixel and SCT layers are reconstructed into *hits*, defined by three-dimensional space points. Hits from either side of the modules are required to form both coordinate in the SCT, and timing information from the TRT is used to construct drift circles. *Track seeds* are formed from three hits in the pixel detector and the first layer of the SCT. These track seeds are extended into the outermost layers of the SCT to give *track candidates*, which are then fit to the hits produced using a Kalman-filter [95, 96]. The Kalman-filter takes into account the scattering of tracks by materials of the detector. Poor quality tracks are rejected by applying a score based on the χ^2 of the fit and the number of missing hits in active detector layers. Ambiguities in space points corresponding to multiple tracks are also removed by selecting the highest-scoring tracks. The remaining tracks are then extended to the TRT to

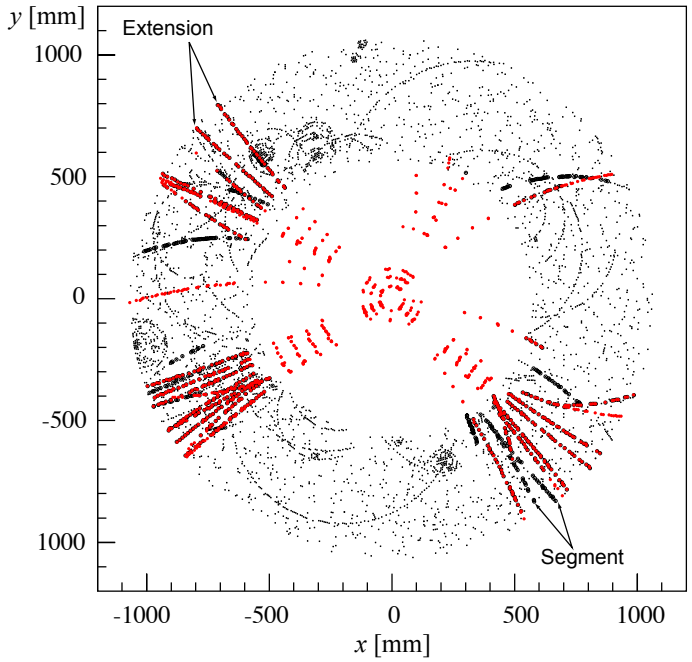

Figure 6.1 Track finding for a simulated $t\bar{t}$ event. Hits are indicated by small black dots in the transverse plane. Red dots show hits in associated with tracks that originate from following the SpacePoint seeded tracks into the TRT Black circles indicate hits that form track segments in the TRT , which builds the start point of the back tracking application [95].

provide many more additional hits. Final reconstructed tracks are then formed by fitting to all the detector components simultaneously.

A subsequent algorithm extending inwards from hits in the TRT is used to find track segments that were missed by the previous method. Tracks segments in the TRT not associated with tracks in the first algorithm are extrapolated inwards to hits in the SCT and pixel detectors. An example of such track segments detected in the inner detector is shown in Figure 6.1. A similar ambiguity-resolving criteria as the first algorithm based on the χ^2 is also applied.

There are multiple pp collisions per bunch crossing at the LHC due to its high instantaneous luminosity. Figure 6.2 shows the distribution of the number of interactions per bunch crossing. The vertex of an interaction indicates the location at which the physical process has occurred. Once all tracks have been fitted, vertex finder algorithms are used to assign the tracks to their corresponding vertex. Reconstructed vertices are required to have at least two tracks associated

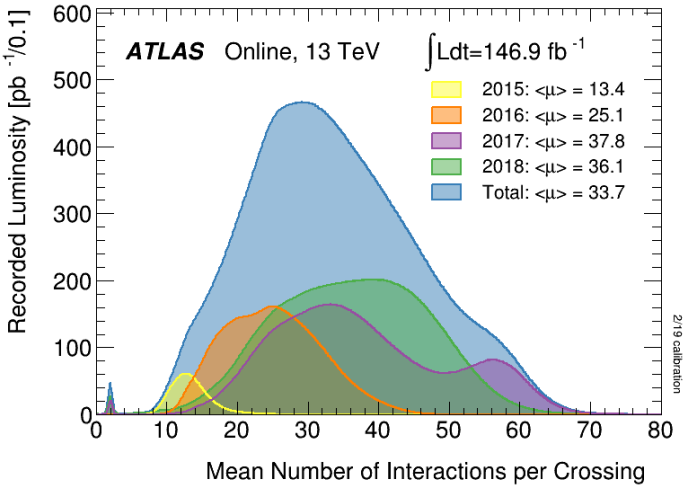

Figure 6.2 Distribution of number of interactions per pp bunch crossing in ATLAS for the 2015+2018 data-taking period [86].

with them. The primary vertex is determined as the pp interaction vertex with the highest sum of the transverse momentum of its associated tracks, indicating it as the vertex at which the hard scattering is most likely to have originated. The other pp interactions are referred to as *pileup*. Vertex reconstruction is essential in removing objects that originate from pileup interactions and for measurements of properties of long-lived particles.

6.2.2 Electrons

Electrons and positrons have the same experimental signature in the EM calorimeter. They are only distinguishable due to the difference in the curvature of their tracks in the ID. In this thesis, positrons will also be referred to as electrons.

Electron reconstruction involves using track information from the ID with calorimeter information from the EM calorimeter and the pattern of electrons transition radiation as they pass through the TRT.

Electron reconstruction

The measurement of an electron signature can be characterised by a localised energy deposit (cluster) in the EM calorimeter and charged tracks in the ID that are matched to the cluster that forms the final electron candidate. Electrons lose energy when traversing the ID due to bremsstrahlung, resulting in radiated photons. These photons can then be converted into electrons which then undergo further bremsstrahlung. Most of the energy of the electrons and photons are deposited within the EM calorimeter as they are collimated. This effect can result in multiple tracks being matched to the same electromagnetic cluster.

A sliding window algorithm [97] is utilised to search for localised clusters in the EM calorimeter. The EM calorimeter is divided into an $\eta \times \phi$ matrix. Initially, windows which correspond to a 3×5 granularity in the second layer of the EM calorimeter (0.025×0.025) are formed. The matrix is searched using the windows for energy deposits with $E_T > 2.5\,\text{GeV}$. The identified clusters are used as seeds to match corresponding reconstructed tracks in the ID. The Gaussian Sum Filter (GSF) method [98] is used to refit the reconstructed tracks, which takes into account the effects bremsstrahlung energy loss characteristic to electrons. If no suitable GSF-track is matched to an EM calorimeter cluster, the cluster is labelled as originating from photons. After matching the track, the cluster is then rebuilt by summing the energies of all the cells within the 3×7 (5×5) window in the barrel (end-cap).

The efficiency of the sliding window algorithm to reconstruct EM-cluster candidates in the EM calorimeter varies as a function of η and E_T. Figure 6.3 shows that the reconstruction efficiency as a function of E_T, ranging from 65% at $E_T = 4.5\,\text{GeV}$ to more than 99% above $E_T = 15\,\text{GeV}$. This efficiency is determined from simulation.

From 2017 a new clustering algorithm has been adopted based on topological clusters (topo-cluster) [100]. The topological clusters allow for the recovery of low energy deposits from bremsstrahlung photons and associate them to the electron cluster, forming a *supercluster*. Figure 6.4 shows a diagram of this procedure. In contrast to the sliding window algorithm, the cell significance, $\zeta_{\text{cell}}^{\text{EM}}$, is responsible for the seeding in a topo-cluster and is defined as

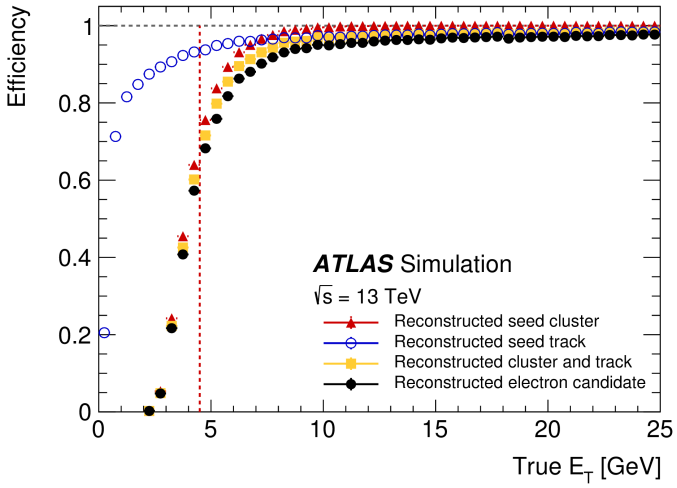

Figure 6.3 The total reconstruction efficiency for simulated electrons in a single-electron sample as a function of truth level transverse energy, E_T, for each step of electron candidate formation [99].

$$\zeta_{\text{cell}}^{\text{EM}} = \left| \frac{E_{\text{cell}}^{\text{EM}}}{\sigma_{\text{cell,noise}}^{\text{EM}}} \right|, \tag{6.1}$$

where $\left|E_{\text{cell}}^{\text{EM}}\right|$ is the absolute cell energy and $\sigma_{\text{cell,noise}}^{\text{EM}}$ is the expected cell noise. The steps of the clustering algorithm are:

1. A *proto-cluster* is formed from calorimeter cells with $\zeta_{\text{cell}}^{\text{EM}} \geq 4$.
2. All immediate neighbouring cells with $\zeta_{\text{cell}}^{\text{EM}} \geq 2$ around the proto-cluster are added.
3. Finally, cells with $\zeta_{\text{cell}}^{\text{EM}} \geq 0$ adjacent to the cells that were previously included are also added to the cluster.

This formalism is known as the "4-2-0" topo-cluster reconstruction. A supercluster is built from a topo-cluster seed after satellite candidates, possibly emerging from bremsstrahlung radiation around a seed candidate, have been resolved. A cluster is accepted as a satellite if it falls within a window of $\Delta\eta \times \Delta\phi = 0.075 \times 0.125$ around the seed cluster barycentre. Once a satellite cluster has been identified it is vetoed from future usage.

Figure 6.5 shows the efficiency for the different components of the supercluster-based reconstruction. The same track fitting method used in the sliding window algorithm is used to refit the reconstructed tracks.

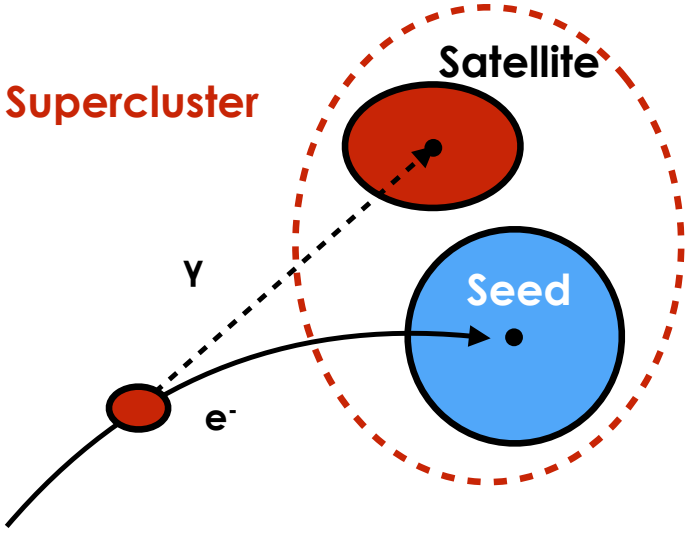

Figure 6.4 Diagram of an example supercluster showing a seed electron cluster and a satellite photon cluster [101].

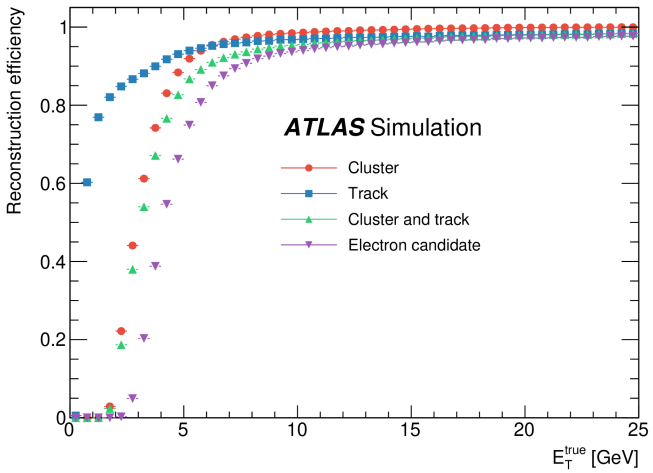

Figure 6.5 Supercluster-based cluster, track, cluster and track, and electron reconstruction efficiencies as a function of the generated electron E_T [100].

The supercluster-based algorithm provides an improved energy resolution compared to the sliding window algorithm by collecting more energy deposits. The peak energy response E_{calib}/E_{true} does not deviate by more than 0.5% for the different particles, where E_{true} is the energy of the particles before detector simulation and E_{calib} is the calibrated reconstructed energy. The *effective interquartile range* (IQE) compares the width (resolution) of the energy response and is used to quantify the performance of the supercluster algorithm compared to the sliding window algorithm. The IQE is given by

$$IQE = \frac{Q_3 - Q_1}{1.349}, \tag{6.2}$$

where Q_1 and Q_3 are the first and third quartiles of the E_{calib}/E_{true} distribution. The normalisation factor of 1.349 is chosen such that the IQE of a Gaussian distribution equals its standard deviation. Figure 6.6 shows the IQE as a function of energy is shown for the two approaches. An improvement in the IQE can be seen for the supercluster-based algorithm, where the difference is larger at lower energies.

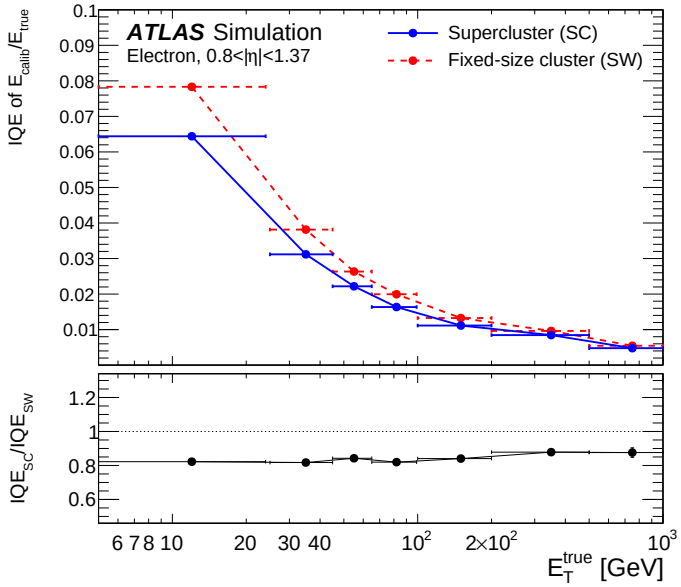

Figure 6.6 Calibrated energy response resolution, expressed in terms of IQE, for simulated electrons. The response for fixed-size clusters based on the sliding window method is shown in dashed red, while the supercluster-based one is shown in full blue. The bottom panel shows the ratio between the supercluster-based algorithm and the sliding window algorithm [100].

Electron identification

Physics processes can *fake* the prompt electron signature that can pass the reconstruction algorithms. Prompt electrons are defined as electrons which originate from the hard scattering vertex and are not the result of hadronic decays. Fake prompt electrons can arise from sources such as, hadronic showers which mimic an electron shower, and electrons from photon conversions. Non-prompt electrons can originate from the semileptonic decays of heavy-flavour hadrons.

Further criteria referred to as *identification* is defined to select a sample of pure prompt electrons. A likelihood-based identification method is employed in the identification of prompt electrons. The method combines signal and background probability density functions of discriminating variables from quantities measured from the detector. These quantities include transition radiation in the TRT and shower shape in the EM calorimeter. An overall probability for an object to be constructed as an electron is calculated using the variables described above. The discriminating variable $d_{\mathcal{L}}$ is defined as

$$d_{\mathcal{L}} = \frac{\mathcal{L}_S}{\mathcal{L}_S + \mathcal{L}_B}, \tag{6.3}$$

with

$$\mathcal{L}_{S(B)}(\overrightarrow{x}) = \prod_{i=1}^{n} P_i^{S(B)}(x_i), \tag{6.4}$$

where $\overrightarrow{x}$ is the vector of the n discriminating variables, $P_i^{S(B)}$ is the evaluation of the signal probability density function for the i^{th} discriminating variable at the value x_i under the signal (background) hypothesis.

Three identification working points are defined for electron identification: *loose*, *medium* and *tight*. Due to the non-exclusive nature of the working points, reconstructed electrons identified as tight also belong to the medium identification category, and electrons identified as medium belong to the loose identification category. The efficiencies of the identification

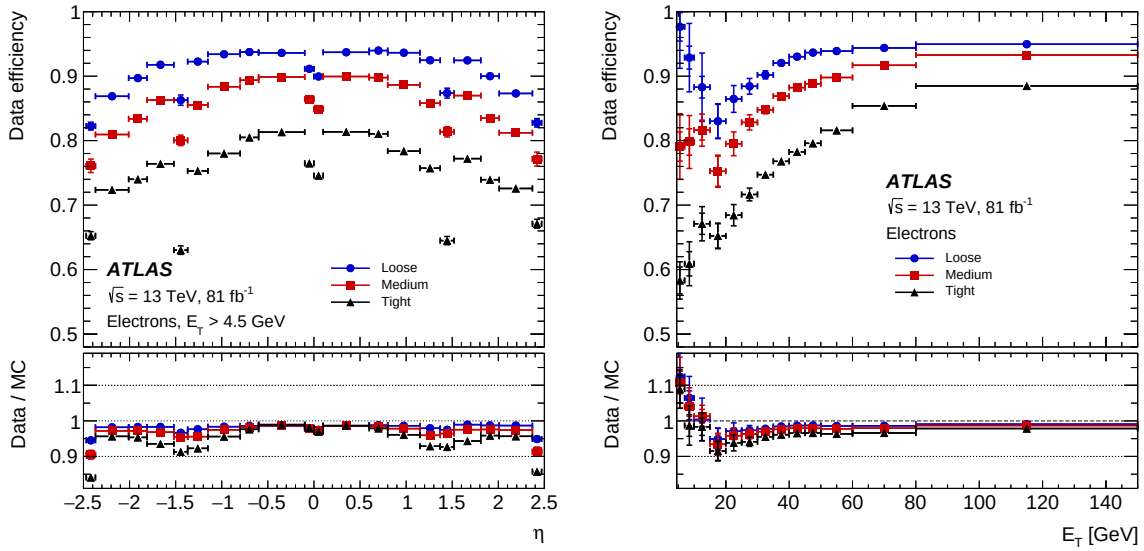

(a) **(b)**

Figure 6.7 Electron identification in data as a function of (a) E_T and (b) η for the loose, medium and tight identification working points. The inner uncertainties are the statistical. The total uncertainties are statistical and systematic uncertainties in the data-to-simulation efficiency ratio added in quadrature [100].

working points are measured in data and simulation using $Z \to ee$ and $J/\psi \to ee$ decays in bins of $|\eta|$ and E_T [100]. Figure 6.7 shows the efficiencies of the identification working points. These working points offer prompt electron identification efficiencies of 97%, 95% and 91%, with background rejection efficiencies of 99.7%, 99.8% and 99.9%, respectively. Even though the medium and tight efficiencies are lower compared to the loose criteria, the reduction in efficiency is accompanied by an increase in rejection of background processes by a factor of 2.0 and 3.5, respectively. The discontinuity in the efficiencies at $E_T = 15\,\text{GeV}$ is caused by a known mismodelling of the variables used in the likelihood discriminant at low E_T.

Electron isolation

To further improve the purity of the prompt electron sample, and reject the background from hadronic decays, isolation requirements are applied based on the transverse energy around the electron candidate. Two types of isolation criteria are used: calorimeter and track-based isolation [100].

For the raw calorimeter isolation ($E_{T,\text{raw}}^{\text{isol}}$), the sum of the transverse energy of positive energy topo-clusters whose barycenter falls within a cone around the electron cluster is used. The raw EM particle energy ($E_{T,\text{core}}$) is also contained within the cone and is required to be subtracted. This subtraction is done by removing the energy of EM calorimeter cells contained in a $\eta \times \phi = 5 \times 7$ around the EM particle cluster. Leakage corrections as a function of η and ϕ are applied since the subtraction does not subtract all of the EM particle energy. A correction for the pileup and underlying-event contributions to the isolation cone is also estimated [102]. Many factors are taken into account when calculating the pileup correction. These include: in-time and out-of-time pileup, described in Section 6.2.1, and collisions between the proton bunch and residual gas inside the beam-pipe. Additionally, detector conditions will need to be taken into account, where the calculation will be effected by noise from different components.

The corrected calorimeter isolation variable is computed as

$$E_T^{\text{coneXX}} = E_{T,raw}^{\text{isolXX}} - E_{T,\text{core}} - E_{T,\text{leakage}}(E_T, \eta, \Delta R) - E_{T,\text{pile-up}}(\eta, \Delta R), \tag{6.5}$$

where XX refers to the size of the cone, $\Delta R = XX/100$. A cone size $\Delta R = 0.2$ is used for electron working points.

The track isolation (p_T^{coneXX}) is computed by summing the transverse momentum of selected tracks within a cone centered around the reconstructed electron track, excluding tracks matched to electron or converted photons. Track isolation for electrons is defined with a variable cone size ($p_T^{\text{varconeXX}}$), which accounts for electrons produced in high-momentum particle decays where the decay products can be very close to the electron track. Therefore, the cone size gets smaller for larger transverse momentum, given by the equation:

$$\Delta R = \min\left(\frac{10}{p_T[\text{GeV}]}, \Delta R_{\text{max}}\right), \tag{6.6}$$

where ΔR_{max} is maximum cone size, typically $\Delta R_{max} = 0.2$.

The definitions of the different electron isolation working points are shown in Table 6.1. The working points result from a need for compromise between the efficiency of identification

Working point	Calorimeter isolation	Track isolation
Gradient	$\epsilon = 0.1143 \times p_{\mathrm{T}} + 92.14\%$ (with $E_{\mathrm{T}}^{\mathrm{cone20}}$)	$\epsilon = 0.1143 \times p_{\mathrm{T}} + 92.14\%$ (with $p_{\mathrm{T}}^{\mathrm{varcone20}}$)
HighPtCaloOnly	$E_{\mathrm{T}}^{\mathrm{cone20}} < \max(0.015 \times p_{\mathrm{T}}, 3.5\ \mathrm{GeV})$	-
Loose	$E_{\mathrm{T}}^{\mathrm{cone20}}/p_{\mathrm{T}} < 0.20$	$p_{\mathrm{T}}^{\mathrm{varcone20}}/p_{\mathrm{T}} < 0.15$
Tight	$E_{\mathrm{T}}^{\mathrm{cone20}}/p_{\mathrm{T}} < 0.06$	$p_{\mathrm{T}}^{\mathrm{varcone20}}/p_{\mathrm{T}} < 0.06$

Table 6.1 Definition of the electron isolation working points and isolation efficiency ϵ. In the Gradient working point definition, the unit of p_{T} is GeV. All working points use a cone size of $\Delta R = 0.2$ for calorimeter isolation and $\Delta R_{\mathrm{max}} = 0.2$ for track isolation [100].

of prompt electrons and a good rejection of electrons from hadronic processes. The gradient working point is defined by a fixed value of efficiency designed to give an efficiency of 90% at $p_{\mathrm{T}} = 25\,\mathrm{GeV}$, uniform in η. The three other working points have a fixed requirement on calorimeter and track isolation variables. The efficiencies for the electron isolation working points are shown on Figure 6.8. The results are obtained using a sample enriched in $Z \to ee$ events. A jump in the efficiency for the gradient working point is observed at 15 GeV due to the cut maps being optimised with $J/\Psi \to ee$ events below 15 GeV, while the measurement is performed on $Z \to ee$ events in the full range. The tight working point gives the highest background rejection below 60 GeV. The HighPtCaloOnly working point gives the highest rejection in the high-E_{T} region ($E_{\mathrm{T}} > 100\,\mathrm{GeV}$). For electrons with E_{T} higher than 500 GeV no measurement can be performed because of the limited number of data events. Therefore, the results from the E_{T} bin [300,500] GeV are used with an additional systematic uncertainty varying between 0.1% and 1.7% depending on the isolation working point.

6.2.3 Muons

Muon reconstruction is performed individually in the ID (described in Sections 5.2.1 and 6.2.1) and muon spectrometer (described in Section 5.2.3). The information from these sub-detectors is then combined to form the muon tracks that are used in the thesis. Similar reconstruction criteria to electrons is also applied to the muon identification and isolation [103].

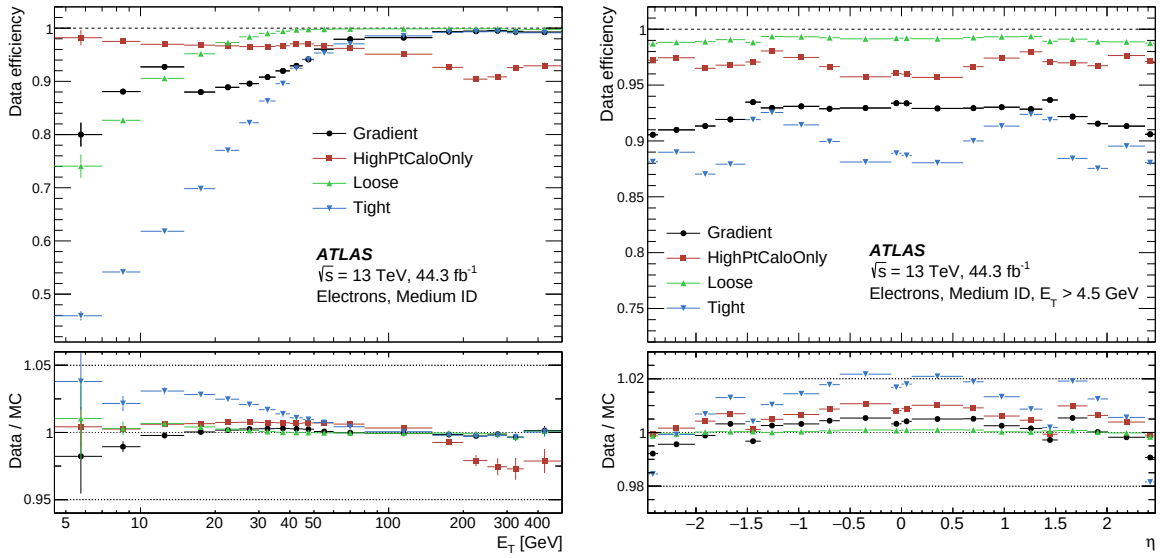

(a) **(b)**

Figure 6.8 Efficiency of the different isolation working points for electrons from inclusive $Z \to e^+e^-$ events as a function of the electron (a) E_{T} and (b) η. The electrons are required to fulfil the Medium selection from the likelihood-based electron identification. The lower panel shows the ratio of the efficiencies measured in data and in MC simulations. The total uncertainties are shown, including the statistical and systematic components [100].

An important quantity in the reconstruction of muons in the ATLAS detector is its transverse momentum, defined as:

$$p_{\mathrm{T}} = p \sin\theta = \frac{\sin\theta}{|q/p|}, \tag{6.7}$$

where q/p is the ratio of the muon charge to its momentum and is measured from the track curvature. The muon track sagita, described in Section 5.2.3 is used when the muon tracks segments originate from all stations of the muon spectrometer. For muons with track segments in only two stations, the curvature is determined from the angular difference between the two segments.

Muon reconstruction

Reconstruction of tracks in the muon spectrometer starts with the formation of segments found using search patterns inside each of muon spectrometer stations. In the MDT layers and the trigger chamber, a Hough transform [104] is used to search for hits and a straight line fit is performed on the hits found in each layer. The RPC and TGC hits measure the coordinate orthogonal to the bending plane. Track segments in the CSC layers are built using a separate combinatorial search in the η and ϕ planes [103].

The muon track candidates are then formed by fitting together the hits from segments in the different layers. Segments from the middle layers of the detector, where more hits are available, are used as seeds when the algorithm performs a combinatorial search. The search is then extended to use segments in the inner and outer layers as seeds. Several tracks can be built initially from the same segment. However, an overlap removal is later applied to select the best assignment to a single track, or it allows the segment to be shared between two tracks. A global χ^2 fit is performed on the hits associated with each track. The track candidate is accepted if the χ^2 satisfies the selection criteria. Hits providing a fit with a large χ^2 are removed, and the track fit is repeated. Additional hits found to be consistent with the track candidate trajectory are added and then refit.

Several algorithms are used to combine the muon track candidates in ID and muon spectrometer, where each algorithm uses different sets of information related to the detector components. Four main algorithms are used depending on the sub-detector used in the reconstruction:

- **Combined (CB) Muon:** A global fit using the track candidates found in the ID and muon spectrometer is performed to form a CB muon. To improve the fit quality hits can either be added or removed from the track during the global fit. Most muons are first reconstructed in the muon spectrometer and then extrapolated inwards to the ID hits. Additionally, a complementary approach is utilised where the ID tracks are extrapolated outwards and matched to muon spectrometer hits. This approach accounts for a small fraction of the muons reconstructed. CB muons are the primary type used within ATLAS as they have the highest purity among the different classes of muons.

- **Segment-tagged (ST) Muons:** An ID track is classified as a muon if, when extrapolated to the muon spectrometer, it is matched with at least one track segment in the MDT or CSC chambers. It has the lowest purity amount all classes of muons.

- **Calorimeter-tagged (CT) Muons:** Tracks in the ID are matched to energy deposits in the calorimeter compatible with a minimum ionising particle.

- **Extrapolated (ME) Muons:** The muon trajectory is reconstructed from information based only on the muon spectrometer track and can be extrapolated to the interaction point, taking into account energy loss of the muons traversing through the calorimeters.

An overlap removal procedure between the different types of muons is used, where if two types of muons share the same track, preference is given to CB, followed by ST, and then to CT muons. The overlap removal procedure for ME muons are performed by analysing the track hit content and selecting tracks with better fit quality.

Muon identification

Muons which originate from decays of hadrons will have a characteristic deflection in their reconstructed tracks. This deflection will result in poor track quality and may not be compatible

with the measured momentum in the ID and muon spectrometer. Several variables are selected to identify prompt muons. For CB tracks, the variables used in identification are:

- **q/p significance:** The absolute difference between the charge and momentum ratio of the muons measured in the ID and MS divided by sum in quadrature of the uncertainties.
- $\boldsymbol{p'}$**:** The absolute difference between the p_{T} measurements in the ID and muon spectrometer divided by the p_{T} of the combined track.
- χ^2 of the fit.

In addition, requirements on the number of hits in the ID and muon spectrometer are also used.

Four muon identification criteria are used to address the requirements of different physics analyses. The identification working points provided are:

- **Medium:** These are the default selection for ATLAS analysis. The selection minimises the systematic uncertainties associated with the reconstruction. CB muon tracks are required to have ≥ 3 hits in at least two MDT layers (excluding $|\eta| < 0,1$). ME tracks are required to have at least three MDT/CSC layers in the range $2.5 \geq |\eta| \geq 2.7$. q/p significance is required to be less than seven.
- **Loose:** CB and ME muons satisfying the medium selection are included in the loose selection. Furthermore, CT and ST muons are restricted to the $|\eta| < 0.1$ region.
- **Tight:** CB muons with hits in two stations and satisfying the medium selection are considered. Additionally, the normalised χ^2 is required to be less than eight. Finally, a two dimensional cut on q/p significance and p' is also applied.
- **High-**$\boldsymbol{p_{\mathrm{T}}}$**:** The High-$p_{\mathrm{T}}$ muon selection is used in the selection of muons in the analysis presented in this thesis. High-p_{T} muons are chosen to maximise the momentum resolution for tracks with p_{T} above 100 GeV and is optimised for analyses that extend far into high p_{T} regions. CB muons which have at least three hits in at least three muon stations are selected. A veto is applied on muons with hits in specific regions of the muon spectrometer

	$4\,\text{GeV} \leq p_\text{T} \leq 20\,\text{GeV}$		$20\,\text{GeV} \leq p_\text{T} \leq 100\,\text{GeV}$	
Selection	ϵ_μ^{MC} [%]	$\epsilon_{Hadrons}^{MC}$ [%]	ϵ_μ^{MC} [%]	$\epsilon_{Hadrons}^{MC}$[%]
Loose	96.7	0.53	98.1	0.76
Medium	95.5	0.38	96.1	0.17
Tight	89.9	0.19	91.8	0.11
High-p_T	78.1	0.26	80.4	0.13

Table 6.2 Efficiency for prompt muons from W decays and hadrons decays misidentified as prompt muons computed using a $t\bar{t}$ MC sample. The results are shown for the four identification selection criteria separating low and high momentum for muon candidates [103].

with suboptimal alignment. This procedure reduces the reconstruction efficiency by 20%, but improves the muon p_T resolution by 30%.

Table 6.2 shows the signal and background efficiencies of the different working points for muons in the range of $20\,\text{GeV} < p_\text{T} < 100\,\text{GeV}$ obtained from $t\bar{t}$ simulation. An isolation requirement is not applied in the samples shown. When an isolation requirement is applied the misidentification rate is expected to be reduced by approximately an order of magnitude.

Muon isolation

Similar to electrons, isolation criteria are also applied on muon candidates to improve background rejection. Three isolation variables are defined to asses the muon isolation: two track-based and a calorimeter-based isolation variable:

- Variable track-based $p_T^{varcone30}$: Defined as the sum of transverse momentum of tracks in a cone of $\Delta R = min(10\,\text{GeV}/p_T^\mu, 0.3)$ with $p_\text{T} > 1\,\text{GeV}$, around the candidate muon track.

- Fixed track-based p_T^{cone20}: Defined as the sum of the transverse momentum of all tracks within a cone of $\Delta R = 0.2$ around the candidate muon track.

- Calorimeter based E_{T}^{cone20}: Defined as the sum of the transverse momentum of all topological clusters within a cone of $\Delta R = 0.2$ from the candidate muon.

Several isolation working points are available depending on the needs of the analysis. In many isolation working point a ratio of the isolation variable and the muon p_{T} is used to improve the efficiency over the full p_{T} spectrum. For the analysis discussed in this thesis, the *FCTightTrackOnly* isolation is used, which requires $p_{\mathrm{T}}^{varcone30}/p_{\mathrm{T}} < 0.6$.

6.2.4 Jets

Jet reconstruction

Jets are collimated showers of particles produced from the hadronisation of gluons emerging from proton-proton collisions, resulting in energy deposits in the calorimeters. Their energy is deposited in the hadronic calorimeters distinguishing them from electrons or photons. There are various algorithms available for jet reconstruction [105]. The ATLAS experiment focuses on the *anti-k_T* algorithm [106], where topo-clusters are built from calorimeter cells as input. The *anti-k_T* algorithm calculates distances between every pair of inputs i and j as:

$$d_{ij} = \min\left(k_{ti}^{2p}, k_{tj}^{2p}\right) \frac{\Delta_{ij}^2}{R^2}, \tag{6.8}$$

with the distance to the beam axis,

$$d_{iB} = k_{ti}^{-2}. \tag{6.9}$$

where $\Delta_{ij} = (y_i - y_j)^2 - (\phi_i - \phi_j)^2$, k_{ti}, y_i and ϕ_i are the transverse momentum, rapidity and azimuthal angle of particle i, respectively. The jet radius parameter R can vary depending on the analysis using the algorithm and is typically set to $\Delta R = 0.4$.

For each set of inputs, the algorithm compares the distances d_{ij} and d_{iB}. If $d_{ij} < d_{iB}$ then the four-momenta of the input j is combined with input i. If, $d_{ij} > d_{iB}$, then i is declared a

final jet and removed from the list of entities. The algorithm terminates when the list of entries is empty and all of the inputs have been classified.

6.2.5 Missing transverse momentum

Weakly interacting particles (e.g. neutrinos) can traverse through the ATLAS detector without interacting with any of the detector material. Therefore, they cannot be reconstructed. This leaves a characteristic missing transverse momentum signature in the detector defined as:

$$E_{\mathrm{T}}^{miss} = -\left[\sum_{i}^{\text{all objects}} p_{\mathrm{T}}^{i} + E_{\mathrm{T}}^{cl} \right], \tag{6.10}$$

where the summation includes the transverses momentum p_{T}^{i} of all leptons, jets and photons. E_{T}^{cl} accounts for all energy clusters in the calorimeters that are not associated with a reconstructed object [107].

Part III

Search for non-resonant signals in dilepton final states

Analysis overview

Historically, signatures with dilepton final states have been central in shaping the SM, from discoveries of new particles such as the Z and J/ψ [108–112], through many precision measurements [113–116], and in searches for new BSM physics [2, 3, 47, 117]. Traditionally, the dilepton channel has been used due to its clean and fully reconstructible experimental signature with excellent detector efficiency. The following chapters outline a novel search for new non-resonant phenomena in final states with two electrons (e^+e^-) or two muons ($\mu^+\mu^-$) at 139 fb^{-1} of data collected in pp collisions at the LHC in $\sqrt{s} = 13\,\text{TeV}$. This analysis complements the search for heavy resonances [3] by using the same dataset and selection criteria. The non-resonant signatures have a broad deviation in the tails of the smoothly falling invariant-mass spectrum (defined in Section 5.2), where the main background is the irreducible Z/γ^* (Drell-Yan, DY) process. The results are provided in a model-independent format, and is also interpreted in the context of the frequently tested benchmark Contact Interaction (CI) models. A detailed overview of the theoretical motivation for contact interaction searches was given in Chapter 2. The e^+e^- and $\mu^+\mu^-$ invariant-mass spectrum is chosen as the main observable in the analysis as it offers the best discriminating power against signal and background for non-resonant signals like CIs.

Several changes have been introduced in this analysis with respect to previous ATLAS results [2]. This is the first non-resonant dilepton search at the LHC to use a background estimate from a data-driven fit method instead of relying on simulation. The background at high invariant mass is estimated from a fit to a low-mass control region (CR), utilising an extrapolation procedure. The impact of MC mismodelling is significantly reduced when estimating the background using the data. Additionally, the search is performed in a high mass

single-bin signal region (SR), where both the regions and the function choice are optimised to maximise the sensitivity of observing a CI process. There are four SRs used in the analysis, two SRs for the electron selection and two SRs for the muon selection. The SRs are optimised to be sensitive to the constructive and destructive interference CI models, resulting in two SRs for each channel: constructive and destructive SRs. Using the single bin approach the results are presented as a model-independent number of signal events in the SRs and also interpreted as the CI energy scale parameter Λ. The benefit of a model-independent search is to facilitate the reinterpretation of the results by theorists, which allows for a wider use of the results produced by the analysis.

The following chapters will describe the analysis strategy and results from the Run-2 ATLAS search for non-resonant phenomena using $139\,\text{fb}^{-1}$ of data at a $\sqrt{s} = 13\,\text{TeV}$. Figure 6.9 outlines the analysis model of the search. The terms in the diagrams will be explained in the following chapters. The object and event selection is described in Chapter 7. The selection is validated in terms of data/MC comparisons, where the MC samples used are outlined in Chapter 8. The "transfer function" described in Section 8.4 is a parametrisation of the detector mass resolution introduced in the analysis to produce smooth MC templates, which are used to validate the functional fit. The background estimation procedure is described in Chapter 10. An important part of the background fit model choice is understanding and estimating the uncertainties associated with it. The uncertainties are described in Chapter 11. Once a function has been chosen, the optimisation procedure to pick a CR and SR are described in Section 10.4. The statistical analysis used is described in Chapter 4. Finally, the results are presented in Chapter 12.

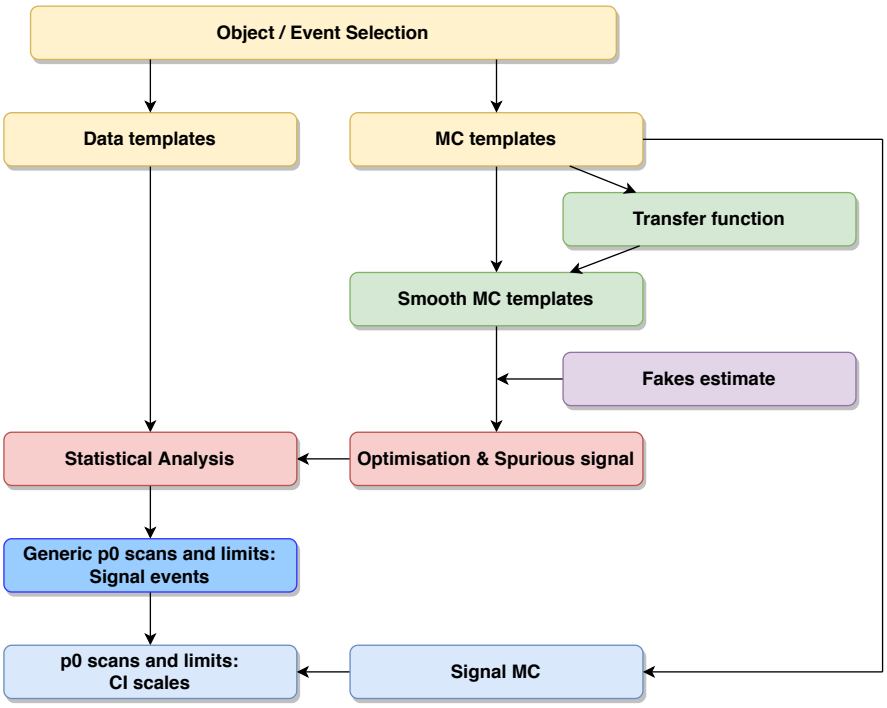

Figure 6.9 Analysis model of the full Run-2 dilepton non-resonant search.

Chapter 7

Object and event selection

The dataset is filtered to select collision events which match the desired signature of dielectron or dimuon final states. The cuts are chosen to ensure a good purity of signal electrons or muons in the selected samples, whilst reducing contamination from background processes. A series of object and event selections are made after the reconstruction of the electron and muon events. The selection for the analysis is performed using the SUSYTools package [118] within the Athena framework [119].

7.1 Event selection

Events undergo a selection based on the data quality and trigger requirements (described in Section 5.2.4), requiring events to satisfy a set of baseline "data quality" (DQ) requirements. Events are required to be measured during a period where all detector subsystems were operating at nominal run conditions. Vetoes are applied to reject corrupted events based on data quality flags from certain detector subsystems. These requirements are only applied to data. The selected events are then required to have a primary vertex with at least two associated tracks following the definition from Section 6.2.1. Events in the electron channel are recorded using dielectron triggers, which require the dielectron system to pass the E_{T} threshold between 12 and 24 GeV for both electrons, depending on the data-taking year. To reduce the trigger rate, additional identification criteria are applied at the trigger level. Single muon triggers are used

for the muon channel, which have a p_{T} thresholds of 26 and 50 GeV. The trigger with the 26 GeV also requires the muon candidate to be isolated [120].

7.2 Object Selection

All electrons and muons considered are reconstructed by the algorithms described in Section 6.2.

7.2.1 Electrons

The electrons candidates are required to be in the central region of the detector of $|\eta| < 2.47$, to ensure that majority of the electrons from the electromagnetic shower are considered. Events found in the the transition region, $1.37 < |\eta| < 1.52$, between the barrel and the endcap electromagnetic calorimeters are rejected. This requirement vetoes any electrons with poor energy resolution due to the lower cell granularity and significant additional inactive material in the transition region. Additionally, the electron candidates are required to have $E_{\mathrm{T}} > 30$ GeV. All electrons are required to pass the medium likelihood identification criteria as described in Section 6.2.2, which gives a good balance of reduction of other background processes (e.g. QCD, W+Jets) that fake electrons and high signal efficiency. To further reduce the fake background processes, the electrons are required to pass the gradient isolation criteria as described in Section 6.2.2. However, there is a small fraction of fake electrons which pass the selection criteria. Therefore, to model the contribution of fake electrons that arise, a data-driven method is used, which is described in Chapter 8. The matrix method requires a data set consisting of an enhanced contribution of fake electrons formed using the loose likelihood identification criteria. To ensure the electron candidates originate from the primary vertex the electron candidate track is required to have a d_0 significance below five, and $|z_0 \sin\theta| < 0.5$ mm for the transverse impact parameter. Section 6.2.1 provides a detailed description of the reconstruction of tracks.

7.2.2 Muons

The muon selection requires muons with $p_{\mathrm{T}} > 30\,\mathrm{GeV}$ and $|\eta| < 2.5$. Muon candidates are required to pass the high-p_{T} identification criteria, which is designed for analyses in the high p_{T} regime, ensuring a good momentum resolution at high p_{T} (Section 6.2.3). A requirement to reject "bad muons" is placed on the relative uncertainty of the q/p measurement with a p_{T} dependent cut to ensure better reconstruction properties. A detailed description of the bad muon veto is given below. Similarly to electrons, a requirement on the transverse impact parameter of $d_0 < 3\sigma$ and a requirement on the longitudinal impact parameter of $|z_0 \sin\theta < 4\,\mathrm{mm}|$ is required. The *FCTightTrackOnly* isolation criteria is used for the muon isolation as described in Section 6.2.3.

Bad muon veto

The bad muon veto is optimised to reject muons in the tails of the $\sigma_{p_{\mathrm{T}}}/p_{\mathrm{T}}$ distributions, that consists of muons with poor reconstruction residing in the tails of the p_{T} distributions. The efficiency of the veto diminishes with increasing p_{T} due to the cut on the relative q/p measurement. The expected muon momentum resolution is parameterised as a function of p_{T} defined as [103]

$$\frac{\sigma_{p_{\mathrm{T}}}}{p_{\mathrm{T}}} = \frac{r_0}{p_{\mathrm{T}}} \oplus r_1 \oplus r_2 \cdot p_{\mathrm{T}}, \tag{7.1}$$

where the first term models the fluctuations of energy loss in the traversed materials. The second terms accounts for multiple scatterings, local magnetic field fluctuations and local radial displacements. Finally, the last term describes the intrinsic resolution effects caused by the spatial resolution of the hit measurements.

The expected resolution is then parameterised as a function of p_{T} coinciding with specific regions of the ATLAS detector. The bad muon veto applies a cut on the relative error on the

Reject	Against	Criteria
electron	muon	shared track, $p_{T,e} < p_{T,\mu}$
muon	electron	calorimeter-tagged muon and shared ID track
electron	muon	shared ID track

Table 7.1 Overlap removal criteria for the analysis selection.

q/p measurement of the muon as:

$$\frac{\sigma_{q/p}}{q/p} < C(p_{\mathrm{T}}) \cdot \sigma, \tag{7.2}$$

where σ is the expected muon resolution as described above as a function of p_{T} and η, C(p_{T}) is a p_{T}-dependent coefficient equal to 1.8 if $p_{\mathrm{T}} < 1\,\mathrm{TeV}$ and linearly decreases if $p_{\mathrm{T}} > 1\,\mathrm{TeV}$. The C($p_{\mathrm{T}}$) cut was optimised to improve the efficiency by 5% with respect to the previous definition [2], where a fixed value of $C(p_{\mathrm{T}}) = 2.5$ was chosen [3].

7.2.3 Overlap removal

The same detector signal can be shared by multiple reconstruction algorithms. Therefore, a detector signal used to construct one object can be used to construct another. To remove these ambiguities, the algorithm considers spatially overlapping pairs of objects and elements are removed from the event depending on a defined set of criteria. Table 7.1 outlines the overlap removal criteria for the analysis selection.

7.3 Dilepton selection

All events passing the dilepton selection for the electron and muon channels are required to contain at least two same-flavour leptons (electrons or muons). The leading and subleading leptons are then selected depending on their E_{T} (p_{T}) in the electron (muon) channel. The muon channel imposes an opposite charge requirement. This requirement results in a better p_{T}

reconstruction in muons since muons with misidentified charges will have strongly distorted p_{T} measurements. However, for the electron channel, no opposite charge requirement is applied, due to the significant loss of efficiency in the high E_{T} regime, and no significant reduction of background processes is expected. Finally, a dilepton invariant mass of $m_{ll} > 130\,\mathrm{GeV}$ is required (described in Chapter 10), where additional restrictions on the invariant mass are placed in the statistical analysis and background estimation. For cases where events are selected for both the electron and muon channels, the electron channel is preferred over the muon channel due to the better invariant mass resolution in that channel. The rejected overlapping dimuon events only account for a small fraction of the observed events. This cut allows for two independent data sets to be formed, allowing for the statistical combination of the two channels. Table 7.2 provides an overview of the full analysis selection.

	Electron channel	**Muon channel**
	Event level	
Trigger	Lowest unprescaled dielectron trigger	Lowest unprescaled single muon trigger
Event Cleaning	Applied	Applied
	Lepton level	
$\|\eta\|$ range	$\|\eta\| < 1.37$, $1.52 < \|\eta\| < 2.47$	$\|\eta\| < 2.5$
p_T or E_T	$> 30\,\text{GeV}$	$> 30\,\text{GeV}$
$\|d_0^{BL}(\sigma)\|$	< 5	< 3
$\|\Delta z_0^{BL} \sin\theta\|$	$< 0.5\,\text{mm}$	$< 0.5\,\text{mm}$
Identification WP	MediumLLH, LooseAndBLayerLLH (Fakes)	High-p_T
Isolation	Gradient	FCTightTrackOnly
	Dilepton level	
Lepton number	≥ 2	≥ 2
Object	Highest E_T pair	Highest p_T pair
Opposite Sign	Not required	Required
Invariant-mass	$\geq 130\,\text{GeV}$	$\geq 130\,\text{GeV}$

Table 7.2 Selection definitions for the analysis selection in the electron and muon channels, including event level, object level and dilepton selection. The parameters p_T and E_T are the transverse momentum and energy and d_0 and z_0 are the transverse and longitudinal displacements of the track associated with the electron vertex.

Chapter 8

Data, background and signal samples

This section outlines the datasets and the background samples considered in this thesis. Section 8.1 outlines the datasets used and their corresponding luminosity. The background processes considered in the analysis for the electron and muon channels are the Drell-Yan, top-quark, diboson, multijet and W+jet processes. Simulated samples are produced for these samples, which are used to validate the data-driven approach described in Chapter 10. The description of the simulated samples used and their corresponding generators are outlined in Section 8.2. A transfer function approach, outlined in Section 8.4, is used to produce smooth and large-statistic samples of the DY and top-quark backgrounds. A data-driven method is used to estimation of the multijet and QCD, and it is described in Section 8.3. The CI samples are produced using a reweighting procedure and is described in Section 8.2.2. Finally, data and MC comparisons are provided in Section 8.5.

8.1 Data

The analysis presented in this thesis is performed on pp collision data collected by ATLAS and delivered by the LHC Run-2, between 2015 and 2018, corresponding to a total integrated luminosity of $139\,\text{fb}^{-1}$. The breakdown of the luminosity collected in each year by ATLAS available for physics analysis is outlined in Table 8.1. The luminosity uncertainty is determined

from the calibration of the luminosity scale using the Van Der Meer scans described in Section 5.3.

Year	luminosity fb^{-1}
2015	3.2
2016	33.0
2017	44.3
2018	59.9
Total	139 ± 1.7%

Table 8.1 Summary of the luminosities of datasets taken between 2015 and 2018 [86].

Figures 8.1 to 8.4 show the data yields (events per $[\text{pb}^{-1}]$), normalised to the integrated luminosity, after applying the analysis selection for different data-taking periods during the runs between 2015 to 2018. The yields are expected to be consistent for each data-taking period. A deficit would indicate a problem during data taking and an increase would indicate a longer run, resulting in more data being taken than planned for. For example Figure 8.3 in period A, two runs can be seen to have a significant deficit compared to the other runs. This is due to a problem with the resistive plate chambers of the muon detector during the run period that resulted in a lower yield than expected.

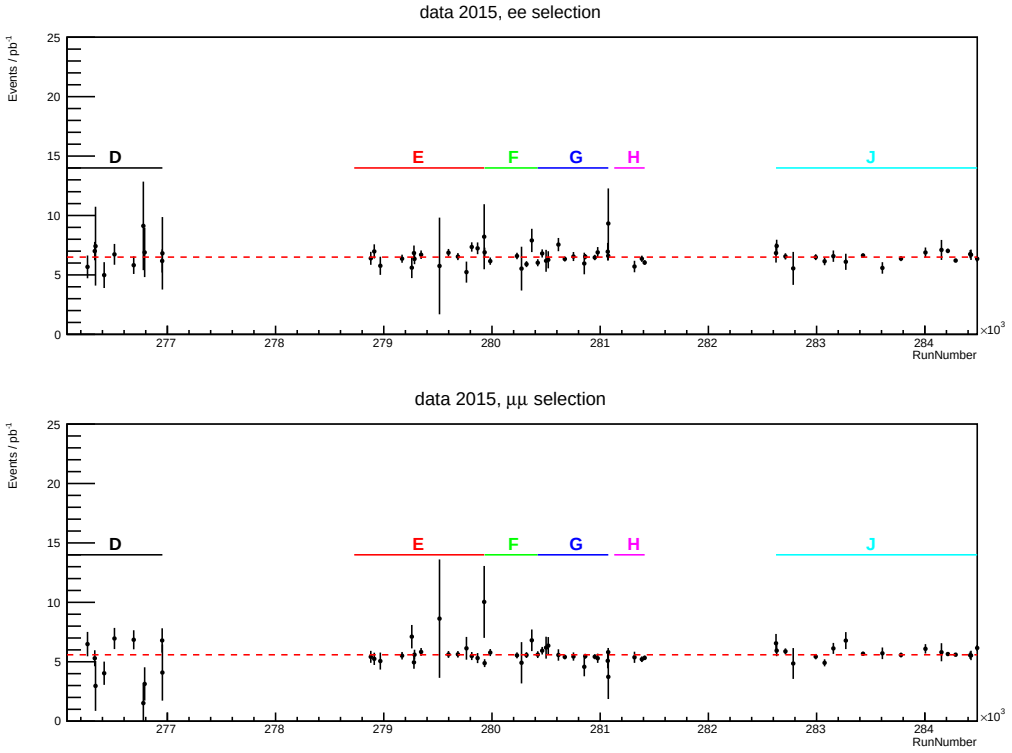

Figure 8.1 Data yields for the 2015 run period for the ee (above) and $\mu\mu$ (below) selections. Each letter on the legend correspond to the different data taking periods within a year [3].

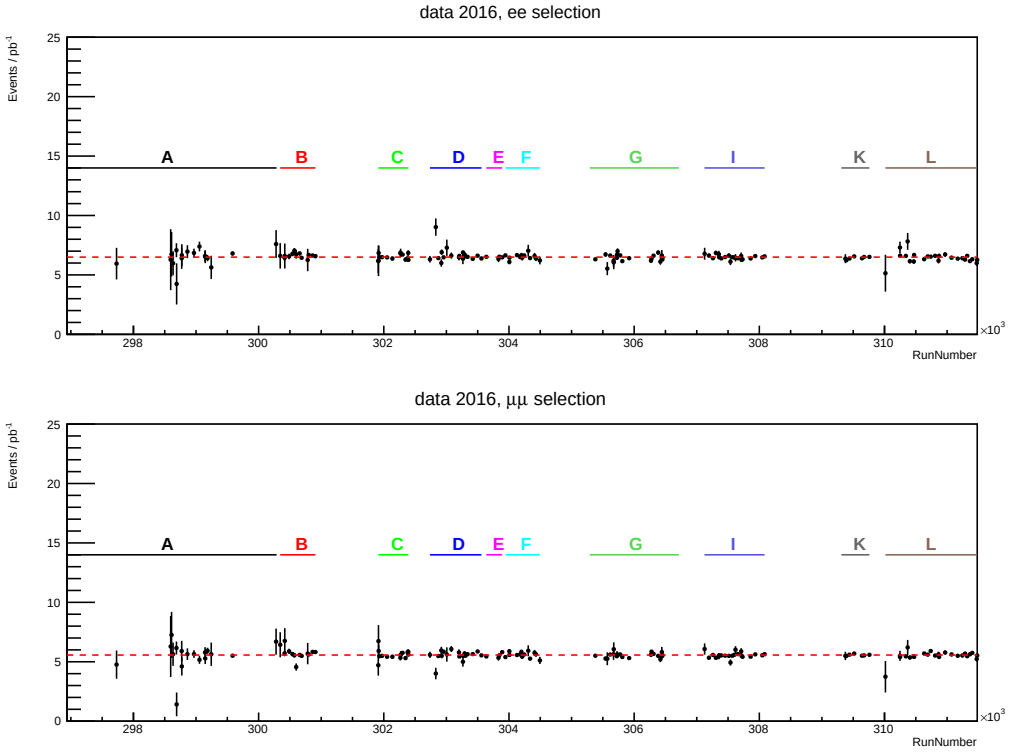

Figure 8.2 Data yields for the 2016 run period for the *ee* (above) and $\mu\mu$ (below) selections. Each letter on the legend correspond to the different data taking periods within a year [3].

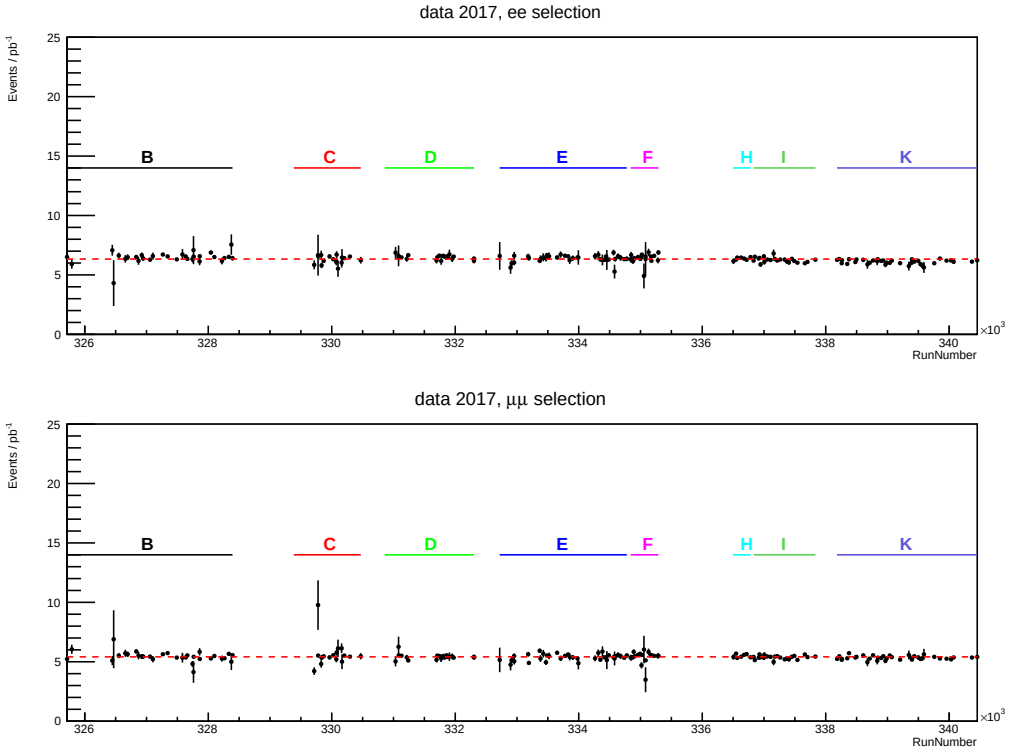

Figure 8.3 Data yields for the 2017 run period for the ee (above) and $\mu\mu$ (below) selections. Each letter on the legend correspond to the different data taking periods within a year [3].

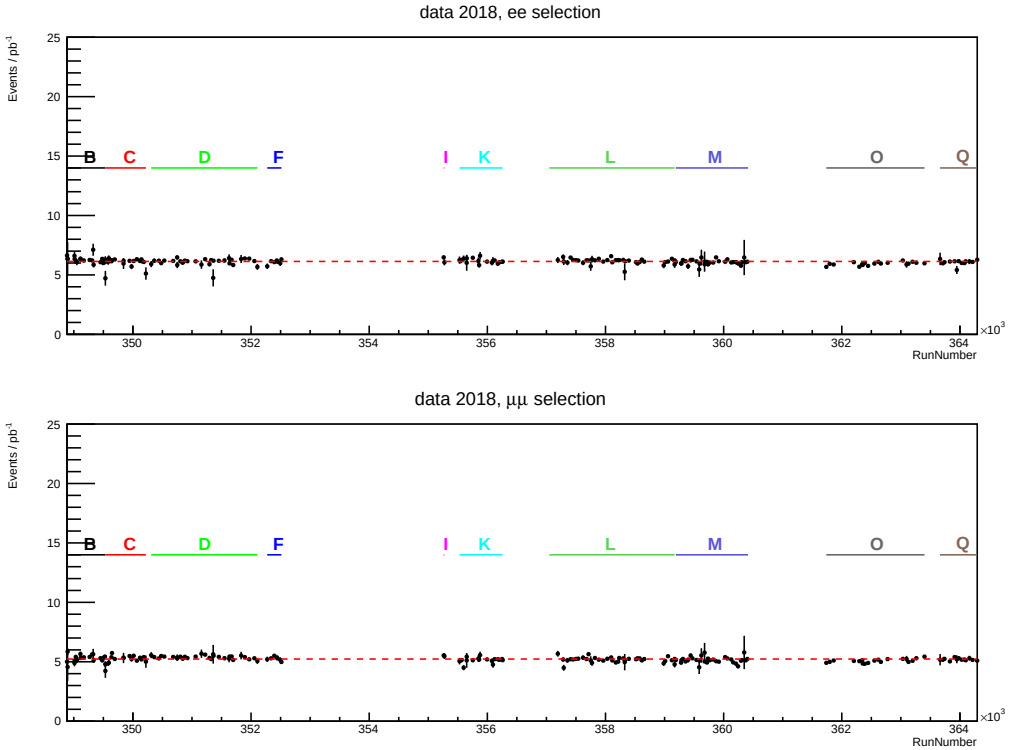

Figure 8.4 Data yields for the 2018 run period for the ee (above) and $\mu\mu$ (below) selections Each letter on the legend correspond to the different data taking periods within a year [3].

8.2 Monte Carlo samples

Whilst the analysis is performed using a data-driven methodology, simulated samples for the background and signal are used to determine the appropriate functional form to fit the data, study background compositions, estimate uncertainties and evaluate the expected signal contribution in the signal regions. This section outlines the MC samples used for the background and signal samples.

There are generators used to produce events using higher-order matrix elements. However, it is often required to enhance the description of the process beyond the order of the generator used. Higher-order QCD and EW corrections can modify the shape of the invariant mass distributions. Mass-dependent K-factors are derived from taking the ratio of the higher-order differential cross-section calculation over the available sample, e.g. next-to-next-to-leading order (NNLO) over the next-to-leading order (NLO). The K-factors are then applied to the invariant mass distribution on an event by event basis to produce the higher-order samples.

Simulated samples include the effects of pileup interactions, performed with Pythia v8.186 using the ATLAS A3 set of tuned parameters [121] and the NNPDF23LO PDF set, and weighted accordingly to the number of pileup interactions observed in data. The simulated samples then pass through the full detector simulation as described in Section 6.1.

8.2.1 Background samples

The main backgrounds considered in the analysis, in decreasing order of importance, are Drell-Yan (DY), top-quark ($t\bar{t}$), single-top-quark and diboson production. For the electron channel, is it prohibitive to produce MC with enough events to accurately represent the expected QCD multijet distribution, due to the small probability of jets faking electrons that pass the analysis selection. Therefore, the QCD and W+jets processes in the dielectron channel are estimated with a data-driven method [2], described in Section 8.3. For the muon channel, the multijet background was studied and found to be negligible [2]. Therefore, the contribution is neglected.

The SM Drell-Yan process is modelled using the NLO POWHEG-BOX [122, 123] event generator using the CT10 PDF [124] and is interfaced with PYTHIA v8.186 [125] parton shower generator. The DY samples are generated in slices of dilepton invariant mass, where 19 mass-binned samples were created with dilepton invariant mass ranging from 120 GeV and $>$ 5000 GeV, to increase the statistics of the samples in the high-mass regions. Corrections are applied to the DY samples to correct them from NLO to NNLO using a mass-dependent K-factor. The K-factor calculated with VRAP v0.9 [126] and the CT14 NNLO PDF set [127] for QCD effects. MCSANC [128] is used for QED corrections. The diboson processes (WW, WZ and ZZ) are generated at NLO using SHERPA 2.1.1 [129] with the CT10 PDF. Similar to the DY samples, the diboson samples were generated in invariant mass slices to increase the statistics of the sample. The $t\bar{t}$ background is generated at NLO using POWHEG-BOX with the NNPDF3.0NLO [6] PDF. Single top (s/t-channel) uses POWHEG-BOX with NNPDF3.0NLO PDF. A top quark mass of 172.5 GeV is used for the generation of these samples. The top quark samples are normalised to the cross-section at NNLO in QCD including resummation of the NNLO leading order soft gluon terms as provided by TOP++2.0 [130].

The MC event generators for the hard-scattering process, showering and PDFs are listed in Table 8.2. A detailed description of the event simulation procedure is given in Section 6.1. "Afterburner" generators such as PHOTOS [131] for the final-state photon radiation (FSR) modelling, MADSPIN [132] to preserve top-quark spin correlations, and EVTGEN [133], used for the modelling of c- and b-hadron decays, are also included in the simulation.

8.2.2 Signal samples

The PYTHIA v8.230 generator is used to produce CI signal samples at leading-order (LO) using the NNPDF23LO PDF. Five benchmark values of Λ from 10-30 TeV in steps of 5 TeV were generated for each of the CI models. The CI shapes contain both the SM DY background and the interference between the DY and CI.

Background Process	ME Generator and ME PDFs	PS and non-perturbative effect with PDFs
NLO Drell–Yan	POWHEG-BOX [122, 123], CT10 [124], PHOTOS	PYTHIA v8.186 [125], CTEQ6L1 [134, 135], EVTGEN1.2.0
$t\bar{t}$	POWHEG-BOX, NNPDF3.0NLO [6]	PYTHIA v8.230, NNPDF23LO [136], EVTGEN1.6.0
Single top s-channel, Wt	POWHEG-BOX, NNPDF3.0NLO	PYTHIA v8.230, NNPDF23LO, EVTGEN1.6.0
Single top t-channel	POWHEG-BOX, NNPDF3.04fNLO, MADSPIN	PYTHIA v8.230, NNPDF23LO, EVTGEN1.6.0
Diboson (WW, WZ and ZZ)	SHERPA 2.1.1 [129], CT10	SHERPA 2.1.1, CT10
Signal Process		
LO Drell–Yan	PYTHIA v8.186, NNPDF23LO	PYTHIA v8.186, NNPDF23LO, EVTGEN1.2.0
LO CI	PYTHIA v8.186, NNPDF23LO	PYTHIA v8.186, NNPDF23LO, EVTGEN1.2.0

Table 8.2 The event generators used for PDFs and generating matrix element (ME) and parton shower (PS) simulation of the signal and background processes. The top-quark mass is set to 172.5 GeV.

It is possible to reweight the SM background to BSM signals when both the signal and background have the same initial and final states. Event-by-event weights are calculated and applied to the DY events passing the event selection, resulting in the DY sample being *reweighted* into corresponding CI signal events. This allows the production of unique samples of CI signal events, which match the signal samples produced using MC, but with a significant reduction in the computing power required [2].

The signal templates include the same set of experimental and theoretical corrections as applied with other samples described in Section 8.2. In addition, higher order QCD and EW corrections are also applied, resulting in the same LO-to-NNLO mass-dependent k-factors as the background MC. While higher-order QCD corrections are expected to be the same for signals and background, it is not clear if the electroweak corrections can be treated the same. The addition of the electroweak corrections may be less conservative. However, it is deemed to be closer to the theoretically correct treatment than being over conservative and not including the corrections.

Signal templates are produced from the reweighting of the PYTHIA v8.186 LO DY simulation. The general procedure is to replace the DY differential cross-section with the corresponding

cross-section of the CI process, where

$$\frac{d\sigma}{d\hat{t}}(q\bar{q} \to \gamma^*/Z \to e^+e^-) \to \frac{d\sigma}{d\hat{t}}(q\bar{q} \to CI \to e^+e^-), \tag{8.1}$$

where $\hat{t}$ corresponds to any kinematic quantity. The above can be achieved using the analytic expressions for the DY and CI matrix elements. The ratio between the two matrix elements, evaluated with the truth-level kinematic information of the dielectron and dimuon events, defines the weight, w_{RW}, used to reweight the DY event to the corresponding CI event. The weight is given by [2]

$$w_{\mathrm{RW}} = |\mathcal{M}(CI)|^2 \ / \ |\mathcal{M}(\gamma^*/Z)|^2 \ , \tag{8.2}$$

where the numerator refers to the BSM differential cross-section and the denominator refers to the SM process only. The weights are applied to the LO DY events to transform into CI signal shapes, in steps of 2 TeV between $\Lambda = 12$ TeV and $\Lambda = 100$ TeV.

The dedicated CI samples are used to validate the reweighting procedure, Figure 8.5 shows an example of a LL chiral, constructive interference, CI mass slice between 3000 - 4000 GeV where the reweighted CI interaction sample and the dedicated sample is compared. Figure 8.6 shows the invariant mass distributions for the LL chiral constructive and destructive interference models reweighted using the procedure described above. Figure 8.7 depicts the shapes of the LL chiral CI interaction signals relative to the DY background These depict the evolution of the shapes as the interference and Λ of the CI models change. The CI samples include the full cross-section (including the DY component) as defined in Section 3.3.

Signal template morphing

The CI samples are produced in steps of 2 TeV from 12-100 TeV using the reweighting procedure outlined in Section 8.2.2. The DY component is subtracted from the simulated signals, leaving the pure CI and interference terms. The signal model used in the analysis (Section 10.3) requires a continuous description of the signal model as a function of Λ to fit possible signal

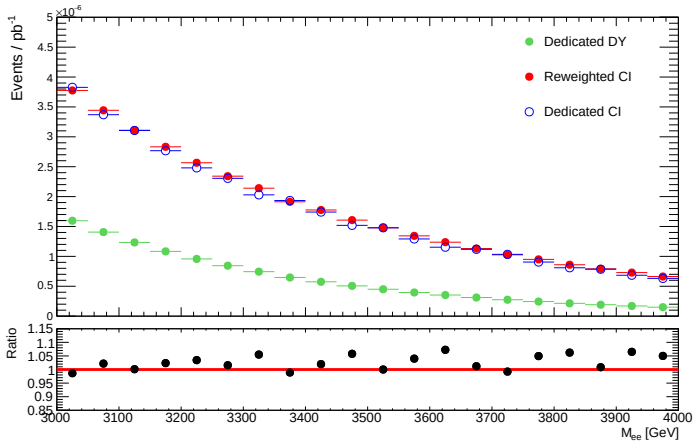

Figure 8.5 Comparison of dedicated and reweighted LL chiral, constructive interference, CI sample in the invariant mass range from 3000 - 4000 GeV is shown in the top pad. The DY sample used to reweight is also shown. The bottom pad shows the ratio between the reweighted and dedicated CI signal.

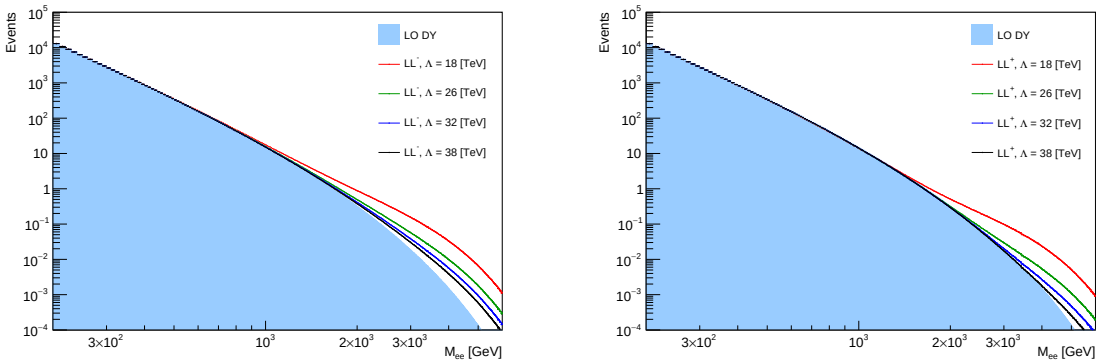

Figure 8.6 Invariant mass distributions for LL chiral, constructive (left) and destructive (right) interference CI models with the DY sample used to reweight it. The interference of the CI interaction is shown by the - (constructive) and + (destructive) sign on the legend.

contributions that may be between the reweighted signal masses. To implement the signal template morphing a custom signal probability distribution class was created derived from two available RooFit [137]. A linear interpolation is used to provide a smoothly changing PDF that is dependent on the parameter Λ. Figure 8.8 depicts the morphed signal PDF for various values of Λ for constructive and destructive CI interference models. It shows the morphed signals for

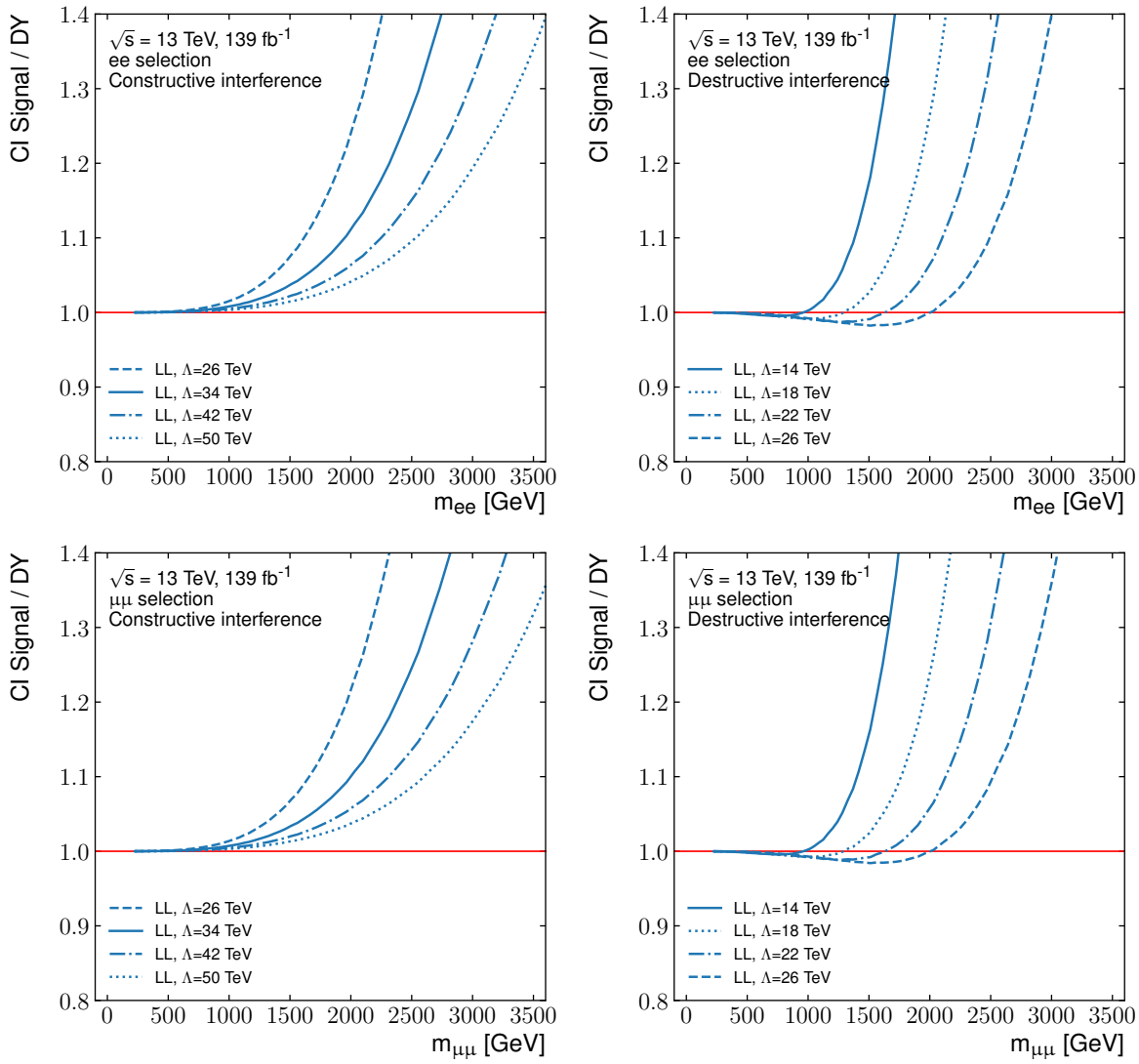

Figure 8.7 The ratio of the contact interaction signal with the DY background is shown for various contact interaction scales, Λ. For constructive cases, the ratio is purely positive, while for destructive cases the impact of destructive interference is seen at lower masses. Shown from left to right and top to bottom, e^+e^- constructive, e^+e^- destructive, $\mu^+\mu^-$ constructive, and $\mu^+\mu^-$ destructive.

the LL chirality model, but, the signal PDFs are produced for all chirality models considered in the analysis. For constructive models, the shape of the signal does not change significantly as a function of Λ. However, for the destructive models, a strong relationship between the shape of the signal and Λ can be seen. The downward *dip* in the destructive plots corresponds to the point at which the destructive interference is dominant and hence where a negative signal yield is expected. Figure 8.9 shows the comparison of a CI template for $\Lambda = 20\,\text{TeV}$ compared with the corresponding morphed signal template, and a good agreement between the two is shown in the ratio panel. Statistical fluctuations in the reweighted samples result in small differences between the morphed and reweighted templates.

Furthermore, the morphed signal PDFs can be used in the statistical analysis to describe the signal model. For the search of non-resonant signals like CI, it is prohibitive to describe the signal model with a floating signal strength parameter, μ. When searching for resonances, it is natural to use μ as the parameter of interest, which describes the strength of the signal. However, due to the shape and normalisation changes of the signal models as a function of Λ, it is more accurate to define the parameter of interest as a function of Λ. Further details of the statistical analysis and choice of the parameter of interest is given in Section 4.5

8.3 Estimation of fake background

Processes involving jets or electron and a jet can be reconstructed as electrons in the algorithms, described in Section 6.2.2, and pass the analysis selection. The dominant contribution for the electron plus jet final state is mainly due to the W+jets processes. Light-flavour jets containing charged and neutral pions can be misidentified as electrons during reconstruction. Due to the high energies of collisions at the LHC, the decays of neutral pions, $\pi^0 \to \gamma\gamma$, are highly boosted and can lead to narrow electromagnetic energy depositions. These processes can give rise to signatures that are difficult to distinguish from those of the desired electrons. The desired electrons are referred to as *real electrons*, whereas the objects which mimic the electrons are referred to as *fake electrons*. The fake background is difficult to estimate using simulation.

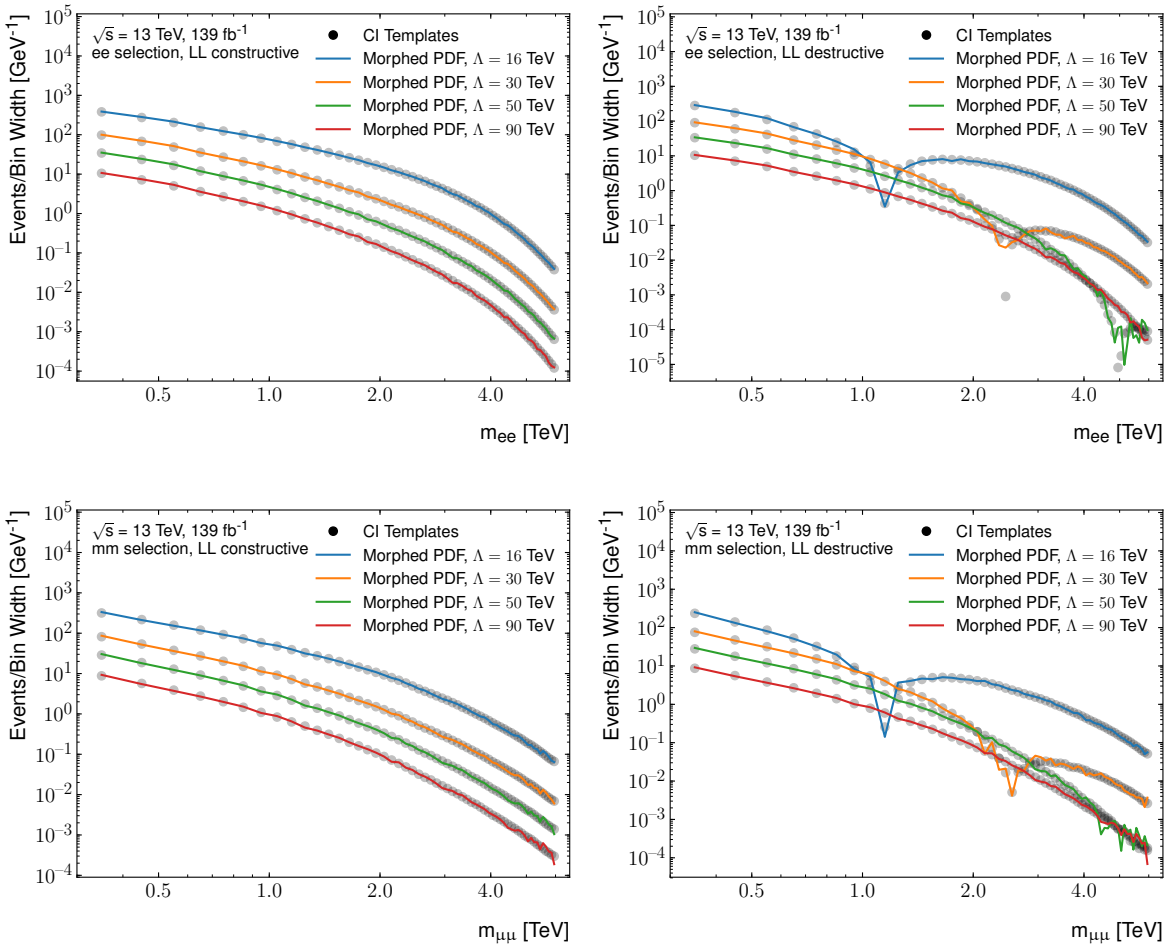

Figure 8.8 Comparison of morphed PDF signals for a CI signal for various Λ values. for constructive (left) and destructive (right) interference for the electron (top) and muon (bottom) channels. Absolute number of events is plotted in each bin.

Therefore, data-driven techniques are often used. This is mainly due to increased computing power needed to model the detector simulation of many jet interactions with the detector.

The analysis uses the likelihood matrix method [138] to estimate the fake background contribution using two levels of electron identification criteria: a *tight* (T) selection which corresponds to the nominal analysis selection, and a *loose* (L) identification criteria which relaxes the nominal identification. The set of objects passing the *tight* selection, N_{tight}, is a subset of those passing the *loose* selection, N_{loose}. Pairs of electron candidates are considered denoted by N_{xy} with $x, y \in T, L$, giving the number of electron pairs passing a specific selection.

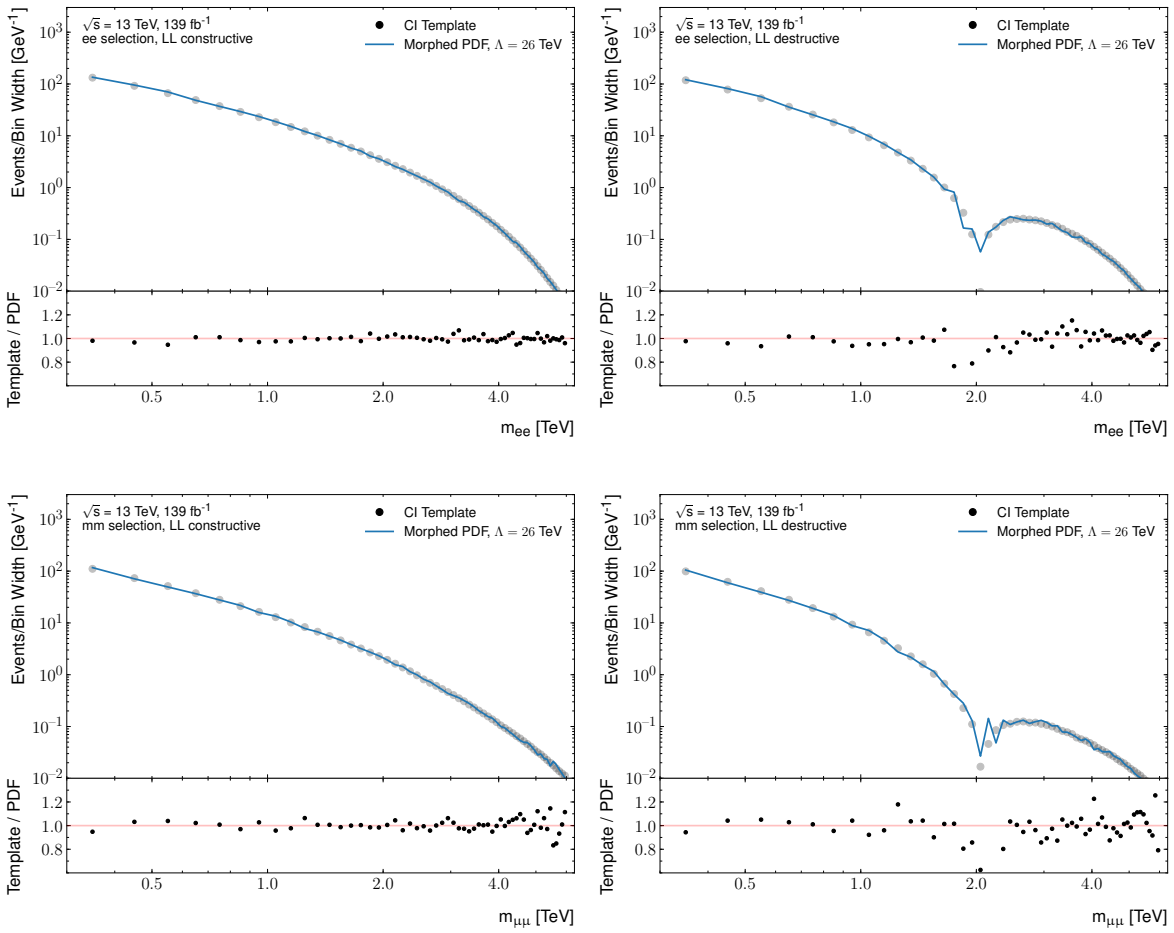

Figure 8.9 Comparison of Morphed PDF signals for a CI signal with $\Lambda = 26\,\text{TeV}$ for constructive (left) and destructive (right) interference for the electron (top) and muon (bottom) channels. The bottom pad shows the ratio of the MC template with the morphed signal PDF. Absolute number of events is plotted in each bin.

The fist index representing the leading electron ($p_{T,lead} > p_{T,sublead}$) and the second one the subleading electron. An additional set of quantities N_{xy} with $x, y \in R, F$ can be defined to denote whether an electron is real (R) or fake (F). The relationship between the two sets of quantities is given by [2]

$$\begin{pmatrix} N_{TT} \\ N_{TL} \\ N_{LT} \\ N_{LL} \end{pmatrix} = M \begin{pmatrix} N_{RR} \\ N_{RF} \\ N_{FR} \\ N_{FF} \end{pmatrix}, M = \begin{pmatrix} r_1 r_2 & r_1 f_2 & f_1 r_2 & f_1 f_2 \\ r_1 \tilde{r2} & r_1 \tilde{f2} & f_1 \tilde{r2} & f_1 \tilde{f2} \\ \tilde{r1} r_2 & \tilde{r1} f_2 & \tilde{f1} r_2 & \tilde{f1} f_2 \\ \tilde{r1} \tilde{r2} & \tilde{r1} \tilde{f2} & \tilde{f1} \tilde{r2} & \tilde{f1} \tilde{f2} \end{pmatrix} \tag{8.3}$$

where $\tilde{x} = 1 - x$. The vectors on the right- (left-) hand side contain exclusive measurable (not measurable) quantities, e.g. L would denote an electron that passes the *loose* selection and not the *tight* selection. The coefficients r and f correspond to the real and fake rates, respectively. The real efficiency is the probability of real electrons to be reconstructed as *tight* electrons and is calculated using MC. In contrast, the fake efficiency is the probability of a fake electron selected as *loose* to be reconstructed as a *tight* electron. The fake efficiency is calculated using data. Index 1 and 2 correspond to the efficiencies of the leading and subleading electrons.

The number of misidentified events within the electron selection is estimated by measuring the number of events passing the signal selection (N_{TT}), which contains at least one fake electron. These fake events arise from events where at least one electron is misidentified (RF and FR), or events where both electrons are misidentified (RR). The total number of fake electrons is be then obtained from the sum of these contributions

$$N_{TT}^{\text{fake}} = r_1 f_2 N_{RF} + f_1 r_2 N_{FR} + f_1 f_2 N_{FF}, \tag{8.4}$$

A likelihood is formed to include poisson constraints on N_{xy} with $x, y \in T, L$:

$$\mathcal{L} = \prod_{x,y \in T,L} P(N_{xy}, N_{xy}^{pred}), \tag{8.5}$$

where P represents the Poisson constraint on the observed number of events in each electron category and is consistent with the predicted number of fake and real leptons. The predicted values can be expressed in terms of a linear combination of N_{xy} with $x, y \in R, F$ terms by using Equation 8.3

$$\begin{aligned} N_{TL}^{pred} &= (r_1 r_2)N_{RR} + (r_1 f_2)N_{RF} + (f_1 r_2)N_{FR} + (f_1 f_2)N_{RR}, \\ N_{LT}^{pred} &= (r_1 \tilde{r_2})N_{RR} + (r_1 \tilde{f_2})N_{RF} + (f_1 \tilde{r_2})N_{FR} + (f_1 \tilde{f_2})N_{RR}, \\ N_{LL}^{pred} &= (\tilde{r_1} \tilde{r_2})N_{RR} + (\tilde{r_1} \tilde{f_2})N_{RF} + (\tilde{f_1} \tilde{r_2})N_{FR} + (\tilde{f_1} \tilde{f_2})N_{RR}. \end{aligned} \tag{8.6}$$

The likelihood is minimised, and the number of fakes can be extracted using Equation 8.4, which is then applied as an event by event weight used to produce an invariant mass distribution for the fake background contribution. The background template produced is smoothed using a functional fit [2].

The uncertainty on the functional fit is calculated by varying the start of the fit, which results in an envelop of possible estimates for the fitted template template. The start range of the fit is varied from 130 GeV to 150 GeV in steps of 2 GeV. The resulting envelop of the fits are taken as the uncertainty of the fake electron estimate. The uncertainty of the fake estimation varies from from 50% at 2 TeV to 110% at 5 TeV.

8.4 Transfer functions

The Transfer function approach offers an alternative method to produce large statistic and smooth DY and $t\bar{t}$ samples [3, 139]. This method is used to overcome the limitations of insufficient MC statistics at lower invariant masses. The available MC samples for the previous analysis using the 2015−16 dataset [2] had statistical uncertainties that the same as the statistical uncertainty in data, resulting in a loss of sensitivity to new physics models. Consequently, complicated background smoothing techniques with functional fits were adopted in the analysis in an attempt to tackle the loss of sensitivity.

The TF approach provides a smooth transformation between the truth and reconstruction level invariant-mass spectrum. A functional form is not imposed on the TF, and the transformation is analytically parametrised using the detector resolution. The electron and muon channels require separate TFs due to the different reconstruction properties of the two channels.

The transition between a known truth spectrum, $S_t(m_{\ell\ell,t})$, and an unknown reconstructed spectrum, $S_r(m_{\ell\ell,r})$, is be parametrised by a TF, $P(m_{\ell\ell,r} \mid m_{\ell\ell,t})$. The TF describes the probability to reconstruct an event at invariant mass of $m_{\ell\ell,r}$ for events with truth mass $m_{\ell\ell,t}$ that passes the selection. Full simulation MC is used to construct the TFs. The TFs are obtained fitting the detector response, with simultaneous fits to $m_{\ell\ell,t}$ bins, where the convolution of a Gaussian and a Crystal-ball is used to model the detector response. The truth invariant mass spectrum is obtained from very large truth-only MC samples. Larger samples can be produced at truth-level efficiently compared to fully reconstructed samples due to significantly smaller CPU times and disk space required to produce them. The truth-only sample is produced such that it is produced at luminosity 55 times larger than the available dataset. The following convolution is used to obtain the reconstruction level spectrum:

$$S_r(m_{\ell\ell,r}) = P(m_{\ell\ell,r} \mid m_{\ell\ell,t}) \otimes \left[S_t(m_{\ell\ell,t}) \cdot A\varepsilon(m_{\ell\ell,t}) \right], \tag{8.7}$$

where $A\varepsilon(m_{\ell\ell,t})$ is the acceptance times efficiency. $A\varepsilon(m_{\ell\ell,t})$ is the probability that a event with truth invariant mass passes the selection. The probability is calculated by taking the fraction of events accepted in a truth invariant mass bin and the total number of generated events in that bin.

8.5 Data and background comparisons

Figures 8.10 and 8.11 show the comparisons of the invariant mass distributions between the data and MC expectation with the addition of some benchmark CI interaction signals overlaid on top. The fake electron contribution was only estimated for the invariant-mass distributions Figures 8.12 and 8.13 show the p_{T} distributions for the leading and subleading leptons.

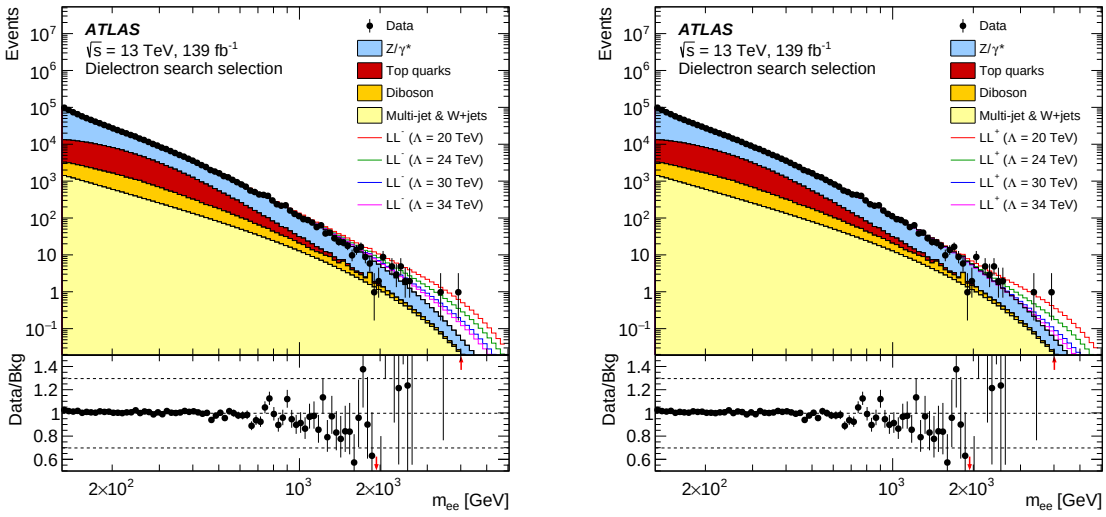

Figure 8.10 Invariant mass distribution for the e^+e^- selection for the full $2015-2018$ dataset and the respective MC campaign. The constructively interfering CI contributions are shown in (left),while destructive contributions are shown in (right). The bottom panel shows the ratio between the data and MC.

The η distributions for the leading and subleading leptons are shown in Figures 8.14 and 8.15. In the electron channel, the maximum can be seen at $\eta = 0$ and falls towards higher values of $|\eta|$. The transition region corresponds to $1.37 < |\eta| < 1.52$. The muon channel shows dips in the η distributions that correspond to poorly aligned chambers in the muon spectrometer. Figures 8.16 and 8.17 show the ϕ distributions for the leading and subleading leptons. A flat distribution is shown in the electron channel. The ϕ distribution for muons show small dips due to support structures on which the ATLAS detector is placed.

The comparison is mainly produced for illustrative purposes, since the MC background prediction is used only for validation of the choice of functional fit. However, a good agreement is between the data and MC expectation is required for the MC to be used to validate the data-driven fit strategy. Furthermore, the comparisons allow for an early indication of issues that may have occurred when deciding on a selection.

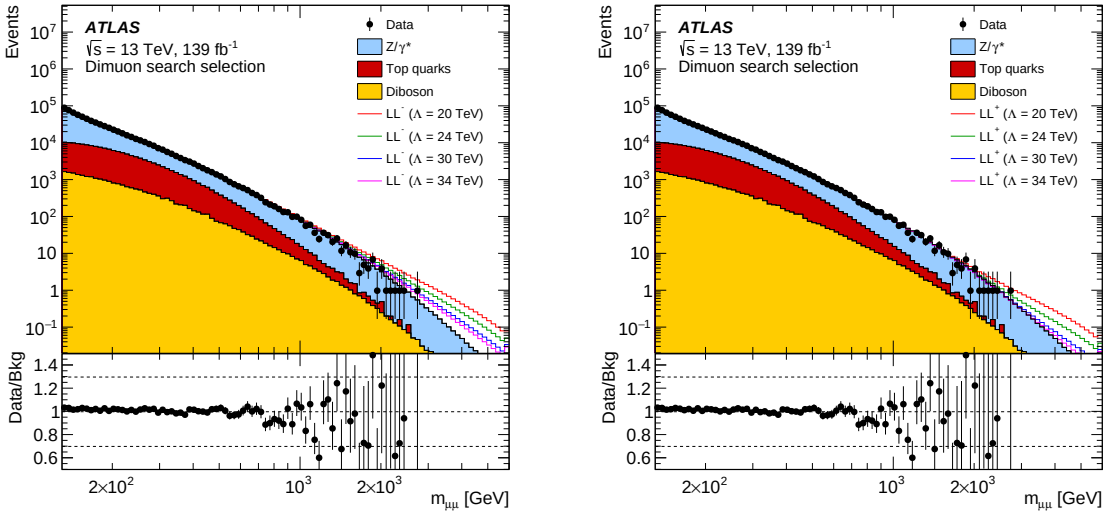

Figure 8.11 Invariant mass distribution for the $\mu^+\mu^-$ selection for the full $2015-2018$ dataset and the respective MC campaign. The constructively interfering CI contributions are shown in (left), while destructive contributions are shown in (right). The bottom panel shows the ratio between the data and MC.

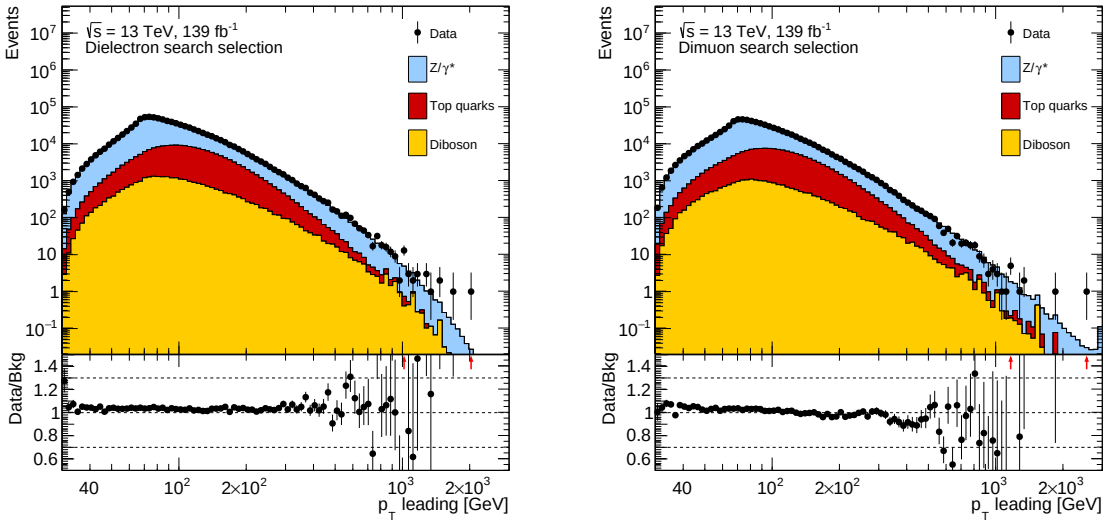

Figure 8.12 p_{T} distribution of the leading lepton for the dilepton selections for the full $2015-18$ dataset and the respective MC campaigns. The e^+e^- channel is shown in (left) and $\mu^+\mu^-$ channel in (right). The bottom panel shows the ratio between the data and MC.

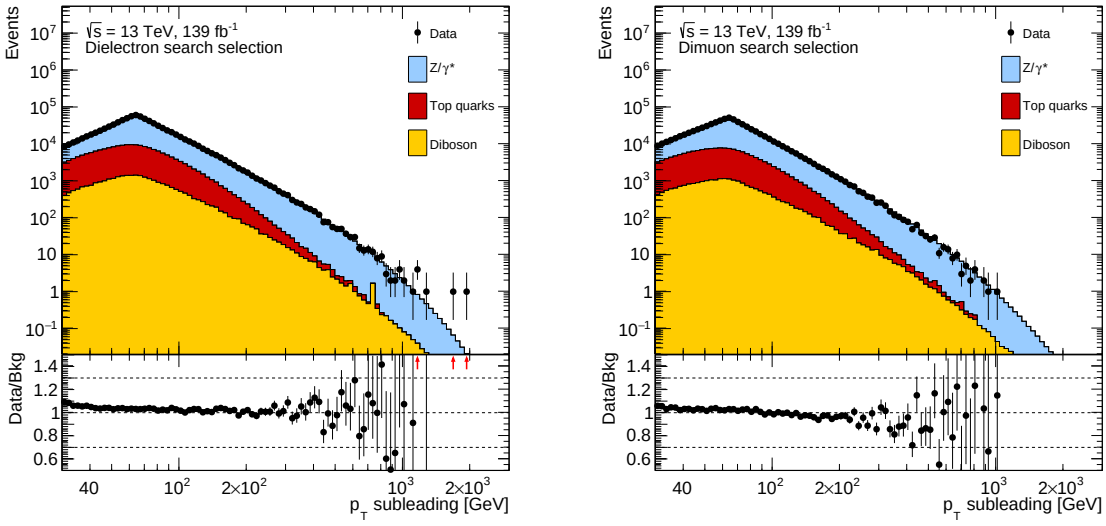

Figure 8.13 p_{T} distribution of the subleading lepton for the dilepton selections for the full $2015-18$ dataset and the respective MC campaigns. The e^+e^- channel is shown in (left) and $\mu^+\mu^-$ channel in (right). The bottom panel shows the ratio between the data and MC.

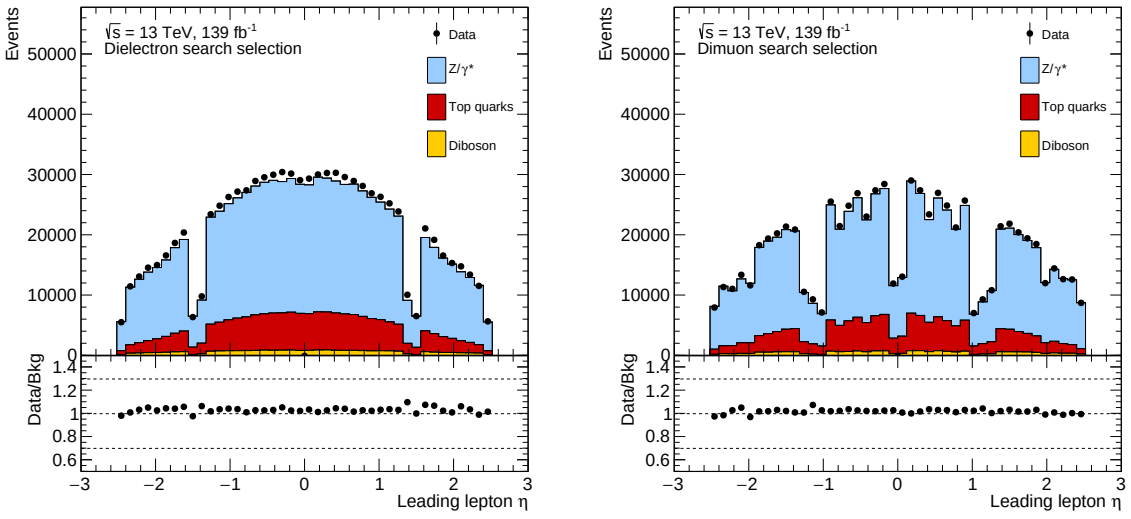

Figure 8.14 η distribution of the leading lepton for the dilepton selections for the full $2015-18$ dataset and the respective MC campaigns. The e^+e^- channel is shown in (left) and $\mu^+\mu^-$ channel in (right). The bottom panel shows the ratio between the data and MC.

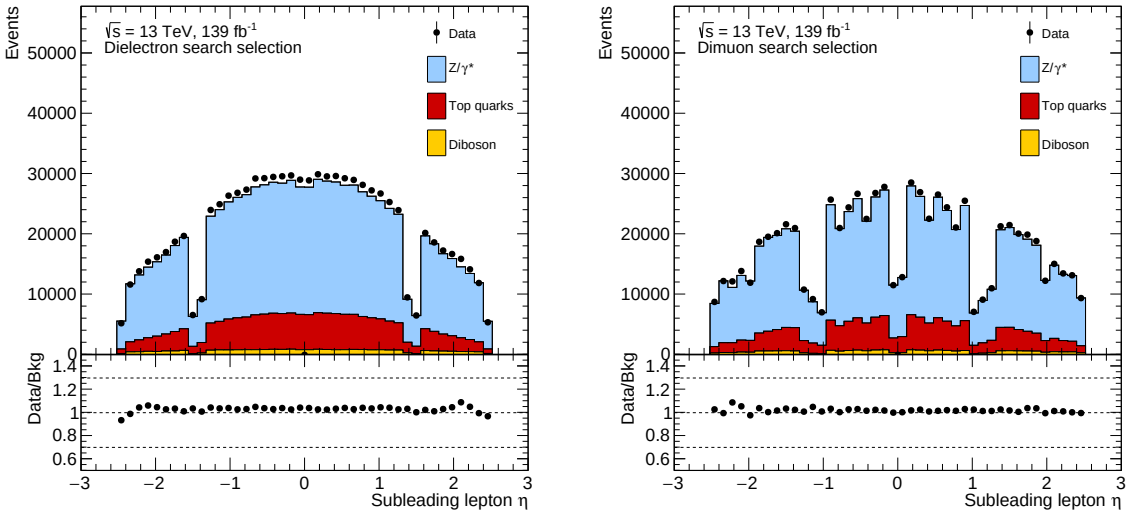

Figure 8.15 η distribution of the subleading lepton for the dilepton selections for the full $2015-18$ dataset and the respective MC campaigns. The e^+e^- channel is shown in (left) and $\mu^+\mu^-$ channel in (right). The bottom panel shows the ratio between the data and MC.

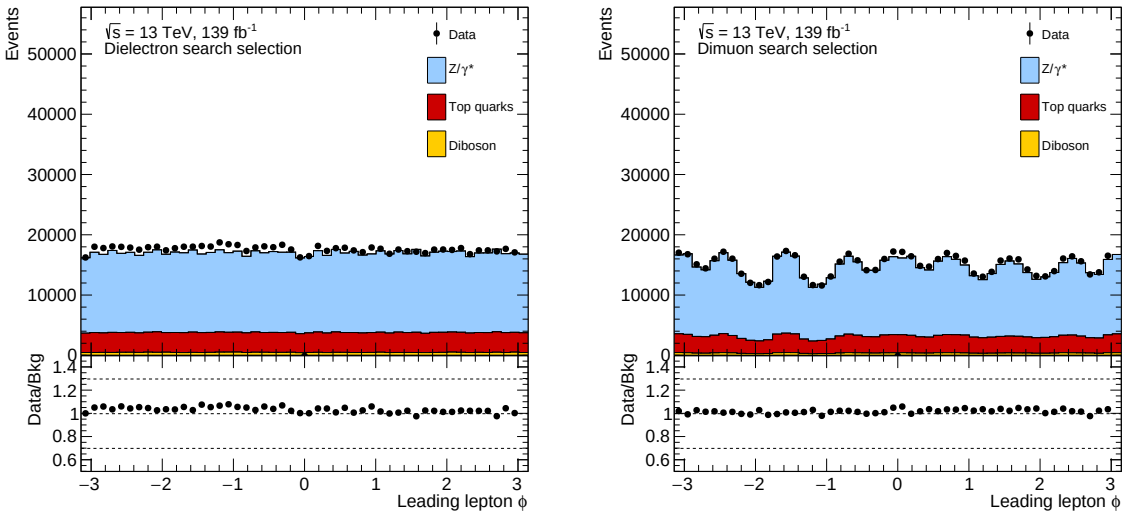

Figure 8.16 ϕ distribution of the leading lepton for the dilepton selections for the full $2015-18$ dataset and the respective MC campaigns. The e^+e^- channel is shown in (left) and $\mu^+\mu^-$ channel in (right). The bottom panel shows the ratio between the data and MC.

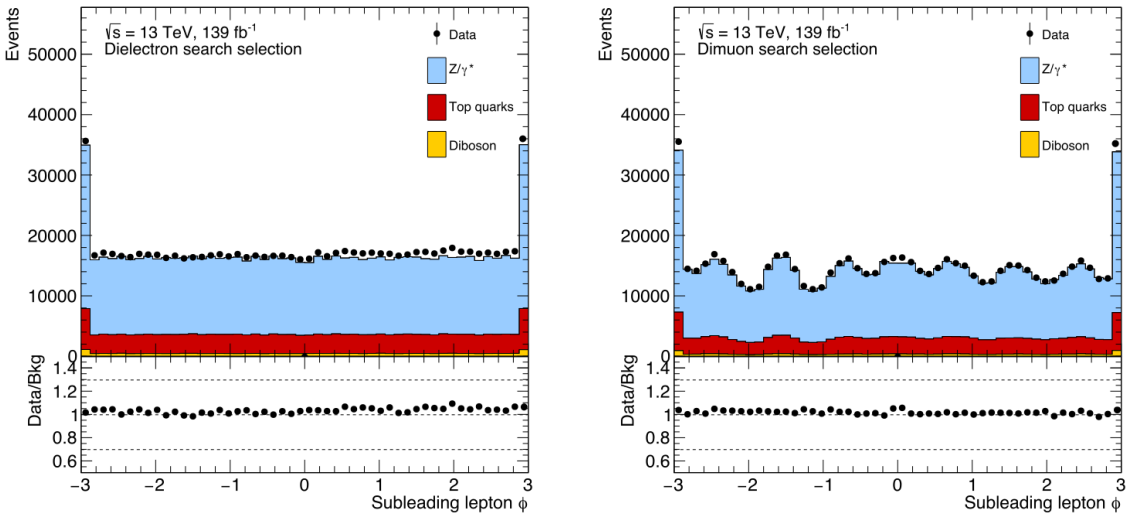

Figure 8.17 ϕ distribution of the subleading lepton for the dilepton selections for the full $2015-18$ dataset and the respective MC campaigns. The e^+e^- channel is shown in (left) and $\mu^+\mu^-$ channel in (right). The bottom panel shows the ratio between the data and MC.

Chapter 9

Systematic uncertainties on simulated samples

Due to the data-driven nature of the analysis, uncertainties related to the simulated samples are not directly applied since the simulated samples are only used to validate the data-driven background estimation. Instead, these uncertainties enter as a second order effect and are used to calculate the uncertainty associated with the data-driven background estimation. Uncertainties that exhibit normalisation changes have marginal impact on the data-driven background estimation. The largest impact arises from the systematic uncertainties which are related to changes in the shape of the invariant-mass distribution. This is discussed further in Chapter 10. The sources of systematic uncertainties on the simulated samples are outlined in this section.

There are several systematic uncertainties that affect the background modelling of the simulated samples, and these uncertainties can be divided into two distinct categories: experimental uncertainties related to the event (e.g. luminosity measurement) and to the reconstruction of the physics objects described in Chapter 6, and uncertainties from theoretical predictions from the PDF. The experimental uncertainties are outlined in Section 9.1 and the theoretical uncertainties are outlined in Section 9.2. The theoretical background uncertainty variations are estimated as a function of the true invariant-mass, where the transfer function approach, described in Section 8.4, is applied to generate high-statistic and smooth reconstructed tem-

plates for the uncertainties. The experimental uncertainties are provided by dedicated groups in charge of the performance of electron and muon reconstruction.

9.1 Experimental uncertainties

9.1.1 Event uncertainties

Uncertainties on the luminosity and the pileup measurements affect the overall normalisation of the processes being studied. The measurement of the luminosity is described in Section 5.3 and the uncertainty is calculated using the method described in [140]. For the full Run-2 dataset used in this analysis, the luminosity uncertainty is calculated to be ±1.7%. The uncertainty on the pileup distributions is measured by taking the difference between the pileup distribution observed in data and those expected at the time of producing the MC simulations. Additionally, uncertainties on the efficiency of the triggers used in the analysis are also considered. Figure 9.1 depicts the effect of the pileup uncertainty on the invariant mass distribution for the electron and muon channels. The figure shows that contribution from the pileup reweighting uncertainty is less than 1% for both the electron and the muon channels. This will result in a negligible impact on the background estimation. The difference in shape of the systematic variation between the electron and muon channel is due to statistical fluctuation in the muon channel that result in a less smooth distribution.

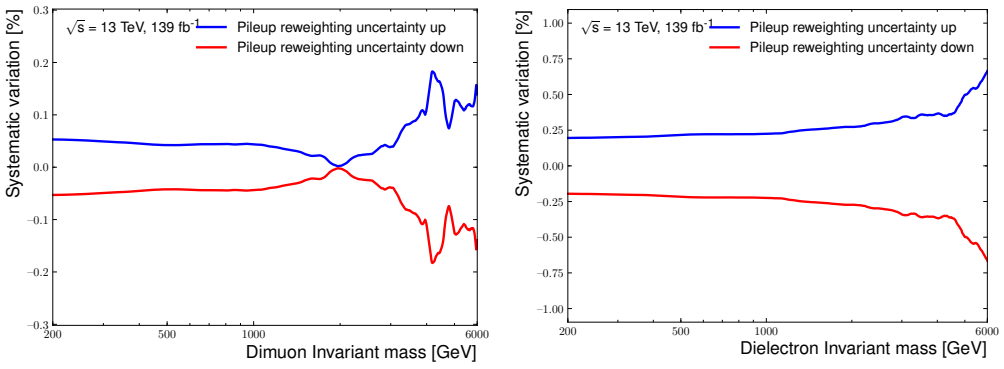

Figure 9.1 Systematic uncertainties due to pileup in the muon (left) and electron (right).

9.1.2 Lepton uncertainties

Efficiencies

The electron and muon efficiency uncertainties are obtained by using the tag-and-probe method [103, 141] by varying the selection of reconstruction, identification, isolation and trigger criteria individually [100, 103]. The tag-and-probe method uses $Z \to \ell\ell$ samples, where events are elected with pairs of leptons with opposite charge, that have an invariant mass in a window around the Z peak. When one of the leptons passes the tight working point for the criteria above, it is taken as the *tag* lepton, while the other is taken as the probe. The efficiency for a selection criteria can then be calculated by taking the number of probes which pass the tight selection over the total number of probes. Further detail on the efficiency uncertainty calculations are provided in [100, 103] for electrons and muons, respectively.

The systematic variations for reconstruction, isolation and identification are shown in Figures 9.3 and 9.4. The isolation efficiency systematic variation for both the electron and muon channels are less than 1%. The identification efficiency systematic variation for the electron channel increases from 2% at low-mass to 4% at high-mass. Whereas, for the muon channel the identification systematic variation is $< 1\%$ at low invariant masses with a sharp jump to 20% at high-mass, resulting in a dramatic change in the shape of the invariant-mass distribution. The reconstruction efficiency variation for the electron channel follows a similar shape to the identification with a negligible impact $<0.1\%$. In the muon channel the reconstruction efficiency has a larger impact on the shape of the invariant-mass distribution with the uncertainty ranging from 2% at low-mass to 30% at high-mass. For both the electron and muon channels there is a negligible contribution from the trigger efficiency systematic variation, with a flat contribution $<$ 0.001% throughout the entire invariant-mass spectrum considered. Therefore, it is not included in the figure.

Resolution

Smearing of the electron energies in MC accounts for the differences in energy resolution between data and MC. A full correlation model for energy resolution uncertainty consists of several nuisance parameters where all uncertainties have been decorrelated in bins of η [100].

The muon resolution corrections are calculated by fitting several correction coefficients that are used to match the invariant mass distributions between MC and data. Each fit parameter in the model is associated with a source of potential disagreement between data. The uncertainty on the resolution is derived by taking the variations of the fit procedure, the background parameterisation and muon spectrometer alignment [103].

The systematic variations for the resolution uncertainty in the electron and muon channel is shown in Figures 9.3 and 9.4. The muon resolution is <1% at low invariant masses up to 2000 GeV with a sharp increase up to 28% at 6000 GeV. Whereas, the electron resolution uncertainty follows a similar shape, but with a much smaller impact, ranging from <0.1% at low invariant mass to 0.75% at 6000 GeV. The uncertainty in both channel will result in a sharp change in the shape of the invariant-mass distribution. However, the effect is significantly larger in the muon channel.

Figure 9.2 depicts the dielectron and dimuon mass resolution as a function of the generated mass of the dilepton pair. In contrast to the dielectron channel, it can be seen in the dimuon channel that the mass resolution significantly deteriorates at higher invariant-mass. The impact of the muon resolution uncertainty on the data-driven extrapolation method, discussed in Chapter 11, was studied in detail. In particular, the impact of increasing the muon resolution uncertainty on the data-driven uncertainties was studied. It was concluded that there is negligible impact on the data-driven uncertainties when the muon resolution uncertainty is increased by 90% of it's initial value. This indicates that the functional form used is robust enough to take into account significant variations in the measurement of the muon resolution.

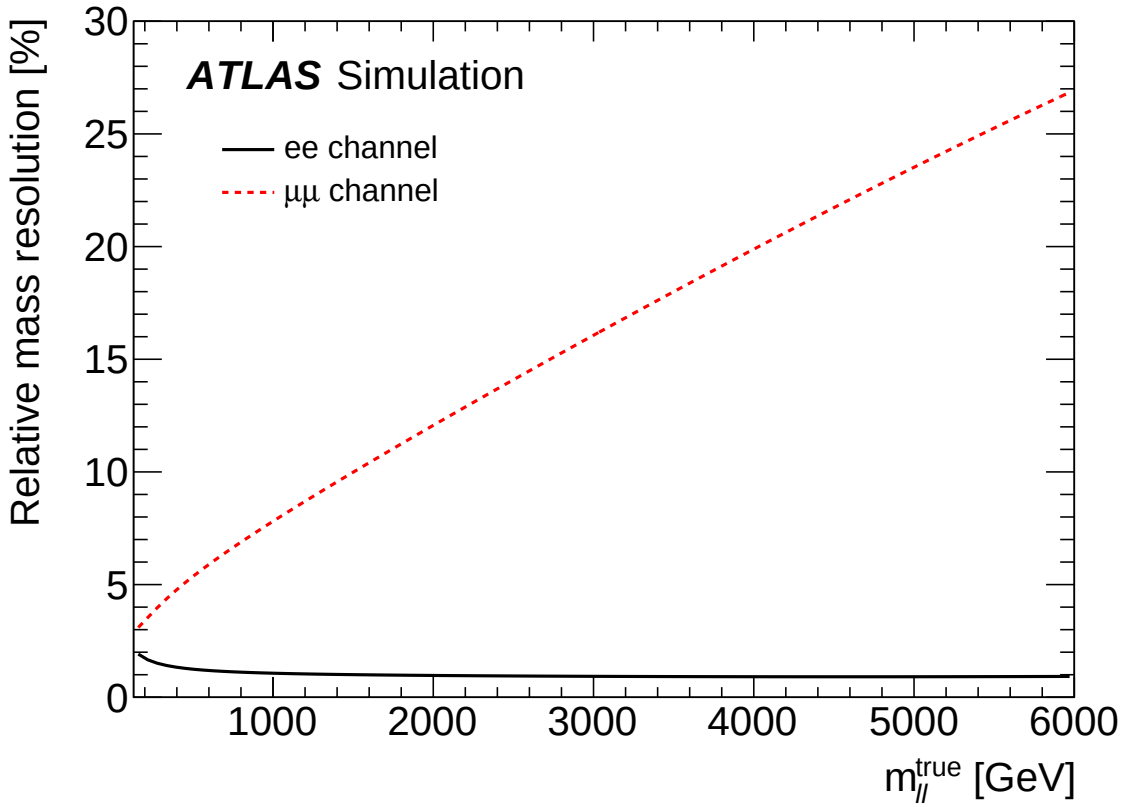

Figure 9.2 Dielectron and dimuon mass resolution as a function of the generated mass of the dilepton pair ($m_{\ell\ell}^{true}$) [3].

Energy scale

Electron and muon energy scale corrections are applied only on data. The effects of varying the respective uncertainties associated with the energy scale corrections up and down is calculated to determine the systematic uncertainty. The resulting distributions are used to determine the systematic uncertainty and is calculated on MC due to the higher statistics available [100].

Figures 9.3 and 9.4 show the size of the energy scale systematic variations. For the electron channel the uncertainty ranges from 0.35% at low-mass to 0.65% at high-mass. Whereas, for the muon channel the uncertainty is <0.1% at low mass with a sharp increase to 15% at high-mass.

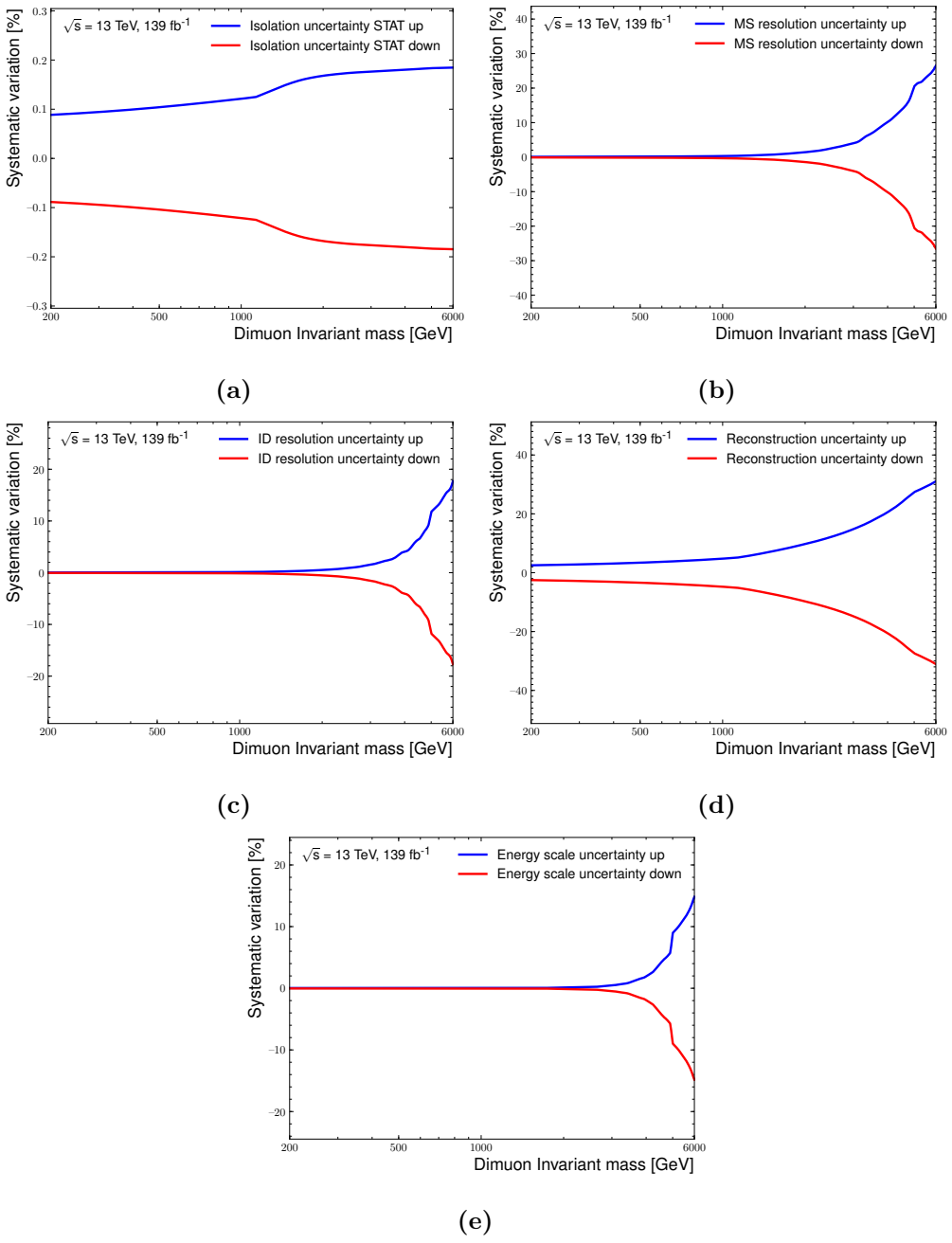

Figure 9.3 Muon systematic uncertainties due to experimental sources. The uncertainty related to isolation (a), momentum resolution in the muon spectrometer (b) and inner detector (c), muon reconstruction (d), and muon energy scale (e) are shown.

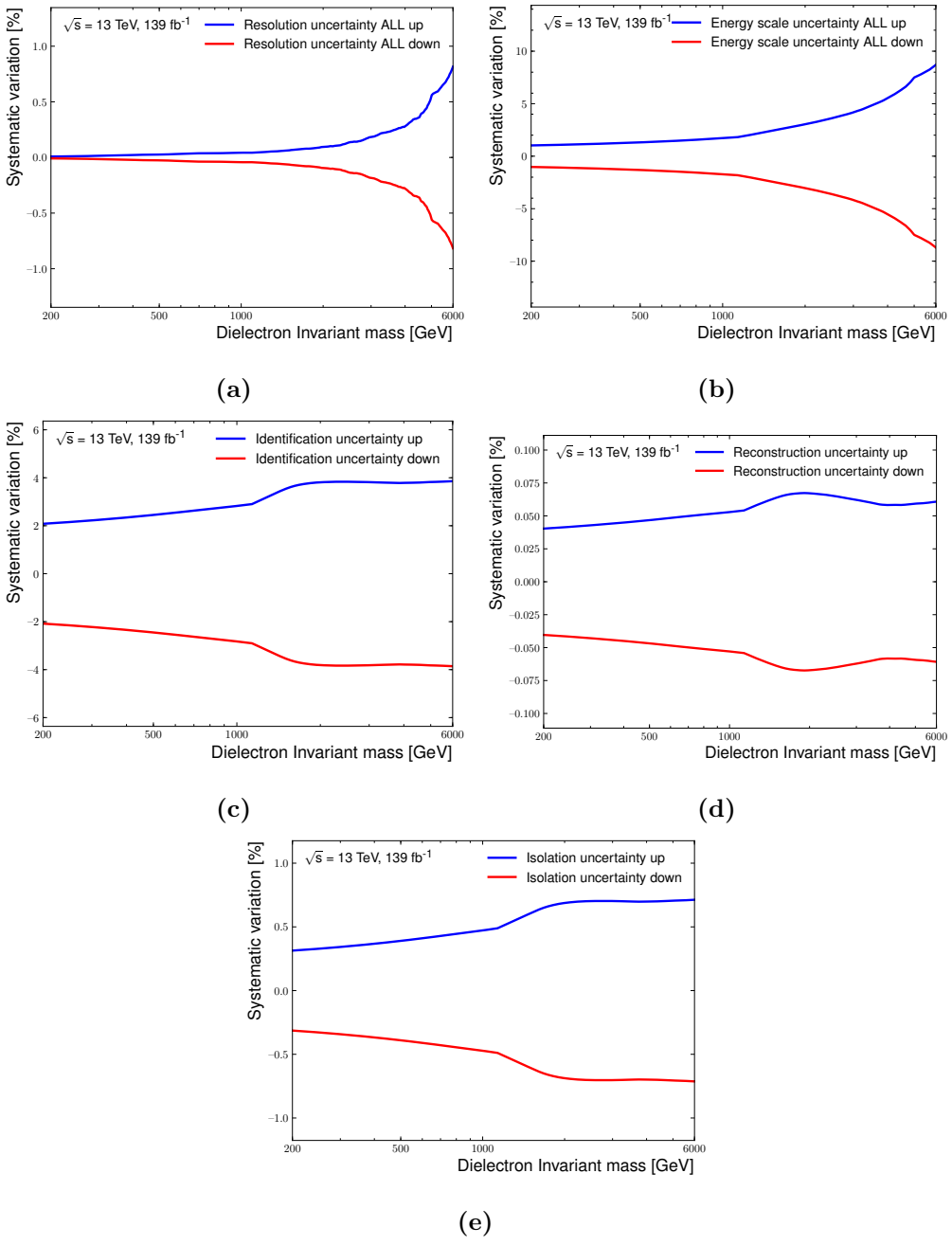

Figure 9.4 Electron systematic uncertainties due to experimental sources. The uncertainty related to electron energy resolution (a), energy scale (b), identification (c), reconstruction (d) and isolation (e) are shown.

9.2 Theoretical uncertainties

The theoretical uncertainties on the simulated samples are only used to determine the uncertainty of the background modelling. High-energy searches like the one described in this thesis probe previously uncharted kinematic regions as their mass predictions extend to TeV energy scales. Therefore, a detailed understanding of systematic uncertainties related to the knowledge of the partonic structure of the proton is required. The kinematic range probed extends beyond the range where the PDF is calculated from in data. The uncertainties related to the PDF are separated into those which arise from the variations of the eigenvectors fo the PDF, the choice of the PDF with respect to other available PDFs, referred to as PDF choice uncertainty, and the scale uncertainties associated with the EW and and strong coupling constants. Additionally, the uncertainty on the top-quark and diboson background is also summarised in below.

PDF eigenvector uncertainties

The PDF uncertainties are studied for the leading DY background. Each available PDF has a set of independent parameters known as eigenvectors associated with it. These eigenvectors can be varied in orthogonal directions to quantify systematic uncertainties associated with a PDF set. For each eigenvector variation at the 90% Confidence Level in the CT10NNLO [124] parameterisation, the DY cross-section is calculated at NNLO as a function of $m_{\ell\ell}$. The eigenvector variation uncertainty is taken as the relative deviation of the cross-sections of the PDF resulting from the eigenvector variations and the nominal PDF. For each $m_{\ell\ell}$ bin in a histogram, the asymmetric uncertainty on the cross-section is obtained using

$$\begin{aligned} \Delta\sigma^{+} &= \sqrt{\sum_{i=1}^{n} \mathrm{Max}\left(\sigma_i^{+} - \sigma_0, \sigma_i^{-} - \sigma_0, 0\right)}, \\ \Delta\sigma^{-} &= \sqrt{\sum_{i=1}^{n} \mathrm{Max}\left(\sigma_0 - \sigma_i^{+}, \sigma_0 - \sigma_i^{-}, 0\right)}, \end{aligned} \tag{9.1}$$

where n is the number of PDF eigenvectors, $\sigma_i^{+/-}$ is the cross-section for the higher and lower values for the corresponding PDF eigenvector variation, and σ_0 is the cross-section for the

central value for the PDF. A total of seven eigenvector variations are considered in this analysis. The total asymmetric uncertainty at each invariant mass bin is calculated using the above equation. The effects of the PDF eigenvector variations is shown in Figures 9.5 and 9.6. The eigenvector variations result in large changes in the shape of the invariant-mass distributions. The uncertainties show a large increase at high invariant-masses indicating the poor theoretical understanding of the PDF in the high-energy regime.

PDF choice uncertainty

The uncertainty related to the choice of PDF is determined by comparing the central value of CT10NNLO PDF to similar PDFs. Two alternatives for the nominal PDF are considered, the NNPDF3.0 and HERAPDF20 PDFs. At low masses $< 3\,\text{TeV}$ the PDF sets are in good agreement. At invariant masses $< 3\,\text{TeV}$ the PDF sets are in good agreement. However, at higher masses, the PDFs begin to diverge, with some PDF enveloped becoming very large. When the PDF difference between the nominal PDF and an alternative is larger than the uncertainty related to the PDF eigenvector variations, the maximum deviation of the envelope of the comparisons is taken as the PDF choice uncertainty. Figure 9.7 depicts the PDF choice uncertainty comparing the nominal PDF to NNPDF3.0 and HERAPDF20 in the electron and muon channels. The figure shows the agreement between the PDFs at low-masses, where the uncertainty is small, and a large increase at high invariant-mass indicating the point at which the PDFs start to diverge from their predictions. Similar to the PDF eigenvector uncertainties there is a significant change in shape of the uncertainties shown in the figure.

PDF scale uncertainty

The uncertainty on the PDF scales are calculated by varying the factorisation and renormalisation scales of the nominal PDF simultaneously by a factor of two. The resulting maximum variations are taken as the PDF scale uncertainties. Figure 9.8 shows the effects of the scale uncertainty on the invariant mass distribution for the electron and muon channels.

Uncertainties on the PDF also arise from the uncertainty of the strong coupling constant, α_s. The uncertainty associated with α_s is accounted for by studying the effect of changing α_s by ± 0.003. The nominal value of 0.118 is taken for α_s in the cross-section calculation [142].

The combination of EW and QCD corrections is not fully known. Therefore, the EW correction systematic uncertainty was calculated by comparing the additive $(1 + \delta_{EW} + \delta_{QCD})$ versus factored $((1+\delta_{EW})(1+\delta_{QCD}))$ computation of the EW k-factor. The difference between the two methods is taken as the uncertainty. The additive computation is used to obtain the nominal invariant mass distribution used in the search.

Figure 9.9 show the uncertainties due to the EW and strong coupling constant on the invariant mass distributions for the electron and muon channels. The impact of the uncertainties are smaller compared to the eigenvector and PDF choice uncertainties.

Top-quark and diboson background uncertainty

An uncertainty arises from the cross-section to which the top and diboson samples are normalised to. The normalisation uncertainty for the top background is estimated to be a 4% [130]. The uncertainty on the diboson production cross-section is estimated to be between 5% and 10% [143]. A conservative normalisation uncertainty of 10% is assigned to the diboson background. Since both uncertainties are normalisation uncertainties with a flat change of the invariant-mass distribution, the impact on the data-driven background estimate is expected to be negligible.

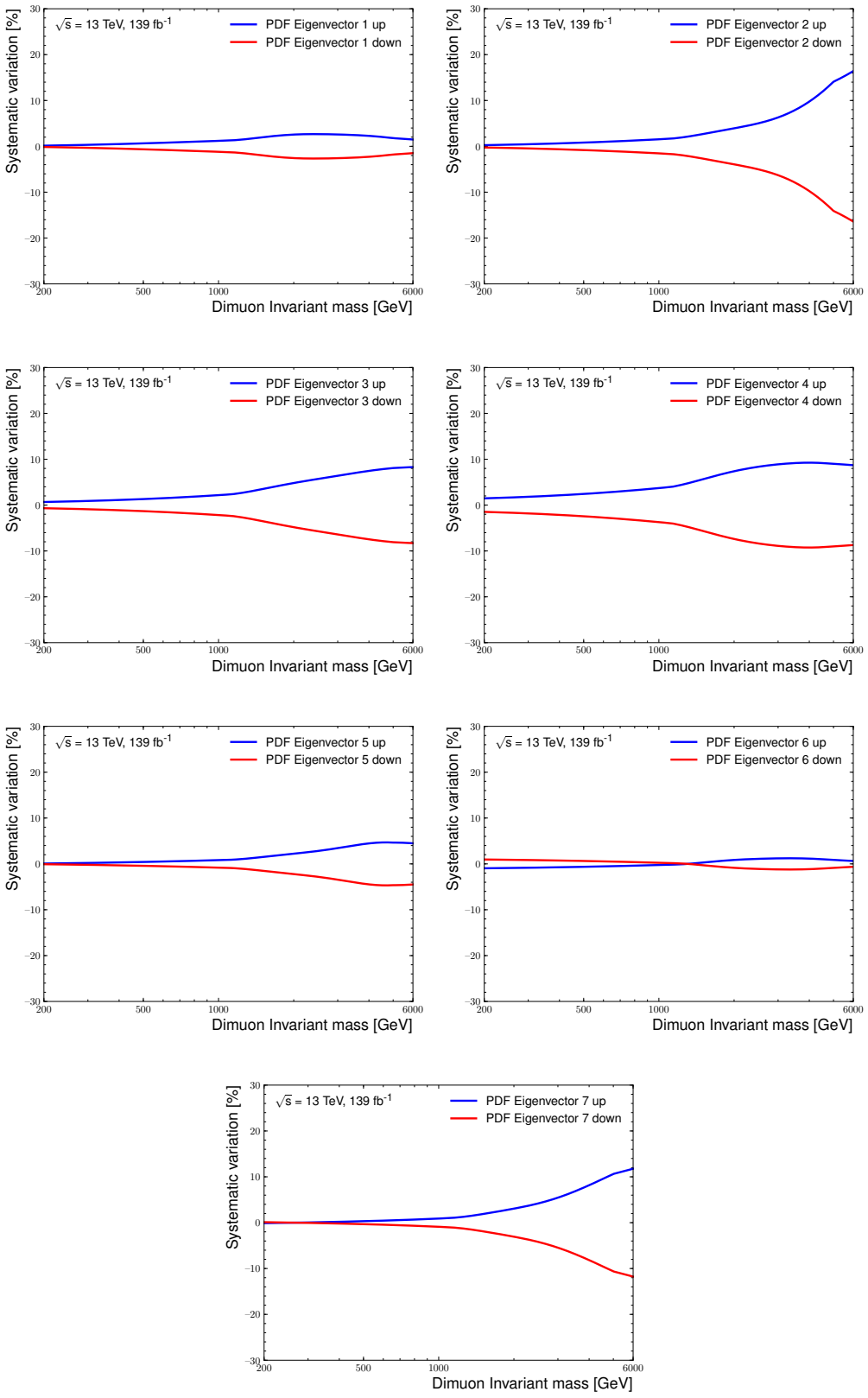

Figure 9.5 Systematic uncertainties due to theoretical sources in the muon channel. The uncertainties corresponding to the seven eigenvector variations of the CT10NNLO PDF are shown in the figure.

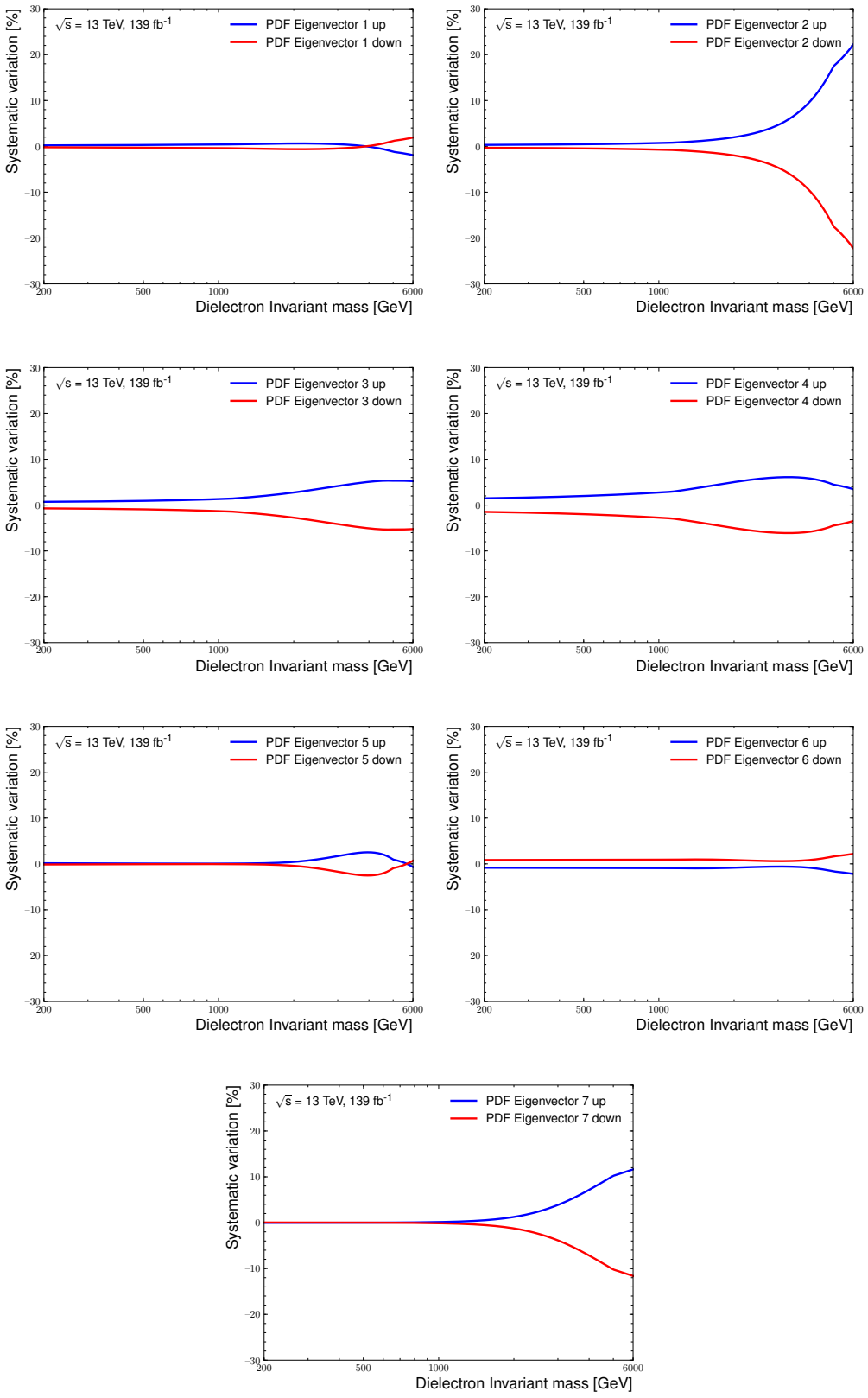

Figure 9.6 Systematic uncertainties due to theoretical sources in the electron channel. The uncertainties corresponding to the seven eigenvector variations of the CT10NNLO PDF are shown in the figure.

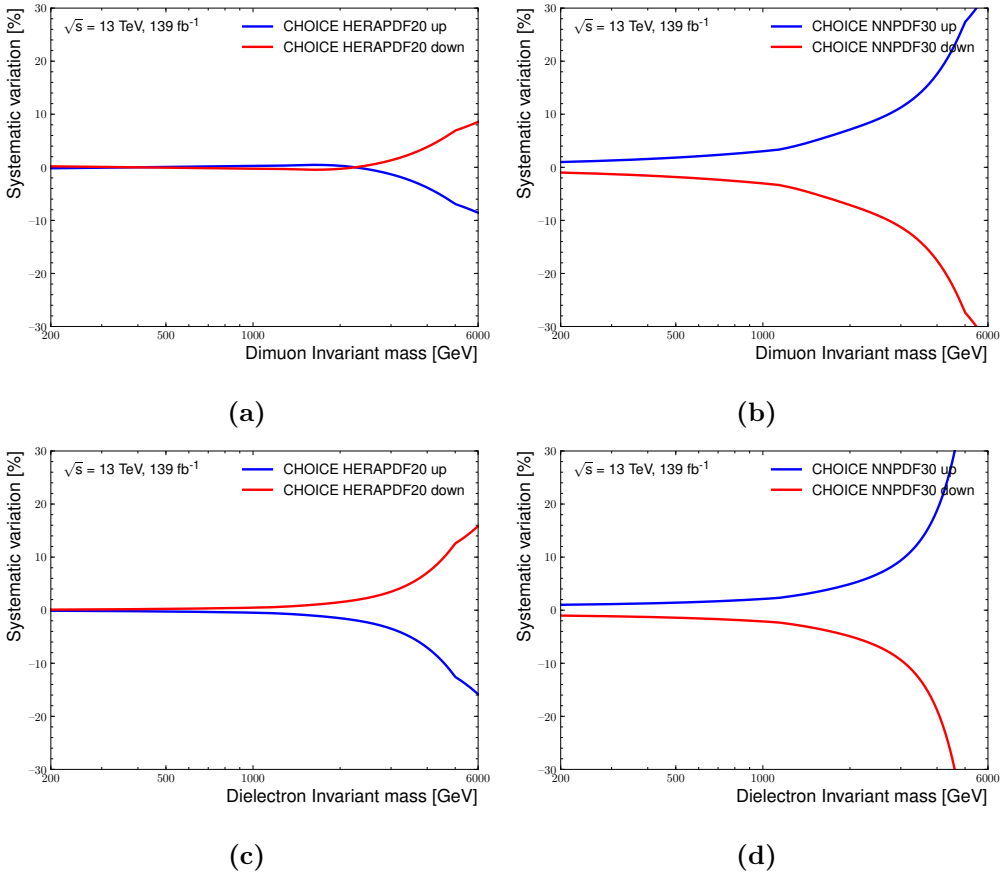

Figure 9.7 Systematic uncertainties due to the choice of the nominal with respect to HERAPDF20 (a)/(b) and NNPDF30 (c)/(d) in the muon and electron channels, respectively.

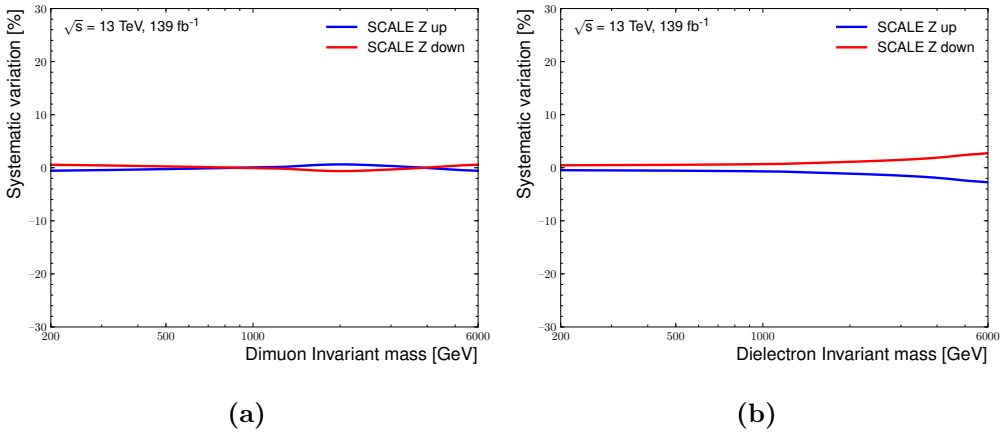

Figure 9.8 Systematic uncertainties due to factorisation and renormalisation scales of the CT10NNLO PDF in the muon (a) and electron (b) channels.

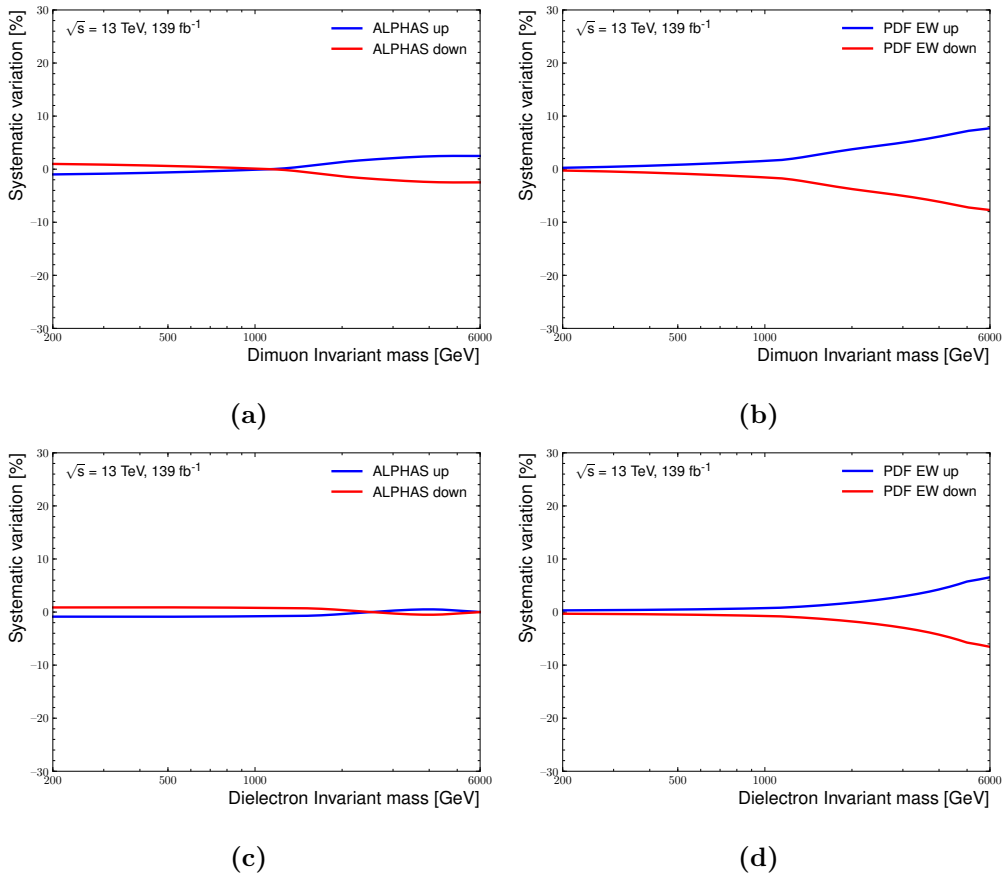

Figure 9.9 Systematic uncertainties due to corrections applied to the CT10NNLO PDF. The uncertainty related to the strong coupling constant (α_s) (a)/(b) and EW (c)/(d) corrections in the electron and muon channels, respectively.

Chapter 10

Data-driven background estimation

This section outlines the procedure for the estimation of the background using the data-driven extrapolation approach. The procedure is motivated in chapter Section 10.1. There are several challenges involved with the method. One challenge is the choice of function picked to model the fit in the low-mass CR and extrapolation to the high-mass SR. An optimisation procedure is performed in two consecutive steps. The first involves the choice of the fit function. An initial sample of 25 functions are validated in a set of potential CR and SR. The method used to chose the functional form is outlined in Section 10.2. A signal+background function is defined in Section 10.3, which is used to validate the CR and SR choice. Once the function is fixed, the CRs and SRs are optimised to maximise sensitivity and reduce the bias of the background estimation. The optimisation procedure is described in Section 10.4. All fits are performed within the RooFit [137] framework.

10.1 Motivation

The previous ATLAS search for non-resonant signals in the dilepton invariant-mass spectra was published with 36.1 fb^{-1} [2]. The analysis used a MC template based approach to model the background contributions. The dominant uncertainties in the analysis were were from systematic uncertainties on the PDF, which are described in Chapter 9. These uncertainties are estimated using unintuitive methods, and in some cases provide an overestimate of the possible

uncertainty associated with a particular PDF. The impact of these uncertainties lowers the sensitivity of the search by large factor. In addition, it is expected that if the knowledge of the PDFs do not improve, future analyses that reach higher-energy regimes will be even less sensitive as the uncertainty associated with the PDFs are expected to be even larger.

Furthermore, the analysis performed with $36.1\,\text{fb}^{-1}$ of data encountered several problems associated with limited MC statistics, causing delays and compromising the sensitivity. Therefore, ad-hoc smoothing procedures were applied on some of the MC samples using functional fits that resulted in additional uncertainties. To produce adequate statistics for the MC at the full Run-2 luminosity of $139\,\text{fb}^{-1}$ would require significantly larger samples to be produced and to produce adequate MC statistics for Run-3 ($300\,\text{fb}^{-1}$) or High-luminosity LHC ($3000\,\text{fb}^{-1}$) would result in an extraordinary strain on the available computing resources.

To avoid the effects of the unintuitive PDF uncertainties and the limited MC statistics, the analysis adopted a data-driven background modelling strategy. Instead of a MC background estimate, a functional form is used. In doing this, the requirement to produce larger MC samples is significantly reduced and the theoretical uncertainties from the MC are replaced with statistical uncertainties originating from the parameters of the functional form used. This in turn can be understood in a well-defined way. Additionally, it is expected that as the luminosity of the dataset increases the statistical uncertainties associated with the fit will be reduced.

It has been shown previously by the dilepton resonance search [3] and diphoton searches [144, 145] that similar background shapes to the one in this search can be modelled with a suitable function. The fits are constrained in the low-mass regions, where there is an abundance of statistics to provide a reliable background description. However, a fit performed over the full invariant mass spectrum would potentially bais the background estimation, as the fit would attempt to accommodate the broad deviations in the invariant-mass spectrum resulting from non-resonant signals. Therefore, an extrapolation procedure is used to mitigate this effect by relying on the low-mass CR to constrain the extrapolation. The background function is fit in a low-mass CR, and the resulting fit is extrapolated to a high-mass SR. An illustration of the extrapolation procedure outlining the CR and SR is shown in Figure 10.1.

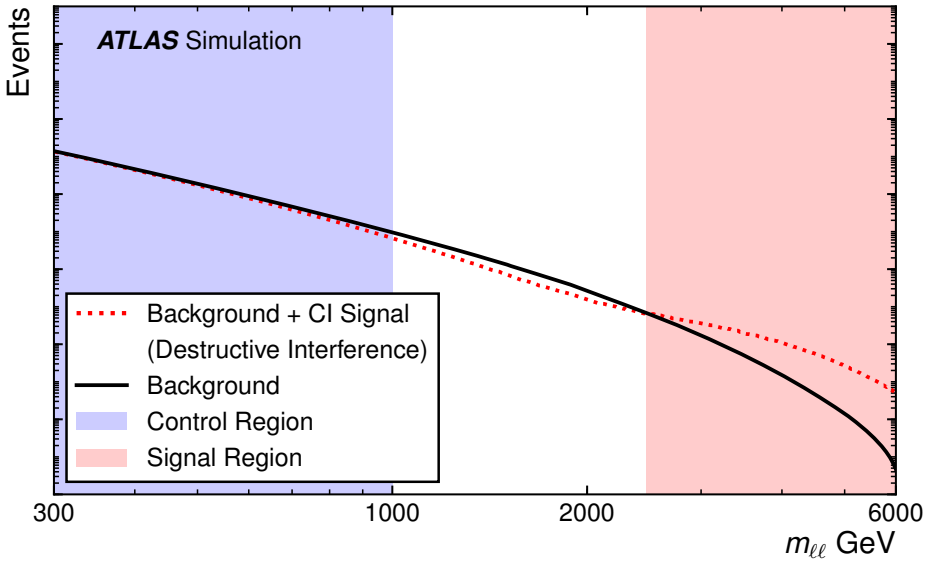

Figure 10.1 A schematic illustration of the possible mass ranges in this analysis. The monotonically falling total background shape is shown by the solid black line, while an example of a CI signal plus the total background shape is shown by the dotted red line. The CI signal is shown after the DY process has been subtracted to show only the interference and pure CI process.

10.2 Background fit function choice

The background function is chosen from a variety of different candidates for its stability during the extrapolation procedure and the ability to accurately model the invariant mass distributions of the e^+e^- and $\mu^+\mu^-$ channels. Each function is fit to the background dilepton invariant mass template, produced by summing together the contributions from all the background processes, in a variety of different CRs and extrapolated to the corresponding SRs. The distribution of the pulls, defined as (fit-simulation)/fit, is obtained for each invariant mass bin for all initial CR and SR ranges considered. Functions which have pulls below two in the CR and SRs pass the initial selection. The functions are also required to have a flat distribution of pulls across the invariant-mass spectrum. These requirements ensures that functions which exhibit unphysical behaviour in the high-mass regions of the invariant mass spectrum are vetoed. Additionally, it ensures that good modelling of the simulated shape in the CR is maintained. There were a possible three functions which satisfied the above conditions. Regardless of the choice of final

function, each function that satisfies the initial selection criteria will have inherent weaknesses in their bias and performance. These are then measured and taken into account as uncertainties, described in Chapter 11. The final function was chosen out of the subset of functions to be consistent with the resonance analysis [3]. The final fit function is given by

$$\begin{aligned} f_{\mathrm{b}}(m_{\ell\ell}) &= f_{\mathrm{BW},Z}(m_{\ell\ell}) \cdot \left(1 - x^{c}\right)^{b} \cdot x^{\sum_{i=0}^{3} p_i \log(x)^i}, \\ f_{\mathrm{BW},Z}(\mathrm{m}_{\ell\ell}) &= \frac{\Gamma_Z}{\left(m_Z - \mathrm{m}_{\ell\ell}\right)^2 + \Gamma_Z^2}, \end{aligned} \tag{10.1}$$

where $x = m_{\ell\ell}/\sqrt{s}$, $f_{\mathrm{BW},Z}(m_{\ell\ell})$ is a non-relativistic Breit–Wigner function with $m_Z = 91.1876\,\mathrm{GeV}$ and $\Gamma_Z = 2.4952\,\mathrm{GeV}$ [146], $(1 - x^c)^b$ ensures that the background fit evaluates to zero as $x \to 1$, to be consistent with the expectation from the collision energy of the LHC. Both b and c are constants that have been evaluated based on pre-fits performed on the full background template. The p_i parameters, with $i = 0, 1, 2, 3$, are left as free parameters to be informed by the fit. The term $x^{\sum_{i=0}^{3} p_i \log(x)^i}$ has been studied in detail and accepted as a good approximation to model distributions with similar smoothly falling spectra [3, 144, 145].

The fits to the data and simulation are both performed with a bin width of 1 GeV. The function $f_b(m_{\ell\ell})$ is treated as a probability density in the fits performed to the CR. It is normalised in the CR to the number of events in the CR (N_{CR}) of the template being fit. Figure 10.2 shows an example of background-only fits to the electron and muon channel in a CR and SR configuration. The plots are shown using constant $\log(\mathrm{m}_{\ell\ell})$ binning for presentation purposes, as the linear binning used to perform the fits are difficult to interpret clearly. The figures show flat pulls below one for the electron and muon channels, indicating good modelling of the background distributions.

Examples of functions that were considered are given in Table 10.1, with their corresponding fits to the data shown in Figure 10.3. Figure 10.3a depicts a function fit that is close to satisfying the function choice selection. However, it poorly models the extrapolated region compared to the function defined in Equation 10.1. Figure 10.3b shows a function that does not satisfy the the requirement that the pulls are below 1 and flat throughout the invariant mass

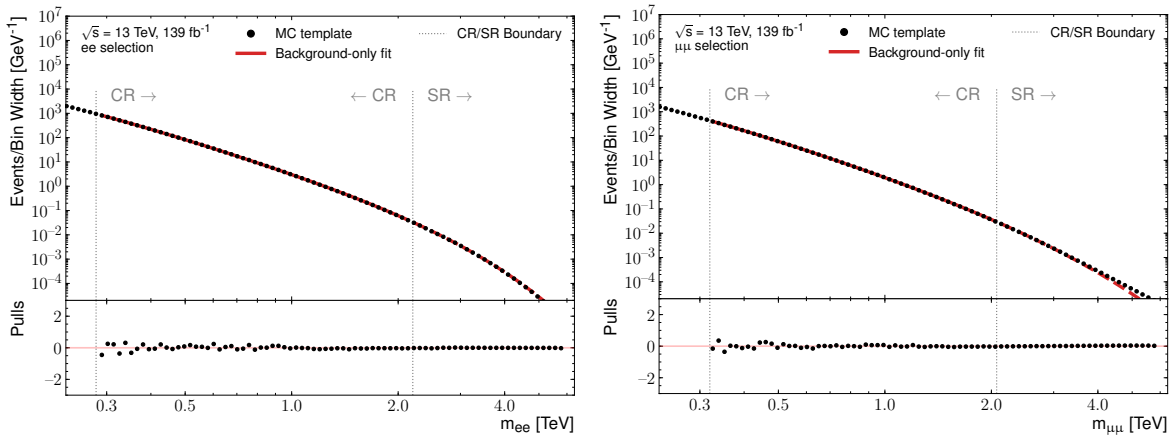

Figure 10.2 Fit to the simulated background template in the electron (left) and muon (right) channels shown in the top pad. The bottom pad shows the pulls of the fit. The CR and SR boundaries are also shown in the figure. The background template points are plotted at the centre of each bin as the number of events divided by the bin width, which is constant in $\log(m_{\ell\ell})$.

distribution. Nonphysical behaviour in the fit and extrapolation can be seen in Figure 10.3c. Figure 10.3d was not selected due to poor modelling of the CR.

	Function definition
1	$(1-x^5)^{\mathrm{p0}} * (x^{(\mathrm{p1}+\mathrm{p2}*\log(x)})$
2	$(1-\log(e*x^{\mathrm{p1}}) + c1*x*e^{\mathrm{p2}/(1+x^{\mathrm{p3}})}$
3	$(x)^{\mathrm{p1}} * e^{\mathrm{p2}*x}$
4	$(1-x)^{\mathrm{p1}} * e^{\mathrm{p2}*x^2}$

Table 10.1 List of functions considered for fit to dilepton spectrum that did not pass the criteria required. x is defined to be $= m_{\ell\ell}/\sqrt{s}$.

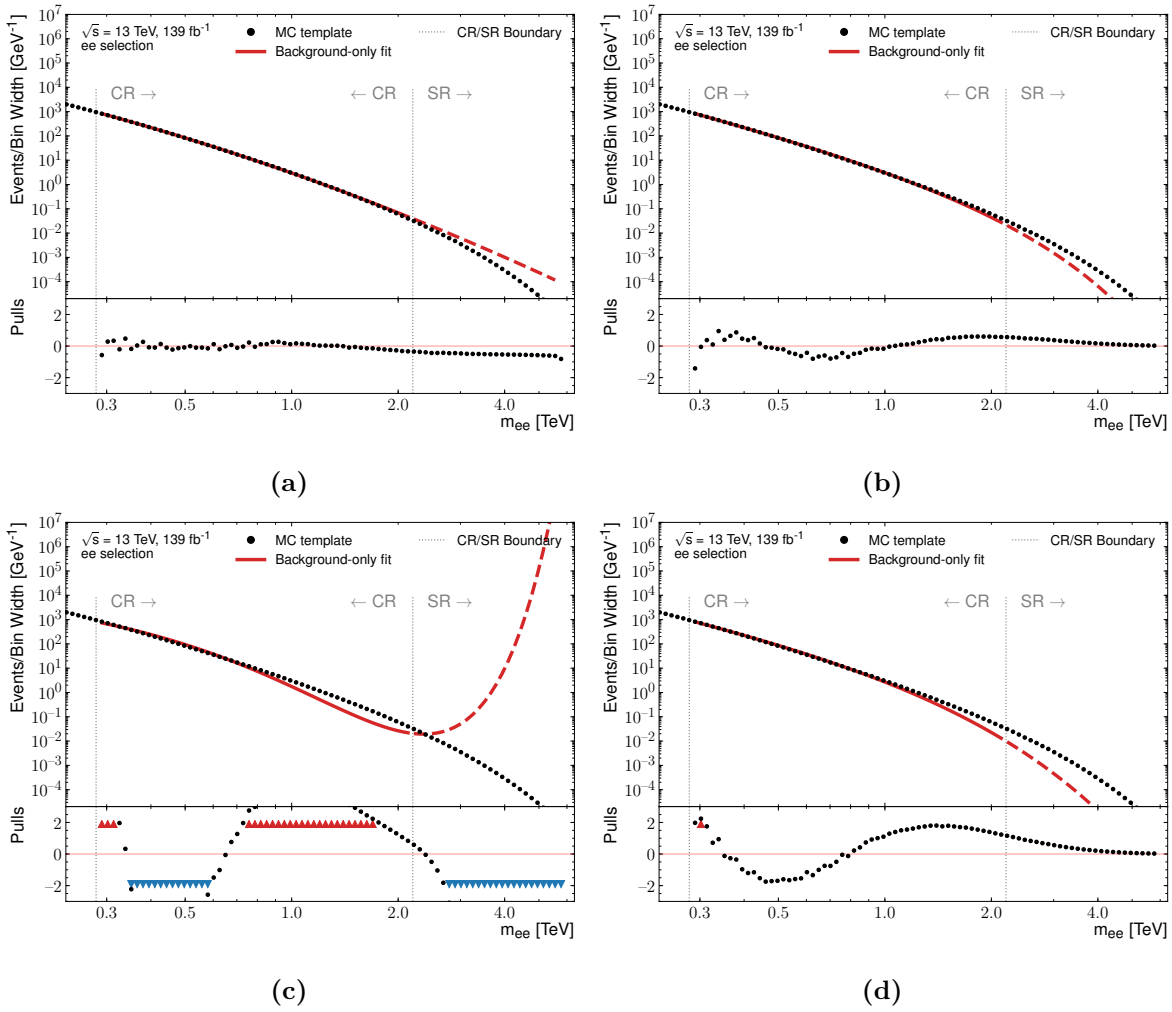

Figure 10.3 Fits using functions that failed the function choice criteria, to the simulated background template in the electron channel shown in the top pad. Figures (a), (b), (c) and (d) correspond to functions 1, 2, 3, and 4 in Table 10.1, respectively. The bottom pad shows the pulls of the fit. The CR and SR boundaries are also shown in the figure. The background template points are plotted at the centre of each bin as the number of events divided by the bin width, which is constant in $\log(m_{\ell\ell})$.

10.3 Signal+background function

The CR choice is validated using a signal+background function in order to avoid bias from possible signal contamination in the CR. The signal+background function is used in *signal injection* tests and to validate the background-only function once the CR and SR choice has been finalised. The signal injection tests are used in the optimisation process, described in Section 10.4, in order to choose a CR and SR configuration that will not be biased by the presence of signals. A collection of signal samples at various Λ values are injected into the background template, and the effect on the background estimation from the fit and extrapolation is checked. The signal+background function is formed by adding a signal component is added to Equation 10.1 to give

$$f_{\mathrm{b+s}}(m_{\ell\ell}, \Lambda) = N_{\mathrm{b}} \cdot f_{\mathrm{b}}(m_{\ell\ell}) + N_{\mathrm{s}}(\Lambda) \cdot f_{\mathrm{s}}(m_{\ell\ell}, \Lambda), \tag{10.2}$$

where $f_{\mathrm{s}}(m_{\ell\ell}, \Lambda)$ is the signal probability density function and $N_{\mathrm{s}}(\Lambda)$ is the number of signal events in the CR. Both $f_{\mathrm{s}}(m_{\ell\ell}, \Lambda)$ and $N_{\mathrm{s}}(\Lambda)$ are determined from simulation. The morphing procedure, described in Section 8.2.2, is used to obtain a smooth description of a given CI model as function of Λ, allowing to determine the signal contribution that fall between the fixed signal shapes from simulation. The parameter N_{b} is the number of background events in the CR, where the total number of events in the CR is given by $N_{\mathrm{b}} + N_{\mathrm{s}}(\Lambda) = N_{\mathrm{CR}}$.

Figure 10.4 depicts signal+background fits to a background template injected with a CI interaction signal at $\Lambda = 26\,\mathrm{TeV}$ in the electron and muon channels. The background component of the signal+background fit is separated and compared with the background template, and the pulls are calculated. The figure shows that the background component of the signal+background fit is not biased by the presence of a signal in the CR.

10.3.1 Signal injection tests

Signal injection tests are used to validate the requirement that the signal+background function can provide an accurate background estimate, regardless of the presence of a signal in the CR.

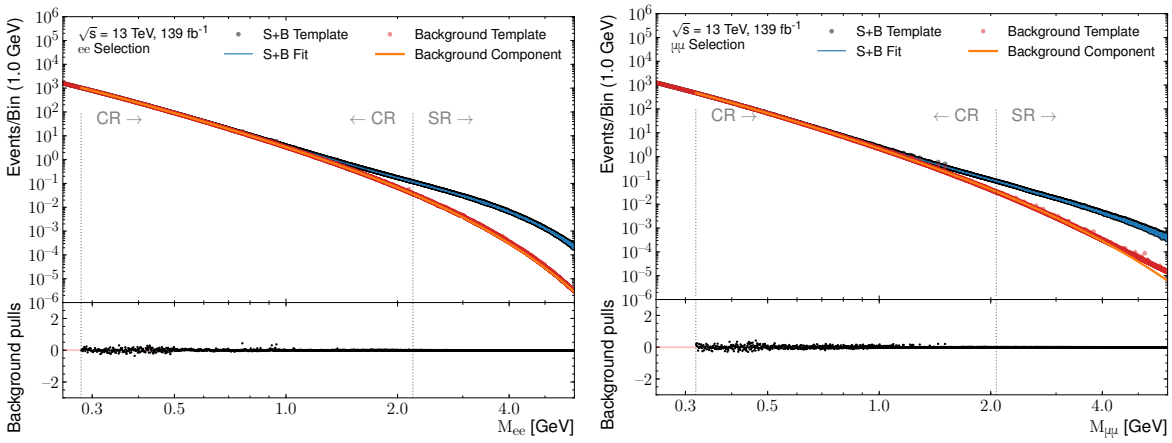

Figure 10.4 Signal+background (S+B) fit to the simulated template injected with a CI signal at $\Lambda = 26\,\text{TeV}$ in the electron (left) and muon (right) channels shown in the top pad. The background template and the background component of the S+B fit corresponds to the blue and red lines, respectively. The background template (red data-points) is injected with a CI signal to form the signal+background template (blue data-points). The bottom pad shows the pulls of the background component of the fit compared to the background template. The CR and SR boundaries are shown in the figure.

The robustness of the signal+background function is validated by quantifying the deflection of the function in the presence of an injected signal in the template. The signal+background function is fit to signal+background MC templates, consisting of the MC background-only template injected with CI models in a range of Λ values. The background expectation from the signal+background function is compared to the background-only MC template in these tests.

Figures 10.5 to 10.8 depict the injection tests in the electron and muon channel for the different chiral and interference models considered. The final CR and SR choices are used to depict the performance of the signal+background function. The figures show that the background estimate from the signal+background function fit does not change significantly in the presence of injected CI signals, and is consistent with the background estimate from fitting the background-only MC template. Statistical fluctuations in the injected signals cause small discrepancies between background estimates, for e.g. Figure 10.5. Additionally, the presence of a destructive interference CI signal can result in the function under-fitting the background distribution, resulting in a lower estimated background compared the fit without an injected

signal. This is due to the destructive component of the interference model. However, the effect is small and well within the uncertainties of the estimated background. The signals are injected from $\Lambda = 18\,\text{TeV}$ to $40\,\text{TeV}$.

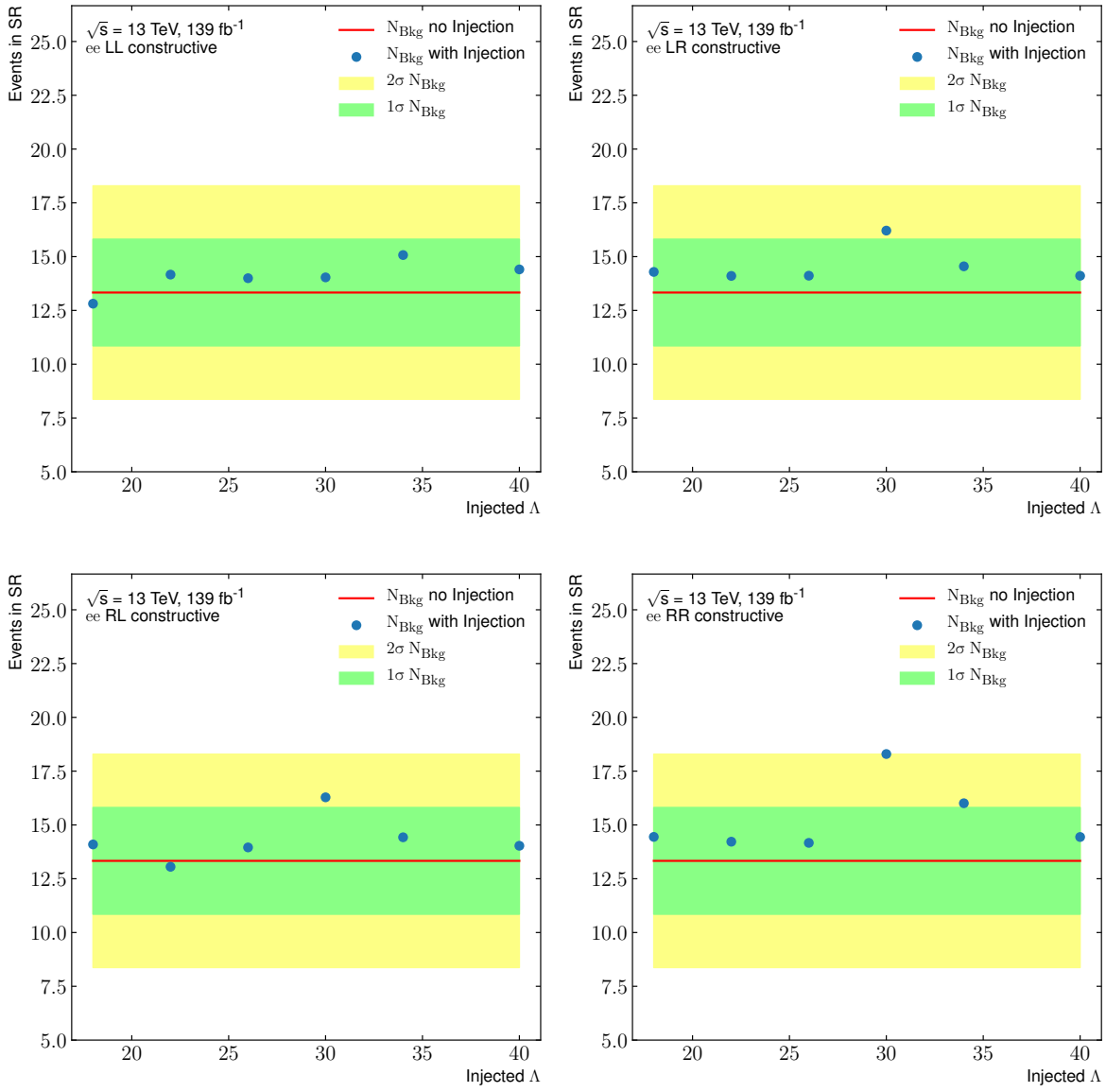

Figure 10.5 Signal injection tests in the electron channel. The background expectation in the SR for the signal+background function is compared for fits to the background template with injections of various chiral CI signals from $\Lambda = 18\,\text{TeV}$ to $40\,\text{TeV}$. The LL, LR, RL, and RR chiral constructive interference models are injected. The background estimation from the fit to the background MC template with its associated uncertainty is also shown.

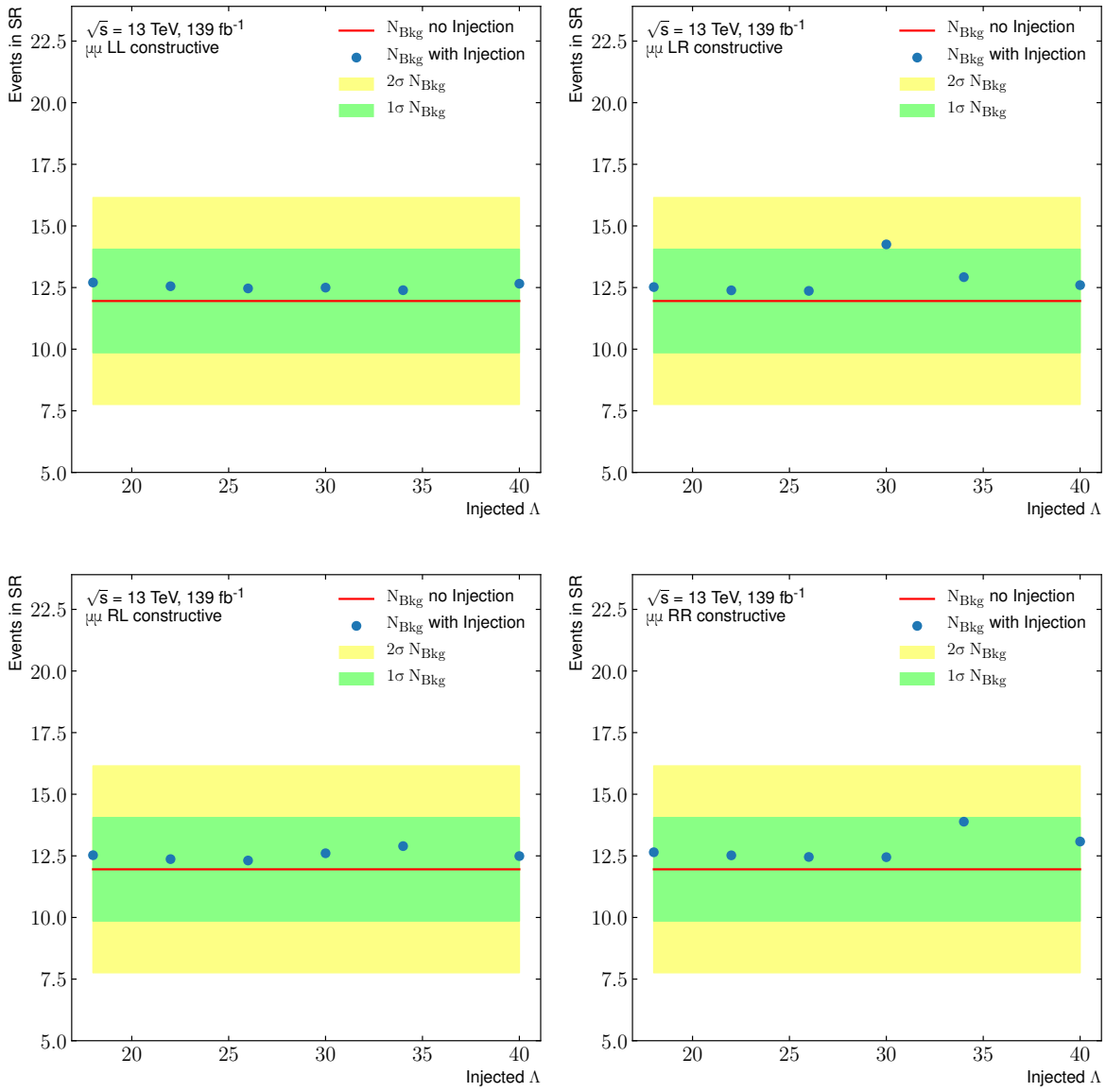

Figure 10.6 Signal injection tests in the muon channel. The background expectation in the SR for the signal+background function is compared for fits to the background template with injections of various chiral CI signals from $\Lambda = 18\,\text{TeV}$ to $40\,\text{TeV}$. The LL, LR, RL, and RR chiral destructive interference models are injected. The background estimation from the fit to the background MC template with its associated uncertainty is also shown.

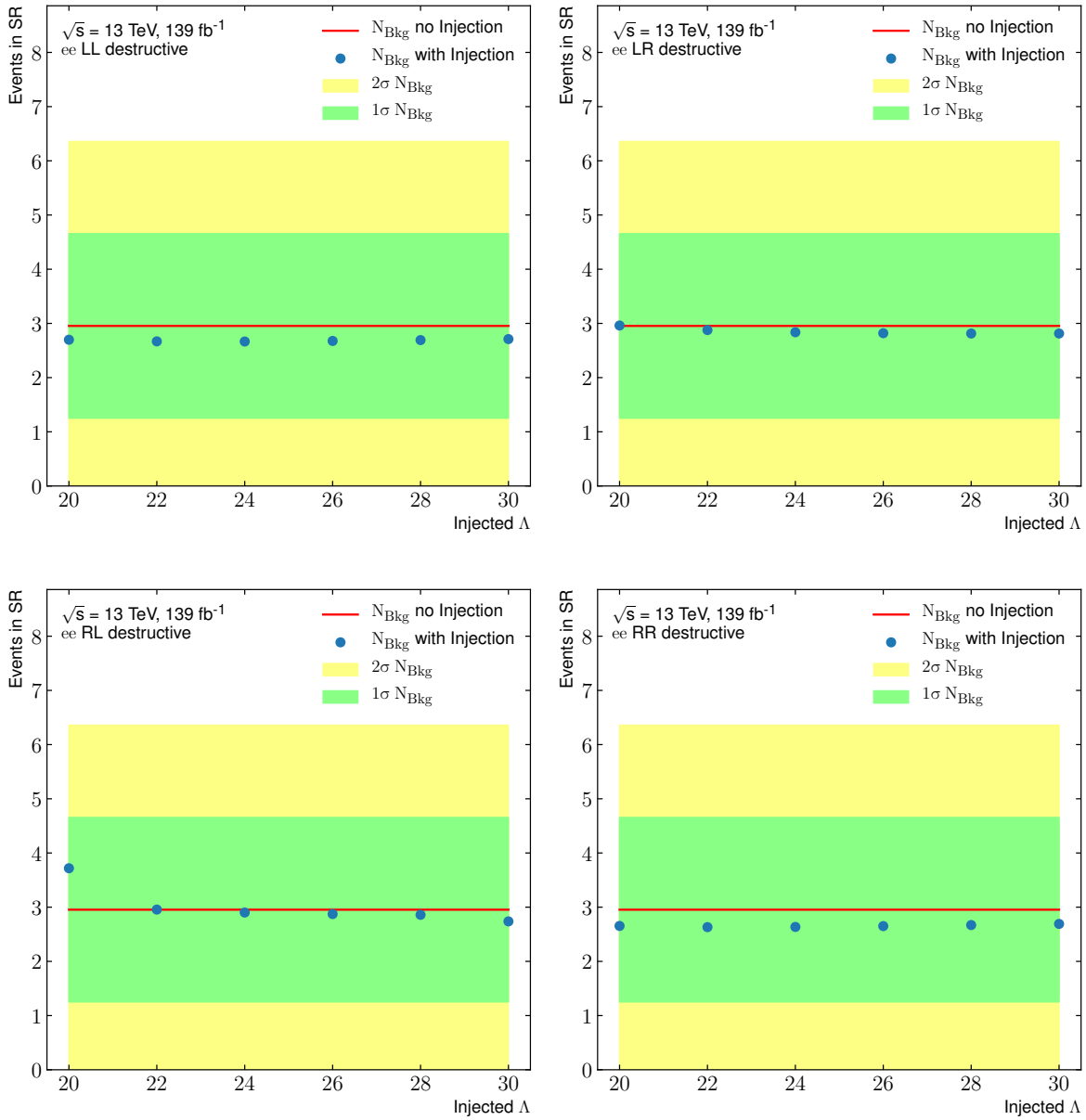

Figure 10.7 Signal injection tests in the electron channel. The background expectation in the SR for the signal+background function is compared for fits to the background template with injections of various chiral CI signals from $\Lambda = 18\,\text{TeV}$ to $40\,\text{TeV}$. The LL, LR, RL, and RR chiral constructive interference models are injected. The background estimation from the fit to the background MC template with its associated uncertainty is also shown.

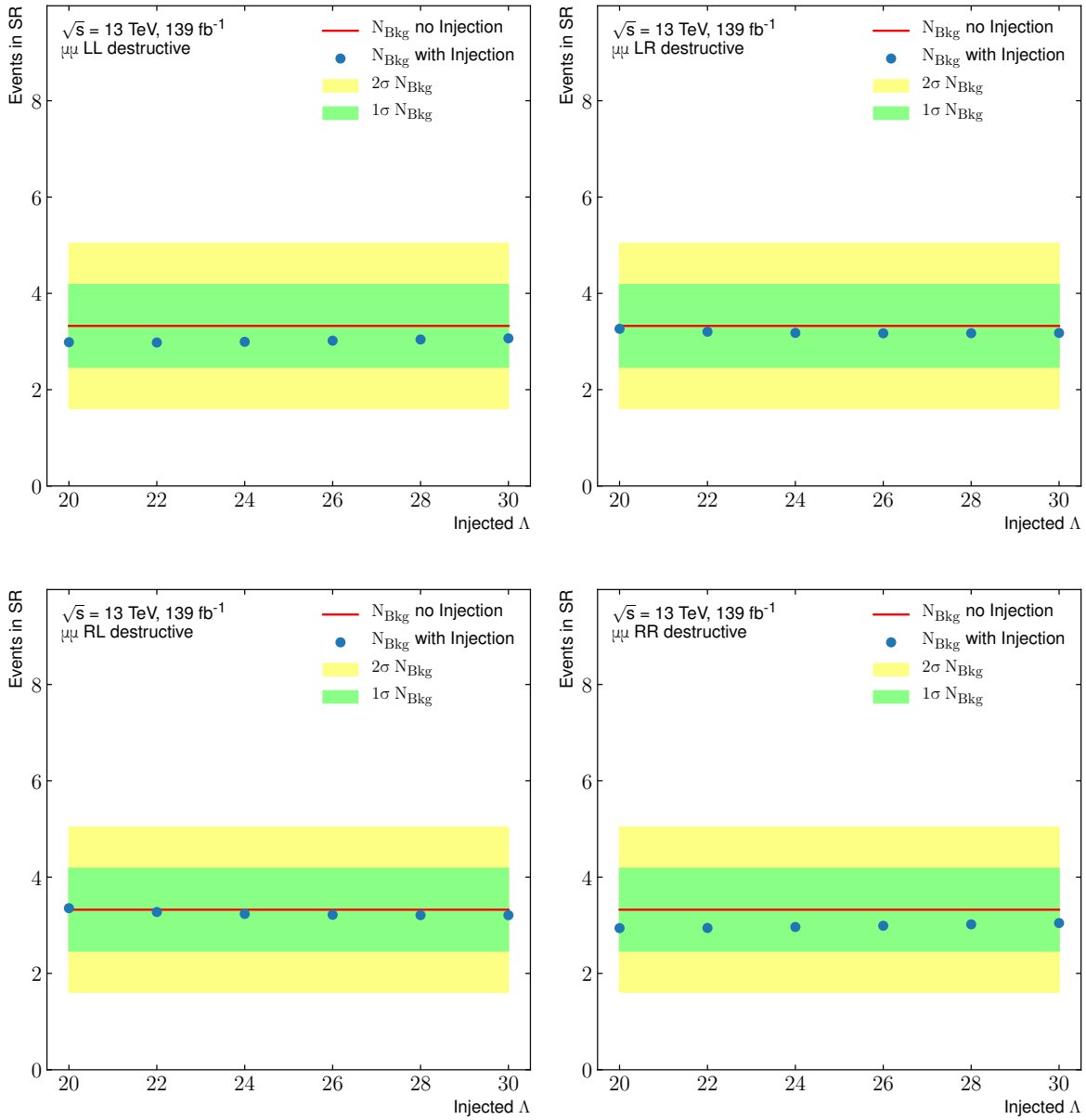

Figure 10.8 Signal injection tests in the muon channel. The background expectation in the SR for the signal+background function is compared for fits to the background template with injections of various chiral CI signals from $\Lambda = 18\,\text{TeV}$ to $40\,\text{TeV}$. The LL, LR, RL, and RR chiral constructive interference models are injected. The background estimation from the fit to the background MC template with its associated uncertainty is also shown.

10.4 Optimisation of control and signal regions

The optimisation procedure attempts to maximise the expected sensitivity to CI signals by varying the CR and SR boundaries. For each CI signal model and channel in consideration the lower and upper boundary of the CR ($\mathrm{CR_{min}}$ and $\mathrm{CR_{max}}$), and the lower boundary of the SR ($\mathrm{SR_{min}}$) are varied to maximise sensitivity to CI signals.

The expected limit is used to test the sensitivity to the CI models. The expected limit includes the background uncertainties, described in Chapter 11, and is included in the statistical model following the procedure described in Chapter 4. An optimisation based solely on the expected limit would prefer CRs that extend to higher masses, as shown in Chapter 11. However, extending the CR to high invariant-mass may result in a possible bias to the background expectation from signals present in data. This is addressed by introducing a second criteria based on minimising the linearity of the signal injection tests. The linearity criteria considers the performance of the recovery of signal events across a range of plausible CI signals injected to the MC background template, and is defined as

$$\text{Linearity} = \sum_{\Lambda=\infty}^{\Lambda=18} \frac{N_{S,\mathrm{rec},\Lambda}}{N_{S,\mathrm{inj},\Lambda}} \frac{1}{\mathrm{N_{tot}}}, \tag{10.3}$$

where Λ is the CI energy scale in the injected MC template that is fit, $\Lambda = \infty$ corresponds to the background-only MC template, while $\Lambda = 18$ corresponds to a 18 TeV CI signal injected. $N_{S,\mathrm{inj},\Lambda}$ is the number of injected signal events in the SR, $N_{S,\mathrm{rec},\Lambda}$ corresponds to the recovered number of signals events, defined as the difference between integrals of the signal+background template that is fit and the background expectation of the fit and extrapolation in the SR, $\mathrm{N_{tot}}$ is the number of different signals that are injected, used to normalise the linearity to unity. The signal+background function is used for the linearity tests.

A combination of both the expected limit and the linearity is used to pick a final CR and SR configuration. A balance between the expected limit and linearity is required for an optimal CR and SR configuration. The different chiral and interference CI signal models are considered in the optimisation. The chiral models correspond to LL, LR, RL, and RR, and

the interference models considered are either constructive or destructive. In the destructive interference cases, if the SR includes a significant contribution from the destructive interference component of the CI signal shape, the integral number of expected events in the SR is reduced. Therefore, the optimisation procedure allows for a gap between the CR and SRs to avoid this effect. Additionally, the inclusion of the destructive component of the signal shape in the CR results in a poor linearity when performing the signal injection tests.

Figure 10.9 shows an example of an optimisation plot used to pick the end of the control region and start of the signal region. Each chirality and interference choice of the CI model is tested with an independent CR and SR configuration. It is found that for models with destructive interference a mass gap of 1320 GeV is preferred by the optimisation procedure, while for the constructive interference models, the optimal CR_{max} coincides with SR_{min}. Similar performance is shown for the resulting ranges for the chirality options at the level of few tens of GeV. Therefore, the ranges for the different chiral models are merged, as shown in Table 10.2, to simply the the rest of the analysis.

Channel	Constructive interference			Destructive interference		
	CR_{min}	CR_{max}	SR_{min}	CR_{min}	CR_{max}	SR_{min}
e^+e^-	280	2200	2200	310	1450	2770
$\mu^+\mu^-$	310	2070	2070	320	1250	2570

Table 10.2 Optimised CR and SR ranges (in units of GeV). For all configurations $SR_{min} = 6000$ GeV.

10.5 Validation of the CR and background function

The robustness of the background estimate resulting from the background-only fit to the final CR configurations chosen is also tested. The background estimate from the background-only fit, and its extrapolation for a given CR and SR configuration is required to be unaffected by the possible contamination of a signal in the CR. Therefore, the signal+background function is used to validate the background-only fit and CR choice. The tests are performed on data once

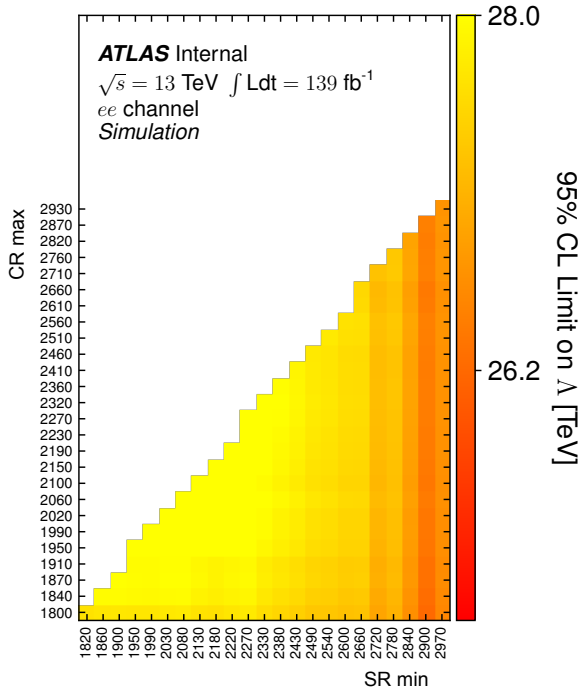

Figure 10.9 Example optimisation scan of the end of the control region (CR_{max}) and start of the signal region (SR_{min}). The Expected limit on the CI interaction energy scale for a contractive interference model is used to optimise the regions. The end point of the signal region is chosen to be 6 TeV.

a CR and SR choice has been chosen following the procedure described in Section 10.4, and the data has been unblinded. This procedure described in the section protects the background-only fit function against unexpected signal contributions in the CR in data.

For a given CR, both the background-only and signal+background functions are fit and the background component of the signal+background fit is compared to the background-only function. If the two background estimates do not differ significantly, then it can be concluded that there is no significant signal contribution present in the CR to bias the background-only fit, and the background-only function can be used. A difference more significant than the uncertainty on the background estimate from the signal+background fit is considered to be large

enough to invalidate a CR choice. Both in the presence and absence of signal, the background component of the signal+background fits are not deflected significantly.

If a significant difference is observed between the two background estimates, then it is concluded that the CR includes an invariant mass range where a signal can impact the background-only fit. It can be concluded due to expected the shape of the non-resonant signals, the bias from the signal is a consequence the CR extending into a high-mass region where the non-resonant signal start to dominate. Therefore, the CR upper edge can be lowered iteratively, each time checking the background estimates from the two fit functions until they agree. A significant difference between the background estimates from the two fit functions is only expected in data if there is CI or other non-resonant signals present. It is also important to note that the SR will remain fixed, and the upper edge of the CR is moved to lower masses, therefore no significant changes be made to the analysis design after unblinding. Additionally, this procedure is will only need to be performed if there is a hint of a possible signal in the CR to invalidate the CR choice.

Examples of test of compatibility of the signal+background and background only fits is shown in Figure 10.10 for the final CR and SR choices, where they have been performed on the background-only MC template. The integrated number of background events in the SR from each fit is shown for the CR and SR configurations. The fits performed on data are shown in Chapter 12. This example depicts a good agreement between the two functions, indicating the background-only function can be used. The uncertainty shown corresponds to the uncertainty on the background estimate from the signal+background fit. The uncertainty on the background-only fit is not included as the main objective is to compare the central value of the background estimate from background-only fit to the signal+background fit. Any difference observed between the two background estimates will be used as an additional uncertainty on the background estimate. Further detail on the estimation of background function uncertainties are given in Chapter 11.

To show an example when there is a significant signal contribution present in the CR, the background estimate resulting from the two functions is compared when a signal has been

injected in an invalid CR choice. This is shown in Figure 10.11. A CI signal corresponding to $\Lambda = 18\,\text{TeV}$ is injected into the MC background template. The CR in this example was chosen to be between 200 GeV and 3500 GeV to exaggerate the effects on the background estimate. The background estimate from the background only fit is significantly deflected due to an excess of signal events in the CR. Figure 10.12 shows the fit distributions of the background-only and signal+background fit when a signal has been injected. When a signal is injected, the background-only fit attempts to accommodate the injected signal, resulting in a incorrect background estimate.

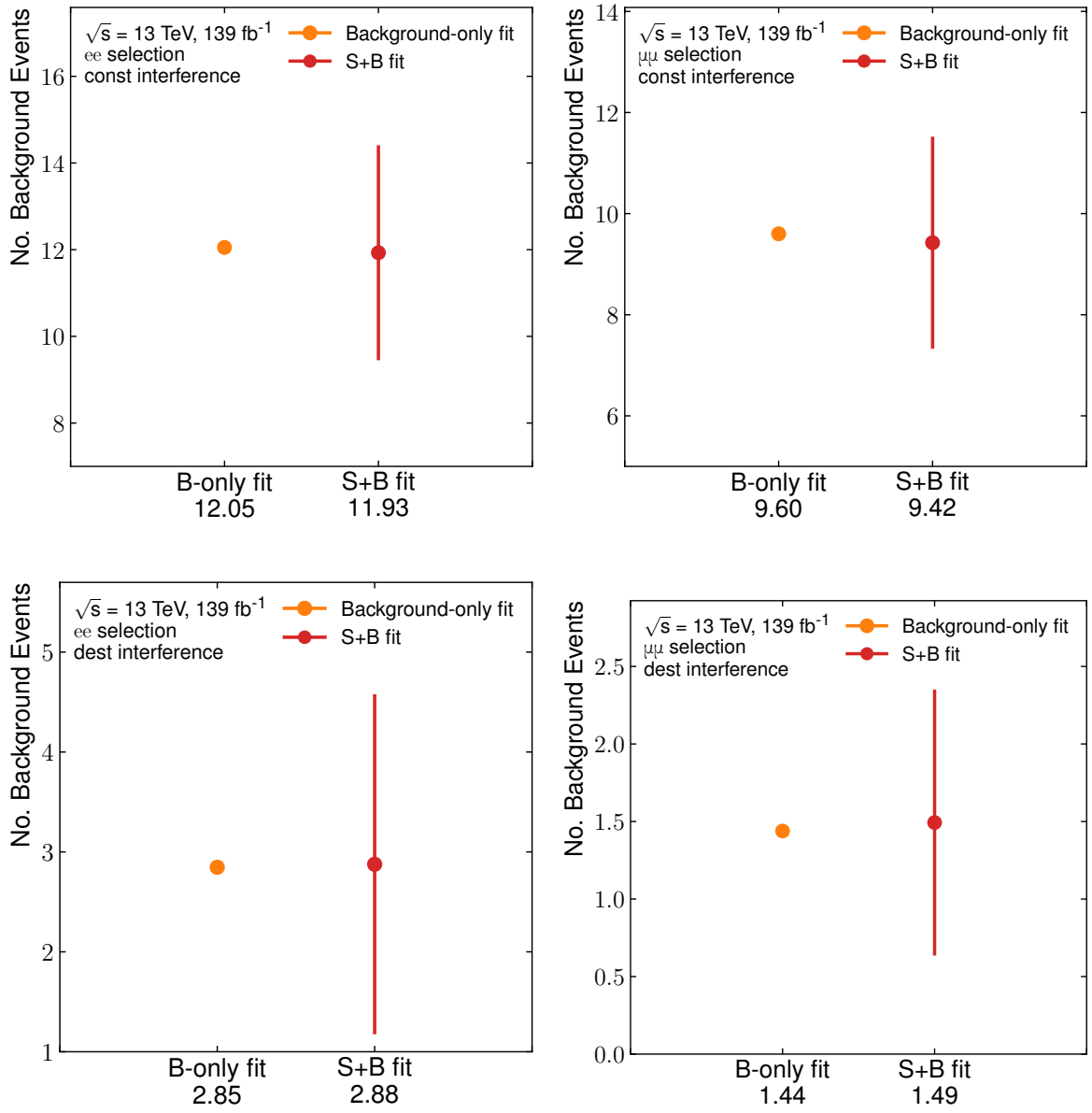

Figure 10.10 Number of background events in the SR from the background only fit and the signal+background (S+B) fit on MC in the constructive (top) and destructive (bottom) interference SRs for the electron channel (left) and muon channel (right). The uncertainty on the background estimate is shown for background only fit. The number of background events from each fit is shown on the x-axis.

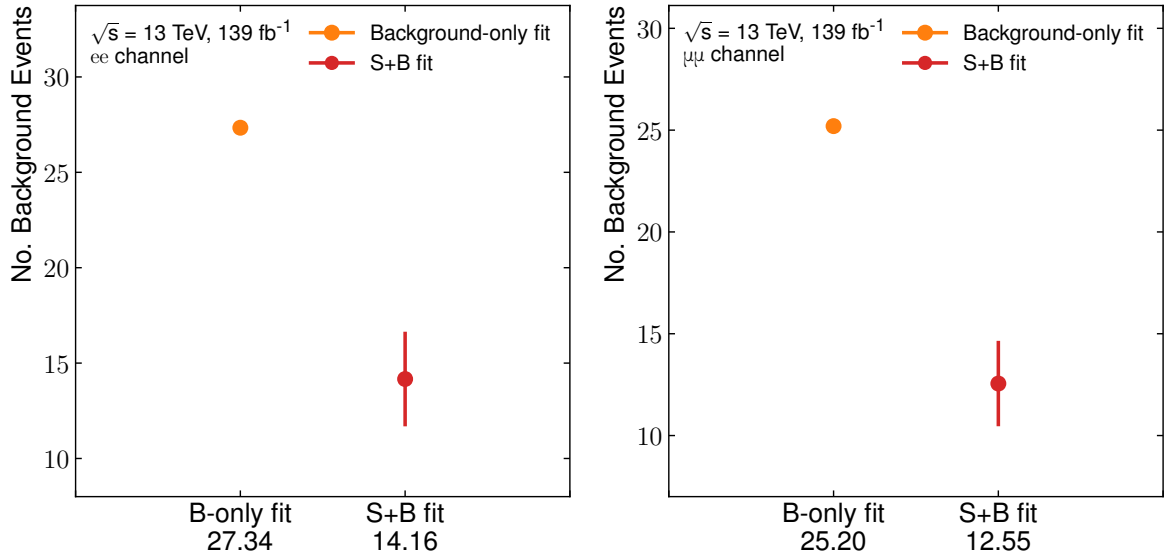

Figure 10.11 Number of background events in the SR from the background-only fit and the signal+background (S+B) fit on MC with an injected CI signal with $\Lambda = 18\,\text{TeV}$, for the electron channel (left) and muon channel (right). The injected number of signals corresponds to 12 and 10 events in the electron and muon channels, respectively. The uncertainty on the background estimate is shown for background-only fit. The number of background events from each fit is shown on the x-axis.

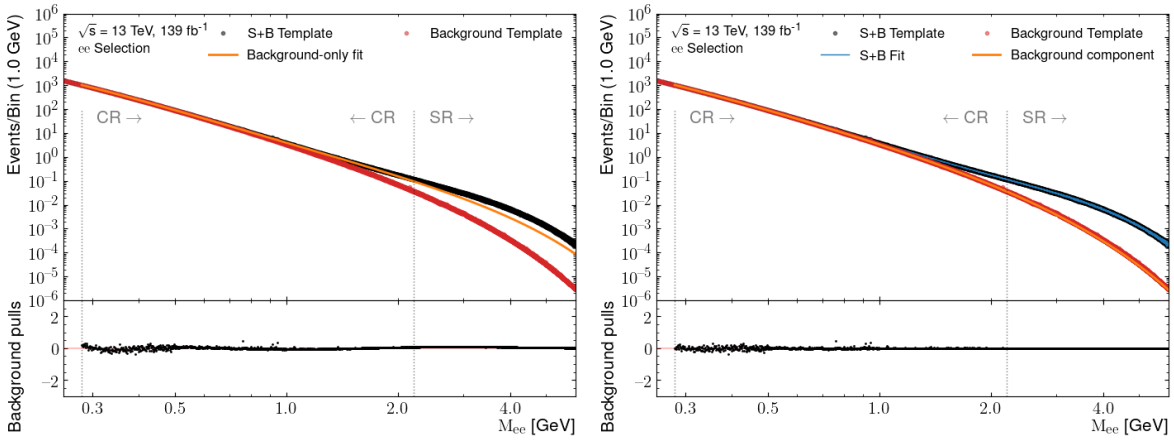

Figure 10.12 Fit distributions from the the background-only fit (left) and the signal+background (right) fit on MC with an injected CI signal with $\Lambda = 18\,\text{TeV}$ (S+B template) in the electron channel. The S+B template is the MC background template with the injected signal. S+B fit is the signal+background fit function.

Chapter 11

Uncertainties

A central part of the analysis is quantifying the potential bias introduced by the choice of a particular function and also quantifying the uncertainty on both the shape and normalisation of the background estimation. The uncertainties related to the background modelling results from three sources: the inherent bias of the function (Section 11.1.1), the statistical uncertainty of the fit (Section 11.1.2) and the residual difference between the signal+background and the background-only functions (Section 11.1.3). The uncertainties are estimated using the background-only function, as it is used for the final background estimate in data.

The interpretation of the results in the context of CI models uses the MC templates, described in Chapter 4. Therefore, the uncertainties associated with the simulated samples are also quantified for the SR choices considered in the analysis (Section 11.2).

11.1 Background estimate uncertainties

11.1.1 Induced spurious-signal uncertainty

For a given underlying PDF that generates an invariant mass spectrum, the extrapolation from the low-mass CR to the high-mass SR will naturally deviate from the underlying distribution, resulting in an excess or deficit compared to the background template. The *induced spurious-*

signal uncertainty ($\sigma_{\mathrm{b}}^{\mathrm{ISS}}$) quantifies the amount to which the background function, when extrapolated to the SR can induce a signal-like excess or deficit.

At high mass the underlying background distribution in data is not known accurately. A $\sigma_{\mathrm{b}}^{\mathrm{ISS}}$ measurement made on the template from only the nominal PDF would assume the underlying distribution to be known precisely. Therefore, the theoretical uncertainties associated with the nominal PDF choice described in Section 9.2 are also considered in the $\sigma_{\mathrm{b}}^{\mathrm{ISS}}$ measurement. Additionally, due to detector and reconstruction effects on the simulated MC template, the experimental uncertainties, described in Section 9.1, are also considered.

The $\sigma_{\mathrm{b}}^{\mathrm{ISS}}$ is measured on the nominal MC background, and its systematic variations. An ensemble of possible simulated shapes are created scaling the nominal simulated background template by a linear combination of all of its systematic uncertainties. Each uncertainty is scaled by a Gaussian factor in the range [-1,1], summed together, and used to scale the simulated background shape to produce a toy distribution. The procedure used to construct each toy background shape is given by

$$\begin{aligned} \text{Toy} &= \sum_i N_{bkg,i} + \sum_j \left(\delta_{i,j} * \alpha_j\right), \\ \alpha_j &= \text{Gaus}(\sigma = 1, \mu = 0), \end{aligned} \tag{11.1}$$

where $N_{bkg,i}$ is the number of background events in invariant mass bin i for the nominal simulated background distribution, $\delta_{i,j}$ is the uncertainty for background uncertainty j, and α_j is a factor sampled from a Gaussian distribution used to scale each uncertainty.

The resulting toy shape is fitted and extrapolated to the SR. The difference between the integral of the extrapolation and the toy background in the SR is taken as the induced spurious signal per toy. The induced spurious-signal is calculated for each toy in the ensemble of toys, producing a distribution for induced spurious-signal values. The sum in quadrature of the mean and standard deviation of the induced spurious-signal distribution is taken as the $\sigma_{\mathrm{b}}^{\mathrm{ISS}}$.

The induced spurious signal distributions, as event yields in the SR, for the CR and SRs considered in the analysis is shown in Figure 11.1. A set of 10000 toy uncertainty templates

are made and fitted using the background-only function. The induced spurious signal for each toy is calculated, resulting in a distribution. The standard deviation and the mean for each CR and SR configuration are calculated from the spurious signal distribution to determine the $\sigma_{\mathrm{b}}^{\mathrm{ISS}}$. The choice of 10000 toys is deemed appropriate as the mean, and standard deviation of the distributions are found to be consistent up to 0.001% when comparing with distributions with 9000 toys.

11.1.2 Statistical uncertainty of fit

Statistical fluctuations in data can lead to variations of the fitted background function in the CR. The resulting variations of the fitted background impact the extrapolated background in the SR. The impact of the statical fluctuations, $\sigma_{\mathrm{b}}^{\mathrm{Stat}}$, is estimated from fitting an ensemble of toy datasets. The invariant mass distribution resulting from the background fit to the data in the CR is used as a probability density function, from which an ensemble of toy datasets are generated by varying each bin using a Poisson distribution. The background function is fit to each of the toy datasets in the ensemble individually, extrapolated and integrated in the SR. The difference between the integral of the toy template in the SR and the fit is calculated. The standard deviation of the distribution of those differences is taken as the $\sigma_{\mathrm{b}}^{\mathrm{Stat}}$. The standard deviation here corresponds to the square root of the average of the squared deviations from the mean. The distributions are not expected to follow a Gaussian distribution. However, this calculation is deemed acceptable to provide an estimate of the uncertainty.

The distribution of the toy background estimates is confirmed to be centered at the nominal induced spurious signal, indicating no bias in the estimation of the uncertainty. The sufficient number of toy background distributions are produced to achieve a precise measurement of the uncertainty. The $\sigma_{\mathrm{b}}^{\mathrm{Stat}}$ is the dominant uncertainty in the fit and extrapolation. Extending the CR boundary to higher mass constrains the fit with more information and results in smaller variations due to statistical fluctuations. However, as discussed in Section 10.4, this needs to be balanced with the signal injection tests.

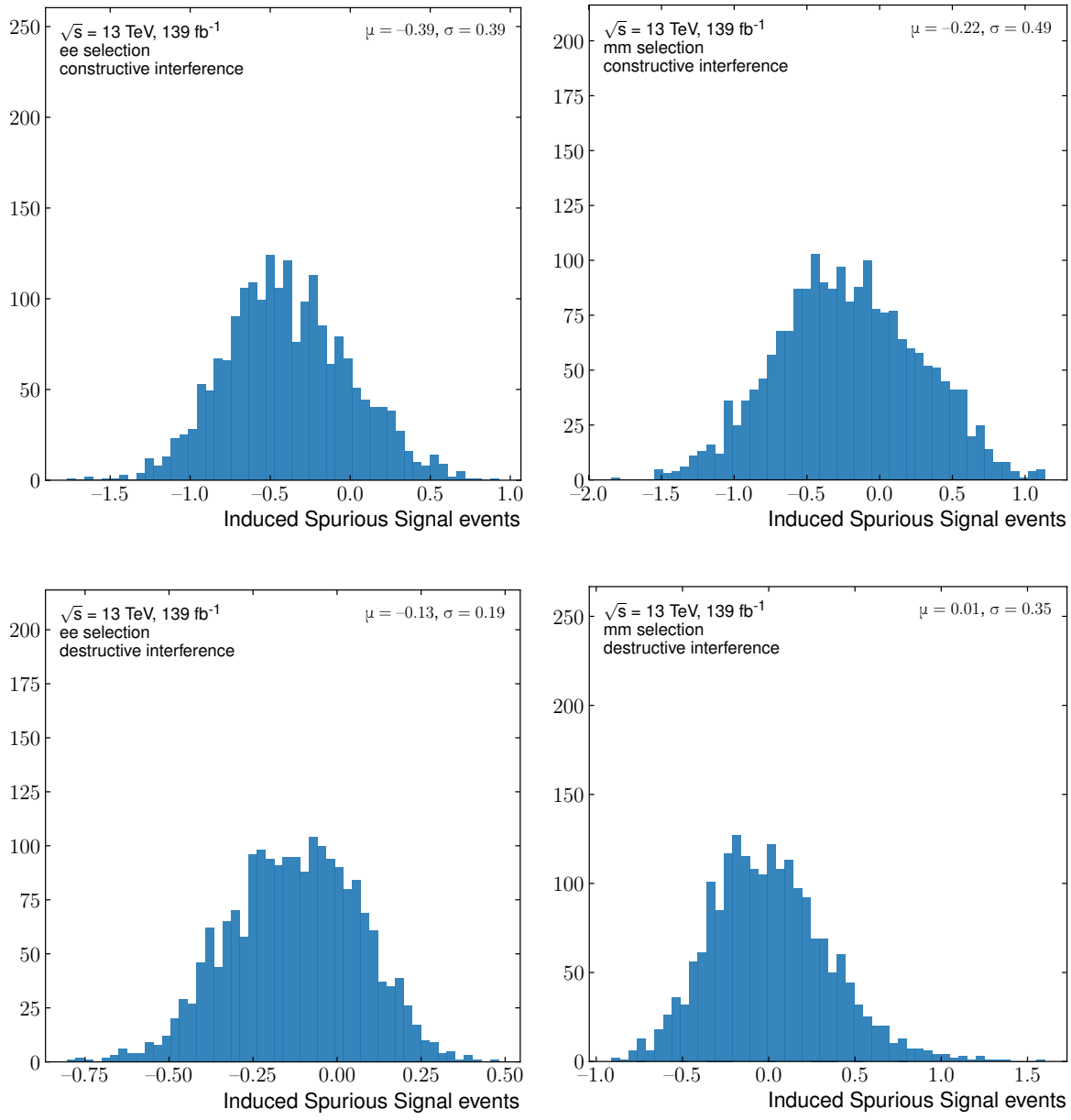

Figure 11.1 Distribution of induced spurious signal values, as number of events, from fits to toy uncertainty shapes. The distributions for the constructive (top) and destructive (bottom) SRs in the electron (left) and muon (right) channels are included. The mean and standard deviation for the induced spurious signal distributions are also shown.

Figure 11.2 depicts the distribution of differences between the background estimate in the SR from the fit to 10000 background toys and the integral of the background toy in the SR. These distributions are centered around the induced spurious signal from the nominal template

as expected. The standard deviation of the distribution is taken as the $\sigma_{\mathrm{b}}^{\mathrm{Stat}}$. The $\sigma_{\mathrm{b}}^{\mathrm{ISS}}$ is calculated for each SR configuration considered in the analysis. The standard deviation of the distribution is confirmed to be consistent at 10000 toys.

11.1.3 Control region bias uncertainty

The *CR bias uncertainty*, $\sigma_{\mathrm{b}}^{\mathrm{CRB}}$, on the expected background quantifies the residual difference between the background-only and the signal+background fit function, with and without the signal component, described in Sections 10.2 and 10.3. Possible signals in data can result in the background estimate from the background-only function being biased, whereas the signal+background function is unaffected by the presence of signals. Using simulated samples, the difference between the two models is negligible by construction due to the optimisation of the CR choice. However, when fitting data, small differences between the two functions can be present. The difference is taken as an additional uncertainty on the background estimate. The uncertainty attempts to quantify the degree to which signal-like shapes exist in data for a given CR choice.

The $\sigma_{\mathrm{b}}^{\mathrm{CRB}}$ is measured by fitting both the background-only and signal+background functions to data in the CR and extrapolating the background components of the two models to the SR. The background estimate is calculated by integrating the extrapolation in the SR. The difference between the resulting background estimates from the two functions is used as the $\sigma_{\mathrm{b}}^{\mathrm{CRB}}$.

11.2 Signal yield uncertainties

The expected number of simulated CI signal events is used in the statistical analysis to produce results in terms of CI interaction models. The simulated contact interaction expected events in the SR are also affected by the theoretical and experimental uncertainties. The expected signal yield is obtained by integrating the simulated signal in the SR. An uncertainty is assigned to the expected yield by summing in quadrature the uncertainties associated with the signal yield.

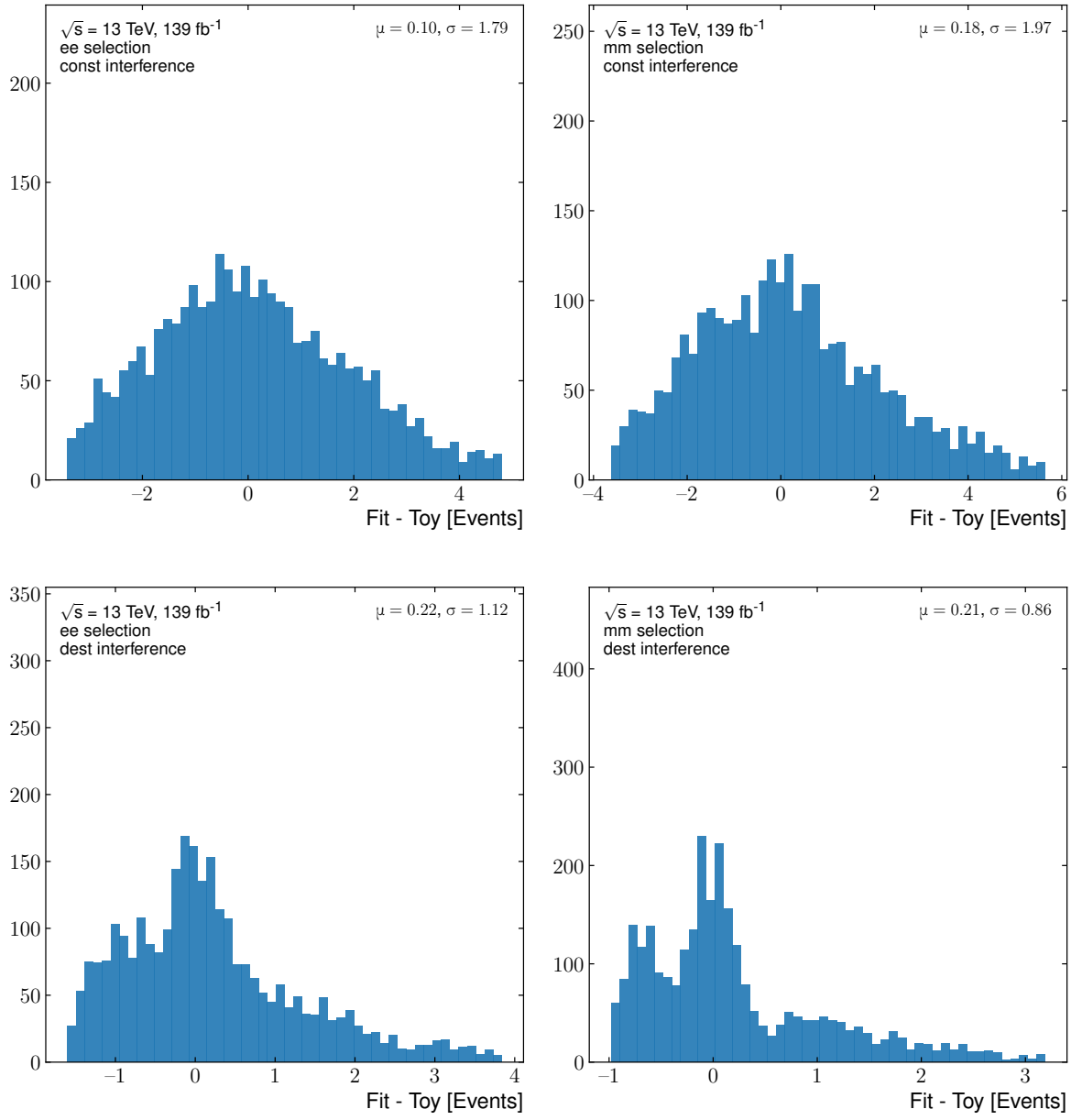

Figure 11.2 Distribution of the difference between the expected background in the SR from fits to poisson generated toys and the background estimation from the toy. The toys have been generated from the fit to the data in the CR. The mean and standard deviation of each distribution is also shown. The constructive (top) and destructive (bottom) SRs for the electron (left) and muon (right) channels are shown.

The theoretical and experimental uncertainties are treated separately and obtained from the

procedure described in Chapter 9. Only the experimental uncertainties on the signal model are used in the statistical analysis as convention.

11.3 Summary of uncertainties

The relative uncertainty on both the background estimate and expected signal yield is summarised in Table 11.1. Due to the smaller size of the destructive SRs, there is a smaller expected number of background events, which results in larger relative uncertainties in the SRs. The $\sigma_{\mathrm{b}}^{\mathrm{CRB}}$ has a minimal impact on the statistical analysis, and the most significant impact is from the $\sigma_{\mathrm{b}}^{\mathrm{Stat}}$. The signal uncertainties are shows for a $\Lambda = 30\,\mathrm{TeV}$, this signal was chosen as it is close to the expected sensitivity of the analysis for the constructive and destructive interference models. Additionally, there is only negligible differences between the uncertainties for signal models $\pm 20\,\mathrm{TeV}$.

		Background uncertainties			Signal uncertainties	
Channel	Interference	$\sigma_{\mathrm{b}}^{\mathrm{Stat}}$	$\sigma_{\mathrm{b}}^{\mathrm{ISS}}$	$\sigma_{\mathrm{b}}^{\mathrm{CRB}}$	$\sigma_{\mathrm{s}}^{\mathrm{Experiment}}$	$\sigma_{\mathrm{s}}^{\mathrm{Theory}}$
e^+e^-	Constructive	14%	4%	2%	8%	$^{+11\%}_{-10\%}$
e^+e^-	Destructive	34%	7%	1%	8%	$^{+14\%}_{-13\%}$
$\mu^+\mu^-$	Constructive	21%	6%	2%	$^{+20\%}_{-17\%}$	$^{+10\%}_{-9\%}$
$\mu^+\mu^-$	Destructive	58%	24%	4%	$^{+27\%}_{-22\%}$	$^{+13\%}_{-12\%}$

Table 11.1 Summary of the relative uncertainties on the background estimate and signal in each SR, where $\sigma_{\mathrm{b}}^{\mathrm{Stat}}$ is the "statistical uncertainty of the fit", $\sigma_{\mathrm{b}}^{\mathrm{ISS}}$ is the "induced spurious signal uncertainty" and $\sigma_{\mathrm{b}}^{\mathrm{CRB}}$ is the "control region bias uncertainty". Experimental and theoretical uncertainties are shown as well with the latter averaged across CI chirality scenarios and quoted for $\Lambda = 30$ TeV only.

Chapter 12

Results

This chapter outlines the results from the functional fit and corresponding profile likelihood fit to the data. The fits to the data are shown in Section 12.1 along with the yields in the SRs considered. Limits are set on the number of signal events in Section 12.3, where extra information has also been provided to aid in the reinterpretation of the results to other non-resonant signals. Additionally, limits are also provided in the context of CI signals in Section 12.4. Finally, the evolution of the analysis sensitivity with different datasets is provided in Section 12.4.

12.1 Fits to data

The background-only fits, and extrapolation to the data in the SR's considered in the analysis are shown in Figure 12.1. The fits are performed in the 1 GeV linear binned datasets corresponding to the full Run-2 luminosity of $139\,\text{fb}^{-1}$. The CR and SRs are defined in Section 10.4. Linear binning is used as it provides enough information for a better-constrained fit to the data in the CR. However, the fits in Figure 12.1 are presented in a constant $\log(m_{\ell\ell})$ binning to aide in visualisation. The parameter values from the fit to the data in the CR are given in Table 12.1.

Figure 12.1 depicts the extrapolation to the SR, where the contents of the SR has been integrated into a single bin to be consistent with the statistical analysis. The data points are

plotted at the centre of each bin as the number of events divided by the bin width, which is constant in $\log(m_{\ell\ell})$. The error bars indicate statistical uncertainties only. A few benchmark CI signal shapes are shown for the LL chirality model, scaled to the data luminosity and superimposed by subtracting the LO DY component and adding the resulting shape to the background shape obtained from the fit. The background-only fit is shown in solid red, with the shaded light red area being its uncertainty. The boundaries of the CR and SR corresponding to the signals used are shown in dotted vertical lines for reference and marked by arrows. A non-significant excess is observed in the electron constructive SR, and a deficit is observed in the remaining signal regions. The excesses and deficits are quantified in terms of significances below. The bottom panel shows the differences between the data and the fit results in units of standard deviations of the statistical uncertainty of data, defined as $(\text{Data} - \text{Fit})/\sigma_{\text{Data}}$.

Parameter	e^+e^-, Constructive	e^+e^-, Destructive	$\mu^+\mu^-$, Constructive	$\mu^+\mu^-$, Destructive
a	$(6.17 \times \pm 0.02) \times 10^{-3}$	$(7.87 \pm 0.03) \times 10^{-3}$	$(6.90 \pm 0.03) \times 10^{-6}$	$(4.39 \pm 0.02) \times 10^{-7}$
b (fixed)	6.1	6.1	1.3	1.3
c (fixed)	1/2	1/2	1/3	1/3
p_0	-12.3±0.1	-12.2±0.1	-14.9±0.2	-17.0±0.2
p_1	-4.15±0.02	-4.16±0.03	-4.41±0.04	-4.70±0.04
p_2	-0.944±0.005	-0.945±0.006	-0.927±0.008	-0.846±0.008
p_3	-0.0832±0.0008	-0.083±0.001	-0.081±0.001	-0.064±0.001

Table 12.1 Parameters for the functional form given in Eq. Equation 10.1 in each of the signal regions considered in the analysis. The uncertainties are statistical only.

ATLAS event displays for the highest mass dielectron and dimuon candidates are shown in Figure 12.2. The dielectron candidate with the highest reconstructed mass corresponds to an electron pair with $m_{ee} = 4.06\,\text{TeV}$. The electrons are emitted with a leading electron $E_{\text{T}} = 2.01\,\text{TeV}$, $\eta = 0.47$ and $\phi = -0.78$. Whereas, the subleading electron is emitted with $E_{\text{T}} = 1.92\,\text{TeV}$, $\eta = 0.03$ and $\phi = 2.37$. The dimuon highest mass candidate has $m_{\mu\mu} = 2.75\,\text{TeV}$. The leading muon is emitted with $p_{\text{T}} = 1.82\,\text{TeV}$, $\eta = -0.52$ and $\phi = -0.56$, and the subleading muon has $p_{\text{T}} = 1.04\,\text{TeV}$, $\eta = -0.67$ and $\phi = 2.53$. Figure 12.2 includes jets overlapping with the muons, where all jets have $p_{\text{T}} < 50\,\text{GeV}$ indicating that they are induced by the calorimeter deposits of the muons.

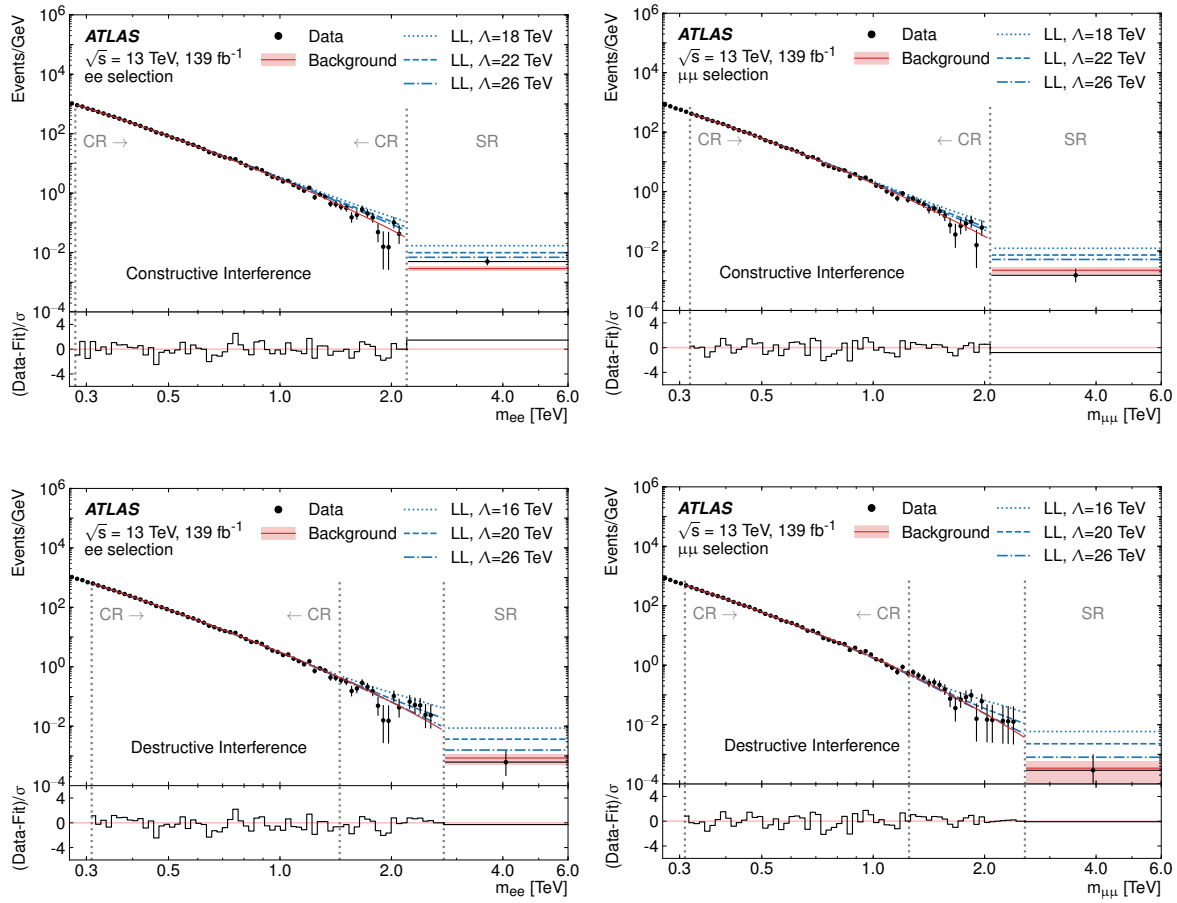

Figure 12.1 Distributions of the invariant mass of dilepton pairs passing the full selection for dielectrons (left) and dimuons (right), and showing CR and SR for constructive interference (top) and destructive interference (bottom). A few CI benchmark signal shapes are shown for the LL chiral model, scaled to the data luminosity and superimposed by subtracting the LO DY component and adding the resulting shape to the background shape obtained from the fit. The background-only fit is shown in solid red, with the shaded light red area being its uncertainty. The boundaries of the CR and SR corresponding to the signals used are shown in dotted vertical lines for reference and marked by arrows. The differences between the data and the fit results in units of standard deviations of the statistical uncertainty are shown in the bottom panels.

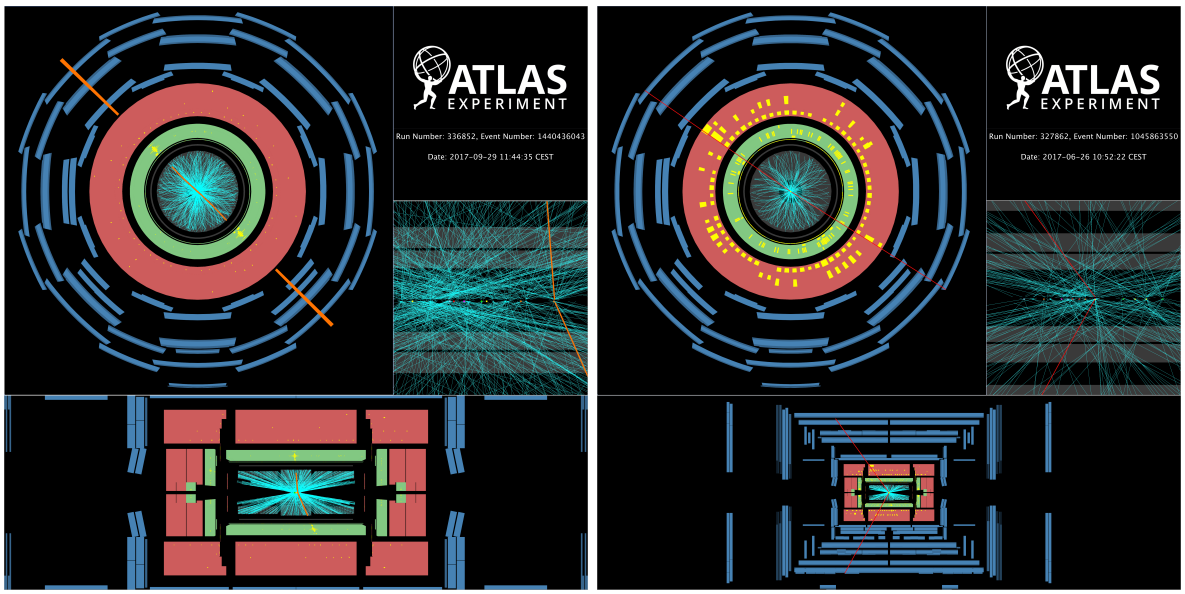

Figure 12.2 Event display of the dielectron (left) and dimuon (right) candidate with the highest invariant mass in the 2015–2018 data taking period with $m_{ee} = 4.06\,\text{TeV}$ and $m_{\mu\mu} = 2.75\,\text{TeV}$ [3].

Control region validation

As discussed in Chapter 10, the CR choice is required to be validated in data by comparing the background estimate from the signal+background function to the background-only function, to mitigate any signal contributions from unexpected signals in the CR. Figure 12.3 shows the comparison of the two background estimates. The background estimates have a very good agreement between the two functions indicating there is no significant contribution from a signal in the CR. The results are comparable to what was shown by the MC study performed in Chapter 10. Therefore, the upper edge of the CR region does not need to be changed, and it is safe to use the background-only function.

Signal region yields and significances

Table 12.2 lists the expected background and observed event yields in each of the SR's defined in Section 10.4. The background uncertainties are also shown in terms of numbers of events in the SR. A single-bin Poisson likelihood is constructed for each of the SR as described

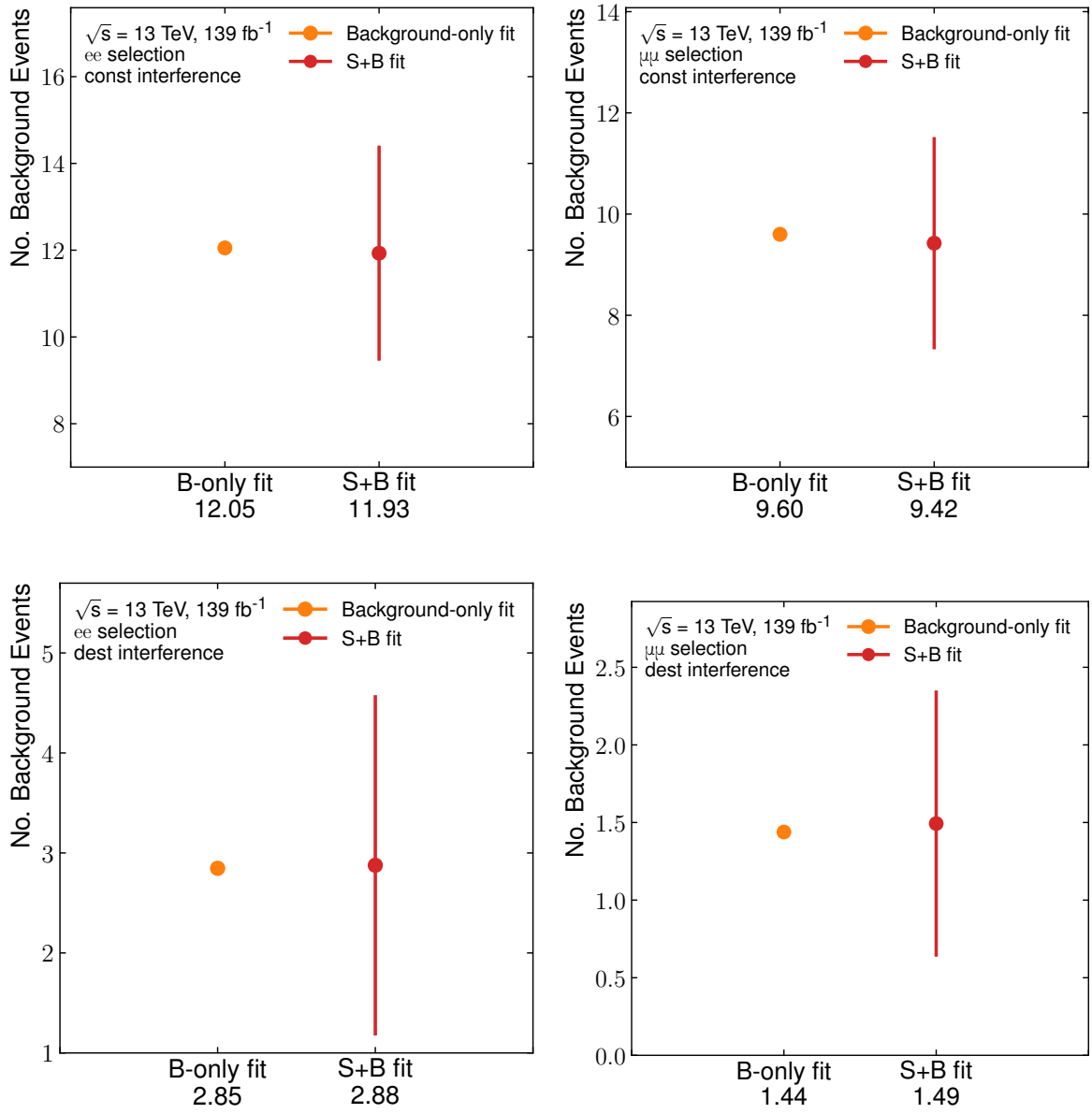

Figure 12.3 Number of background events in the SR from the background only fit and the signal+background (S+B) fit on data in the constructive (top) and destructive (bottom) interference SRs for the electron channel (left) and muon channel (right). The uncertainty on the background estimate is shown for signal+background fit. The number of background events from each fit is shown on the x-axis.

in Chapter 4 and the compatibility of finding the observed data with the background-only hypothesis is tested by fitting the data with the statistical model. The largest deviation from the expected background can be seen in the electron constructive SR, which corresponds to

an observed significance of 1.28σ. There is a small deficit of events observed in the other SRs, where the observed significances range from -0.99σ to -0.17σ. The p-value of each observation is calculated using the statistical procedure described in Chapter 4. The significance is the calculated from the Gaussian cumulative density function of the p-value. The results indicate that there are no significant excesses observed in the data in the SRs to hint at the presence of new physics signatures.

Signal Regions		Yields		Background Uncertainties				Significance
Channel	Interference	Data	Background	σ_b^{Stat}	σ_b^{ISS}	σ_b^{CRB}	Total	
e^+e^-	Constructive	19	12.4	1.7	0.5	0.2	1.8	1.28
e^+e^-	Destructive	2	3.1	1.1	0.2	<0.1	1.1	– 0.72
$\mu^+\mu^-$	Constructive	6	9.6	2.0	0.6	0.2	2.1	– 0.99
$\mu^+\mu^-$	Destructive	1	1.4	0.8	0.3	0.1	0.9	– 0.58

Table 12.2 The dielectron and dimuon event yields for the data, the expected background, the corresponding background uncertainties and the respective significances in the different signal regions used in the analysis. σ_b^{Stat} is the "statistical uncertainty", σ_b^{ISS} is the "induced spurious signal uncertainty" and σ_b^{CRB} is the "control region bias uncertainty". The total uncertainty is calculated by taking the sum in quadrature of the individual components. all uncertainties are described in detail in Chapter 11.

12.2 Nuisance parameter rankings

The pulls and impacts of the nuisance parameters are checked in order to determine if their values have significantly deviated from the original estimate after the fit. The procedure outlined in Section 4.3 is used to calculate the pulls and impact of the nuisance parameters. The pulls and impact are estimated using the model-independent description of the statistical model, where ν_s is taken as the POI. They are presented in Figures 12.4 and 12.5 for the electron and muon channels, respectively, in the SRs considered in the analysis. Only the uncertainties on the background estimate and the luminosity uncertainty on the signal event yield are considered in the model-independent description, due to there being no explicitly defined signal model.

The nuisance parameters are ranked based on their *postfit* impact, where the nuisance parameters are shown according to their impact in descending order. The dominant uncertainty in all signal regions and channels considered is the statistical uncertainty of the fit ($\sigma_{\mathrm{b}}^{\mathrm{Stat}}$), indicating that the sensitivity to non-resonant signals is statistically dominated. The second-largest impact is from the induced spurious signal uncertainty ($\sigma_{\mathrm{b}}^{\mathrm{ISS}}$). The contribution from the luminosity (σ_{Lumi}) and $\sigma_{\mathrm{b}}^{\mathrm{CRB}}$ have a negligible impact on the results. The figure indicates that there are no visible pulls on the nuisance parameters and that they are not constrained, which can be determined by the error bar on the pull. An error on the pull smaller or larger than 1σ would indicate that a nuisance parameter has been constrained *postfit*. Differences between the *postfit* and *prefit* impacts can be inferred from the error bar on the pull, as any residual difference would indicate that the nuisance parameter is constrained.

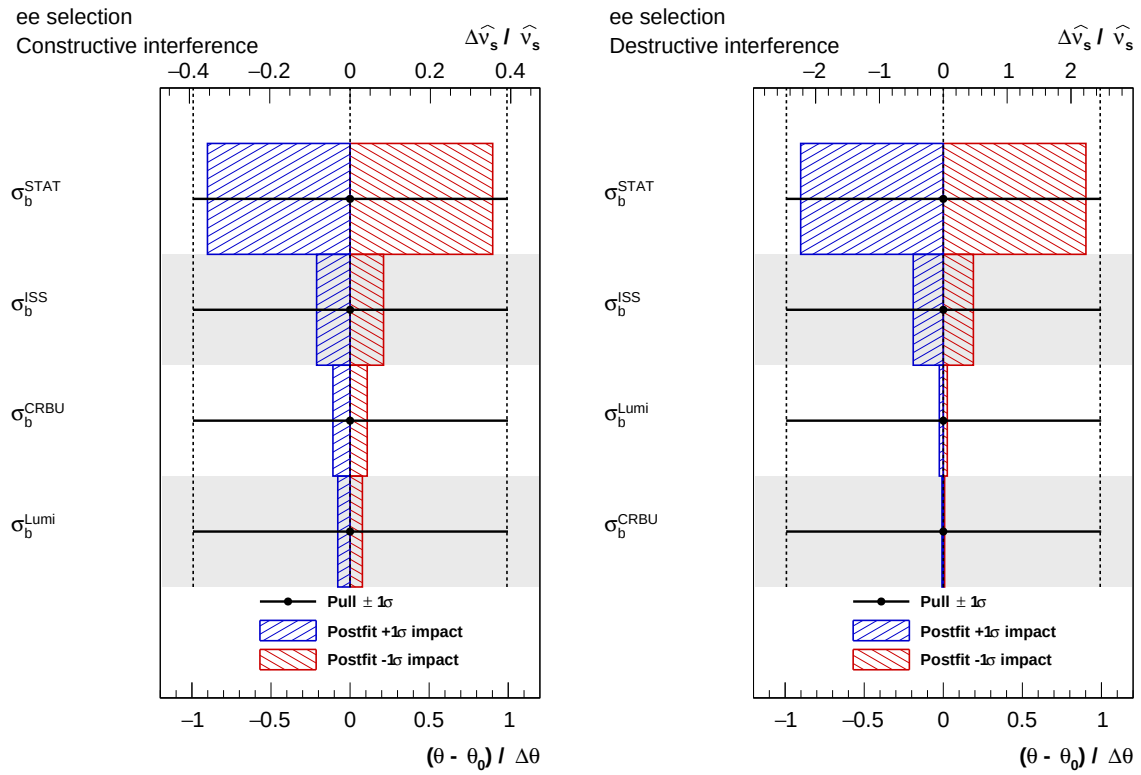

Figure 12.4 Ranking plots for the considered systematic uncertainties for the model independent limits. The impact on the parameter of interest (ν_s) is shown in the signal regions considered in the electron channel. The systematic uncertainties are listed in decreasing order of impact on the parameter of interest. The red and blue bards correspond to the postfit upward and downward variations, respectively, where the impact is referred to on the upper axis. The pulls of the corresponding nuisance parameters are shown by the marked circle, where the pulls are referred to in the bottom axis. The constraint of the nuisance parameter is indicated by the black error bar.

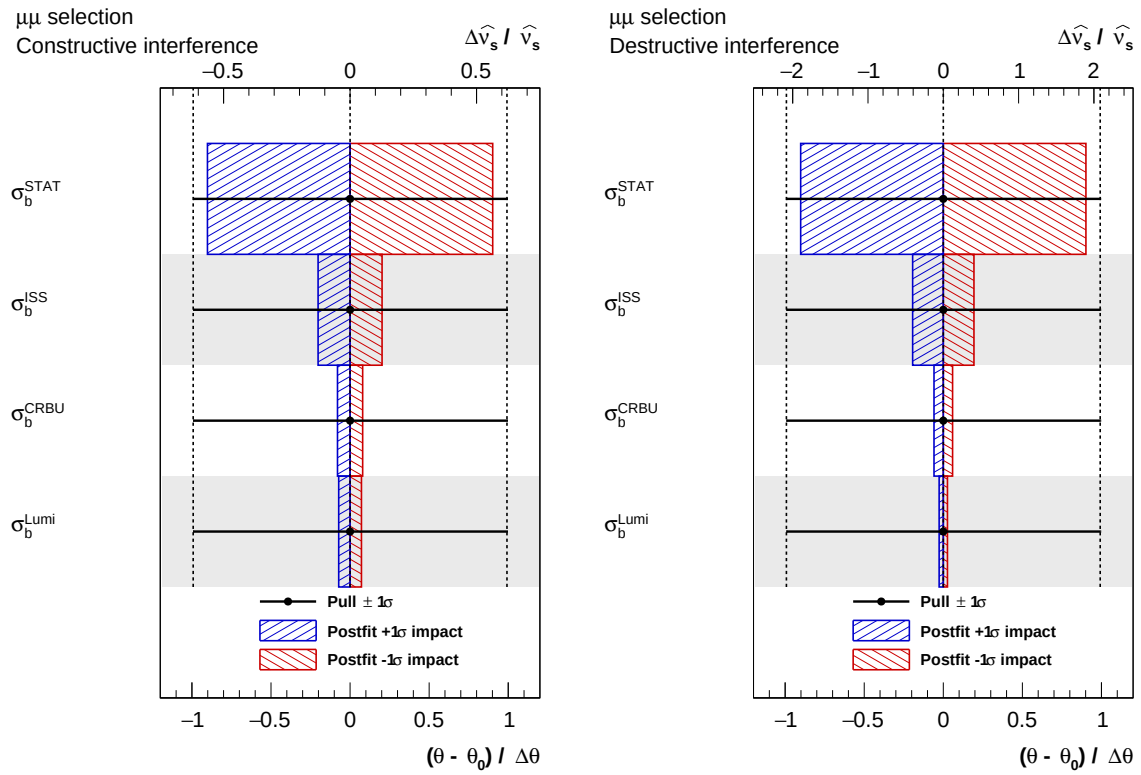

Figure 12.5 Ranking plots for the considered systematic uncertainties for the model independent limits. The impact on the parameter of interest (ν_s) is shown in the signal regions considered in the muon channel. The systematic uncertainties are listed in decreasing order of impact on the parameter of interest. The red and blue bards correspond to the postfit upward and downward variations, respectively, where the impact is referred to on the upper axis. The pulls of the corresponding nuisance parameters are shown by the marked circle, where the pulls are referred to in the bottom axis. The constraint of the nuisance parameter is indicated by the black error bar.

12.3 Model independent exclusion limits

Since no significant excesses have been observed in any of the signal regions, upper limits are extracted on the parameter of interest (POI). The exclusion limits provided in this section are calculated using the signal event yield, ν_s, as the POI in the statistical analysis using 500000 toy MC experiments. The 95% CL limits are calculated on the signal event yield for each of the SRs considered in the analysis. These limits are then used to calculate limits on the visible cross-section ($\sigma_{\text{vis}} \times \text{Br}$) using

$$\sigma_{\text{vis}} \times \text{Br} = \frac{N_{\text{events}}}{\text{Luminosity}}, \tag{12.1}$$

where N_{events} corresponds to the number of events and luminosity is the integrated luminosity of the full Run-2 dataset. The limits on the signal event yield and the visible cross-section can be used by theorists to reinterpret the results in the context of other BSM models. Figure 12.6 shows the expected and observed limits on the number of signal events for each of the SRs in the electron and muon channels. The one and two sigma error on the expected limit are shown by the green and yellow bands, respectively. Due to the excess of observed in the constructive SR of the electron channel, the observed limit is above the one sigma error on the expected limit. Whereas, the deficits in the other signal regions results in the lower observed limit compared to the expected limit. Table 12.3 summarises the observed and expected limit on the number of signal events and the visible cross-section times branching fraction. Expected signal event yields, along with their acceptance times efficiency in the SRs for various CI LL chiral Λ models are also given in Table 12.3. Further detail on the prescribed reinterpretation procedure is given below in Section 12.3.

Ingredients for reinterpretation

To aide with reinterpretation into other non-resonant models, the acceptance times efficiency and number of expected events in the SR for various CI models are also provided. The limits on the number of signal event yield shown in Table 12.3 can be applied to new signal models

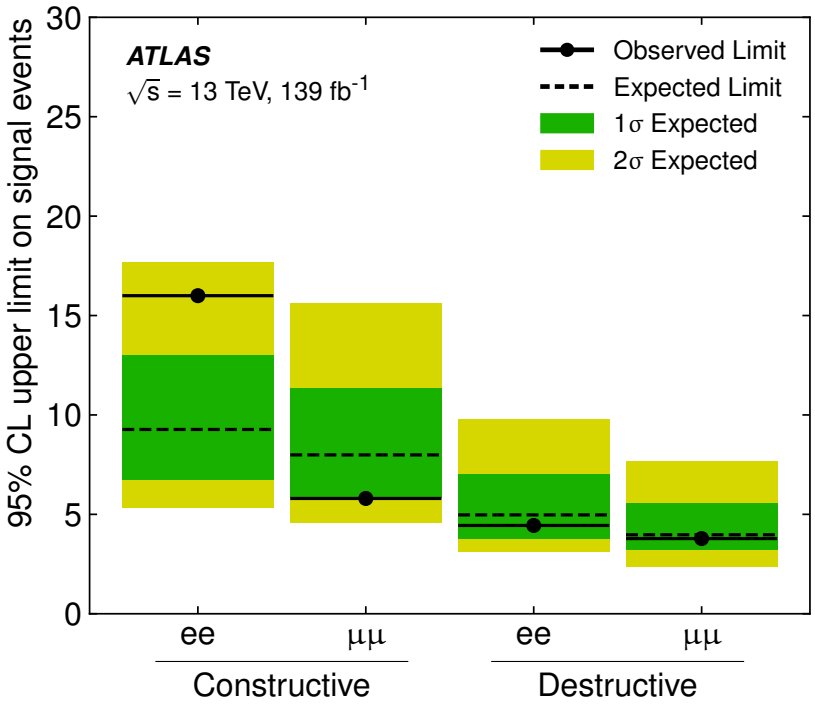

Figure 12.6 Model independent upper limits at 95% CL on the number of signal events in the SRs used in the analysis for electron and muon channels. The green and yellow bands correspond to the one and two sigma uncertainty on the expected limit.

SR	Limit on $\sigma_{\text{vis}} \times \text{Br}$ [fb]		Limit on N_{sig}		Signal (LL chirality only)					
					$\Lambda = 20$ TeV		$\Lambda = 30$ TeV		$\Lambda = 40$ TeV	
	Exp.	Obs.	Exp.	Obs.	N_{sig}	$\mathcal{A} \times \epsilon_{\text{sig}}$ [%]	N_{sig}	$\mathcal{A} \times \epsilon_{\text{sig}}$ [%]	N_{sig}	$\mathcal{A} \times \epsilon_{\text{sig}}$ [%]
e^+e^- Const.	0.067	0.115	9.3	16.0	39.1	69	10.3	69	4.4	69
e^+e^- Dest.	0.036	0.032	5.0	4.4	9.6	70	1.0	70	-0.1	69
$\mu^+\mu^-$ Const.	0.057	0.042	8.0	5.8	28.5	43	7.7	43	3.4	43
$\mu^+\mu^-$ Dest.	0.029	0.027	4.0	3.8	7.1	43	0.6	42	-0.2	44

Table 12.3 The observed model-independent upper limit on the visible cross-section times branching fraction ($\sigma_{\text{vis}} \times \text{Br}$) and the number of signal events (N_{sig}) in the dielectron and dimuon SRs used in the analysis. The expected yields for a few CI signal points (LL chirality only) are listed along with the signal acceptance times efficiency ($\mathcal{A} \times \epsilon_{\text{sig}}$) values for reference.

that predict non-resonant enhancements in the SRs that are used. A requirement for a model to be interpretable is that the contribution from the signal in the CR is negligible compared to the background estimation. A generator (truth) level number of signal events predicted for a BSM model can be multiplied by the signal acceptance times efficiency, shown in Table 12.4, to obtain an expected number of signal events for that model, N'_{sig}. Once N'_{sig} has been calculated, models predicting N'_{sig} greater than or equal to the observed limit can be excluded with a confidence level of 95%.

Table 12.4 shows the acceptance times efficiency and number of events in the SR for CI models at various Λ values in the SRs. The acceptance times efficiency is defined as the probability to reconstruct and select events with $m_{\ell\ell}$(truth), and is determined from the full simulation MC samples

$$\mathcal{A} \times \epsilon_{\text{sig}} = \frac{\text{Events passing selection cuts}}{\text{Truth events in generated sample}}. \tag{12.2}$$

where $\mathcal{A} \times \epsilon_{\text{sig}}$ is calculated for each invariant-mass bin the sample is generated. The acceptance times efficiencies for the CI model show consistent behaviour between signal models, therefore, they can be applied to most spin-1 particles. However, the acceptance times efficiency for models featuring other particles, e.g. spin-2, is expected to be slightly different.

12.4 Exclusion limits on CI models

As discussed in Chapter 3, the CI energy scale, Λ, can be used to infer at which energy scales the new physics interactions are expected to occur. The exclusion limits provided in this section are calculated using Λ as the POI in the statistical analysis and using 500000 toy MC experiments. This follows the procedure defined in Section 4.5. The signal model used for each hypothesis test uses the morphed PDF templates produced using the custom class defined in Section 8.2.2. The experimental uncertainties defined in Chapter 9 are used in the signal model as additional Gaussian constraints.

Channel	Interference	$\Lambda = 20$ TeV		$\Lambda = 30$ TeV		$\Lambda = 40$ TeV	
		N_{sig}	$\mathcal{A} \times \epsilon_{\text{sig}}$ [%]	N_{sig}	$\mathcal{A} \times \epsilon_{\text{sig}}$ [%]	N_{sig}	$\mathcal{A} \times \epsilon_{\text{sig}}$ [%]
Signal(LL)							
e^+e^-	constructive	39.1±3.1	69	10.3±0.8	69	4.4±0.4	69
e^+e^-	destructive	9.6±0.8	70	0.96±0.08	70	-0.10±0.01	69
$\mu^+\mu^-$	constructive	28.5±5.8	43	7.7±1.6	43	3.4±0.7	43
$\mu^+\mu^-$	destructive	7.1±1.9	43	0.55±0.15	42	-0.21±0.05	44
Signal(LR)							
e^+e^-	constructive	34.0±2.7	69	8.0±0.6	69	3.1±0.25	69
e^+e^-	destructive	11.7±1.0	70	1.9±0.2	70	0.41±0.03	70
$\mu^+\mu^-$	constructive	24.6±5.0	43	5.9±1.2	43	2.4±0.5	43
$\mu^+\mu^-$	destructive	9.0±2.4	43	1.4±0.4	43	0.25±0.07	42
Signal(RL)							
e^+e^-	constructive	33.8±2.7	69	7.9±0.6	69	3.1±0.2	69
e^+e^-	destructive	11.7±1.0	70	1.9±0.2	70	0.40±0.03	70
$\mu^+\mu^-$	constructive	24.3±4.9	43	5.8±1.2	43	2.3±0.5	43
$\mu^+\mu^-$	destructive	9.0±2.4	43	1.4±0.4	43	0.26±0.07	42
Signal(RR)							
e^+e^-	constructive	38.6±3.1	69	10.1±0.8	69	4.3±0.3	69
e^+e^-	destructive	9.9±0.8	70	1.1±0.1	70	< 0.01	67
$\mu^+\mu^-$	constructive	28.2±5.7	43	7.6±1.5	43	3.3±0.7	43
$\mu^+\mu^-$	destructive	7.3±2.0	43	0.65±0.17	42	-0.15±0.04	44

Table 12.4 Signal yields for each chirality. The uncertainties on the signal yield correspond to the theoretical uncertainties on the simulation. The corresponding acceptance times efficiency ($\mathcal{A} \times \epsilon_{\text{sig}}$) is included for reference.

Figure 12.7 shows the exclusion limits provided for the CI chiral and interference models for the electron, muon and combined dilepton channel. The one and two sigma error bands are shown by the green and yellow bars, respectively. Due to the relationship between Λ and the cross-section defined in Chapter 3 an observed excess with respect to the expected events would result in a lower observed limit on Λ compared to the expected limit, as the higher Λ models correspond to a smaller number of expected events. Therefore, the deficits in the other SRs results in larger observed limits compared to the expected limit. The asymmetry in the error bands are a result of the limited statistics in the signal regions. The exclusion limits are interpreted as lower limits on the CI energy scale Λ. Table 12.5 summarises the exclusion limits on the CI models. The electron channel drives the combined limit due to the larger signal region and smaller uncertainties associated with the electron signal regions.

Int.	Channel	Exp./Obs.	LL	LR	RL	RR
Constructive	ee	Expected	31.1	28.9	28.7	30.9
		Observed	26.1	24.7	24.6	26.0
	$\mu\mu$	Expected	29.2	27.1	27.0	29.0
		Observed	32.7	30.0	29.8	32.6
	$\ell\ell$	Expected	37.6	34.0	33.7	37.3
		Observed	35.8	32.5	32.3	35.5
Destructive	ee	Expected	23.0	24.4	24.4	23.2
		Observed	23.5	25.1	25.1	23.7
	$\mu\mu$	Expected	22.0	23.6	23.6	22.2
		Observed	22.3	23.9	23.9	22.5
	$\ell\ell$	Expected	25.6	28.0	28.0	25.9
		Observed	26.0	28.8	28.8	26.5

Table 12.5 Expected and observed lower limits at 95% CL on Λ in TeV for the dielectron and dimuon channels separately and for the combined electron-muon channel and for CI signal hypotheses with constructive and destructive interference and different chiralities.

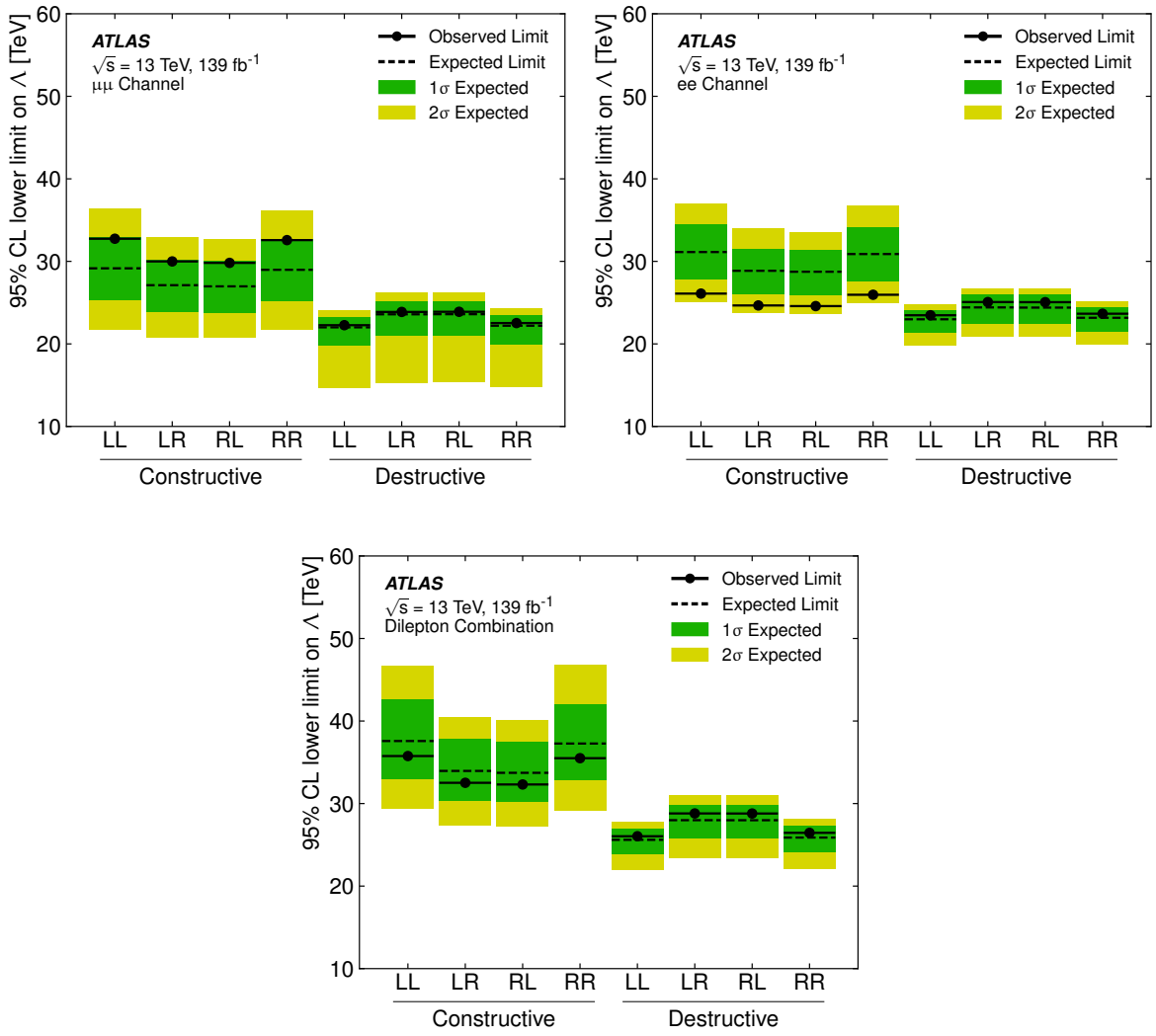

Figure 12.7 Lower limits at 95% CL on Λ for the muon channel (left). the electron channel (right) and the combined dilepton channel (bottom) for different signal chiralities in the (constructive/destructive interference) SRs of the analysis. The green and yellow bands correspond to the one and two sigma uncertainty on the expected limit.

Evolution of analysis sensitivity

Exclusion limit at 95% CL obtained by previous ATLAS analyses are summarised in Figure 12.8 for the combined dilepton channel. The previous ATLAS analyses used a MC template-based approach to model the background estimation and used a Bayesian statistical analysis. Two separate sets of results were available using two different choice of priors on the signal model: one on $1/\Lambda^2$ and one on $1/\Lambda^4$. Due to these differences, an exact comparison is not possible. Comparing the expected limit of the constructive interference model with the analysis performed on the 36.1 fb^{-1} shows an increase in sensitivity of 7 TeV between the two analyses. The observed limit has a smaller increase of 1 TeV. The smaller increase is due to the deficit of events in the electron channel in the previous analysis, which results in a larger observed limit compared to the expected and drives the combination of the two channels. The figure shows the results using the $1/\Lambda^4$ prior. The results using the $1/\Lambda^2$ prior are slightly higher.

The most recent result by CMS was performed at $\sqrt{s} = 13$ TeV and an integrated luminosity of 36.1 fb^{-1} [47]. The CMS analysis also uses a MC template approach to estimate its background and a Bayesian analysis. A flat prior on the cross-section is used for the CMS analysis. An expected (observed) limit of 31 TeV (32 TeV) are obtained for the LL constructive CI model in the $\ell\ell$ channel.

Looking at a broader context, contact interactions searches were also carried out by the ZEUS, ALEPH and DØ collaborations. The strongest limits from ALEPH on the scale of the energy scale Λ are in the range of 2 - 17 TeV. Whereas, the HERA and DØ collaborations set limits on Λ in the range of 1.7 - 6.2 TeV and 3.3 - 5.1 TeV, respectively.

The majority of the improved sensitivity can be attributed to the increased luminosity between the datasets, as the systematic uncertainties resulting from the MC and data-driven method have comparable values. However, the data-driven method is less reliant on MC production, reducing the strain on available resources. It provides a more coherent estimation of the uncertainties associated with the background estimation, rather than having a large dependence on the PDF uncertainties.

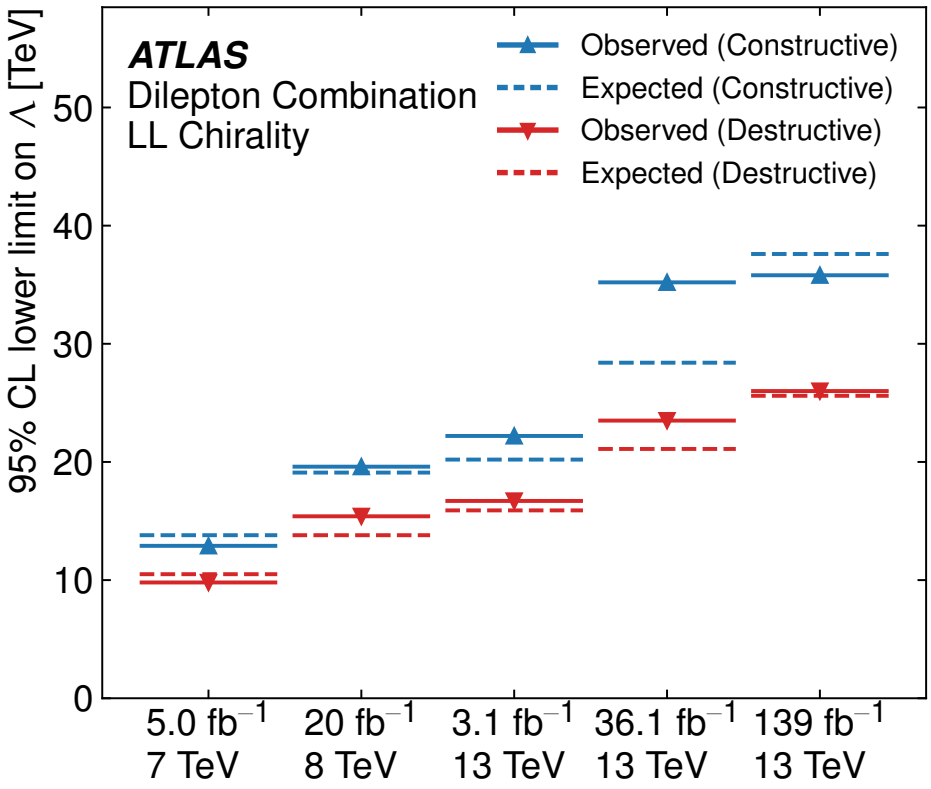

Figure 12.8 Comparison of the $\ell\ell$ constructive (blue) and destructive (red) limits with previous ATLAS results. ($\sqrt{s} = 13$ TeV 36.1 fb^{-1}: [2], $\sqrt{s} = 13$ TeV 3.1 fb^{-1}: [147], $\sqrt{s} = 8$ TeV 20 fb^{-1}: [148], $\sqrt{s} = 7$ TeV 5.0 fb^{-1}: [149].)

Chapter 13

Conclusion and outlook

A search for non-resonant signals, with an interpretation of contact interactions, has been performed in dilepton final states using 139 fb^{-1} of pp collision data collected by the ATLAS experiment during Run 2 of the LHC at $\sqrt{s} = 13$ TeV. The analysis uses a novel approach to estimate the background contribution, where a data-driven extrapolation procedure is utilised. Two SRs each for the electron and muon channels are used to search for constructive and destructive interference models, resulting in four SRs in the analysis. The statistical uncertainty on the fit dominates the search in all of the SRs considered, therefore indicating that the search is statistics dominated. However, the unintuitive PDF uncertainties have a much smaller impact on the analysis compared to previous iterations. Additionally, the analysis provides a background estimation method that reduces the dependence on very large amount of MC samples to be produced to estimate the background, significantly reducing the strain on resources. The results are provided in the context of model independent limits, to facilitate the reinterpretation into other interesting non-resonant models. The analysis also directly interprets its results in the context of the four-fermion CI model, where lower limits are set on the CI energy scale Λ.

The background expectation is compared to the data, and possible deviations have been quantified in terms of significances using a profile-likelihood ratio test. A small excess is observed in the electron constructive SR corresponding to a significance of 1.28σ. The other SRs observe a small deficit ranging between -0.99σ and -0.19σ. The significances show that

the data are compatible with the background expectation, indicating that there is no new physics found.

Since no significant excess or deficit is observed, upper limits on the number of signal events, as well as lower limits on the CI energy scale Λ are set. Additionally, the acceptance times efficiency values for the CI signal models are also provided to aid in the reinterpretation of the limits on the number of signal events. The electron and muon channel results are statistically combined to provide limits on the combined dilepton channel. The strongest limits are set on the combined-channel LL constructive model, where the observed and expected limits exclude this model for Λ up to 35.8 and 37.6 TeV at 95% CL, respectively.

The expected sensitivity of the analysis has increased by 7 TeV compared to the previous iteration of the analysis performed with $36.1\,\text{fb}^{-1}$ of data. Due to the excess observed in the electron constructive signal region, the resulting observed limits show a smaller increase compared to the previous analysis. Additionally, a deficit was observed in the previous analysis which resulted in higher observed limits.

Future analyses will benefit from the increased statistics if they use a similar background estimation method. As the statistics of the dataset increases, the statistical uncertainty associated with the fit will decrease. Therefore, resulting in improvement of analysis sensitivity. However, as the search extends to higher invariant masses, the functional form used may not be suitable and more ad-hoc parameters may be required to be added. Additionally, other functions may also need to be tested once more. One possible alternative is the use of Gaussian process to model the background [150]. A Gaussian process provides a generalisation of a particular distribution without being tied to a functional form. Using the method the background distribution can be modelled using Gaussian processes rather than a parametric form. It also allows to incorporate the understanding of the underlying physics to construct the Gaussian process, making it a more physically motivated approach.

References

[1] ATLAS, G. Aad *et al.*, *Search for new non-resonant phenomena in high-mass dilepton final states with the ATLAS detector*. JHEP **11** (2020) p. 005, arXiv:2006.12946 [hep-ex].

[2] ATLAS Collaboration, *Search for new high-mass phenomena in the dilepton final state using* $36\,fb^{-1}$ *of proton–proton collision data at* $\sqrt{s} = 13$ *TeV with the ATLAS detector*. JHEP **10** (2017) p. 182, arXiv:1707.02424 [hep-ex].

[3] ATLAS Collaboration, *Search for high-mass dilepton resonances using 139* fb^{-1} *of pp collision data collected at* $\sqrt{s}$ *=13 TeV with the ATLAS detector*. Phys. Lett. **B796** (2019) pp. 68–87, arXiv:1903.06248 [hep-ex].

[4] Wikipedia contributors, *Standard Model — Wikipedia, The Free Encyclopedia*, 2020. https://en.wikipedia.org/w/index.php?title=Standard_Model&oldid=962563337 (accessed on 13/07/2019).

[5] M. Tanabashi *et al.* (Particle Data Group), *Review of Particle Physics*. Physical Review D **98**(030001) (2018) .

[6] NNPDF, R. D. Ball *et al.*, *Parton distributions for the LHC run II*. JHEP **04** (2015) p. 040, arXiv:1410.8849 [hep-ph].

[7] CMS, S. Chatrchyan *et al.*, *Observation of a New Boson at a Mass of 125 GeV with the CMS Experiment at the LHC*. Phys. Lett. B **716** (2012) pp. 30–61, arXiv:1207.7235 [hep-ex].

[8] ATLAS, G. Aad *et al.*, *Observation of a new particle in the search for the Standard Model Higgs boson with the ATLAS detector at the LHC*. Phys. Lett. B **716** (2012) pp. 1–29, arXiv:1207.7214 [hep-ex].

[9] WMAP, G. Hinshaw *et al.*, *Nine-Year Wilkinson Microwave Anisotropy Probe (WMAP) Observations: Cosmological Parameter Results*. Astrophys. J. Suppl. **208** (2013) p. 19, arXiv:1212.5226 [astro-ph.CO].

[10] Planck, P. Ade *et al.*, *Planck 2013 results. I. Overview of products and scientific results*. Astron. Astrophys. **571** (2014) p. A1, arXiv:1303.5062 [astro-ph.CO].

[11] M. E. Peskin and D. V. Schroeder, *An Introduction to Quantum Field Theory*. Westview Press, 1995.

[12] H. Lehmann, K. Symanzik, and W. Zimmermann, *Zur Formulierung quantisierter Feldtheorien*. Il Nuovo Cimento **1**(1) (1955) pp. 205–225.

[13] M. Thomson, *Modern particle physics*. Cambridge University Press, New York, 2013.

[14] E. Noether, *Invariante Variationsprobleme*. Nachrichten von der Gesellschaft der Wissenschaften zu Göttingen, Mathematisch-Physikalische Klasse (1918) pp. 235–257. https://eudml.org/doc/59024.

[15] S. Haywood, *Symmetries and conservation laws in particle physics: An introduction to group theory for particle physicists*. World Scientific, 2010.

[16] G. Zweig, *An SU(3) model for strong interaction symmetry and its breaking. Version 2*, pp. 22–101. 2, 1964.

[17] M. E. Peskin and D. V. Schroeder, *An Introduction to quantum field theory*. Addison-Wesley, Reading, USA, 1995.

[18] P. A. Dirac, *The quantum theory of the electron*. Proc. Roy. Soc. Lond. A **117** (1928) pp. 610–624.

[19] SNO Collaboration, *Direct Evidence for Neutrino Flavor Transformation from Neutral-Current Interactions in the Sudbury Neutrino Observatory*. Physical Review Letters **89**(011301) (2002) .

[20] S. L. Glashow, *The renormalizability of vector meson interactions*. Nuclear Physics **10** (1959) pp. 107–117.

[21] A. Salam and J. C. Ward, *Weak and electromagnetic interactions*. Il Nuovo Cimento **11**(4) (1959) pp. 568–577.

[22] S. Weinberg, *A Model of Leptons*. Physical Review Letters **19**(21) (1967) pp. 1264–1266.

[23] P. W. Higgs, *Broken Symmetries and the Masses of Gauge Bosons*. Physical Review Letters **13**(16) (1964) pp. 508–509.

[24] F. Englert and R. Brout, *Broken Symmetry and the Mass of Gauge Vector Mesons*. Physical Review Letters **13**(9) (1964) pp. 321–323.

[25] J. Goldstone, A. Salam, and S. Weinberg, *Broken Symmetries*. Phys. Rev. **127** (Aug, 1962) pp. 965–970. https://link.aps.org/doi/10.1103/PhysRev.127.965.

[26] S. Drell and T.-M. Yan, *Partons and their Applications at High-Energies*. Annals Phys. **66** (1971) p. 578.

[27] J. M. Campbell, J. Huston, and W. Stirling, *Hard Interactions of Quarks and Gluons: A Primer for LHC Physics*. Rept. Prog. Phys. **70** (2007) p. 89, arXiv:hep-ph/0611148.

[28] Super-Kamiokande, Y. Fukuda *et al.*, *Evidence for oscillation of atmospheric neutrinos*. Phys. Rev. Lett. **81** (1998) pp. 1562–1567, arXiv:hep-ex/9807003.

[29] G. F. Giudice, *Naturally Speaking: The Naturalness Criterion and Physics at the LHC*. arXiv:0801.2562 [hep-ph].

[30] S. P. Martin, *A Supersymmetry primer*. Adv. Ser. Direct. High Energy Phys. **21** (2010) pp. 1–153, arXiv:hep-ph/9709356.

[31] N. Arkani-Hamed, S. Dimopoulos, and G. Dvali, *The Hierarchy problem and new dimensions at a millimeter*. Phys. Lett. B **429** (1998) pp. 263–272, arXiv:hep-ph/9803315.

[32] A. V. Manohar, *Introduction to Effective Field Theories* in Les Houches summer school: EFT in Particle Physics and Cosmology, 4, 2018. arXiv:1804.05863 [hep-ph].

[33] R. Contino, A. Falkowski, F. Goertz, C. Grojean, and F. Riva, *On the Validity of the Effective Field Theory Approach to SM Precision Tests*. JHEP **07** (2016) p. 144, arXiv:1604.06444 [hep-ph].

[34] S. Weinberg, *Baryon and Lepton Nonconserving Processes*. Phys. Rev. Lett. **43** (1979) pp. 1566–1570.

[35] E. E. Jenkins, A. V. Manohar, and P. Stoffer, *Low-Energy Effective Field Theory below the Electroweak Scale: Operators and Matching*. JHEP **03** (2018) p. 016, arXiv:1709.04486 [hep-ph].

[36] W. Buchmuller and D. Wyler, *Effective Lagrangian Analysis of New Interactions and Flavor Conservation*. Nucl. Phys. B **268** (1986) pp. 621–653.

[37] B. Grzadkowski, M. Iskrzynski, M. Misiak, and J. Rosiek, *Dimension-Six Terms in the Standard Model Lagrangian*. JHEP **10** (2010) p. 085, arXiv:1008.4884 [hep-ph].

[38] J. de Blas, M. Chala, and J. Santiago, *Global Constraints on Lepton-Quark Contact Interactions*. Phys. Rev. D **88** (2013) p. 095011, arXiv:1307.5068 [hep-ph].

[39] E. Eichten, I. Hinchliffe, K. D. Lane, and C. Quigg, *Super Collider Physics*. Rev. Mod. Phys. **56** (1984) pp. 579–707. [Addendum: Rev. Mod. Phys.58,1065(1986)].

[40] E. Eichten, K. D. Lane, and M. E. Peskin, *New Tests for Quark and Lepton Substructure*. Phys. Rev. Lett. **50** (1983) pp. 811–814. [,369(1983)].

[41] ALEPH, S. Schael *et al.*, *Fermion pair production in e^+e^- collisions at 189-209-GeV and constraints on physics beyond the standard model*. Eur. Phys. J. C **49** (2007) pp. 411–437, arXiv:hep-ex/0609051.

[42] DELPHI, J. Abdallah *et al.*, *Measurement and interpretation of fermion-pair production at LEP energies above the Z resonance*. Eur. Phys. J. C **45** (2006) pp. 589–632, arXiv:hep-ex/0512012.

[43] H1, ZEUS, M. Wing, *Measurements of deep inelastic scattering at HERA* in 32nd International Symposium on Physics in Collision, 1, 2013, pp. 93–106. arXiv:1301.7572 [hep-ex].

[44] ZEUS, S. Chekanov *et al.*, *Search for contact interactions, large extra dimensions and finite quark radius in e p collisions at HERA*. Phys. Lett. B **591** (2004) pp. 23–41, arXiv:hep-ex/0401009.

[45] CDF, D0, W. Orejudos, *Searches at the Tevatron* in 31st International Conference on High Energy Physics, 10, 2002, pp. 749–752.

[46] D0, B. Abbott *et al.*, *Measurement of the high mass Drell-Yan cross-section and limits on quark electron compositeness scales*. Phys. Rev. Lett. **82** (1999) pp. 4769–4774, arXiv:hep-ex/9812010.

[47] CMS Collaboration, *Search for contact interactions and large extra dimensions in the dilepton mass spectra from proton-proton collisions at $\sqrt{s} = 13$ TeV*. JHEP **04** (2019) p. 114, arXiv:1812.10443 [hep-ex].

[48] G. D. Cowan, *Statistical Data Analysis*. Oxford University Press, 1998.

[49] J. Plato, *A.N. Kolmogorov, Grundbegriffe der wahrscheinlichkeitsrechnung (1933)*. Landmark Writings in Western Mathematics 1640-1940 (12, 2005) pp. 960–969.

[50] F. James and M. Roos, *Errors on ratios of small numbers of events*. Nuclear Physics B **172** (12, 1980) p. 475.

[51] K. Cranmer, *Practical Statistics for the LHC* in Proceedings, 2011 European School of High-Energy Physics (ESHEP 2011): Cheile Gradistei, Romania, September 7-20, 2011, 2015, pp. 267–308. arXiv:1503.07622 [physics.data-an].

[52] F. James and M. Roos, *Minuit: A System for Function Minimization and Analysis of the Parameter Errors and Correlations*. Comput. Phys. Commun. **10** (1975) pp. 343–367.

[53] G. Cowan, K. Cranmer, E. Gross, and O. Vitells, *Asymptotic formulae for likelihood-based tests of new physics*. Eur. Phys. J. C **71** (2011) p. 1554, arXiv:1007.1727 [physics.data-an].

[54] ATLAS, M. Aaboud *et al.*, *Combination of searches for invisible Higgs boson decays with the ATLAS experiment*. Phys. Rev. Lett. **122**(23) (2019) p. 231801, arXiv:1904.05105 [hep-ex].

[55] T. Junk, *Confidence level computation for combining searches with small statistics*. Nucl. Instrum. Meth. A **434** (1999) pp. 435–443, arXiv:hep-ex/9902006.

[56] A. L. Read, *Presentation of search results: The CL(s) technique*. J. Phys. G **28** (2002) pp. 2693–2704.

[57] S. Wilks, *The Large-Sample Distribution of the Likelihood Ratio for Testing Composite Hypotheses*. Annals Math. Statist. **9**(1) (1938) pp. 60–62.

[58] L. Evans and P. Bryant, *LHC Machine*. Journal of Instrumentation **3**(S08001) (2008) .

[59] K. Schindl, *The Injector Chain for the LHC* in Proceedings of the 9th LEP-SPS Performance Workshop, Chamonix, France, 1999, pp. 47–52. https://cds.cern.ch/record/384396.

[60] CERN, *The Large Hadron Collider*. https://home.cern/science/accelerators/large-hadron-collider (accessed on 13/07/2019).

[61] CERN, *The CERN Accelerator Complex*. https://cds.cern.ch/record/2636343 (accessed on 13/07/2019).

[62] CMS Collaboration, *The CMS experiment at the CERN LHC*. Journal of Instrumentation **3**(S08004) (2008) .

[63] ATLAS Collaboration, *The ATLAS Experiment at the CERN Large Hadron Collider*. Journal of Instrumentation **3**(S08003) (2008) .

[64] LHCb Collaboration, *The LHCb Detector at the LHC*. Journal of Instrumentation **3**(S08005) (2008) .

[65] ALICE Collaboration, *The ALICE experiment at the CERN LHC*. Journal of Instrumentation **3**(S08002) (2008) .

[66] TOTEM, G. Anelli *et al.*, *The TOTEM experiment at the CERN Large Hadron Collider*. JINST **3** (2008) p. S08007.

[67] LHCf, O. Adriani *et al.*, *The LHCf detector at the CERN Large Hadron Collider*. JINST **3** (2008) p. S08006.

[68] ATLAS Experiment, CERN, *Computer generated image of the whole ATLAS detector*. https://cds.cern.ch/record/1095924 (accessed on 14/07/2019).

[69] ATLAS Collaboration, *ATLAS inner detector: Technical Design Report*. CERN-LHCC-97-016, ATLAS-TDR-4, 1997. https://cdsweb.cern.ch/record/331063.

[70] ATLAS Collaboration, *ATLAS Insertable B-Layer Technical Design Report*. CERN-LHCC-2010-013, ATLAS-TDR-19, 2010. https://cdsweb.cern.ch/record/1291633.

[71] A. La Rosa, *The ATLAS Insertable B-Layer: from construction to operation*. Journal of Instrumentation **11** (2016) p. C12036.

[72] ATLAS Experiment, CERN, *Computer generated image of the ATLAS Liquid Argon*. https://cds.cern.ch/record/1095928 (accessed on 31/07/2019).

[73] ATLAS Collaboration, *ATLAS liquid-argon calorimeter: Technical Design Report*. CERN-LHCC-96-041, ATLAS-TDR-2, 1996. https://cdsweb.cern.ch/record/331061.

[74] ATLAS Collaboration, *ATLAS tile calorimeter: Technical Design Report*. CERN-LHCC-96-042, ATLAS-TDR-3, 1996. https://cdsweb.cern.ch/record/331062.

[75] M. Aharrouche *et al.*, *Energy linearity and resolution of the ATLAS electromagnetic barrel calorimeter in an electron test-beam*. Nuclear Instruments and Methods in Physics Research A **568** (2006) pp. 601–623.

[76] ATLAS Collaboration, *Results from a new combined test of an electromagnetic liquid argon calorimeter with a hadronic scintillating-tile calorimeter*. Nuclear Instruments and Methods in Physics Research A **449** (2000) pp. 462–477.

[77] ATLAS Collaboration, *ATLAS muon spectrometer: Technical Design Report*. CERN-LHCC-97-022, ATLAS-TDR-10, 1997. https://cdsweb.cern.ch/record/331068.

[78] E. W. Weisstein, *Sagitta*. From *MathWorld* – A Wolfram Web Resource. http://mathworld.wolfram.com/Sagitta.html (accessed on 2019-08-18).

[79] ATLAS Experiment, CERN, *Computer generated image of the ATLAS Muons subsystem*. https://cds.cern.ch/record/1095929 (accessed on 31/07/2019).

[80] A. Ruiz Martínez, *The Run-2 ATLAS Trigger System*. Journal of Physics **762**(012003) (2016) .

[81] E. Simioni, *The Hardware Topological Trigger of ATLAS: Commissioning and Operations*. ATL-DAQ-SLIDE-2018-102, 2016. https://cds.cern.ch/record/2305791.

[82] ATLAS Collaboration, *ATLAS high-level trigger, data-acquisition and controls: Technical Design Report*. CERN-LHCC-2003-022, ATLAS-TDR-16, 2003. https://cdsweb.cern.ch/record/616089.

[83] W. Herr and B. Muratori, *Concept of luminosity* in CERN Accelerator School: Intermediate Course on Accelerator Physics, 2006.

[84] V. Balagura, *Notes on van der Meer Scan for Absolute Luminosity Measurement*. Nucl. Instrum. Meth. A **654** (2011) pp. 634–638, arXiv:1103.1129 [physics.ins-det].

[85] S. van der Meer, *Calibration of the effective beam height in the ISR*. CERN-ISR-PO-68-31. ISR-PO-68-31, 1968. http://cds.cern.ch/record/296752.

[86] ATLAS Collaboration, *Luminosity Public Results Run-2*. https://twiki.cern.ch/twiki/bin/view/AtlasPublic/LuminosityPublicResultsRun2 (accessed on 15/01/2020).

[87] Y. L. Dokshitzer, *Calculation of the Structure Functions for Deep Inelastic Scattering and e+ e- Annihilation by Perturbation Theory in Quantum Chromodynamics*. Sov. Phys. JETP **46** (1977) pp. 641–653.

[88] V. N. Gribov and L. N. Lipatov, *Deep inelastic e p scattering in perturbation theory*. Soviet Journal of Experimental and Theoretical Physics **15** (1972) pp. 438–450.

[89] G. Altarelli and G. Parisi, *Asymptotic freedom in parton language*. Nuclear Physics B **126** (1977) pp. 298–318.

[90] B. Andersson *et al.*, *Parton fragmentation and string dynamics*. Physics Reports **97**(2-3) (1983) pp. 31–145.

[91] B. R. Webber, *A QCD model for jet fragmentation including soft gluon interference*. Nuclear Physics B **238** (1984) pp. 492–528.

[92] S. Agostinelli *et al.*, *Geant4 – a simulation toolkit*. Nuclear Instruments and Methods in Physics Research A **506** (2003) pp. 250–303.

[93] J. Allison *et al.*, *Geant4 Developments and Applications*. IEEE Transactions on Nuclear Science **53** (2006) pp. 270–278.

[94] J. Allison *et al.*, *Recent developments in Geant4*. Nuclear Instruments and Methods in Physics Research A **835** (2016) pp. 186–225.

[95] T. Cornelissen *et al.*, *Concepts, Design and Implementation of the ATLAS New Tracking (NEWT)*. ATL-SOFT-PUB-2007-007, 2007. https://cds.cern.ch/record/1020106/.

[96] R. Frühwirth, *Application of Kalman filtering to track and vertex fitting*. Nuclear Instruments and Methods in Physics Research A **262** (1987) pp. 444–450.

[97] W. Lampl, S. Laplace, D. Lelas, P. Loch, H. Ma, S. Menke, S. Rajagopalan, D. Rousseau, S. Snyder, and G. Unal, *Calorimeter Clustering Algorithms: Description and Performance*. ATL-LARG-PUB-2008-002. ATL-COM-LARG-2008-003, Apr, 2008. https://cds.cern.ch/record/1099735.

[98] ATLAS Collaboration, *Improved electron reconstruction in ATLAS using the Gaussian Sum Filter-based model for bremsstrahlung*. ATLAS-CONF-2012-047, 2012. https://cdsweb.cern.ch/record/1449796.

[99] ATLAS Collaboration, *Electron reconstruction and identification in the ATLAS experiment using the 2015 and 2016 LHC proton-proton collision data at* $\sqrt{s}$ *= 13 TeV*. Eur. Phys. J. **C79**(8) (2019) p. 639, arXiv:1902.04655 [physics.ins-det].

[100] ATLAS Collaboration, *Electron and photon performance measurements with the ATLAS detector using the 2015–2017 LHC proton-proton collision data*. JINST **14**(12) (2019) p. P12006, arXiv:1908.00005 [hep-ex].

[101] ATLAS Collaboration, *Electron and photon reconstruction and performance in ATLAS using a dynamical, topological cell clustering-based approach*. ATL-PHYS-PUB-2017-022, Dec, 2017. http://cds.cern.ch/record/2298955.

[102] M. Cacciari and G. P. Salam, *Pileup subtraction using jet areas*. Phys. Lett. **B659** (2008) pp. 119–126, arXiv:0707.1378 [hep-ph].

[103] ATLAS Collaboration, *Muon reconstruction performance of the ATLAS detector in proton–proton collision data at* $\sqrt{s}$ *=13 TeV*. Eur. Phys. J. **C76**(5) (2016) p. 292, arXiv:1603.05598 [hep-ex].

[104] J. Illingworth and J. Kittler, *A survey of the Hough transform*. Computer Vision, Graphics, and Image Processing **44** (1988) pp. 87–116.

[105] R. Atkin, *Review of jet reconstruction algorithms*. Journal of Physics: Conference Series **645** (Oct, 2015) p. 012008. https://doi.org/10.1088%2F1742-6596%2F645%2F1%2F012008.

[106] M. Cacciari, G. P. Salam, and G. Soyez, *The anti-k_t jet clustering algorithm*. Journal of High Energy Physics **2008**(063) (2008) .

[107] ATLAS Collaboration, *Performance of missing transverse momentum reconstruction for the ATLAS detector in the first proton-proton collisions at at $\sqrt{s}$= 13 TeV.* , Jul, 2015. https://cds.cern.ch/record/2037904.

[108] J. J. Aubert *et al.*, *Experimental Observation of a Heavy Particle J*. Phys. Rev. Lett. **33** (Dec, 1974) pp. 1404–1406.

[109] J. E. Augustin *et al.*, *Discovery of a Narrow Resonance in e^+e^- Annihilation*. Phys. Rev. Lett. **33** (Dec, 1974) pp. 1406–1408.

[110] S. W. Herb *et al.*, *Observation of a Dimuon Resonance at 9.5 GeV in 400-GeV Proton-Nucleus Collisions*. Phys. Rev. Lett. **39** (Aug., 1977) pp. 252–255.

[111] U. Collaboration, *Experimental observation of lepton pairs of invariant mass around 95 GeV/c^2 at the CERN SPS collider*. Phys. Lett. B **126**(5) (1983) pp. 398 – 410.

[112] U. Collaboration, *Evidence for $Z^0 \to e^+e^-$ at the CERN pp collider*. Phys. Lett. B **129**(1) (1983) pp. 130 – 140.

[113] ALEPH, DELPHI, L3, OPAL, SLD, LEP Electroweak Working Group, SLD Electroweak Group, SLD Heavy Flavour Group, S. Schael *et al.*, *Precision electroweak measurements on the Z resonance*. Phys. Rept. **427** (2006) pp. 257–454, arXiv:hep-ex/0509008 [hep-ex].

[114] ATLAS Collaboration, *Measurement of the double-differential high-mass Drell-Yan cross section in pp collisions at $\sqrt{s} = 8$ TeV with the ATLAS detector*. JHEP **08** (2016) p. 009, arXiv:1606.01736 [hep-ex].

[115] ATLAS Collaboration, *Measurement of the angular coefficients in Z-boson events using electron and muon pairs from data taken at $\sqrt{s} = 8$ TeV with the ATLAS detector*. JHEP **08** (2016) p. 159, arXiv:1606.00689 [hep-ex].

[116] CMS Collaboration, *Measurement of the weak mixing angle using the forward-backward asymmetry of Drell-Yan events in pp collisions at 8 TeV*. Eur. Phys. J. **C78**(9) (2018) p. 701, arXiv:1806.00863 [hep-ex].

[117] CMS Collaboration, *Search for high-mass resonances in dilepton final states in proton-proton collisions at $\sqrt{s} = 13$ TeV*. JHEP **06** (2018) p. 120, arXiv:1803.06292 [hep-ex].

[118] *SUSYTools TWiki page*. https://twiki.cern.ch/twiki/bin/view/AtlasProtected/SusyObjectDefinitionsr2113TeV.

[119] *ATLAS Collaboration, ATLAS Athena Guide.* https://atlassoftwaredocs.web.cern.ch/athena/.

[120] ATLAS Collaboration, *Performance of the ATLAS Trigger System in 2015.* Eur. Phys. J. **C77**(5) (2017) p. 317, arXiv:1611.09661 [hep-ex].

[121] ATLAS Collaboration, "The Pythia 8 A3 tune description of ATLAS minimum bias and inelastic measurements incorporating the Donnachie–Landshoff diffractive model." ATL-PHYS-PUB-2016-017, 2016. https://cds.cern.ch/record/2206965.

[122] S. Alioli, P. Nason, C. Oleari, and E. Re, *A general framework for implementing NLO calculations in shower Monte Carlo programs: the POWHEG BOX.* JHEP **06** (2010) p. 043, arXiv:1002.2581 [hep-ph].

[123] S. Frixione, P. Nason, and C. Oleari, *Matching NLO QCD computations with parton shower simulations: the POWHEG method.* JHEP **11** (2007) p. 070, arXiv:0709.2092 [hep-ph].

[124] H.-L. Lai *et al.*, *New parton distributions for collider physics.* Phys. Rev. D **82** (2010) p. 074024, arXiv:1007.2241 [hep-ph].

[125] T. Sjöstrand, S. Mrenna, and P. Z. Skands, *A brief introduction to PYTHIA 8.1.* Comput. Phys. Commun. **178** (2008) p. 852, arXiv:0710.3820 [hep-ph].

[126] C. Anastasiou, L. J. Dixon, K. Melnikov, and F. Petriello, *High-precision QCD at hadron colliders: Electroweak gauge boson rapidity distributions at next-to-next-to leading order.* Phys. Rev. D **69** (2004) p. 094008, arXiv:hep-ph/0312266.

[127] S. Dulat, T.-J. Hou, J. Gao, M. Guzzi, J. Huston, P. Nadolsky, J. Pumplin, C. Schmidt, D. Stump, and C. P. Yuan, *New parton distribution functions from a global analysis of quantum chromodynamics.* Phys. Rev. **D93**(3) (2016) p. 033006, arXiv:1506.07443 [hep-ph].

[128] A. Arbuzov, D. Bardin, S. Bondarenko, P. Christova, L. Kalinovskaya, U. Klein, V. Kolesnikov, L. Rumyantsev, R. Sadykov, and A. Sapronov, *Update of the MCSANC Monte Carlo integrator, v. 1.20.* JETP Lett. **103**(2) (2016) pp. 131–136, arXiv:1509.03052 [hep-ph].

[129] T. Gleisberg, S. Höche, F. Krauss, M. Schönherr, S. Schumann, *et al.*, *Event generation with SHERPA 1.1.* JHEP **02** (2009) p. 007, arXiv:0811.4622 [hep-ph].

[130] M. Czakon and A. Mitov, *Top++: A Program for the Calculation of the Top-Pair Cross-Section at Hadron Colliders.* Comput. Phys. Commun. **185** (2014) p. 2930, arXiv:1112.5675 [hep-ph].

[131] P. Golonka and Z. Was, *PHOTOS Monte Carlo: a precision tool for QED corrections in Z and W decays*. Eur. Phys. J. C **45** (2006) pp. 97–107, arXiv:hep-ph/0506026.

[132] P. Artoisenet, R. Frederix, O. Mattelaer, and R. Rietkerk, *Automatic spin-entangled decays of heavy resonances in Monte Carlo simulations*. JHEP **03** (2013) p. 015, arXiv:1212.3460 [hep-ph].

[133] D. J. Lange, *The EvtGen particle decay simulation package*. Nucl. Instrum. Meth. A **462** (2001) pp. 152–155.

[134] ATLAS Collaboration, "ATLAS Pythia 8 tunes to 7 TeV data." ATL-PHYS-PUB-2014-021, 2014. https://cds.cern.ch/record/1966419.

[135] D. Stump, J. Huston, J. Pumplin, W.-K. Tung, H. L. Lai, S. Kuhlmann, and J. F. Owens, *Inclusive jet production, parton distributions, and the search for new physics*. JHEP **10** (2003) p. 046, arXiv:hep-ph/0303013.

[136] R. D. Ball *et al.*, *Parton distributions with LHC data*. Nucl. Phys. B **867** (2013) pp. 244–289, arXiv:1207.1303 [hep-ph].

[137] W. Verkerke and D. Kirkby, "The RooFit toolkit for data modeling," 2003. arXiv:physics/0306116 [physics.data-an].

[138] E. W. Varnes, *A Poisson likelihood approach to fake lepton estimation with the matrix method*. arXiv:1606.06817 [hep-ex].

[139] P. J. Falke, *Search for new heavy resonances in the dilepton final state and calibration of the LAr Phase-1 Upgrade demonstrator at the ATLAS experiment. Recherche de nouvelles résonances à haute masse dans l'état final dilepton et calibration du démonstrateur pour l'upgrade Phase-1 du calorimètre électromagnétique dans l'expérience ATLAS*, Oct, 2019. Presented 20 Sep 2019. http://cds.cern.ch/record/2693468.

[140] ATLAS Collaboration, *Luminosity determination in pp collisions at $\sqrt{s}$ = 8 TeV using the ATLAS detector at the LHC*. Eur. Phys. J. C **76**(CERN-EP-2016-117. CERN-EP-2016-117. 12) (Aug, 2016) p. 653. 71 p. https://cds.cern.ch/record/2208146.

[141] ATLAS Collaboration, *Electron efficiency measurements with the ATLAS detector using 2012 LHC proton–proton collision data*. Eur. Phys. J. **C77**(3) (2017) p. 195, arXiv:1612.01456 [hep-ex].

[142] J. Butterworth *et al.*, *PDF4LHC recommendations for LHC Run II*. J. Phys. G **43** (2016) p. 023001, arXiv:1510.03865 [hep-ph].

[143] J. Butterworth, E. Dobson, U. Klein, B. Mellado Garcia, T. Nunnemann, J. Qian, D. Rebuzzi, and R. Tanaka, *Single Boson and Diboson Production Cross Sections in pp Collisions at sqrts=7 TeV*. ATL-COM-PHYS-2010-695, Aug, 2010. https://cds.cern.ch/record/1287902.

[144] ATLAS, ATLAS Collaboration, *Search for resonances in diphoton events at $\sqrt{s}$=13 TeV with the ATLAS detector*. JHEP **09** (2016) p. 001, arXiv:1606.03833 [hep-ex].

[145] ATLAS Collaboration, *Search for new phenomena in high-mass diphoton final states using 37 fb^{-1} of proton–proton collisions collected at $\sqrt{s} = 13$ TeV with the ATLAS detector*. Phys. Lett. **B775** (2017) pp. 105–125, arXiv:1707.04147 [hep-ex].

[146] Particle Data Group, M. Tanabashi, K. Hagiwara, K. Hikasa, K. Nakamura, and Sumino, *Review of Particle Physics*. Phys. Rev. D **98** (Aug, 2018) p. 030001.

[147] ATLAS Collaboration, *Search for high-mass new phenomena in the dilepton final state using proton–proton collisions at $\sqrt{s} = 13$ TeV with the ATLAS detector*. Phys. Lett. B **761** (2016) p. 372, arXiv:1607.03669 [hep-ex].

[148] ATLAS Collaboration, *Search for contact interactions and large extra dimensions in the dilepton channel using proton–proton collisions at $\sqrt{s} = 8$ TeV with the ATLAS detector*. Eur. Phys. J. C **74** (2014) p. 3134, arXiv:1407.2410 [hep-ex].

[149] ATLAS Collaboration, *Search for contact interactions and large extra dimensions in dilepton events from pp collisions at $\sqrt{s} = 7$ TeV with the ATLAS detector*. Phys. Rev. D **87** (2013) p. 015010, arXiv:1211.1150 [hep-ex].

[150] M. Frate, K. Cranmer, S. Kalia, A. Vandenberg-Rodes, and D. Whiteson, *Modeling Smooth Backgrounds and Generic Localized Signals with Gaussian Processes*, 2017.